Universidade de Lisboa
Faculdade de Ciências
Departamento de Física

Radiological Protection and Nuclear Engineering Studies in Multi-MW Target Systems

Raul Fernandes Luís

Doutoramento em Física

2013

Universidade de Lisboa
Faculdade de Ciências
Departamento de Física

Radiological Protection and Nuclear Engineering Studies in Multi-MW Target Systems

Raul Fernandes Luís

Tese orientada pelo Prof. Doutor Pedro Vaz e pelo Prof. Doutor José Marques, especialmente elaborada para a obtenção do grau de Doutor em Física

2013

Acknowledgements

It would not have been possible to accomplish this work without the help of many people, to whom I am deeply grateful. In particular, I would like to thank:

To Doctor Pedro Vaz, whose example of uncompromising professionalism I have strived to follow during the past 5 years; the importance of his continuous support, advice, guidance and friendship, at all times throughout this period, can never be overstated. To him I owe my greatest debt of gratitude, for having always contributed with more than I could ask for.

To Doctor José Marques, for the enthusiastic supervision of my work; for his continual willingness to discuss results and for his support in my computational work, at all stages of my PhD programme; for giving the best advices at the right times; and last, but certainly not least, for the importance of his words in my decision to follow this route.

To Doctor Yacine Kadi, for welcoming me at CERN for the first time and for the opportunity to work in the EURISOL Project. The lessons I learned in the first year of my PhD fellowship, and mostly from our invaluable discussions, were solid foundations for the rest of my work. It is a privilege to continue to learn under his supervision to this day.

To Doctor Thierry Stora, for the supervision, guidance and support during the past 3 years; it was his determination in improving the performance of the target system of ISOLDE that gave me the opportunity to develop most of the work presented in this thesis. I cannot overemphasise the importance of the construction of the prototype target system, as well as the possibility to take part in the experimental measurements at ISOLDE. I must also acknowledge the invaluable support I received from a very friendly group of people at ISOLDE during the experimental tests, which included Alexander Gottberg, Tânia Mendonça, João Pedro Ramos and Christoph Seiffert. The contributions of Stefano Marzari and Bernard Crepieux to the construction and operation of the prototype target system are also acknowledged.

To my friends at IST-CTN, who played the important role of turning my daily routine into such a pleasant experience. In particular, I would like to thank my colleague and friend Yuriy Romanets, not only for the countless occasions on which he has helped me with his advice and expertise, but also for his friendship and example of willingness to help others.

I would like to acknowledge the financial support from the following institutions:

- Instituto Superior Técnico, Campus Tecnológico e Nuclear (IST-CTN), for welcoming me in its campus and for the fellowship CERN/FP/83586/2008 – “Colaboração com o CERN no âmbito da participação portuguesa no projecto "EURISOL Design Study (2º ano)”;

- Fundação para a Ciência e Tecnologia (FCT), for the PhD fellowship SFRH/BD/60255/2009;

- The European Community, under the FP6 project: EURISOL DS, contract no. 515768 RIDS;
- The European Organisation for Nuclear Research (CERN).

I thankfully acknowledge the computer resources, technical expertise and assistance provided by CENTRA/IST. Many computations in this work were performed at the cluster "Baltasar-Sete-Sóis", supported by the DyBHo–256667 ERC Starting Grant. In particular, the activation studies for the ISOLDE target system would not have been possible without this computer cluster and the great expertise and efficiency of its administrator, Sérgio Almeida.

Finally, and most importantly, this thesis is dedicated to my family and to Rita, for the unconditional support.

Resumo

Diversos projectos inovadores envolvendo Tecnologias Nucleares emergiram nas últimas duas décadas por todo o Mundo, tendo em vista aplicações como fontes de espalação, sistemas ADS (*accelerator-driven systems*) e instalações para a produção de feixes de iões radioactivos (RIB). Nas últimas três décadas, e ao contrário do que tem sucedido nos reactores nucleares, as intensidades dos feixes de neutrões disponíveis em fontes de espalação têm aumentado continuamente, e essa tendência deverá manter-se ao longo do século XXI. Projectos inovadores como ESS, MYRRHA ou EURISOL encontram-se na linha da frente do desenvolvimento de fontes de neutrões cada vez mais intensas, utilizando feixes de protões com energias até 2 GeV e intensidades até alguns mA. A construção das referidas instalações envolve estudos complexos de Tecnologia Nuclear e Protecção Radiológica executados por equipas multidisciplinares de cientistas de diferentes áreas científicas. Os fluxos de neutrões com intensidades sem precedentes previstos para essas instalações podem ter aplicações em diversas áreas como Física e Astrofísica Nucleares, Medicina e Ciência dos Materiais.

Nesta tese foram estudados em detalhe os sistemas de alvos de duas instalações para a produção de RIBs usando o método ISOL (*Isotope Separation On-Line*): a instalação ISOLDE, que opera no CERN desde 1967, e a instalação EURISOL, que se pretende construir na Europa. Para o sistema de alvos de alta potência da instalação EURISOL efectuou-se um estudo detalhado de Protecção Radiológica, utilizando o programa de Monte Carlo FLUKA, envolvendo cálculos de fluxos de neutrões, taxas de cisão, dose equivalente ambiental e produção de resíduos radioactivos nos alvos e zonas adjacentes. Testaram-se diferentes materiais para os diversos componentes do sistema de alvos, tendo como objectivo melhorar a performance neutrónica do sistema e manter as actividades residuais resultantes da activação de materiais tão baixas quanto possível.

O segundo objectivo consistiu no estudo do sistema de alvos da instalação ISOLDE, que foi simulado utilizando o FLUKA e os programas de cálculo de secções eficazes ABRABLA e TALYS. O objectivo era propor optimizações que permitissem maximizar o desempenho do sistema para a produção de isótopos ricos em em neutrões, suprimindo a produção de isobares ricos em protões. Para esse efeito, dois sistemas de alvos alternativos foram propostos; o mais simples dos dois foi usado como modelo para a construção de um protótipo, que foi testado na instalação ISOLDE no CERN. Os resultados experimentais mostram claramente que é possível, com alterações simples nas configurações dos sistemas de alvos, produzir feixes mais puros de isótopos ricos em neutrões na região dos nuclidos duplamente mágicos ^{78}Ni e ^{132}Sn. Efectuou-se ainda um estudo de Protecção Radiológica comparando o desempenho do protótipo com o dos sistemas de alvos normalmente utilizados na instalação ISOLDE.

Palavras-chave: Protecção Radiológica, Tecnologia Nuclear, RIB, Simulações Monte Carlo, FLUKA, ABRABLA, TALYS, EURISOL, ISOLDE, Dose, Activação, Isótopos Ricos em Neutrões

Abstract

Several innovative projects involving nuclear technology have emerged around the world in recent years, for applications such as spallation neutron sources, accelerator-driven systems for the transmutation of nuclear waste and radioactive ion beam (RIB) production. While the available neutron fluxes from nuclear reactors did not increase substantially in intensity over the past three decades, the intensities of neutron sources produced in spallation targets have increased steadily, and should continue to do so during the 21st century. Innovative projects like ESS, MYRRHA and EURISOL lie at the forefront of the ongoing pursuit for increasingly bright neutron sources; driven by proton beams with energies up to 2 GeV and intensities up to several mA, the construction of their proposed facilities involves complex Nuclear Technology and Radiological Protection design studies executed by multidisciplinary teams of scientists and engineers from different branches of Science. The intense neutron fluxes foreseen for those facilities can be used in several scientific research fields, such as Nuclear Physics and Astrophysics, Medicine and Materials Science.

In this work, the target systems of two facilitites for the production of RIBs using the Isotope Separation On-Line (ISOL) method were studied in detail: ISOLDE, operating at CERN since 1967, and EURISOL, the next-generation ISOL facility to be built in Europe. For the EURISOL multi-MW target station, a detailed study of Radiological Protection was carried out using the Monte Carlo code FLUKA. Simulations were done to assess neutron fluences, fission rates, ambient dose equivalent rates during operation and after shutdown and the production of radioactive nuclei in the targets and surrounding materials. Different materials were discussed for different components of the target system, aiming at improving its neutronics performance while keeping the residual activities resulting from material activation as low as possible.

The second goal of this work was to perform an optimisation study for the ISOLDE neutron converter and fission target system. The target system was simulated using FLUKA and the cross section codes TALYS and ABRABLA, with the objective of maximising the performance of the system for the production of pure beams of neutron-rich isotopes, suppressing the contaminations by undesired neutron-deficient isobars. Two alternative target systems were proposed in the optimisation studies; the simplest of the two, with some modifications, was built as a prototype and tested at ISOLDE. The experimental results clearly show that it is possible, with simple changes in the layouts of the target systems, to produce purer beams of neutron-rich isotopes around the doubly magic nuclei ^{78}Ni and ^{132}Sn. A study of Radiological Protection was also performed, comparing the performances of the prototype target system and the standard ISOLDE target system.

Keywords: Radiological Protection, Nuclear Technology, RIB, Monte Carlo simulations, FLUKA, ABRABLA, TALYS, EURISOL, ISOLDE, Dose rates, Activation, Neutron-rich isotopes

Contents

List of Figures

List of Tables

List of Acronyms, Symbols and Abbreviations

UC_x	Uranium Carbide
ADS	Accelerator-Driven System
ALARA	As Low as Reasonably Achievable
ARIEL	Advanced Rare Isotope Laboratory
ATW	Accelerator Transmutation of Waste
BSS	Basic Safety Standards
CADS	China Accelerator Driven System
CARIF	China Advanced Rare Ion Beam Facility
CERN	Organisation Européenne pour la Recherche Nucléaire
EFIT	European Facility for Industrial Transmutation
EGS	Electron Gamma Shower
EL	Exemption Limit
ENIAC	Electronic Numerical Integrator and Computer
ESS	European Spallation Source
EURISOL	European Isotope Separation On-Line
EU	European Union
FAIR	Facility for Antiproton and Ion Research
FLUKA	Fluktuierende Kaskade (German: Fluctuating Cascade)

FRIB	Facility for Rare Isotope Beams
GANIL	Grand Accélérateur National d'Ions Lourds
GEANT	Geometry and Tracking
GPS	General Purpose Separator
HIE-ISOLDE	High Intensity and Energy ISOLDE
HRS	High Resolution Separator
IAEA	International Atomic Energy Agency
IAEA	International Atomic Energy Agency
ICRP	International Commission on Radiological Protection
ICRU	International Commission on Radiation Units & Measurements
ING	Intense Neutron Generator
ISAC	Isotope Separator and Accelerator
ISOLDE	Isotope Separation On-Line Device
ISOL	Isotope Separation On-Line
J-PARC	Japan Proton Accelerator Research Complex
JAEA	Japan Atomic Energy Agency
JSNS	Japanese Spallation Neutron Source
KoRIA	Korea Rare Isotope Accelerator
LBE	Lead Bismuth Eutectic
LET	Linear Energy Transfer
LGE	Lead Gold Eutectic
LINAC	Linear Accelerator
LNL-INFN	Laboratori Nazionali di Legnaro - Istituto Nazionale di Fisica Nucleare
LNT	Linear-Non-Threshold Model
MAFF	Munich Accelerator for Fission Fragments
MCNPX	Monte Carlo N-Particle Extended

MEGAPIE	MEGAwatt PIlot Experiment
MEL	Multiple of the Exemption Limit
MYRRHA	Multi-purpose hYbrid Research Reactor for High-tech Applications
NSCL/MSU	National Superconducting Cyclotron Laboratory / Michigan State University
NuPECC	Nuclear Physics European Collaboration Committee
NUSTAR	Nuclear Structure, Astrophysics and Reactions
PHITS	Particle and Heavy Ion Transport code System
PIAFE	Projet d'Ionisation et d'Acceleration de Faisceaux Exotiques
PSB	Proton Synchrotron Booster
PSI	Paul Scherrer Institute
PS	Proton Synchrotron
RARF	RIKEN Accelerator Research Facility
REX	Radioactive beam EXperiment
RIBF	Radioactive Ion Beam Factory
RIB	Radioactive Ion Beam
SC	Synchro-Cyclotron
SINQ	Swiss Spallation Neutron Source
SNS	Spallation Neutron Source
SPES	Selective Production of Exotic Species
SPIRAL	Système de Production d'Ions Radioactifs Accélérés en Ligne
TRIUMF	TRI-University Meson Facility
UNSCEAR	United Nations Scientific Committee on the Effects of Atomic Radiation
WHO	World Health Organization
WNR	Weapons Neutron Research Facility

Part I

Introduction

Chapter 1

Innovative Multi-MW Target Facilities

In recent years, several innovative projects involving nuclear technology have emerged around the world, for applications such as spallation neutron sources (SNS), accelerator-driven systems (ADS) and radioactive ion beam (RIB) production. In these projects, proton beams with intensities up to a few mA and energies from 600 MeV to 2 GeV impinge on a spallation target, which can be made of several different high-density materials, such as liquid-mercury, lead, lead-bismuth or tungsten. The power delivered to the targets has been rising throughout the years, as the quest for increasingly bright neutron sources goes on. Fig. 1.1 shows the evolution of thermal neutron fluxes in different types of neutron sources since the discovery of the neutron in 1932. It is clear that the fluxes available from nuclear reactors have not increased substantially over the past three decades, while the available fluxes from neutron spallation sources have increased steeply and have a margin to become even higher in the future [1]. Such intense neutron fluxes can be used for several different scientific applications, such as Nuclear Physics and Astrophysics, Nuclear Medicine and Materials Science.

Due to the high radiation fields and heat deposition generated through nuclear reactions in the targets, the design of such facilities involves important considerations related to Radiological Protection and Safety (shielding, residual dose rate due to material activation, radiotoxicity of the spallation products) and Nuclear Technology (neutronics assessment, material damage). With power depositions of up to 5 MW foreseen for the near future in spallation targets, the design studies for such projects involve complex scientific and engineering studies carried out by multidisciplinary teams. Computational studies and experimental/prototype tests exploiting the potential of existing facilities are important components of the research and development process which leads to the successful engineering design of such multi-Megawatt facilities. Nuclear safety and licensing issues need to be carefully addressed during the design stage.

This chapter provides an overview of the existing and planned SNS, RIB and ADS facilities in the world. Since they are essential for this work, RIB facilities will be discussed in greater detail.

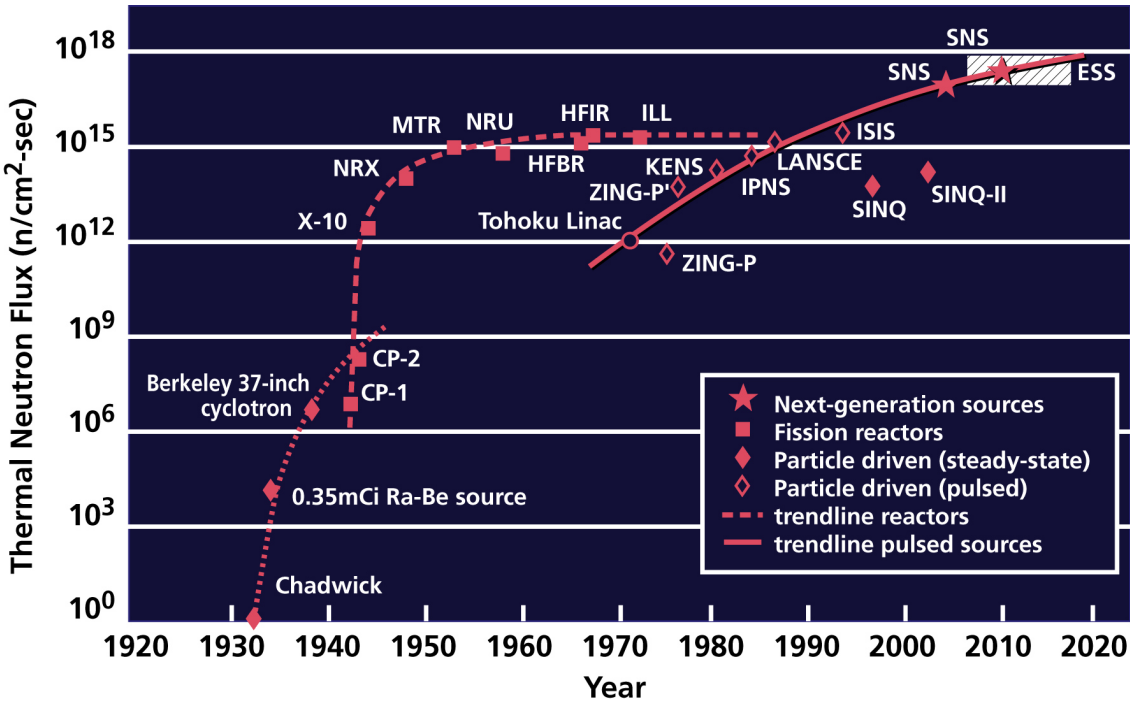

Figure 1.1: Evolution of thermal neutron fluxes in different types of research neutron sources (obtained from [2]).

1.1 Radioactive Ion Beam Facilities

Ever since the discovery of radioactivity, the radioactive isotopes of the nuclear chart have been essential for fundamental physics research and for many applications in various fields of science. During the last decades, previously unaccessible regions of the nuclear chart have been explored, due to developments in the production and study of radioactive species that has occurred in several RIB facilities around the world.

Fig. 1.2 shows the nuclear landscape, with the numbers of protons Z and the number of neutrons N plotted on the vertical and horizontal axes, respectively [3]. The region where nuclei are stable against the emission of neutrons and protons is limited by the proton and neutron drip-lines, which lie mostly in unexplored regions of the landscape. Moving away from the valley of beta stability, the production of the most exotic nuclei is confronted with difficulties related to low production cross sections, very short half-lives and contamination by unwanted species [4]. One of the main objectives of the current and next-generation RIB facilities is to explore the *terra incognita* (unexplored region) of the nuclear landscape.

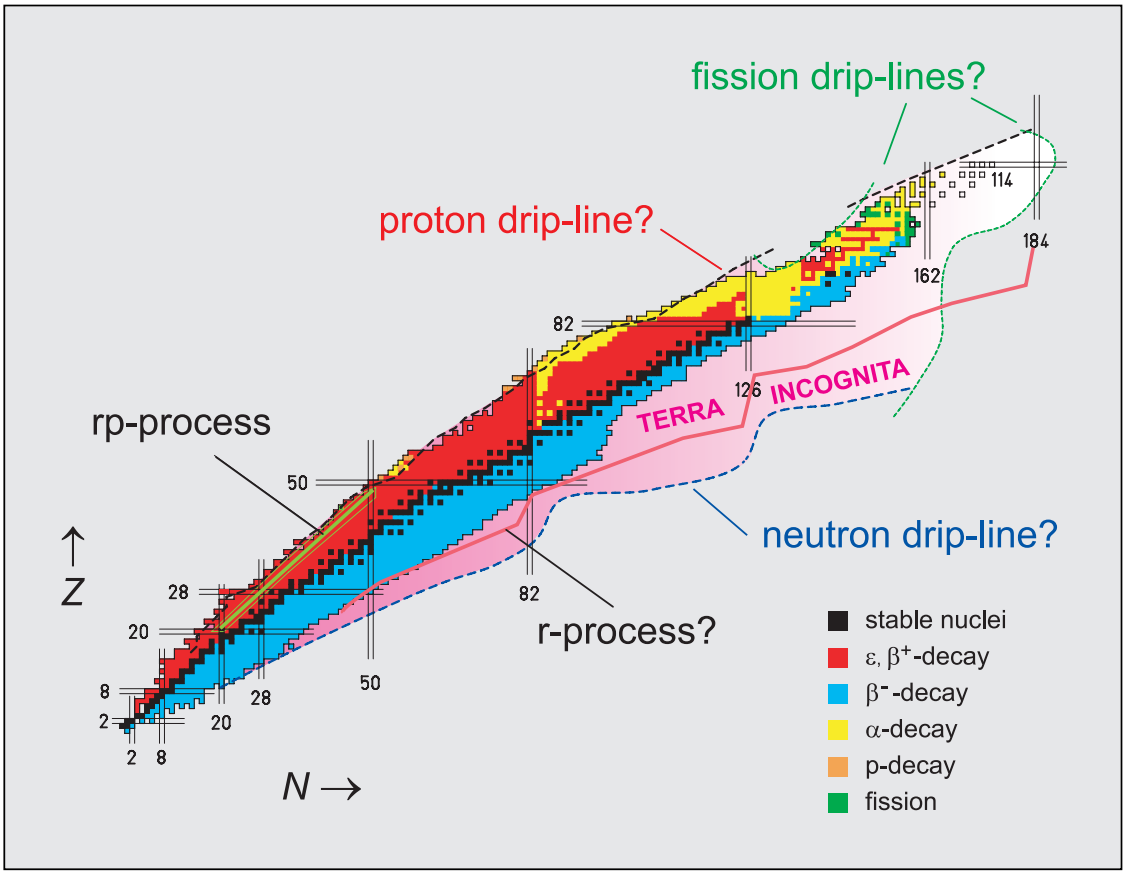

Figure 1.2: Nuclear Landscape (obtained from [3]).

1.1.1 RIB Production Methods - ISOL *vs* In-Flight

The two main methods for the production of RIBs are illustrated in Fig. 1.3: In-Flight and Isotope Separation On-Line (ISOL). In the In-Flight method, heavy ion beams with energies ranging from 100 MeV to 1 GeV per nucleon are directed to a thin target, in which they undergo fragmentation or fission. The fragments are selected in flight by a Fragment Recoil Separator, according to their masses and charges, and directed to a secondary target, for spectroscopy and nuclear reaction studies. In the ISOL method, a beam of light particles from an accelerator (the *driver-accelerator*) hits a thick target, producing radioactive nuclei through fission, spallation and fragmentation reactions. The radioactive nuclei are extracted from the heated target, ionised in an ion source, mass-separated, post-accelerated and delivered to the experimental areas.

The two methods are complementary. The ISOL method produces very high-quality beams, with low emittance and good energy resolution, but is limited to RIBs with relatively long half-lives, due to the time it takes to extract the nuclei from the target and transport them to the ion source. The In-Flight method, on the other hand, allows the production of RIBs of nuclides with very short half-lives, but the quality of the beams is lower when compared to the ISOL method and

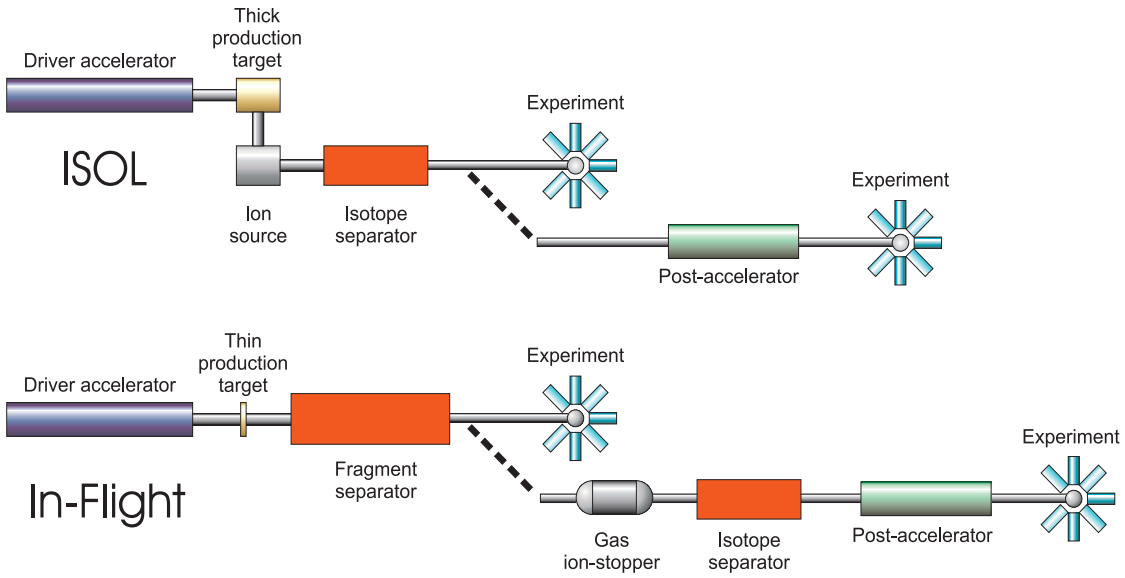

Figure 1.3: A schematic drawing of the ISOL and in-flight based RIB production methods (obtained from [3]).

the RIB energies are restricted to energies close to those of the primary beam [3, 5].

1.1.2 RIB Facilities in the World

1.1.2.1 In-Flight

Table 1.1 lists the main In-Flight facilities for the production of RIBs currently operating in the world: GANIL in Caen (France) [6], NSCL/MSU in East Lansing (MI, USA) [7], GSI in Darmstadt (Germany) [8] and RARF RIKEN in Tokyo (Japan) [9]. The GANIL driver consists of two separated sector cyclotrons which produce heavy ions from C to Ar up to 100 MeV u^{-1} and can accelerate masses up to U at 25 MeV u^{-1}. The NSCL/MSU facility is driven by coupled superconducting cyclotrons while the RIKEN facility has a room temperature cyclotron. The synchrotron at GSI can provide energies up to 2 GeV u^{-1}, but with lower intensities than the ones provided by the cyclotron facilities. Since 2007, Japan has taken the lead in high-energy RIBs using the In-Flight method, with the Radioactive Ion Beam Factory (RIBF) in RIKEN, which is able to produce RIBs with energies up to 350 MeV u^{-1} [4].

1.1.2.2 ISOL

The major existing ISOL facilities for RIB production are listed in Table 1.2. These are the ISOLDE facility at CERN (Geneva, Switzerland) [10], the SPIRAL facility at GANIL [11] and the TRIUMF/ISAC facility in Vancouver (Canada) [12]. The ISAC facility at the TRIUMF laboratory

Facility	Location	Driver	Primary energy	Typical intensity	Fragment separator
GANIL	Caen, France	Two separated sector cyclotrons	Up to 100 MeV u^{-1}	^{36}S 10^{13} pps ^{48}Ca 2×10^{12} pps	SISSI + ALPHA
GSI	Darmstadt, Germany	LINAC + synchrotron	Up to 2 GeV u^{-1}	10^{10} ppspill	FRS
NSCL/MSU	East Lansing, MI, USA	Two coupled superconducting cyclotrons	Up to 200 MeV u^{-1}	^{40}Ar 5×10^{11} pps	A1900
RARF RIKEN	Tokyo, Japan	Ring cyclotron	Up to 100 MeV u^{-1}	^{40}Ar 5×10^{11} pps	RIPS

Table 1.1: Characteristics of the main in-flight facilities in operation (obtained from [4]).

uses a 500 MeV proton cyclotron as driver and two post-accelerators, ISAC1 and ISAC2, which can accelerate RIBs up to 5 and 11 MeV u^{-1}, respectively. A UC_x target has been recently commissioned, greatly expanding the variety of available RIBs. SPIRAL uses the GANIL coupled cyclotrons as driver and a thick graphite target: the radioactive species are produced by fragmentation of the incident heavy ion beam, which is stopped in the target. The available beams are limited to noble gases, oxygen and fluorine, but can reach up to 25 MeV u^{-1}, the highest energy available in existing ISOL facilities [4]. The ISOLDE facility at CERN is the precursor of all existing ISOL facilities worldwide, and will be described in detail in Chapter 6.

Facility	Location	Driver	Post-accelerator	Final energy	Main beams available
REX-ISOLDE	CERN, Geneva	PS Booster, 1.4 GeV protons	REX LINAC	0.3A–3A MeV	Large variety including fission fragments
SPIRAL	Caen, France	GANIL coupled cyclotrons	CIME cyclotron	2.7A–25A	He. Ne, Ar, Kr, N,O. F
TRIUMF/ISAC	Vancouver, Canada	500 MeV proton cyclotron	ISAC I and II RFQ + SC LINAC	0.2–11A MeV	Large variety including fission fragments

Table 1.2: Characteristics of the main ISOL facilities in operation (obtained from [4]). A is the mass of the accelerated isotope.

1.1.3 Intermediate- and Next- Generation RIB Facilities

1.1.3.1 The European Roadmap

NuPECC (Nuclear Physics European Collaboration Committee) published in 2010 the latest issue of its Long Range Plan for Nuclear Physics in Europe [13], which includes a plan for the development of RIB facilities in Europe for the next decades. The NuPECC recommendations contemplate, as a first step, a timely completion of the constructions of FAIR at GSI and SPIRAL2 at GANIL. They also support the construction of HIE-ISOLDE (HIE – High Intensity and

Energy) at CERN and SPES at LNL-INFN Legnaro, which, combined with SPIRAL2, will constitute the group of intermediate-generation ISOL facilities in Europe before the construction of the next-generation facility, EURISOL (European Isotope Separation On-Line) [14, 15].

FAIR (Facility for Antiproton and Ion Research) [16, 17] is one of the most ambitious Nuclear Physics projects of this decade, with various scientific applications which include studies of the structure of nuclei, physics of nuclear reactions, and nuclear astrophysics at the In-Flight RIB facility NUSTAR (Nuclear Structure, Astrophysics and Reactions). Primary beams with intensities two to three orders of magnitude higher than those of the current GSI facility and a fragment separator with improved efficiency will allow the production of RIBs with up to a factor 10^4 improvement in intensity. NUSTAR at FAIR will be the next-generation facility for the production of RIBs using the In-Flight method [4].

The SPIRAL2 facility [18, 19] is an ambitious extension of the GANIL accelerator complex. Its driver accelerator will be a superconducting linear accelerator (LINAC) capable of delivering up to 5 mA of deuterons at 40 MeV to a target system composed of a carbon converter and an uranium target, producing radioactive ion beams in the mass range 60-140 with intensities up to 10^{10} particles per second, which can then be post-accelerated to energies up to 20 MeV u^{-1}.

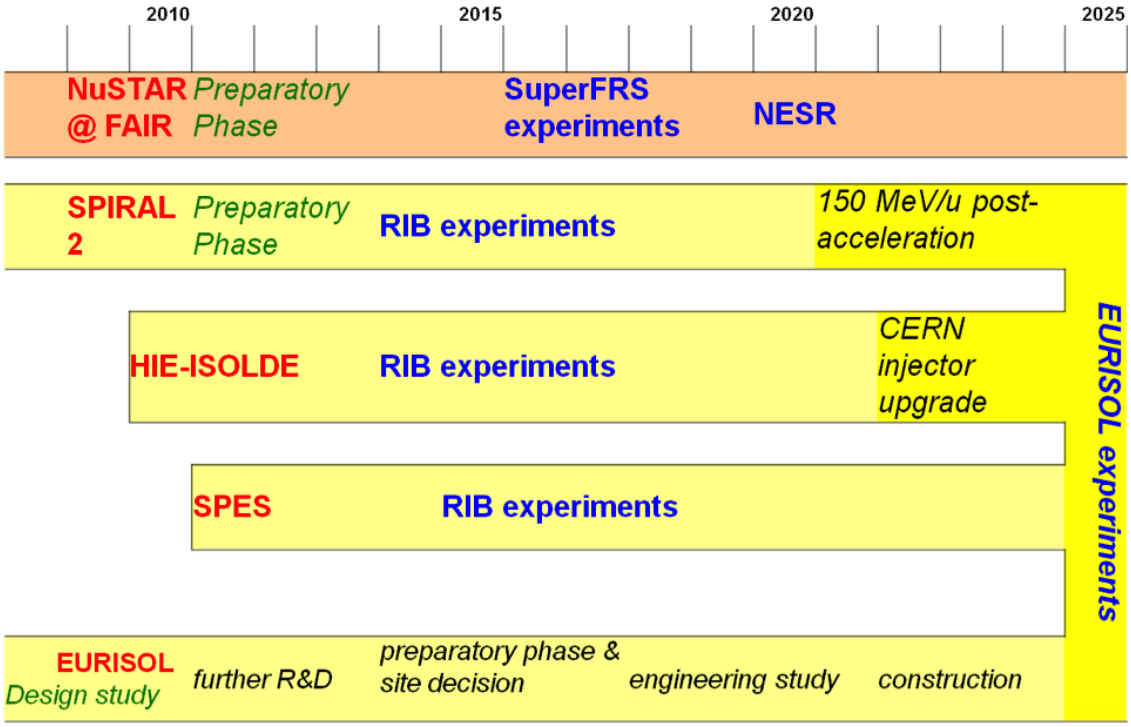

Figure 1.4: The NuPECC roadmap for RIB facilities (obtained from [4]).

SPES [20] is a new ISOL facility at LNL-INFN that will focus on the production of neutron-rich

beams. A proton beam of 40 MeV and 200 μA will hit a uranium carbide target and neutron-rich isotopes will be produced as fission fragments at a rate of 10^{13} fissions per second. The uranium carbide targets have already been developed and represent a technical innovation in terms of their capability to sustain the primary beam power [4]. Besides SPIRAL2 and SPES, HIE-ISOLDE is the remaining of the intermediate-generation ISOL facilities that will serve as a bridge between the first-generation facilities and the ultimate ISOL facility, EURISOL. HIE-ISOLDE and EURISOL will be described in detail in Chapters 6 and 4, respectively. Fig. 1.4 shows the NuPECC roadmap for RIB facilities in Europe.

1.1.3.2 North America and Asia

There are also important RIB facilities planned for the future in North America and Asia. FRIB (Facility for Rare Isotope Beams) [21] will be an new In-Flight RIB facility at MSU, aiming to produce intense beams of rare isotopes; ARIEL (Advanced Rare Isotope Laboratory) [22] is currently under construction at TRIUMF, with the objective of expanding the Rare Isotope Beam program for Nuclear Physics and Astrophysics, Nuclear Medicine and Materials Science. In Asia, the KoRIA (Korea Rare Isotope Accelerator) project [23] aims at building multi-purpose accelerator facility to provide exotic isotopes, using an innovative combination of the In-Flight and ISOL techniques; the CARIF (China Advanced Rare Ion Beam Facility) project [24] in Beijing (China) plans to use neutrons from a research reactor to induce fission in a uranium carbide target, producing fission fragments at a rate of 2×10^{15} fissions per second, close to the fission rate foreseen for EURISOL [4].

1.2 Spallation Neutron Sources

A spallation neutron source is an accelerator-based facility which produces neutron beams by bombarding a thick high-density target with intense (mA) proton beams [25]. The produced neutrons can be used in a multitude of applications in the basic sciences (condensed-matter, material, medicine, protein and biology, geology, hydrogen-rich energy storage) and nuclear sciences (irradiation, rare-isotope production, radiography) [26]. Although there is a relatively small number of spallation neutron sources worldwide, new target systems are currently being developed to be used in next-generation facilities. Those targets should be able to withstand the power deposition of proton beams with several MW [27].

1.2.1 Candidate Materials for Spallation Neutron Sources

Most high-density materials should be good candidates for spallation neutron sources, since the spallation reaction takes place in all elements and the number of released neutrons increases with the atomic number of the material. There are however some constraints which must be taken into account for solid targets: they must have good thermal conductivity at the temperature of operation, a small thermal expansion coefficient, low activation and resistance to corrosion, among others.

The very high melting point of tantalum, its resistance to corrosion and the high neutron yields would make tantalum the most promising candidate material for solid spallation targets, but its high neutron absorption cross section makes it extremely susceptible to activation and afterheat. Tungsten is also a good candidate, due to its high-density (19.3 g cm^{-3}, compared to the 16.6 g cm^{-3} of tantalum) and better thermal conductivity. Its main disadvantage is its susceptibility to corrosion with water under irradiation: to address this issue, it is usually cladded with tantalum. Another candidate would be depleted uranium, since it has 1.8 times higher neutron yield than Ta or W; so far, however, experiments using uranium plate targets as spallation sources for high-power applications have failed [27].

Liquid-metal targets are an attractive option for facilities aiming at very high power beams, since they allow to evacuate the heat generated in the target material away from the impact point of the proton beam, to cool elsewhere. One of the key problems with this concept is the target container window, which remains under irradiation at all times (windowless liquid metal target concepts have been studied to address this issue). For liquid targets, it is imperative that the materials have low melting points, to avoid excessive corrosion damage of the target components. This leaves three options as main candidates: mercury ($T_m = -38.9$ °C), the eutectic mixture of 45% lead and 55% bismuth (LBE, $T_m = 125$ °C) and, eventually, lead ($T_m = 327.5$ °C). The formation of the α-emmiter ^{210}Po, from the activation of bismuth, is a potential problem for LBE targets [28].

Recently, a lead–gold eutectic alloy (LGE) has also been proposed as an alternative for liquid-metal targets, due to its low melting point (212.5 °C), high boiling point (> 1700 °C) (which grants it the two main advantages that LBE has over mercury: being solid at room temperature and non-volatile at high temperatures) and expected neutronics performance. Further investigations are necessary in order to determine if LGE might be a good candidate for high-power spallation neutron sources [29].

1.2.2 Spallation Neutron Sources in the World – Past, Present and Future

Table 1.3 lists the most important projects involving neutron spallation sources from the past, present and future, along with the respective target concepts. The first of these was the Intense Neutron Generator (ING) project [30], launched in 1963 in the Chalk River Laboratory of Atomic Energy of Canada, with the objective of producing intense neutron beams for isotope production and neutron beam experiments. This facility would have a LINAC with 1.5 kilometres delivering a proton beam with 1 GeV and 65 mA to a flowing LBE target. ING was never built because the proposed accelerator was not feasible at the time: although there were significant technical developments during its design studies, the project was cancelled in 1968 [31].

Table 1.3: Overview of target concepts in different spallation neutron sources (obtained from [27]).

Period	Project - Country	Beam Power	Target Concept	Status (2008)
1960s	ING - Canada	60 MW	Flowing PbBi, windowless	Cancelled
Late 1970s	KENS - Japan	3 kW	Solid (U,Ta)	EoL 2005
	IPNS - USA	7 kW	W–Ta solid U	EoL 2008
	WNR - USA	70 kW	Solid W	Operating
Early 1980s	ISIS - UK	160 kW	Solid (U) (Ta) W–Ta	Operating
	SNQ - Germany	5.5 MW	Solid Pb (U), rotat. Flowing PbBi, windowless (opt.)	Cancelled
1997-2007	SINQ - CH	600 kW	Solid Pb	Finished
	MEGAPIE - CH		Liquid PbBi	
Early 2000s	ESS Europe	5 MW		
	SNS USA	1.4 MW		
	JSNS Europe	1 MW		

Several spallation sources were built in the late 1970s and early 1980s, including KENS (Japan) [32], IPNS [33] and WNR [34] (USA), and ISIS (UK) [35], with beam powers ranging from 3 kW to 160 kW. All these projects used solid targets of different materials (materials between parenthesis in Table 1.3 refer to older targets). WNR and ISIS are still operating today with solid tungsten targets (with a tantalum clad in the ISIS case).

The SINQ research facility at the Paul Scherrer Institute (PSI) in Switzerland has been operating since 1997 [36], using a rod target - a target made up from cylindrical lead elements and cooled by water in cross-flow. With a nominal beam power of nearly 1 MW on the target, SINQ was

the first neutron source to reach the MW range, and it is still among the most powerful neutron spallation sources operating today [37]. As part of the SINQ development, the MEGAwatt PIlot Experiment (MEGAPIE) project was started in 2000 by an international collaboration to design, build and operate a liquid LBE spallation target to withstand a 1 MW beam [38]. The MEGAPIE target was operated over a period of four months with a proton beam current of up to 1.35 mA, demonstrating, for the first time, that a LBE target can be operated with a proton beam in the MW range [27]. Dismantling of the MEGAPIE target started in 2009 [39], and 800 MEGAPIE samples were delivered to partners earlier this year for post irradiation investigation [40].

Today, the most important spallation neutron source projects using or planning to use beams in the MW range are JSNS (Japanese Spallation Neutron Source), SNS (Spallation Neutron Source) and ESS (European Spallation Source). JSNS [41], in the Japan Proton Accelerator Research Complex (J-PARC) [42], started its operation in 2008 using a liquid-mercury spallation target. The proton beam power was gradually increased until it reached 200 kW, in November 2010. The aim was to increase the beam power up to 1 MW, but in 11 March 2011 a component of the target vessel was damaged as a consequence of the Great East Japan Earthquake, delaying the goals of the project [43]. The recovery work of the J-PARC accelerator complex took nine months, but additional problems occurred after the restart of user operation [44].

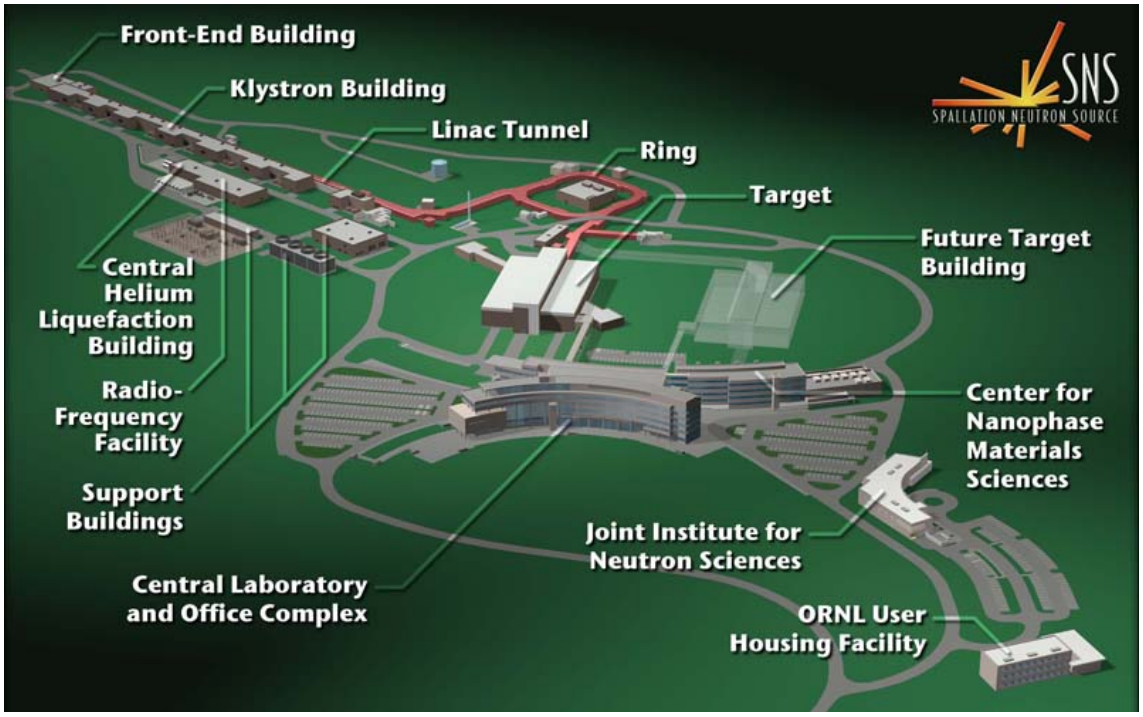

Figure 1.5: Conceptual layout of the SNS facility. At full power, SNS will deliver 1.4 MW of beam power onto the target (obtained from [45]).

SNS [46] is another neutron spallation source using liquid-mercury as target material, operating in the Oak Ridge National Laboratory (USA). Operational since 2006, SNS officially reached 1

MW of beam power on target on September 18, 2009, making it the most powerful spallation source in the world [47]. At full power, SNS will deliver 1.4 MW of beam power to the target (Fig. 1.5).

The ESS project [48] is the result of a joint European effort which aims to build the ultimate neutron spallation source in Europe. In May 2009, it was agreed that ESS would be built on a green-field site in Lund, Sweden. First neutrons will be produced in 2019 and full power operation, at approximately 5 MW (a 2.5 GeV proton beam with 2 mA of average intensity), is foreseen for 2025. Several target concepts have been discussed and studied [49], including a liquid-mercury option, but a decision has been made in 2011 to build a single target station with a rotating helium-cooled tungsten target [50]. The rotating target concept was first considered in 1979 for the SNQ project [51] in Germany, to deal with heat removal and radiation damage problems. SNQ, the first project to propose a neutron spallation source in the multi-MW range (5 MW), was cancelled in 1985, but the concept of a rotating target has been revived in recent years by a number of projects, including ESS [27].

1.3 Accelerator-Driven Systems

An accelerator driven system consists of a subcritical reactor core driven by a high-power proton accelerator through a spallation target, which is coupled to the reactor core. ADS systems have been studied since the early 1990s, as well as their role for nuclear waste transmutation and energy production [52]. Estimations from the International Atomic Energy Agency (IAEA) predict that the current net installed capacity of 370 GW_e in 434 nuclear power reactors worldwide [53] could be doubled by 2030, mainly due to the start of new nuclear power plants in Asian countries (China, India, Republic of Korea, Pakistan, Indonesia and Vietnam). For this reason, and taking into account the opposition of the public to the construction of geologic repositories, many studies have been carried out in recent years in order to find ways to reduce the amount of long-lived radioactive waste through transmutation in ADS systems [54].

The Chinese government is currently supporting the CADS (China Accelerator Driven System) project, aiming to construct an ADS system with a 15 MW LINAC (1.5 GeV and 10 mA) and a LBE spallation target [55], with different stages of operation before it reaches full power by the 2030s [56]. India has also an ADS program which involves design studies for a 1 GeV, 30 mA LINAC and the construction of a LBE spallation target for design validation and materials testing. There are also two testing facilities for transmutation studies planned for J-PARC in Japan, which are part of the long-term strategy of the JAEA (Japan Atomic Energy Agency) to build a dedicated transmutation ADS facility, with a 30 MW LINAC and a LBE spallation target [54].

Technology demonstration of ADS systems is now gaining momentum with the decision of the

Belgian government to build MYRRHA (Multi-purpose hYbrid Research Reactor for High-tech Applications) [57], a 85 MW prototype ADS system, at SCK-CEN, the Belgian Nuclear Research Centre in Mol [52]. MYRRHA will feature a proton accelerator with a proton energy of 600 MeV and an intensity of 2.5 mA (1.5 MW), coupled to a liquid LBE spallation source (Fig. 1.6). The spallation target is located in the centre of a subcritical reactor core with a fast neutron spectrum and cooled with liquid lead-bismuth [58]. MYRRHA will be operational at full power around 2023 [59].

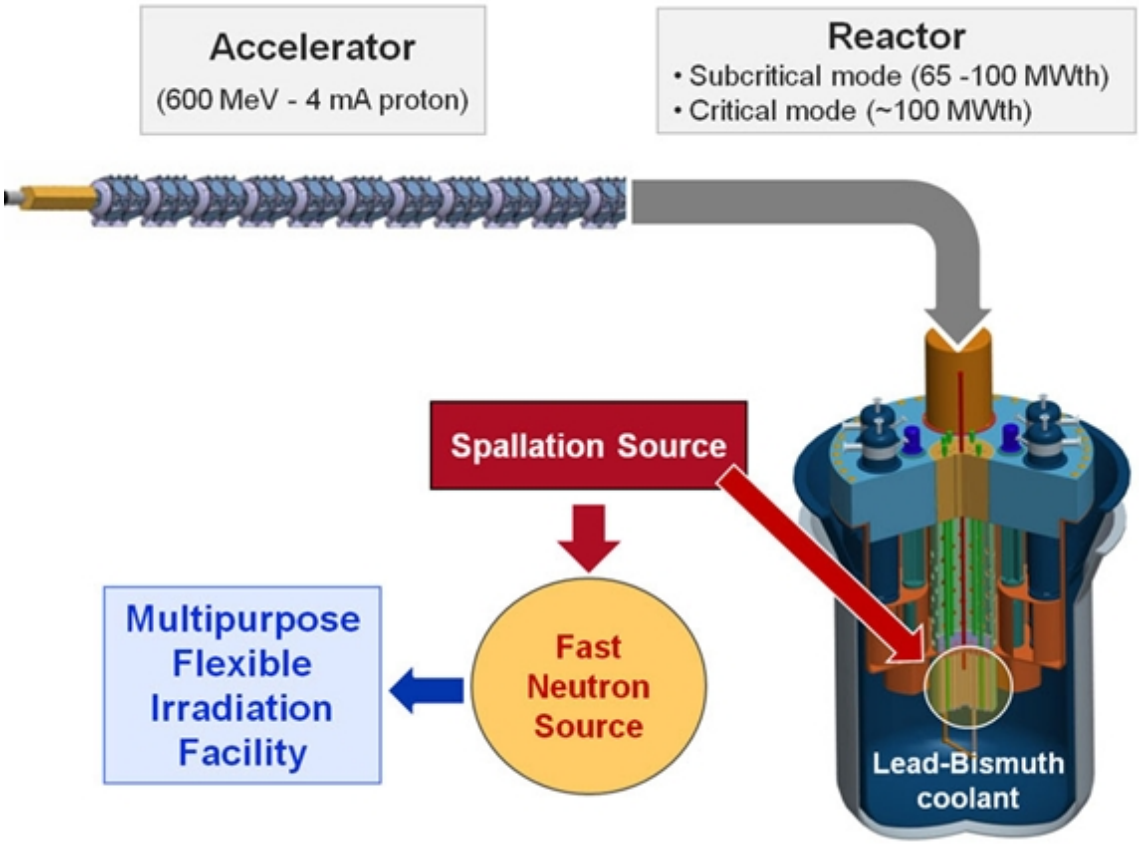

Figure 1.6: Scheme of the MYRRHA facility (obtained from [60]).

Table 1.4 shows the beam energies and intensities required for three reference ADS designs: MYRRHA, aimed at the demonstration of transmutation and ADS technologies, EFIT (European Facility for Industrial Transmutation) [61], aimed at industrial-scale prototypic operation of a single subcritical core, and ATW (Accelerator Transmutation of Waste) [62], an industrial scale facility of higher power with the capability of driving multiple subcritical cores. For demonstration purposes, accelerator and spallation target technologies have been demonstrated in spallation neutron sources at the 1 MW level, a good indicator of the feasibility of the MYRRHA facility. For industrial purposes, it is stated in [52] that *"with appropriate scaling at each step along a technology demonstration path, there are no obstacles foreseen that would preclude the deployment of spallation targets at a power level (10 to 30 MW) needed to meet the application of ADS*

Table 1.4: Driver beam power for three reference ADS Designs (adapted from [52]).

	Transmutation Demonstration (MYRRHA)	**Industrial Scale Facility driving single subcritical core (EFIT)**	**Industrial Scale Facility driving multiple subcritical cores (ATW)**
Beam Energy (GeV)	0.6	0.8	1.0
Beam Power (MW)	1.5	16	45
Beam Current (mA)	2.5	20	45

at an industrial scale". Along with the already-mentioned importance that multi-MW targetry will have for the production of RIBs and for scientific research in spallation neutron sources, the role that ADS systems may play in the future of nuclear energy production is another indication that research and development in multi-MW spallation target technologies will be increasingly important during the 21st century.

Chapter 2

Radiological Protection, Dosimetry and Activation

The International Commission on Radiological Protection (ICRP) was established in 1928 and issued its first general Recommendations in the same year, with the objective of restricting the individual dose of medical practitioners exposed to medical sources. Since then, ICRP has been issuing reports periodically, which reflect the evolution of radiological protection throughout the years. A general system of Radiological Protection aimed at encouraging a feasible and structured approach to protection has been established by a cooperation between ICRP and several international institutions, including the International Commission on Radiation Units and Measurents (ICRU), the United Nations Scientific Committee on the Effects of Atomic Radiation (UNSCEAR), the World Health Organization (WHO) and the International Atomic Energy Agency (IAEA). In this chapter, the quantities used in Radiological Protection and Dosimetry will be described, following closely the definitions given in ICRP Publication 103 [63]. Afterwards, Activation and Radiotoxicity will be briefly introduced.

2.1 Biological Effects and the Principles of Radiological Protection

The biological effects induced by ionising radiation can be grouped in two categories: deterministic and stochastic. The deterministic effects are those which manifest themselves after exposures to doses above certain thresholds, in the form of harmful tissue reactions; the stochastic effects involve either cancer development in exposed individuals owing to mutation of somatic cells or heritable disease associated with mutations in the reproductive cells. The stochastic effects cannot be predicted through cause-effect considerations: their occurrence is associated

with a probability. According to ICRP, at radiation doses below 100 mSv (see Section 2.2) it is assumed that the increase in the incidence of stochastic effects occurs with a small probability and in proportion to the increase of radiation dose over the background dose. This is stated in the Linear-Non-Threshold (LNT) model, seen by the ICRP as a prudent basis for radiological protection at low doses [63].

In the 1990 Recommendations, ICRP defined the three fundamental principles of Radiological Protection:

- **the principle of justification (of practices):** any decision that alters the radiation exposure should do more good than harm.
- **the principle of optimisation (of protection):** the likelihood of incurring exposures, the number of people exposed and the magnitude of their individual doses should be kept as low as reasonably achievable (ALARA), taking into account economic and societal factors.
- **the principle of application of dose limits:** The total dose to any individual from regulated sources in planned exposure situations other than medical exposure should not exceed the appropriate limits recommended by ICRP.

The principle of justification states that the introduction of any radiation source that increases the exposure of an individual or population should achieve the necessary benefit to the society to overcome the detriment it causes. The ALARA principle states that the level of protection must be optimised to maximise the margin of benefit over harm: exposure to ionising radiation must be kept as low as reasonably possible. The principle of application of dose limits states that the exposure of individuals to radiation from regulated sources must be kept below pre-determined limits, recommended by the ICRP and translated into international directives (EU), standards (BSS - Basic Safety Standards) and national legislations. The exception is medical exposure: in that case, it is assumed that the benefit overcomes the detriment [64].

2.2 Quantities Used in Radiological Protection

Throughout the years, special dosimetric quantities have been established which relate the doses in the organs or tissues to radiation risk, taking into account the sensitivity of the biological tissue and the different types of ionising radiation. In ICRP Publication 26 [65], in 1977, the protection quantities *dose equivalent* and *effective dose equivalent* were introduced. In 1991, ICRP Publication 60 [64] changed their definitions, and named them *equivalent dose* and *effective dose*. These quantities cannot be measured directly in body tissues: for this reason, the system of Radiological Protection includes *operational quantities*, which can be used to assess the equivalent and effective doses.

2.2.1 Absorbed Dose

The absorbed dose, D, can be defined as

$$D = \frac{d\bar{\epsilon}}{dm} \tag{2.1}$$

where $d\bar{\epsilon}$ is the mean energy imparted to a mass dm (containing many atoms or molecules) by ionising radiation. The SI unit of absorbed dose is J kg^{-1}, usually referred to as Gray (Gy). It is a measurable quantity.

2.2.2 Equivalent Dose and Radiation Weighting Factors

The equivalent dose in an organ or tissue is defined as

$$H_T = \sum_R w_R D_{T,R}, \tag{2.2}$$

where $D_{T,R}$ is the average absorbed dose in an organ or tissue T and w_R is the radiation weighting factor for radiation R. The equivalent dose in T is thus the sum of the average absorbed doses from each type of radiation multiplied by the corresponding weighting factor. The SI unit is J kg^{-1}, with the special name Sievert (Sv).

Table 2.1 lists the radiation weighting factors for the different types of ionizing radiation. Photons, electrons and muons are considered low-LET[1] radiation and have $w_R = 1$. Protons and pions have $w_R = 2$ and alpha particles, fission fragments and heavy ions have $w_R = 20$, since they have very short ranges in biological tissue and hence high ionisation densities. These types of radiation are therefore of high importance for radiological protection, mainly in internal dosimetry.

Table 2.1: Radiation weighting factors recommended by the ICRP (obtained from [63]).

Radiation Type	**Radiation Weighting Factor,** w_R
Photons	1
Electrons and muons	1
Protons and charged pions	2
Alpha particles, fission fragments, heavy ions	20
Neutrons	A continuos function of the neutron energy (Fig. 2.1)

[1] LET – Linear Energy Transfer – The average linear rate of energy loss of charged particle radiation in a medium.

The radiation weighting factors for neutrons, given by

$$w_R = \begin{cases} 2.5 + 18.2\, e^{-[\ln(E_n)]^2/6}, & \text{if } E_n < 1 \text{ MeV} \\ 5.0 + 17.0\, e^{-[\ln(2E_n)]^2/6}, & \text{if } 1 \text{ MeV} \leq E_n \leq 50 \text{ MeV} \\ 2.5 + 3.25\, e^{-[\ln(0.04E_n)]^2/6}, & \text{if } E_n > 50 \text{ MeV} \end{cases}, \tag{2.3}$$

are strongly dependent on the neutron energy, as can be seen in Fig. 2.1, due to the variation of the secondary radiation with energy. The maximum value is $w_R = 20$, for a neutron energy of the order of 1 MeV. Below this value, a significant fraction of the absorbed dose is deposited by secondary photons from the H(n, γ) reaction, which reduces the biological effectiveness[2]. For energies above above 1 MeV, all experimental data either on animals or cells show a clear decrease of biological effectiveness with increasing neutron energies [66].

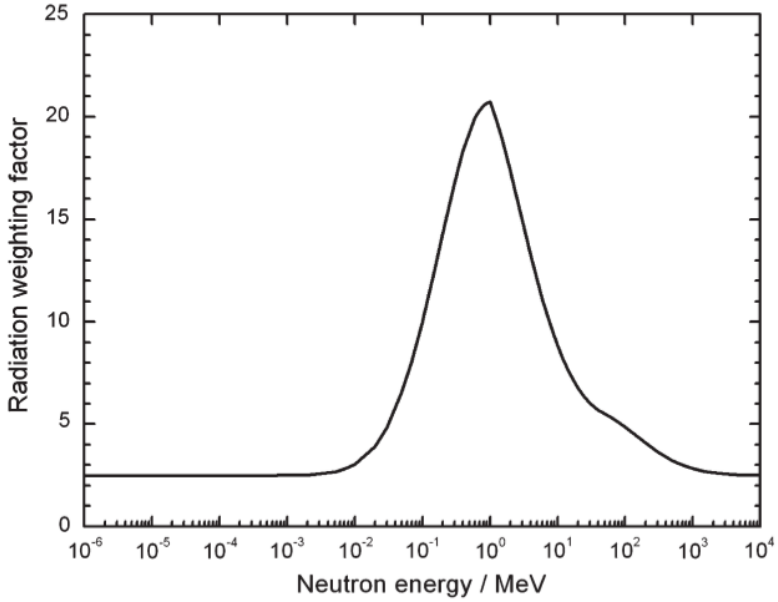

Figure 2.1: Radiation weighting factor, w_R, for neutrons, as a function of their energy (obtained from [63]).

2.2.3 Effective Dose and Tissue Weighting Factors

Different organs and tissues have different sensitivity to ionising radiation. The effective dose is defined as a weighted sum of tissue equivalent doses,

$$E = \sum_T w_T H_T = \sum_T w_T \sum_R w_R D_{T,R}, \tag{2.4}$$

[2]Relative biological effectiveness (RBE) – The ratio of a dose of a low-LET reference radiation to a dose of the radiation considered that gives an identical biological effect [63].

where w_T is the tissue weighting factor for tissue T and $\sum w_T = 1$. The sum is over all organs and tissues of the human body considered to be sensitive to stochastic effects. The unit of effective dose is J kg$^{-}1$ with the special name Sievert (Sv). Table 2.2 lists the organs and tissues for which w_T values are specified. They represent mean values for humans averaged over both sexes and all ages.

Table 2.2: Tissue weighting factors recommended by the ICRP (obtained from [63]).

Tissue	w_T	$\sum w_T$
Bone marrow (red), colon, lung, stomach, breast, remainder tissues	0.12	0.72
Gonads	0.08	0.08
Bladder, oesophagus, liver, thyroid	0.04	0.16
Bone surface, brain, salivary glands, skin	0.01	0.04
	Total	1.00

The effective dose, as well as the equivalent dose, are not measurable in practice. For this reason, computational phantoms may be used for dose assessment in occupational exposures and biokinetic models, reference physiological data and computational phantoms can be useful for the calculation of dose coefficients from intakes of radionuclides. But in most practical applications, operational quantities are used to provide conservative estimates of effective and equivalent doses.

2.2.4 Operational Quantities

The operational quantity used to assess the effective dose for area monitoring is the *ambient dose equivalent*, $H^*(10)$, calculated at a point in a radiation field and defined as the dose equivalent that would be produced by the corresponding expanded and aligned field in the ICRU sphere[3]

[3]ICRU sphere: a sphere of 30 cm diameter made of tissue equivalent material with a density of 1 g/cm^3 and a mass composition of 76.2% oxygen, 11.1% carbon, 10.1% hydrogen and 2.6% nitrogen. Used as a reference phantom in defining dose equivalent quantities [67]. From [63]: "An expanded radiation field, defined as a hypothetical field, is a radiation field in which the spectral and the angular fluence have the same value in all points of a sufficiently large volume equal to the value in the actual field at the point of interest. The expansion of the radiation field ensures that the whole ICRU sphere is thought to be exposed to a homogeneous radiation field with the same fluence, energy distribution and direction distribution as in the point of interest of the real radiation field. If all radiation is aligned in the expanded radiation field so that it is opposed to a radius vector Ω specified for the ICRU sphere, the aligned and expanded radiation field is obtained. In this hypothetical radiation field, the ICRU sphere is homogeneously irradiated from one direction, and the fluence of the field is the integral of the angular differential fluence at the point of interest in the real radiation field over all directions. In the expanded and aligned radiation field, the value of the dose equivalent at any point in the ICRU sphere is independent of the direction distribution of the radiation in the real radiation field. Conversion coefficients relating radiation field quantities to the operational quantities are usually calculated assuming a vacuum outside of the phantom considered."

at a depth of 10 mm on the radius vector opposing the direction of the aligned field. For area monitoring of low-penetrating radiation the operational quantity is the *directional dose equivalent*, $H'(0.07, \Omega)$, or, in rare cases such as when monitoring the dose to the lens of the eye, $H'(0.03, \Omega)$. The directional dose equivalent $H'(d, \Omega)$ at a point in a radiation field is defined as the dose equivalent that would be produced by the corresponding expanded field in the ICRU sphere at a depth d, on a radius in a specified direction Ω.

For individual monitoring, the operational quantity is the *personal dose equivalent*, $H_p(d)$, which is the dose equivalent in ICRU soft tissue and a depth d below a specified point in the human body (typically, the position where the dosimeter is worn). A depth of 10 mm is recommended for assessing the effective dose, while a depth of 0.07 mm is recommended for assessing the equivalent dose to the skin [63]. The relationship between the basic physical quantities, the operational quantities and the protection quantities is summarised in Fig. 2.2.

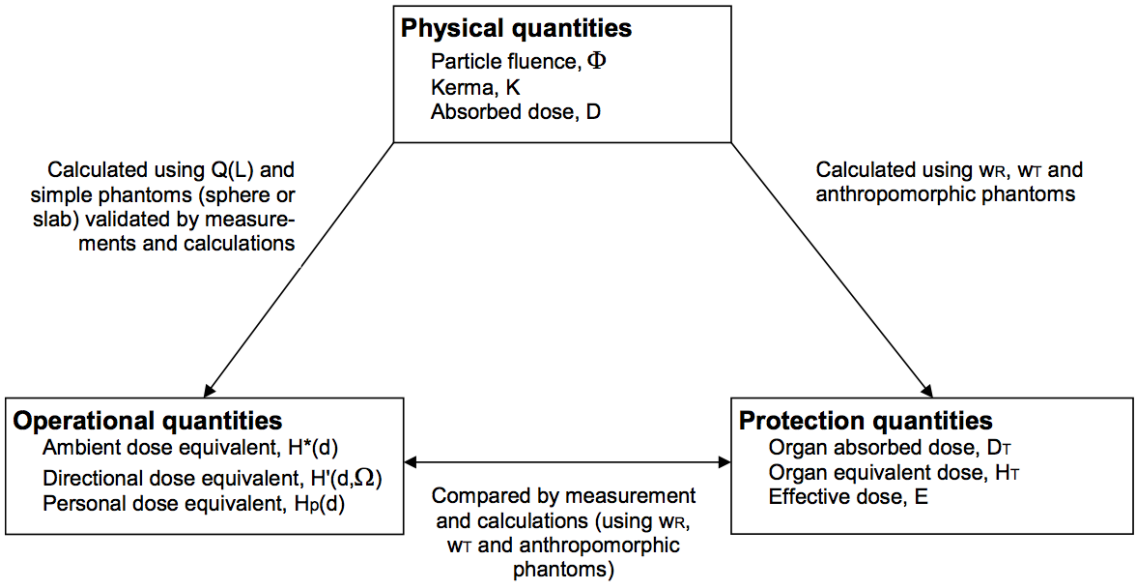

Figure 2.2: Relationship between physical, protection and operational quantities (obtained from [68]).

2.2.5 Radiometric Quantities and Fluence-to-Dose Conversion Coefficients

The fluence of a particle beam is defined as

$$\Phi = \frac{dN}{da}, \tag{2.5}$$

where dN is the number of particles incident on a sphere of cross-sectional area da (the unit of fluence is m^{-2}). In dosimetric calculations, fluence is often computed using the estimator

$$\hat{\Phi} = \frac{dl}{dV}, \tag{2.6}$$

in which dl is the sum of the lengths of the particle trajectories in the volume dV [69, 70]. The fluence rate is given by

$$\dot{\Phi} = \frac{\Phi}{dt} \tag{2.7}$$

and expressed in $m^{-2}\ s^{-1}$.

The transfer of energy from photons and neutrons to matter is made through the liberation and slowing down of secondary charged particles. If dE_{tr} is the mean sum of the initial kinetic energies of all the charged particles liberated in a mass dm of material by photons and neutrons, then Kerma is defined as

$$K = \frac{dE_{tr}}{dm}, \tag{2.8}$$

with units of J kg $^{-1}$, or Gray (Gy) [71, 72]. Equivalent dose and effective dose can be determined using their relationship to radiation field quantities such as particle fluence or from the air kerma, K_a.

Conversion coefficients defined for a reference person providing numerical links between radiation protection and physical field quantities are listed in ICRP Publication 116 [72]. To calculate this conversion coefficients, several Monte Carlo computer programs were used: EGSnrc [73], FLUKA [74, 75], PHITS [76], MCNPX [77] and GEANT4 [78]. These Monte Carlo programs were used to compute absorbed doses in the Reference Male and Reference Female voxel phantoms of the ICRP, described in ICRP publication 110 [79], for whole-body irradiations by different kinds of particles covering broad energy ranges. With the simulations, it is possible to calculate the effective dose $E(\epsilon)$ as a function of particle energy for the different kinds of radiation. The fluence-to-effective dose conversion coefficients are then determined in terms of effective dose per unit of fluence (in Sv m^{-2})

$$f(E) = \frac{E(\epsilon)}{\Phi(\epsilon)}, \tag{2.9}$$

where $\Phi(\epsilon)$ is the fluence of the primary particles of energy ϵ [80]. The same calculations can be done for other quantities, like the dose equivalent in some organ or tissue or the ambient dose equivalent. Fig. 2.3 shows two examples, for photons and neutrons, of flux-to-dose-equivalent coefficients, calculated with different Monte Carlo Programs and using the ICRP reference voxel phantoms. Extensive lists of conversion coefficients are available in [72].

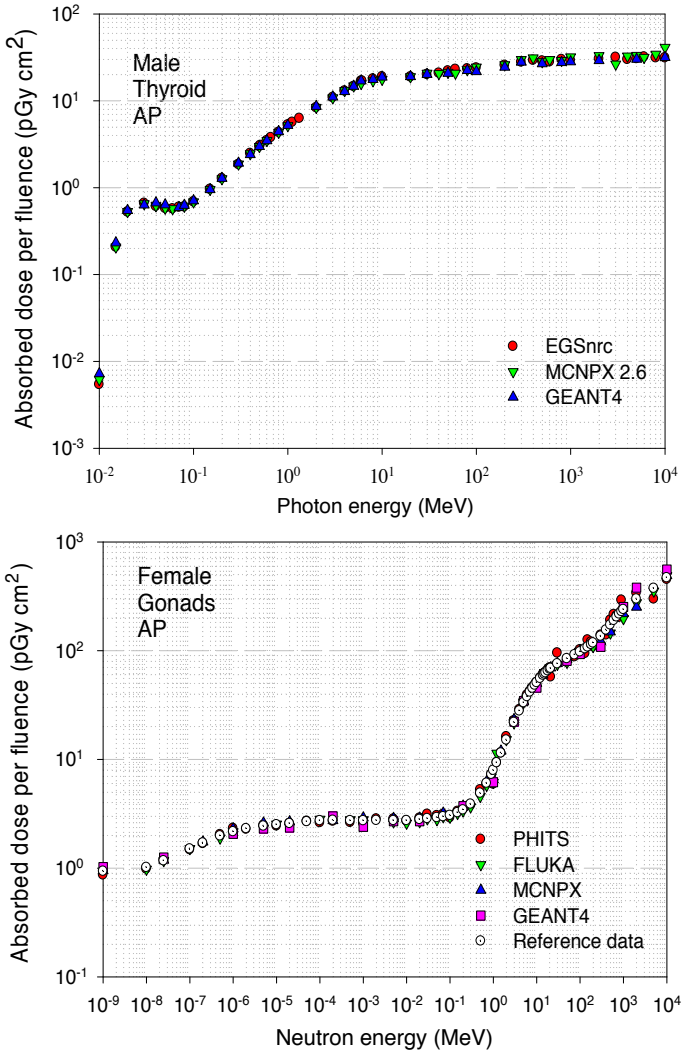

Figure 2.3: Flux-to-equivalent-dose conversion factors, calculated with different Monte Carlo programs, using the ICRP reference voxel phantoms. Top – for photons in the thyroid of the Reference Male. Bottom – for neutrons in the gonads of the Reference Female (obtained from [72]).

2.3 Dose Limits

There are three different kinds of exposures to ionising radiation, according to ICRP: occupational exposures, public exposures and medical exposures of patients. Occupational exposure refers to the exposure of workers to ionising radiation as a result of their work. This distinction is important when discussing dose limits, since different limits apply to different kinds of exposure. As previously stated, there are no dose limits for the exposure of medical patients, since it is assumed that the benefit for the patient always surpasses the detriment. Table 2.3 lists the dose limits proposed by ICRP for occupational and public exposures in planned exposure situations.

Table 2.3: Recommended dose limits in planned exposure situations (obtained from [63]).

Type of Limit	Occupational	Public
Effective dose	20 mSv per year, averaged over defined periods of 5 years	1 mSv in a year
Annual equivalent dose in:		
Lens of the eye	20 mSv per year, averaged over defined periods of 5 years	15 mSv
Skin	500 mSv	50 mSv
Hands and feet	500 mSv	–

ICRP recommends a limit of effective dose for occupational exposure of 20 mSv per year, averaged over 5-year periods (100 mSv in 5 years), and not exceeding 50 mSv in any single year. The same limit for the public is set at 1 mSv per year. This limit may be exceeded in special circumstances, provided that the average exposure over 5-year periods does not exceed 1 mSv per year. These limits do not apply in emergency exposure situations nor to medical exposures.

Table 2.3 also shows the limits in annual dose equivalent for the lens of the eye and localised areas of the skin, since these tissues, due to their high sensitivity to radiation, will not necessarily be protected against tissue reactions by the effective dose limits [63].

2.4 Activation and Radiotoxicity

In applications involving spallation neutron sources, the target is irradiated by high-energy protons and also by neutrons produced in the target, usually with an average energy of several MeV. Due to the irradiation, there are nuclide conversions (see Chapter 3 for a description of the nuclear reactions involved) in the target and surrounding materials, which lead to an accumulation of radioactive products – materials become *activated* [81]. In order to have a quantitative measure of the radiotoxicity of a certain nuclide, it is useful to define radiotoxicity (in Sv) as

$$R = F_d \times A, \tag{2.10}$$

where A is the integral activity in Bq and F_d is a dose coefficient which can be related to external exposure, ingestion or inhalation (Sv/Bq). This coefficient contains information concerning the absorbed dose (Gy) and its biological impact, taking into account radiation and tissue weighting factors. Extensive lists of dose coefficients for intakes of radionuclides by workers and members of the public are provided in ICRP Publication 119 [82].

The evolution of the nuclide chain in a material can be described by the Bateman equations, to

represent the time-dependent number of each nuclide N_i:

$$\frac{dN_i}{dt} = -\lambda_i N_i + \sum_{j \neq i} \lambda_j R_{j \to i} N_j \tag{2.11}$$

The radiotoxicity of each nuclide as a function of time can be calculated as

$$R_i(t) = F_d(i) \times \lambda_i N_i(t), \tag{2.12}$$

where N_i is defined by the Bateman equations [83].

The number of nuclides to be taken into account in heavy element spallation targets is in the range of 1500 – 2000. As an example, Table 2.4 shows a selection of the most important nuclides for safety analyses in a liquid mercury spallation target (which was studied in the past as a possible solution for ESS), along with the predicted target inventory for each nuclide and the corresponding dose coefficients for external exposure, inhalation and ingestion, for 40 years of operation at 5 MW. Fig. 2.5 shows a comparison between the activities in a mercury spallation target and the core of a 20 MW research reactor, for several cooling periods after the shutdown of the installation [84]. It is clear that activation is a major concern in this kind of applications, when the operation and disposal of the radioactive targets is taken into account. One should note, however, that the waste produced by a spallation target is significantly lower than the waste produced by a fission reactor of comparable power, while its neutron flux is approximately three orders of magnitude higher (see Fig. 1.1).

nuclide	**ESS target inventory** [GBq]	**Half life** [d]	**boiling point** [K]	**radiation type**	**dose/emission*** ground-shine (γ) [Sv/GBq]	cloud-	inhalation	ingestion
H-3/HTO	7.9e5 total	4500	373	weak β	0	0	2.3e-9	4.6e-8
H-3/HT			14		0	0	1.5e-11	3.3e-9
I-124	3100	4.2	387	β,γ	1.9e-6	1.0e-8	3.0e-5	3.4e-3
I-125	14000	60	„	γ	1.2e-6	1.0e-10	1.8e-5	**2.3e-3**
I-126	630	13	„	β,γ	2.6e-6	4.2e-9	6.3e-5	7.6e-3
Hg-193	1.9e6	0.16	629	γ	2.4e-8	1.7e-9	6.5e-9	2.5e-10
Hg-194	1.4e5	1.4e5	„	γ	**5.4e-3**	1.3e-13	1.3e-6	3.7e-7
Hg-195	3.2e6	0.42	„	γ	5.0e-8	1.7e-9	8.1e-9	6.3e-10
Hg-197	2.2e7	2.67	„	γ	7.4e-8	5.2e-10	2.0e-8	3.0e-9
Hg-203	1.5e7	47	„	β, γ	4.9e-6	2.2e-9	1.8e-7	8.1e-9
Sr-90	14000	1.05e4	1653	β	0	0	3.5e-5	**5.2E-3**
Gd-148	3.5e4	2.72e4	3546	α	0	0	**2.2e-3**	3.6e-7
Hf-172	7.3e5	683	4875	γ	1.9e-4	7.7e-10	1.3e-5	1.9e-9
Au-195	4.2e6	186	3081	γ	2.1e-6	6.2e-10	2.2e-8	5.9e-10

Figure 2.4: Most relevant nuclides in a 5 MW mercury target for 40 years of operation and 5000 hours per year (obtained from [84]).

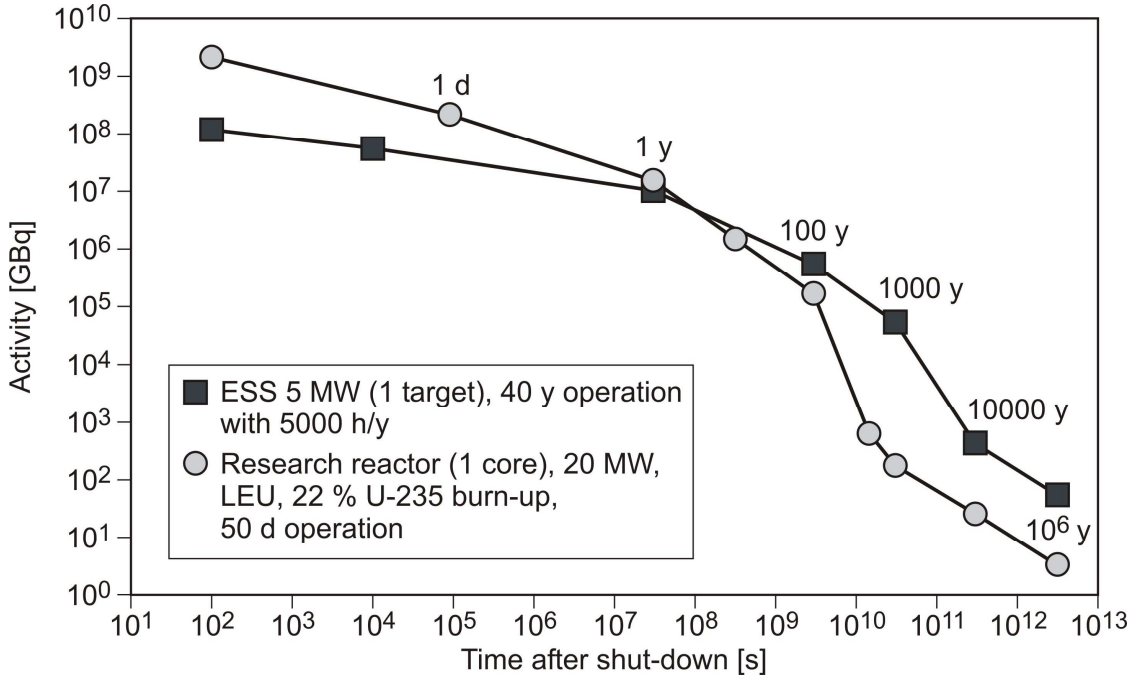

Figure 2.5: Comparison of activities in a mercury spallation target and in the core of a 20 MW research reactor, for several cooling periods after shutdown (obtained from [84]).

Chapter 3

Physics and Monte Carlo Modelling

3.1 The Monte Carlo Method

The Monte Carlo Method uses Probability Theory and statistical methods to describe physical systems and processes with stochastic behaviour, such as the interaction of radiation with matter. When applied to particle transport, it uses (pseudo-) random numbers and sampling techniques to model the transport of particles through matter, simulating the different interactions which occur along their paths according to theoretical physical models or experimental cross sections. The Monte Carlo Method applied to particle transport makes it possible to model very complex systems involving particle beams and radiation sources with great accuracy. The number of applications of the Monte Carlo Method to particle transport has been rising in the past decades, as a result of the fast-paced development of modern computer processors and computational architectures.

3.1.1 A Brief History of the Monte Carlo Method

3.1.1.1 The Buffon Needle Problem

During the decade of 1770, G. Buffon proposed an experiment to calculate the value of π. The Buffon Needle Problem, described in the following paragraphs, is generally seen as the first approach to the Monte Carlo Method.

Fig. 3.1 shows a plane with parallel lines in the x direction, one unit length apart. If needles with the same length as the distance between the parallel lines are dropped randomly on the plane,

they will fall at random angles θ with the x direction. The distance y between the centre of each needle and the closest line is also a random variable. The probability that the needle touches a line depends on these two random variables, θ and y. θ varies between 0 and π, since when the needle rotates from $\theta = 0$ to $\theta = \pi$ it returns to its original position (the needle is symmetric). The distance from the centre of the needle to the closest line varies from $y = 0$ to $y = 1/2$, since for higher values of y it would be closer to another line. The coordinate x does not influence the probability that a needle touches a line.

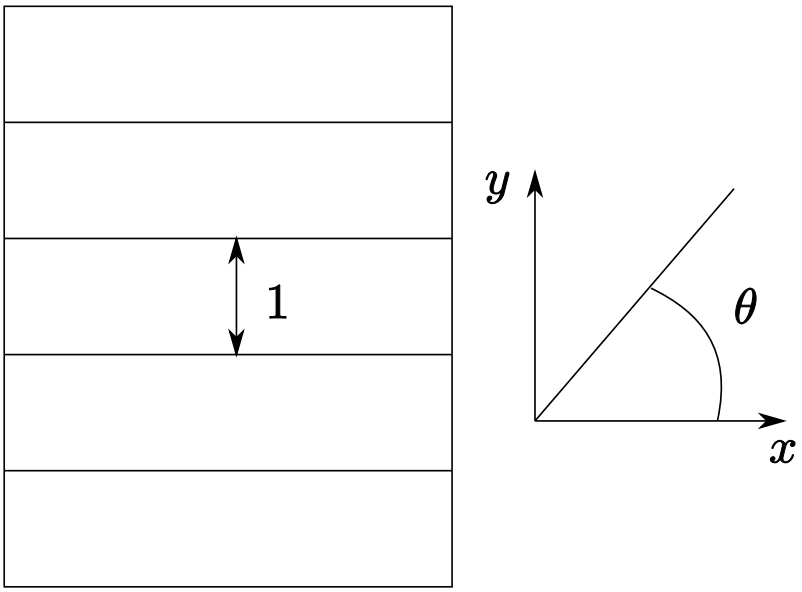

Figure 3.1: Scheme proposed by Buffon to determine the value of π.

Since θ and y are independent, and, by hypothesis, uniformly-distributed variables, the measure of the sample space is

$$(\pi)\left(\frac{1}{2}\right) = \frac{\pi}{2}. \tag{3.1}$$

If a needle touches a line, then (see Fig. 3.2)

$$y \leq d = \frac{1}{2}\sin\theta. \tag{3.2}$$

The measure of the space that meets the conditions for a touch is

$$\int_0^{\pi}\int_0^{\frac{1}{2}\sin\theta} dy\, d\theta = 1. \tag{3.3}$$

The probability that a needle touches a line is then

$$\frac{1}{\frac{\pi}{2}} = \frac{2}{\pi}. \tag{3.4}$$

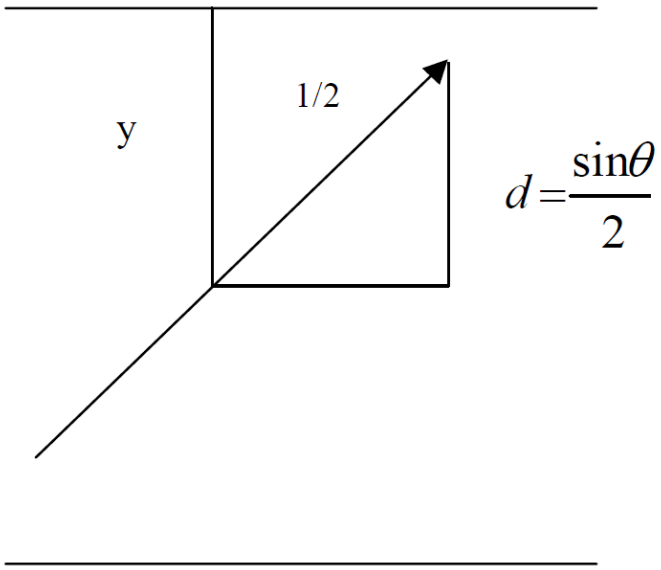

Figure 3.2: The needle has one unit length, equal to the distance between parallel lines (Obtained from [85]).

The empirical probability that a needle touches a line can be equalled to the previous result:

$$\frac{\text{touching needles}}{\text{all needles}} = \frac{2}{\pi}. \tag{3.5}$$

Solving for π, we get

$$\pi = \frac{2 \times \text{all needles}}{\text{touching needles}}. \tag{3.6}$$

In this way, after dropping a large number N of needles, it is possible to obtain an approximate value for π. This prediction gets more accurate as N increases – the exact value of π would be obtained in the asymptotic limit $N \to \infty$ [85].

3.1.1.2 Birth and Development of the Monte Carlo Method

In 1945, two important events took place: the first successful nuclear test in Alamogordo and the construction of the first electronic computer. These events had a huge political and scientific impact all over the world.

During the second world war, a team of scientists and engineers developed the first electronic computer, the ENIAC (Electronic Numerical Integrator And Computer), which contained approximately 18000 thermionic valves (vacuum tubes) and 500000 solder joints. John Von Neumann, Professor of Mathematics at the Institute of Advanced Study in Princeton, was the first to propose a preliminary computational model of a thermonuclear reaction for the ENIAC. The model was implemented and tested by Stanley Frankel, Anthony Turkevitch e Nicholas Metropo-

lis and the results were presented and discussed before Von Neumman, Enrico Fermi and Edward Teller, among others. Despite the simplicity of the model, the results allowed for optimism regarding the feasibility of a thermonuclear weapon.

Statistical sampling techniques had fallen into disuse due to the length and tediousness of the calculations, but the development of the ENIAC showed that with electronic computers they could be applied effectively. The main scientists responsible for the birth of the Monte Carlo Method were John Von Neumann, Stan Ulam and Robert Richtmyer [86], although Enrico Fermi had already used it for 15 years for calculations involving the moderation of neutrons. The name *Monte Carlo* arose from the analogy between the statistical nature of the method and the gambling activities of the Monte Carlo Casino.

Near the end of the decade of 1940, the ENIAC was programmed to perform the first test to the Monte Carlo Method. Nine problems were computed related to neutron transport, with different material configurations, neutron distributions and running times. The neutron histories were subjected to a variety of statistical analysis and comparisons with other approaches, and the conclusions about the efficacy of the method were favourable. After that first test, the Monte Carlo Method spread quickly, with many new applications arising in the following years [87].

The development of the Monte Carlo Method was based on the development of the electronic computer. In the second half of the decade of 1950, bipolar transistors replaced the thermionic valves, greatly reducing the physical dimensions and the price of computers. Integrated circuits allowed the development of microprocessors, in the beginning of the 1970s. Since then, new architectures of growing complexity have been developed at an increasing pace, allowing for a generalisation of the use of computers by making them faster, smaller and cheaper. The Monte Carlo Method has benefited, and it still does, of this development. Personal computers of today are the super-computers of the last decade, and computational calculations using Monte Carlo methods are increasingly available to a growing number of people in the scientific community.

3.1.2 (Pseudo-) Random Numbers

The Monte Carlo Method is based on the generation of sequences of random numbers. A random variable is a variable that can take more than one value, and for which any particular value that will be taken cannot be predicted in advance [88]. In studies using the Monte Carlo Method, the sequences of numbers are sequences which, once determined, are not random from the statistical point of view, but have similar properties to those of a sequence of random numbers. It is then necessary to distinguish between random numbers and pseudo-random numbers.

A sequence of random numbers is unpredictable and non-reproducible. Such a sequence can only be generated by random physical processes, such as the thermal noise in electronic de-

vices, the arrival times of cosmic radiation, the radioactive decay, etc. In practice, however, it is very difficult to build a fast and accurate random number generator based on random physical processes.

The random numbers most often used in real calculations are those known as pseudo-random numbers, which are generated according to some specific algorithm. Such algorithms, known as random number generators, use algebraic techniques and mathematical methods to generate sequences of numbers which always exhibit periodicity, although their period of repetition can be made long enough to guarantee that many (but not all) simulations of physical processes can be performed without repetition of the random number sequence. It is generally accepted that the theory behind the Monte Carlo Method can be correctly applied using pseudo-random numbers instead of random numbers [88].

The first pseudo-random number generator was proposed by John Von Neumann. From an initial number with r digits, the first random numbers are the central $r/2$ digits of that number. Then the first random number is squared, yielding another number with r digits, and the central $r/2$ central digits of than number form the second random number, and so on. If the original number is carefully chosen, this method can originate a relatively long sequence of apparently-random numbers. This generator has a period, since when a number is repeated the whole sequence is repeated. This is a characteristic shared by all pseudo-random number generators.

Nowadays, the pseudo-random number generators have much more sophisticated and efficient algorithms (although they still exhibit periodicity, their periods are much longer). They are also generated from an initial number, termed *seed*, which can be changed to produce different random number sequences (the seed can be extracted from the computer system clock, for example, in order to produce a different sequence each time the random number generator is called). The main programming languages used today in scientific applications have in their libraries one or more functions to generate sequences of pseudo-random numbers.

3.1.3 Modelling of Random Variables

Let ξ be a random variable, distributed in the interval $a < x < b$, $p(x)$ its probability density function and γ another random variable, uniformly distributed between 0 and 1. Values of ξ can be obtained from the equation

$$\int_a^{\xi} p(x)\,dx = \gamma. \tag{3.7}$$

Fig. 3.3 shows how to model a continuous variable. To each value of ξ in the interval $[a, b]$ there

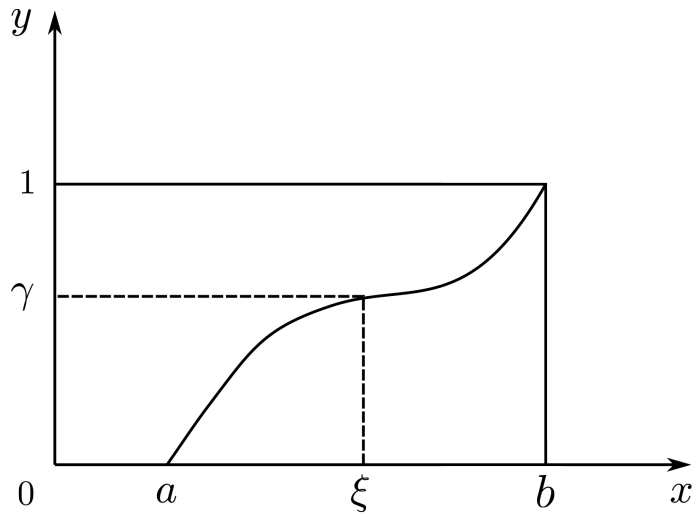

Figure 3.3: The function $\gamma = \int_a^{\xi} p(x)\,dx$ for modelling of a continuous variable (adapted from [89]).

is a corresponding value for γ, between 0 and 1. Let the function $y(x)$ be defined as

$$y(x) = \int_a^x p(x')\,dx'. \tag{3.8}$$

From the properties of $p(x)$ it follows that $y(a) = 0$ and $y(b) = 1$. The derivative of $y(x)$ is $y'(x) = p(x) > 0$, meaning that $y(x)$ increases monotonically between 0 and 1. Any straight line with equation $y = \gamma$ (with $0 < \gamma < 1$) intersects the curve $y(x)$ at a single point (Fig. 3.3). For a random interval $[a', b']$ contained in $[a, b]$, the ordinates of the curve $y(x)$ which satisfy the condition $y(a') < y < y(b')$ correspond to points in the interval $a' < x < b'$ (Fig. 3.4).

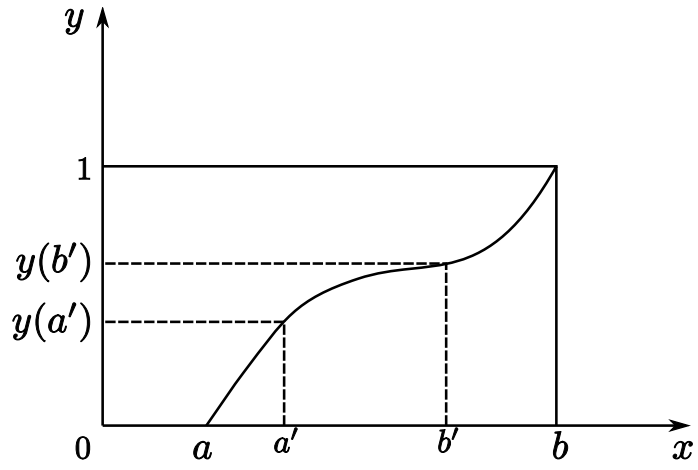

Figure 3.4: One-to-one mapping of the interval $a' < \xi < b'$ onto $y(a') < y < y(b')$ (adapted from [89]).

s

If $\xi \in [a', b']$, then $\gamma \in [y(a'), y(b')]$, meaning that $P(a' < \xi < b') = P[y(a') < \gamma < y(b')]$.

Furthermore, if γ is a random variable uniformly distributed between 0 and 1, then

$$P[y(a') < \gamma < y(b')] = y(b') - y(a') = \int_{a'}^{b'} p(x)\,dx, \tag{3.9}$$

or

$$P[a' < \xi < b'] = \int_{a'}^{b'} p(x)\,dx. \tag{3.10}$$

The example that follows illustrates the importance of these concepts.

3.1.3.1 Example

When a beam of photons hits a material, its intensity decreases according to an exponential attenuation law. The probability density function of the random variable s, the distance covered by the incident particles before being absorbed, is represented in Fig. 3.5. s varies from $s = 0$ (material surface) and $s \to \infty$, Σ is the macroscopic cross section of the particle in the material and λ is the mean free path. If $p(s)$ is the probability density function that the particle covers the distance s, then

$$p(s) = \Sigma \mathrm{e}^{-\Sigma s} \tag{3.11}$$

and

$$E[s] = \int_0^\infty s p(s)\,ds = \int_0^\infty s\Sigma \mathrm{e}^{-\Sigma s}\,ds = \cdots = \frac{1}{\Sigma}, \tag{3.12}$$

$E[s]$ being the expected value of s and $1/\Sigma$ the mean free path of the particle. Values of s can

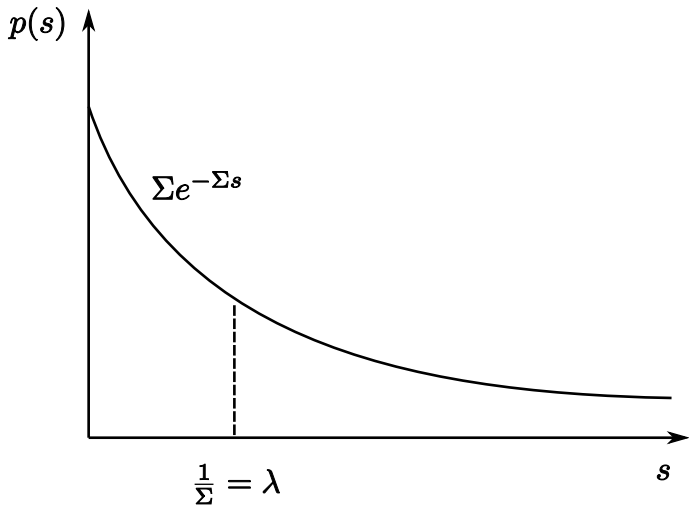

Figure 3.5: Probability density function of the random variable s, the distance traveled by the incident particles between two consecutive interactions in the material.

be randomly generated using the previously mentioned expression

$$\int_0^s \Sigma \mathrm{e}^{-\Sigma y'}\, dy' = \xi. \tag{3.13}$$

For simulation purposes, ξ in the previous expression is a randomly-generated number between 0 and 1. Solving the integral, we get

$$1 - \mathrm{e}^{-\Sigma s} = \xi, \tag{3.14}$$

or

$$s = -\frac{1}{\Sigma}\ln(1-\xi). \tag{3.15}$$

Since $(1-\xi)$ has the same distribution as ξ,

$$s = -\frac{1}{\Sigma}\ln(\xi). \tag{3.16}$$

In this way, generating a random number between 0 and 1 and assigning it to ξ in the previous equation we get a random value for the distance traveled by the particle in the material. The variable s is not, unlike ξ, uniformly distributed – it follows the distribution shown in Fig. 3.5.

From a computational point of view, values for the random distance s covered by the photons inside the material between two consecutive interactions can be obtained with a line of code such as

$$s = -\frac{1}{\Sigma}\ln[\textbf{randfloat()}], \tag{3.17}$$

randfloat() being a function that generates a random number from a probability density function uniformly distributed between 0 and 1 [89, 90].

3.1.4 The Monte Carlo Method Applied to Particle Transport

3.1.4.1 Introduction

The Monte Carlo method has many applications in particle transport. MCNP(X), GEANT4, EGS, PENELOPE and FLUKA are some examples of scientific software which use the Monte Carlo Method to simulate particle transport. In this section, a simple example is shown to illustrate how the results of the previous sections can be applied to simulate the *history* of a particle – the series of events which occur since the particle is created until it is absorbed.

We take as example the transmission of a neutron in a slab of material. The total macroscopic

cross section is the sum of the macroscopic cross sections of absorption and scattering:

$$\Sigma = \Sigma_a + \Sigma_s. \tag{3.18}$$

The probabilities that a neutron is absorbed or scattered are Σ_a/Σ and Σ_s/Σ, respectively (Σ is the probability than an interaction occurs). From results obtained in Section 3.1.3 we know that

$$E[s] = \int_0^\infty sp(s)\,ds = \int_0^\infty s\Sigma \mathrm{e}^{-\Sigma s}\,ds = \cdots = \frac{1}{\Sigma}. \tag{3.19}$$

Generating a random number for ξ (between 0 and 1), we get, as before,

$$\lambda = -\frac{1}{\Sigma}\ln(\xi), \tag{3.20}$$

where λ is the random path length (distance travelled before the next interaction). In the previous step, the determination of the distance covered by the neutron was based on the generation of a random number and the probability of interaction between the neutron and the material. Generating many random numbers and computing many values for λ we would obtain a curve similar to the one presented in Fig. 3.5.

Knowing the distance that the neutron covers before interacting, we need to determine the type of interaction. Fig. 3.6 helps to illustrate how to do this. Let us assume that, according to the interaction cross sections, the neutron has a 60% chance of being absorbed and a 40% chance of being scattered. The following steps are followed:

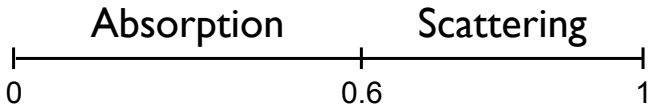

Figure 3.6: Determining the interaction type.

- Generate a random number ξ uniformly distributed in the interval $[0, 1]$;
- Test the condition $\xi < \Sigma_a/\Sigma$?;
- If the answer is *yes*, the neutron is absorbed;
- If the answer is *no*, the neutron is scattered.

If the generated number is smaller than 0.6, the neutron gets absorbed, otherwise it is scattered. If it is absorbed, its history ends. If it is scattered, we need to determine the scattering angle, ϕ.

We now assume that $\cos(\phi)$ is uniformly distributed in $[-1, 1]$, to simplify the calculation of the scattering angle. A random number χ is generated and the scattering angle is obtained with the

expression

$$\cos(\phi) = 2\chi - 1. \tag{3.21}$$

Then we can calculate again the distance that the neutron travels before the next interaction, and so on. In the same way, we can determine if the neutron is transmitted or reflected when it reaches a frontier between two different materials. The entire history of the neutron can thus be determined.

The previous example is extremely simplified. In a real simulation, it is necessary to take into account many different factors to account for the interaction of radiation with matter. The absorption of neutrons can be due to capture or fission, the scattering can be elastic or inelastic, etc. Besides that, the interaction of neutrons with matter produces secondary particles, like photons, and their histories also need to be followed. The Monte Carlo programs used for particle transport are extremely sophisticated and account for many different types of interaction between particles and matter. They are coupled to extensive cross section libraries and take into account the kind of particle being followed, its energy, the properties of the materials it crosses, the temperature of the system, etc [90].

3.1.4.2 Variance Reduction Techniques

There are two distinct types of Monte Carlo simulations: *analog* and *non-analog*. In analog Monte Carlo the particle histories can be terminated by three types of events:

- the particle is absorbed;
- the particle leaves the region of interest;
- the energy of the particle falls below some predetermined *cut-off*.

The first two can be changed through the introduction of *statistical weights*. This is a characteristic of non-analogue Monte Carlo, used when the objective is to reduce the simulation times and the variance (uncertainty) of the results.

Let us now consider a beam of n_0 neutrons hitting a slab of material, each of them following the same trajectory (unrealistic hypothesis, used for illustration purposes only). Admitting that at point x there will be an interaction, we have

- average number of absorbed neutrons $= n_0 \frac{\Sigma_a}{\Sigma_{total}}$;
- average number of scattered neutrons $= n_0 \frac{\Sigma_s}{\Sigma_{total}}$.

Since the trajectory is the same for all neutrons, the number of neutrons scattered in that direction is

$$n_1 = n_0 \frac{\Sigma_s}{\Sigma_{total}}; \tag{3.22}$$

Now we assume that the absorption cross section is much higher than the scattering cross section, by a factor 1000, for example. This means that for every 1000 neutrons arriving at x only 1 is scattered, while 999 are absorbed. If the objective is to study characteristics related with the scattered neutrons the simulation will be highly inefficient, since for every 1000 simulated particles only 1 will be relevant for the study. For this reason, we could opt to ignore absorption and simulate scattering events only, thus greatly reducing the simulation times. In this way, all neutrons arriving at x will be scattered. But the results will be affected, and that has to be accounted for, since the physics of the problem has to be respected in order to produce valid simulation results. To do that, we change the statistical weight of each neutron. If a neutron had a statistical weight 1 it will now have a statistical weight $1/1000 = 0.001$. In general, if a particle has an initial statistical weight w_{i-1}, after the collision its weight w_i will be given by

$$w_i = w_{i-1} \frac{\Sigma_{total} - \Sigma_a}{\Sigma_{total}} = w_{i-1} \frac{\Sigma_s}{\Sigma_{total}}. \tag{3.23}$$

All Monte Carlo simulation results are affected by a statistical uncertainty. The objective is always to minimise the variance of the results. Let us assume that the objective of a specific simulation is to get the flux of particles in some surface, in particles/cm^2/simulated history[1] The smaller the count of particles passing through the surface, the greater the statistical uncertainty associated with the flux will be. A way of minimising that uncertainty is to increase the simulation time, by raising the number of simulated histories and, as a consequence, increasing the number of particles crossing the surface. Another way is to use non-analogue Monte Carlo. The previous example shows how the simulation time can be reduced through the attribution of statistical weights. Some additional variance reduction techniques are discussed in the following paragraphs.

In a particle transport program such as FLUKA or MCNPX, the geometry of the system is implemented through cells (volumes), which fill-up the space. The user can assign to each of those cells an importance ($I = 1, 2, 3, \ldots$), for a certain type of particle. There are two methods of variance reduction based on the importance of the different geometrical regions of the simulated system. One of these methods, termed *Russian Roulette*, is used to terminate histories of particles in low-importance regions. The other method, named *Splitting*, is used to raise the number of particles which propagate in high-importance regions.

[1] In the case of a proton beam hitting a spallation target, it might be necessary to calculate the flux of neutrons in a surface. This flux is always normalised to the number of particles emitted by the source (protons), and the result is expressed in neutrons/cm^2/proton emitted by the source.

The Splitting technique consists in dividing a particle in n "fragments" when the particle with weight w moves from a region of importance ($I_{previous}$) to a region of higher importance (I_{new}), as represented in Fig. 3.7)

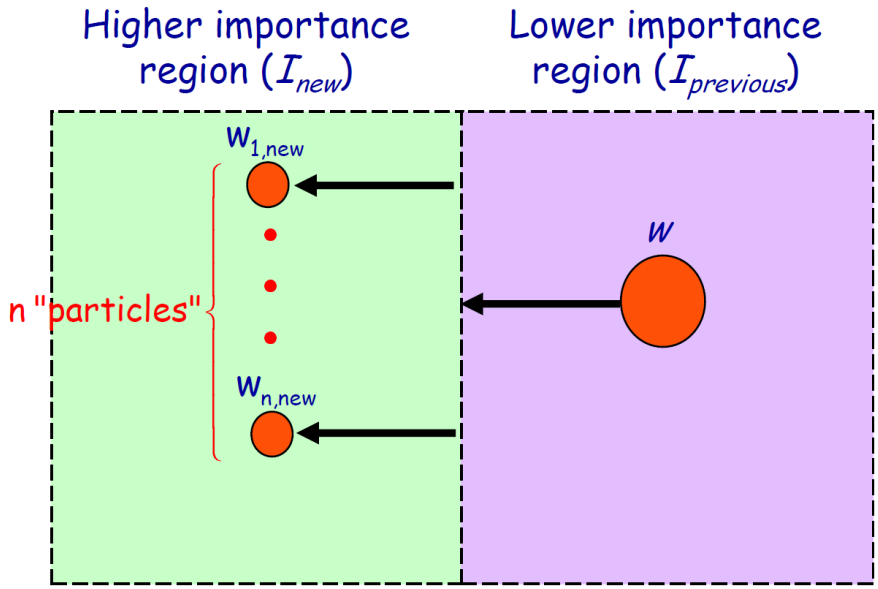

Figure 3.7: Splitting technique.

n can be determined with the following relation:

$$n = \frac{I_{new}}{I_{previous}}. \tag{3.24}$$

If the particle is split into n new particles, the weight of each new particle is

$$w_{new} = \frac{w}{n}. \tag{3.25}$$

The objective of this technique is to raise the number of particles reaching regions of high importance. If the objective of the simulation is to obtain the flux of some kind of particle in a region reached by few particles, this technique can be useful to reduce the variance. More particles are created, with lower statistical weight, and each new history is followed. If in a simulation a detector was reached by a single particle, the statistical uncertainty of the result would be 100%. Assigning a high importance to that region and surrounding regions and using the splitting technique, more particles would hit the detector, with compensated statistical weighs. With more counts, the statistical uncertainty would be reduced.

The Russian Roulette technique does, in a way, the opposite of the Splitting technique. In Russian Roulette, a particle moving from a region with some importance to a region of lower importance is submitted to a trial, from which it can either "survive" or be terminated, according

to a predetermined probability. If the particle survives the trial, its statistical weight is increased (Fig 3.8).

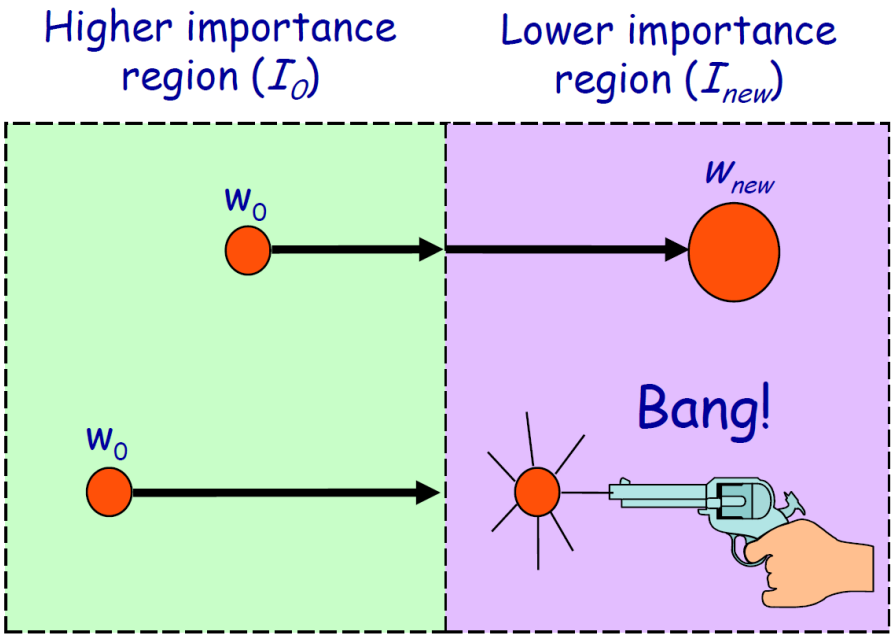

Figure 3.8: Russian Roulete technique.

A particle with initial statistical weight w_0 will emerge with a higher weight w_{new}. To summarise, we have

$$w_{new} = w_0 \frac{I_0}{I_{new}} \qquad \text{with probability} \quad p = \frac{I_{new}}{I_0}$$

and

$$w_{new} = 0 \qquad \text{with probability} \quad 1 - p = 1 - \frac{I_{new}}{I_0}.$$

In this way, it is possible to reduce the number of histories followed in low-importance regions, which have no effect in the results. The simulation time is thus reduced (or the statistical uncertainty of the results). The Splitting and Russian Roulette techniques are highly complementary, and usually work together.

3.1.5 Calculation of Integrals using the Monte Carlo Method

Let the integral I be given by

$$I = \int_a^b f(x)\, dx, \tag{3.26}$$

with $0 \leq f(x) \leq M$ for $a \leq x \leq b$. The domain of integration is the interval $[a, b]$ and the codomain of the function $f(x)$ in that interval is $[m, M]$. A rectangle of area $(b-a) \cdot (M-m)$ can thus be defined. To calculate the integral, we start by generating N random numbers for x e N random numbers for y, with the values of x uniformly distributed in $[a, b]$ and the values of y uniformly distributed in $[m, M]$. To each pair (x, y), we test the condition

$$y_i \leq f(x_i), \tag{3.27}$$

n being the number of times that the condition is verified. Finally, we estimate the integral:

$$I \cong (M-m) \cdot (b-a) \cdot \frac{n}{N}. \tag{3.28}$$

The result of the integral is equal to the area of the rectangle $(b-a) \cdot (M-m)$ multiplied by the ratio between the number of times in which the points y_i are below $f(x)$ and the total number of trials (N) – it represents the area below the function. When $N \to \infty$, the value of the estimated integral tends to the exact value of the integral, according to the empirical definition of probability [91].

As an example, let us consider the following integral:

$$I = \int_0^1 \frac{4}{\pi} \cdot \frac{1}{1+x^2}\, dx. \tag{3.29}$$

To calculate this integral using the Monte Carlo method, the following steps are taken:

1. A random number ξ_1 is generated, and assigned to $x_0 \to x_0 = \xi_1$;
2. A second random number ξ_2 is generated, and assigned to $x_1 \to x_1 = \frac{4}{\pi}\xi_2$ (varies between 0 and $\frac{4}{\pi}$ instead of 0 and 1, as shown in Fig. 3.9);
3. If $x_1 \leq \frac{4}{\pi}\left[\frac{1}{1+x^2}\right] \to n_{hit} = n_{hit} + 1$;
4. If $x_1 \geq \frac{4}{\pi}\left[\frac{1}{1+x^2}\right] \to n_{miss} = n_{miss} + 1$.

Two random variables are used in order to define a point and the *hit-or-miss* is performed (Fig. 3.9) If the generated point is below the function, the counter n_{hit} is increased. Otherwise, the counter n_{miss} is increased.

The value of the integral ca be estimated as

$$\hat{I} \approx \frac{4}{\pi} \cdot \frac{n_{hit}}{n_{hit} + n_{miss}}. \tag{3.30}$$

It is important to underline that what we get is not an exact value of I, but an estimation of this value. The value of the integral is given by the area of the rectangle, $4/\pi \times 1 = 4/\pi$, multiplied

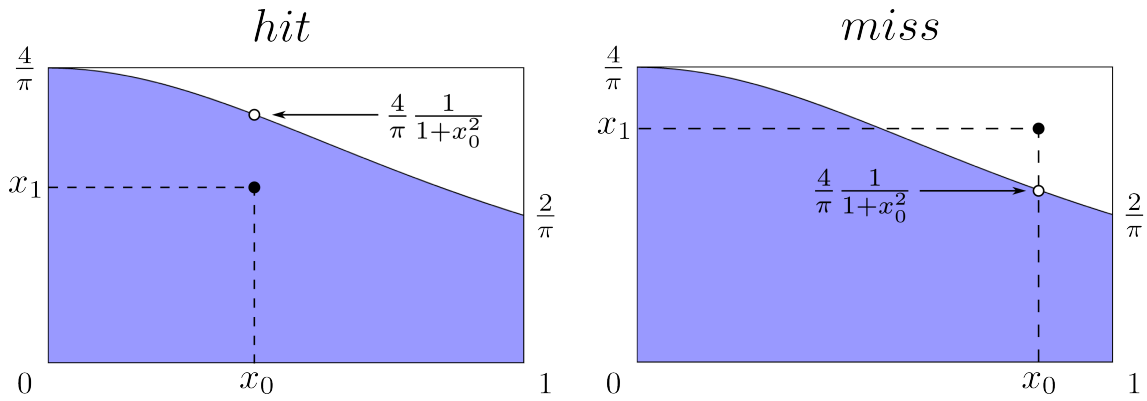

Figure 3.9: Hit-or-miss technique.

by the probability that any randomly generated point falls below the function $f(x)$ [91].

3.2 Neutron Physics

3.2.1 Interaction of Neutrons with Matter

Since neutrons are electrically neutral, they are not subject to Coulomb forces when they interact with the nuclei of a material. They can therefore penetrate the atoms and induce nuclear reactions even when their energy is low, as in the case of thermal neutrons (definition below). Neutrons can be separated into three categories, according to their energies [92]:

Thermal $E \simeq 0.025$ eV (at 20 °C)

Epithermal 0.025 eV $\leq$ E $\leq$ 100 keV

Fast $E \geq 100$ keV

When a neutron ${}^{1}_{0}\mathrm{n}$ hits a nucleus ${}^{A}_{Z}\mathrm{X}$, the resulting reaction can be described as follows:

$$ {}^{1}_{0}\mathrm{n} + {}^{\mathrm{A}}_{\mathrm{Z}}\mathrm{X} \rightarrow {}^{\mathrm{A+1}}_{\mathrm{Z}}\mathrm{X}^{*}. \tag{3.31} $$

A compound nucleus ${}^{\mathrm{A+1}}_{\mathrm{Z}}\mathrm{X}^{*}$ is created from the interaction of the neutron with the nuclei X. The compound nucleus is in an excited state and the way through which it proceeds to the final state of the reaction distinguishes the main reaction types, namely [93]:

- elastic scattering;
- inelastic scattering;
- radiative capture;

- nuclear fission.

The compound nucleus can also decay through the emission of a proton ((n,p) reaction), an alpha particle (n, α) or two or more neutrons ($(\mathrm{n}, 2\mathrm{n})$, $(\mathrm{n}, 3\mathrm{n})$, etc.).

3.2.1.1 Elastic Scattering

Elastic scattering is the process in which a neutron is scattered off a nucleus, transferring part of its kinetic energy to the *recoil nucleus* (Fig. 3.10). The system preserves its kinetic energy and momentum. It is a (n, n) reaction:

$$ {}^{1}_{0}\mathrm{n} + {}^{\mathrm{A}}_{\mathrm{Z}}\mathrm{X} \rightarrow {}^{1}_{0}\mathrm{n} + {}^{\mathrm{A}}_{\mathrm{Z}}\mathrm{X}. \tag{3.32} $$

This reaction will be described with greater detail in Section 3.2.3. It can be written in a simplified notation:

$$ {}^{\mathrm{A}}_{\mathrm{Z}}\mathrm{X}(\mathrm{n}, \mathrm{n}){}^{\mathrm{A}}_{\mathrm{Z}}\mathrm{X}. \tag{3.33} $$

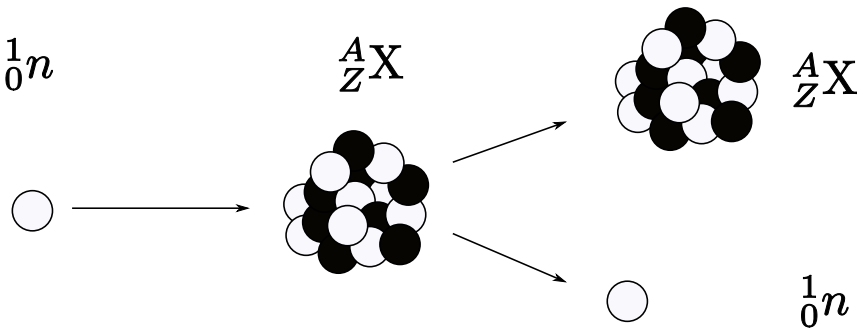

Figure 3.10: Elastic scattering.

3.2.1.2 Inelastic Scattering

When inelastic scattering occurs, the compound nucleus decays through the emission of a neutron, but not necessarily the same neutron that hit the nucleus in the first place. For this reason, this reaction is represented as $(\mathrm{n}, \mathrm{n}')$. If the resulting nucleus is still left in an excited state, it decays to the fundamental state through the emission of γ radiation. There is no conservation of kinetic energy, as the variation of kinetic energy is used to leave the nucleus in the excited state.

3.2.1.3 Radiative Capture

The compound nucleus decays to its fundamental state through the emission of one or more photons (Fig. 3.11). It is a (n, γ) reaction:

$$ {}^{1}_{0}\mathrm{n} + {}^{\mathrm{A}}_{\mathrm{Z}}\mathrm{X} \rightarrow {}^{\mathrm{A+1}}_{\mathrm{Z}}\mathrm{X}^{*} \rightarrow {}^{\mathrm{A+1}}_{\mathrm{Z}}\mathrm{X} + \gamma \tag{3.34} $$

or

$$ {}^{\mathrm{A}}_{\mathrm{Z}}\mathrm{X}(\mathrm{n}, \gamma)^{\mathrm{A+1}}_{\mathrm{Z}}\mathrm{X}. \tag{3.35} $$

The final nuclide is a different isotope of the same element.

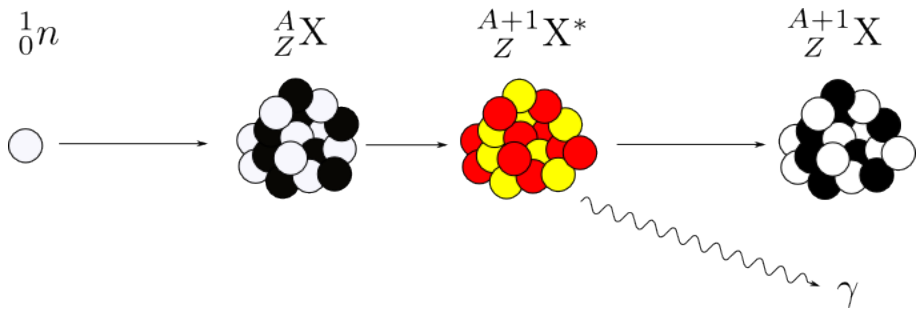

Figure 3.11: Radiative capture.

3.2.1.4 Nuclear Fission

Nuclear fission is another reaction which results from the formation of a compound nucleus. The compound nucleus is split into two lighter nuclei, termed *fission fragments* (Fig. 3.12). Additionally, a variable number of neutrons is also emitted, as well as γ radiation.

An example of a fission reaction induced by a neutron is

$$ {}^{1}_{0}\mathrm{n} + {}^{235}_{92}\mathrm{U} \rightarrow {}^{236}_{92}\mathrm{U}^{*} \rightarrow {}^{93}_{37}\mathrm{Rb} + {}^{141}_{55}\mathrm{Cs} + 2{}^{1}_{0}\mathrm{n}. \tag{3.36} $$

The distribution of masses of the two fission products is shown In Fig. 3.13, for fission in ^{235}U by thermal neutrons. The distribution has no symmetry around the centre – for each heavy fragment there is a corresponding light fragment. The most probable numbers for the masses of the fission products are $A_1 = 95$ and $A_2 = 140$ (accounting for 6.5% of fissions). A symmetric fission occurs once in every 20000 fissions, approximately.

The fission fragments in the neighbourhood of $A_1 = 95$ and $A_2 = 140$ should share 92 protons (number of protons of an uranium atom). If that is the case, the corresponding nuclides must be $^{95}_{37}$Rb and $^{140}_{55}$Cs. These nuclides have an excess of neutrons, and emit one or more neutrons in during the fission process (or up to 10^{-16} seconds after fission). These are the *prompt neutrons*,

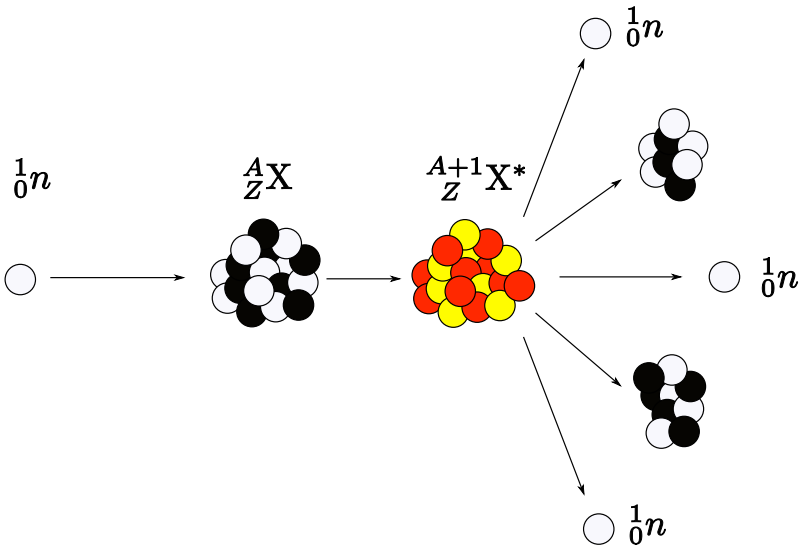

Figure 3.12: Nuclear fission.

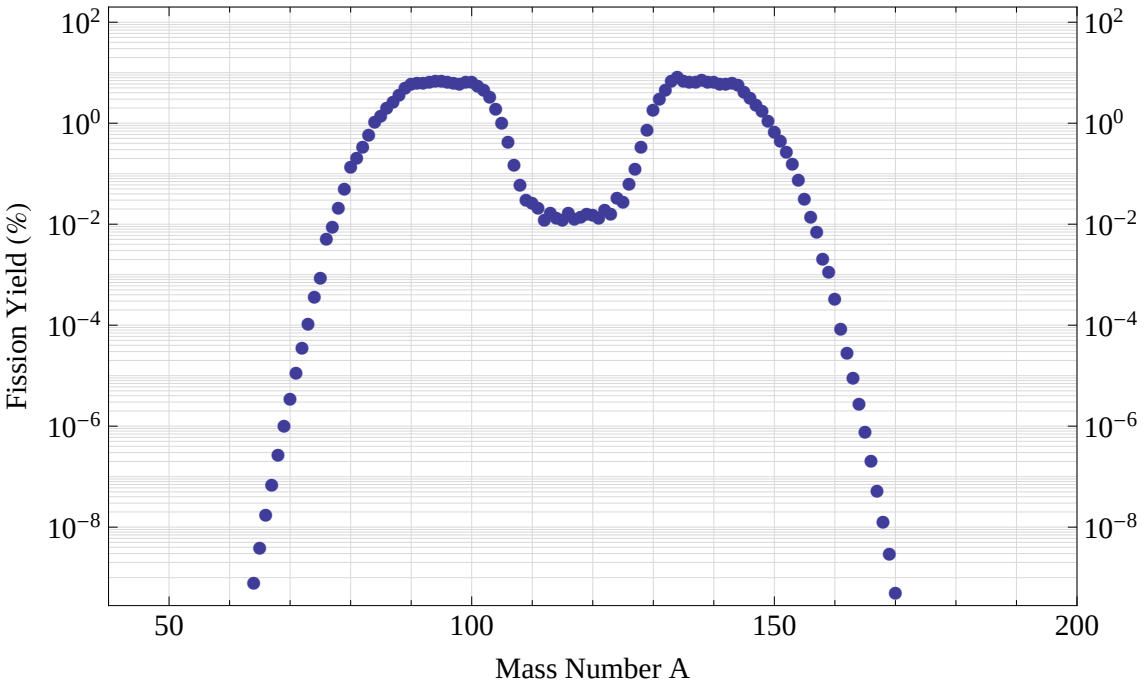

Figure 3.13: Mass distribution of the fission fragments of ^{235}U, for incident thermal neutrons [94].

and the average number of prompt neutrons emitted during the fission process, typically between 2 and 3, depends on the fissile nucleus and the energy of the incident neutron. For fission induced by thermal neutrons in ^{235}U, an average of 2.42 prompt neutrons are emitted per fission. The average energy of these neutrons is approximately 2 MeV (see Fig. 3.18).

The fission products are still highly radioactive and decay to stable isobars through the emission

of γ and β radiation, as in the following examples:

$$^{93}\mathrm{Rb} \xrightarrow{6\mathrm{s}} {}^{93}\mathrm{Sr} \xrightarrow{7\mathrm{m}} {}^{93}\mathrm{Y} \xrightarrow{10\mathrm{h}} {}^{93}\mathrm{Zr} \xrightarrow{10^6\mathrm{a}} {}^{93}\mathrm{Nb} \tag{3.37}$$

$$^{141}\mathrm{Cs} \xrightarrow{25\mathrm{s}} {}^{141}\mathrm{Ba} \xrightarrow{18\mathrm{m}} {}^{141}\mathrm{La} \xrightarrow{4\mathrm{h}} {}^{141}\mathrm{Ce} \xrightarrow{33\mathrm{d}} {}^{141}\mathrm{Pr}. \tag{3.38}$$

In the β^- decay the excess neutrons are converted into protons. In some cases, the excited nucleus decays through the emission of a neutron, instead of γ decay. These neutrons are called *delayed neutrons*, since they are emitted some time after the fission products, depending on the half-lives of the involved nuclides. The delayed neutrons are a small fraction of all the emitted neutrons ($\simeq 0,65\%$ for ^{235}U) [92].

The released energy per fission is characteristic of each fissile nuclide, being close to 200 MeV. This energy is released mostly as kinetic energy of the fission fragments, but also through the prompt neutrons, the prompt γ radiation and the decay of the fission products.

There are some fissile nuclides in nature, such as ^{235}U (0,72% of natural uranium), ^{238}U (99,28% of natural uranium) and ^{232}Th (100% of natural thorium). ^{233}U and ^{239}Pu are examples of fissile nuclides produced artificially.

3.2.2 Cross Sections

When a neutron beam hits a target, the rate of nuclear reactions induced by the neutrons in the target material must be proportional to the intensity of the neutron beam I (neutrons/cm^2/s) and to the number of atoms in the target per unit area N_A (atoms/cm^2). If the constant of proportionality is σ, the reaction rate in the material is given by

$$R = \sigma \cdot I \cdot N_A. \tag{3.39}$$

The constant σ is known as microscopic cross section and quantifies the probability of occurrence of some nuclear reaction induced by a neutron in a nuclide. Then we have

$$\sigma = \frac{R/N_A}{I}, \tag{3.40}$$

the microscopic cross section having the units of area. For convenience, cross section values are usually presented in barn (b), with $1\mathrm{b} = 10^{-24}$ cm^2.

The concept of cross section can be used to characterise any kind of nuclear reaction, like the ones presented in Section 3.2.1. Cross sections can be defined for scattering, radiative capture or fission, for example. The scattering cross section of a nuclide for some incident neutron equals

the sum of its elastic and inelastic cross sections:

$$\sigma_s = \sigma_e + \sigma_{in}. \tag{3.41}$$

In the same way, the absorption cross section can be defined as the sum of all the cross sections of reactions in which a nuclide absorbs a neutron, forming a compound nucleus. The total cross section σ_t characterises the probability of occurrence of any type of nuclear reaction induced by an incident neutron:

$$\sigma_t = \sigma_s + \sigma_a = \sigma_e + \sigma_{in} + \sigma_\gamma + \sigma_{n\alpha} + \dots \tag{3.42}$$

The cross sections depend heavily on the kinetic energy of the incident neutrons [95]. Fig. 3.14 shows the variation of the total cross section of ^{197}Au with the energy of the neutron.

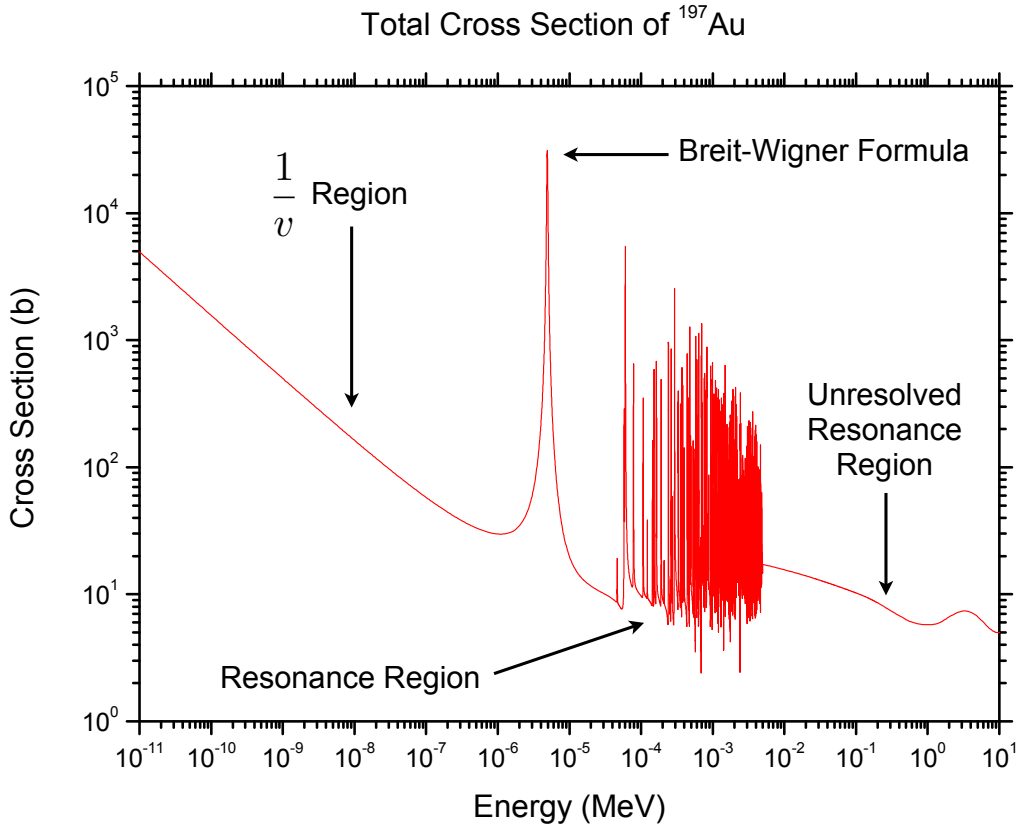

Figura 3.14: Total cross section of ^{197}Au [96].

There are basically three regions in the cross section plots like the one presented in Fig. 3.14. In the low-energy region, the cross sections vary approximately as $1/v$, v being the neutron speed [97]. Then there is the *resonance region*. In the vicinity of an isolated resonance with energy E_0 the cross section is given by the Breit-Wigner formula:

$$\sigma(E_n) = g_n \frac{\pi}{k_n^2} \frac{\Gamma_n \Gamma}{(E_n - E_0)^2 + (\Gamma/2)^2}, \tag{3.43}$$

with

- E_0 – energy of the resonance;
- $g_n = (2J+1)/((2s+1)(2I+1))$ – spin factor, in which

  I is the spin of the target nucleus,

  J is the total angular momentum of the compound nucleus and

  s is the neutron spin;
- $k_n = 2.196771 \times 10^{-3} \frac{A}{A+1} \sqrt{E_n}$;
- Γ – Full width at half maximum (FWHM) of the resonance corresponding to the total cross section;
- Γ_n – FWHM of the resonance corresponding to the scattering cross section.

Γ is the sum of the individual reaction widths [98],

$$\Gamma = \Gamma_n + \Gamma_\gamma + \Gamma_f + \Gamma_p + \cdots . \tag{3.44}$$

For energies above the resonance region the cross section decreases smoothly. In this region the resonances are so close to each other that they cannot be resolved – it is usually referred to as the *unresolved resonance region*. The plot shows the average values of the superimposed unresolved resonances.

The macroscopic cross section is the cross section that characterises all the nuclei of a material. If N is the atomic density of the material (atoms/cm^3), the macroscopic cross section is given by

$$\Sigma_t = N \cdot \sigma_t. \tag{3.45}$$

The macroscopic cross section has units of cm^{-1}. The term *macroscopic* comes from the fact that Σ_t characterises the probability of interaction of the neutrons in a macroscopic volume of material, while the microscopic cross section refers to the probability of interaction with a single nucleus. The total macroscopic cross section is given by

$$\Sigma_t = \Sigma_s + \Sigma_a = \Sigma_e + \Sigma_{in} + \Sigma_\gamma + \Sigma_{n\alpha} + \ldots = N(\sigma_e + \sigma_{in} + \sigma_\gamma + \sigma_{n\alpha} + \cdots) \tag{3.46}$$

When a neutron beam with intensity I_0 hits a material, its intensity decreases with the distance covered inside the material according to an exponential attenuation law:

$$I(x) = I_0 \cdot e^{-\Sigma_t x}. \tag{3.47}$$

The *mean free path* (λ) of a neutron is defined as the average distance covered by a neutron in the material before it interacts with a nucleus:

$$\lambda = \frac{1}{\Sigma_t}. \tag{3.48}$$

3.2.3 Neutron Moderators

The fission cross section of ^{235}U is smaller for high-energy neutrons than for neutrons with very low energies, as can be seen in Fig. 3.15. Neutron moderation is the process in which the neutrons gradually lose energy through elastic collisions with nuclei of appropriate materials. Ultimately, their kinetic energy can be reduced to such an extent that the average becomes the same as that of the atoms (or molecules) of the medium. Since the value of the kinetic energy then depends on the temperature, it is called thermal energy, and neutrons at these energies are called thermal neutrons. At ordinary temperatures, the most probable energy of such neutrons is 0.025 eV [93], which corresponds to a speed of 2200 m/s. During this *thermalisation* process, the probability of inducing fission in ^{235}U increases. If the objective is to induce fission in ^{235}U, the possibility of using neutron moderators must be explored.

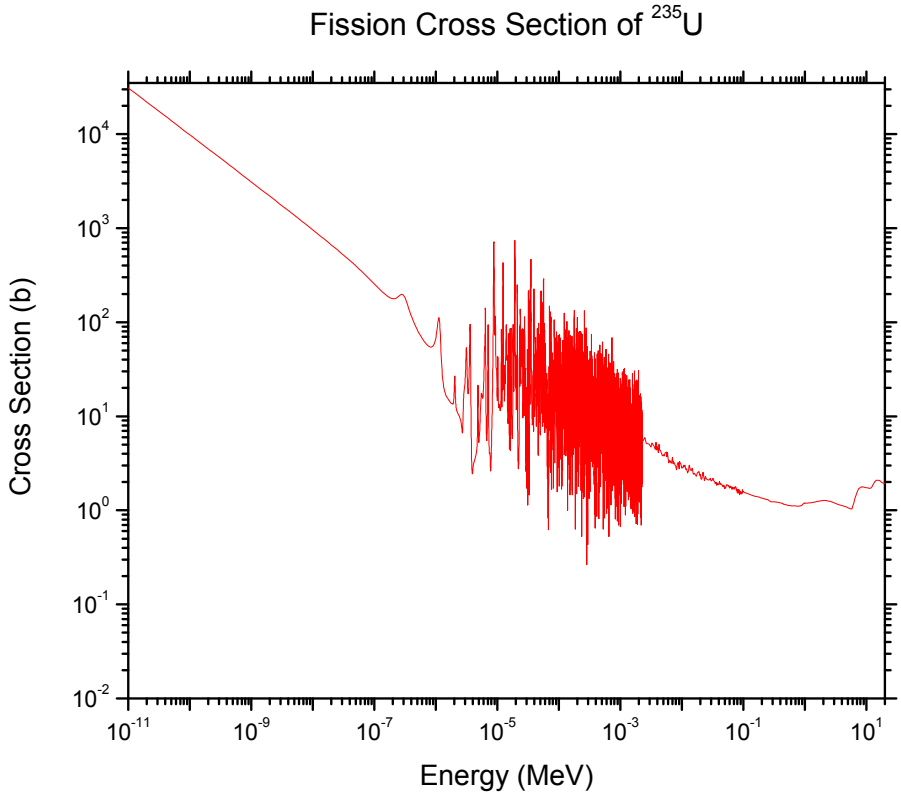

Figure 3.15: Fission cross section of ^{235}U [96].

A neutron involved in a scattering reaction with a stationary nucleus loses a fraction of its

energy. In elastic scattering, the principles of conservation of kinetic energy and momentum from classical mechanics can be used calculate the energy of the neutron and recoil nucleus after the collision, by treating the interaction in the same way as a collision between billiard balls. In that analogous case, the maximum energy transfer occurs when a moving ball hits a stationary ball of the same mass, in a frontal collision, coming to rest after transferring all its kinetic energy to the other ball. The same happens when a neutron transfers most of its energy to a nuclei of hydrogen, which has approximately the same mass as the neutron.

On the other hand, when the masses involved are different, as when a ball hits a cushion, the incident ball loses less energy. The same happens when a neutron is scattered off a heavy nuclei – it looses a very small fraction of its initial energy. To summarise, a neutron can lose all its energy in a collision with an hydrogen atom, but loses very little energy in a collision with a heavy nucleus.

As previously stated, there is conservation of kinetic energy and momentum in elastic scattering. It can be shown that when a neutron hits a stationary nuclei, the maximum kinetic energy transferred to the recoil nucleus is

$$\Delta E_{max} = E\left[1 - \left(\frac{A-1}{A+1}\right)^2\right], \tag{3.49}$$

in which E is the energy of the incident neutron and A is the mass number of the target nucleus (which is the same as the ratio between its mass and the mass of the neutron). Since the transferred energy varies from zero to ΔE_{max}, the final energy of the neutron varies from its initial value E to a minimum value given by

$$E_{min} = E - \Delta E_{max} = \alpha E, \tag{3.50}$$

ou seja,

$$\frac{E_{min}}{E} = \alpha. \tag{3.51}$$

Equation 3.51 shows that α is the smallest fraction a neutron can have of its initial energy after being scattered off a nucleus with mass number A [99].

It is useful to define the *average logarithmic energy loss*, given by

$$\xi = \overline{\ln\left(\frac{E}{E'}\right)} = \overline{\ln(E) - \ln(E')} = 1 + \frac{\alpha \ln \alpha}{1-\alpha}, \tag{3.52}$$

in which E is the neutron energy before the collision and E' is the neutron energy after the collision. The average number of collisions needed in order to reduce the neutron energy from

E_0 to E_{final} is

$$\frac{1}{\xi}\ln\left(\frac{E_0}{E_{final}}\right). \tag{3.53}$$

If the initial energy is the average energy of the neutrons produced in fission (2 MeV) and the final energy is the energy of thermal neutrons (0.025 eV), $\ln(E_0/E_{final}) \simeq 18$ [100]. Knowing the values of ξ for several moderator materials, it is possible to compare the number of collision needed to thermalise the fission neutrons. Table 3.1 shows these values for some elements [101].

Table 3.1: Average number of collisions needed to thermalise fission neutrons (2 MeV to 0.025 eV), in several elements.

Element	A	ξ	Number of collisions
H	1	1	18
D	2	0.725	25
Be	9	0.209	87
C	12	0.158	114
O	16	0.120	150
Na	23	0.0825	218
Fe	56	0.0357	504
U	238	0.00838	2148

Heavier elements require a higher number of collisions to thermalise the neutrons. In hydrogen, for example, 18 collisions are enough to thermalise a fission neutron, while in uranium it takes 2148 collisions. It is also seen that higher values of ξ mean less collisions to thermalise the fission neutrons.

A moderator must have, besides a high scattering cross section, a low absorption cross section, since otherwise many neutrons will be absorbed during the moderation process. The moderating power is a useful concept to quantify the efficiency of a material to moderate neutrons, which can be defined as ξ/l_s, l_s being the absorption mean free path of the neutrons in the material. Also important is the moderating ratio, define as

$$R = \frac{\xi l_{aT}}{ls} = \frac{\xi\sigma_s}{\sigma_{aT}}. \tag{3.54}$$

In Equation (3.54) l_{aT} s the absorption mean free path of the thermal neutrons, σ_{aT} is the absorption cross section of the thermal neutrons and σ_s is the scattering cross section. The best moderators are the materials with the highest moderating ratios [102]. Table 3.2 shows the moderating powers and ratios of some moderator materials, together with other important attributes of good moderators [103].

The materials listed in Table 3.2 are the most common moderator materials. Heavy water is theoretically the best material to serve as a moderator in many applications. In practice, however,

Table 3.2: Moderating powers and ratios of some moderator materials [103].

Moderator	H_2O	D_2O	Be	BeO	C
Density (g/cm^3)	1	1.1	1.85	2.69	1.8
σ_s (barn)	44	11	6	9.8	4.8
σ_a (barn)	0.66	0.0026	0.009	0.009	0.0045
Moderating Power (cm^{-1})	1.53	0.37	0.176	0.125	0.064
Moderating Ratio	60	5600	125	170	190
Moderating Length (cm)	5.74	10.93	10	12.22	19.7
Thermal Diffusion Length (cm)	2.88	116	20.8	29	54.4

there is always some fraction of light water in heavy water. If the proportion of light water is 0.5%, the moderating ratio falls to 1/4 of the value presented in Table 3.2 [100]. Even in that case, it is still the best moderator. Light water has a much higher absorption cross section, and thus its moderating ratio is low when compared to heavy water. Nonetheless, light water is widely used, since it is much cheaper than heavy water.

3.2.4 Neutron Reflectors

The neutron reflectors surround the fuel elements containing fissile material in the core of nuclear reactors and have the role of minimising the leakage of neutrons, in order to increase the number of fissions in the fissile material. In general, good moderators are good reflectors [104]. The materials of Table 3.2 can therefore be used as neutron reflectors [105].

3.3 Spallation Physics

An introduction to the physics of spallation is provided in this section, following closely the first three chapters of reference [106]. The most important figures and references from that text, mainly the ones related to experimental results, are also included here.

3.3.1 Description of the Spallation Process

Spallation can be defined as a nonelastic nuclear interaction induced by a high-energy particle ($E \geq 50$ MeV), producing numerous secondary particles. Spallation, unlike fission, is not an exothermal process; it occurs when energetic particles, like protons, deuterons, neutrons, pions or muouns, with energies above several tens of MeV, interact with an atomic nucleus [106]. For

incident protons, the de Broglie wavelength λ is given by (cm)

$$\lambda = h/\sqrt{2 \cdot m_p \cdot E_p} = (h \cdot c)/\sqrt{2 \cdot m_p \cdot c^2 \cdot E_p} \tag{3.55}$$

where $m_p = 938.2$ MeV/c^2 is the rest mass of the proton, E_p is the energy of the proton in MeV, $h = 6.626 \times 10^{-34}$ (J s) $= 4.136 \times 10^{-21}$ (MeV s) is the Planck constant and $h \cdot c \approx 1240 \times 10^{-7}$ (eV cm) [107]. For proton energies between 100-150 MeV, $\lambda \approx 2.8 - 2.3 \times 10^{-13}$ cm, which is smaller than the size of the nucleus; for $E_p = 1$ GeV, $\lambda \approx 9.0 \times 10^{-14}$ cm; for $E_p = 10$ MeV, $\lambda \approx 10^{-12}$ cm, the size of the nucleus. Therefore, for low energies, the proton does not interact with the individual nucleons, but with the whole nucleus instead.

For energies from 100-150 MeV, the de Broglie wavelength is short enough to allow the incident particle to interact with the individual nucleons inside the nucleus. The collision between the incident proton and the nucleus leads to a series of reactions in which individual nucleons or small groups of nucleons are ejected from the nucleus - this series of reactions is called *intranuclear cascade*. After the intranuclear cascade, the nucleus is left in an excited state. A scheme of the spallation process is show in Fig. 3.16.

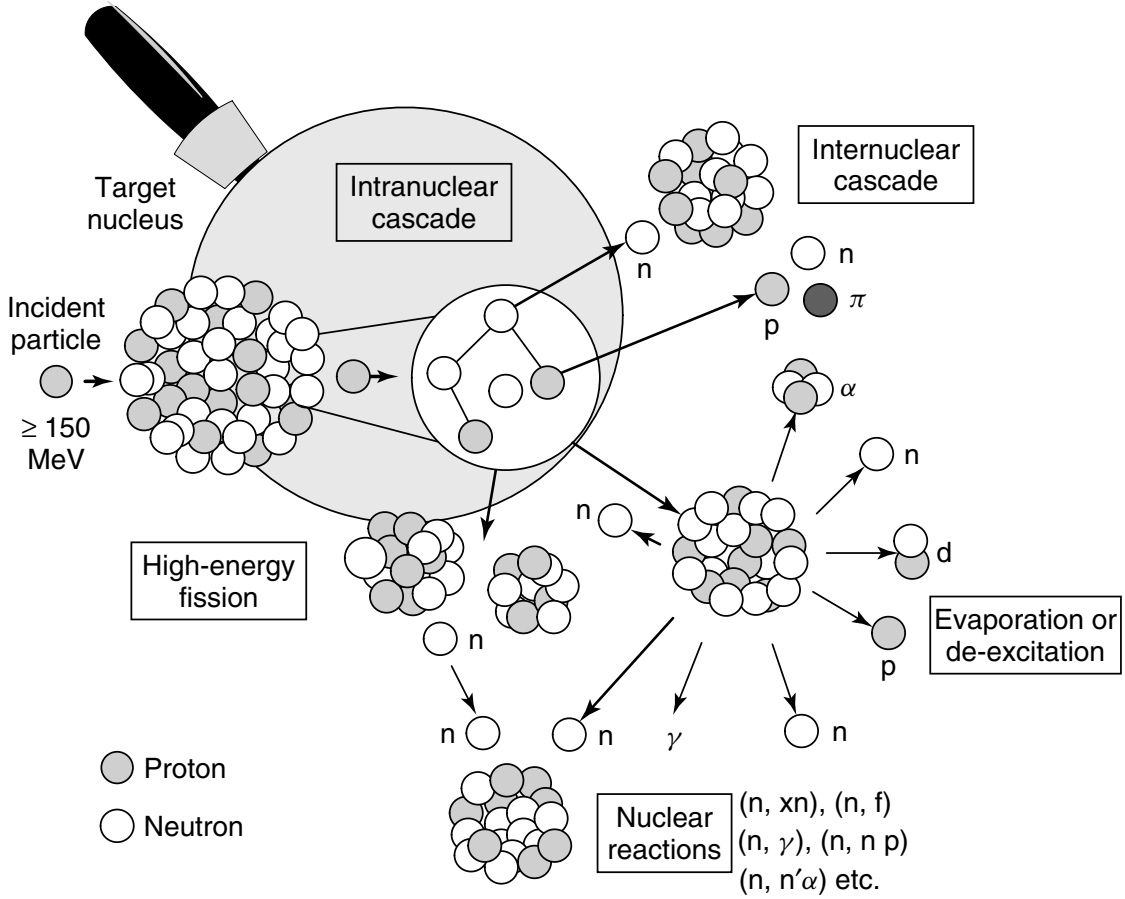

Figure 3.16: Schematic illustration of the spallation process (obtained from [106]).

In the cascade/pre-equilibrium stage, the incident particle is involved in a series of reactions with the neutrons and protons of the target nucleus, producing, in an intranuclear cascade, high-energy secondary particles like protons, neutrons and pions with energies between 20 MeV and the energy of the incident particle. Some of these high-energy hadrons escape from the nucleus as secondary particles, as well as pre-equilibrium particles in the low-MeV range, which leave the nucleus in a highly excited state. During the second stage, the evaporation process takes place – the main path for de-excitation is the emission of low-energy neutrons (< 20 MeV), but protons, alpha particles, and light ions are also ejected from the nucleus. De-excitation through the emission of gamma rays will take place after the evaporation process, if the remaining nucleus is still left in an excited state. For heavy nuclei like lead, tungsten, thorium and natural depleted uranium, high-energy fission can also occur during the evaporation phase (fission by low-energy neutrons will also occur in thorium and uranium).

The high-energy secondary particles that escape from the nucleus move roughly in the direction of the incident particle, and can interact with other nuclei of the target material in a series of secondary spallation reactions that generate more secondary particles and low-energy neutrons, in a hadronic cascade usually referred to as *internuclear cascade*.

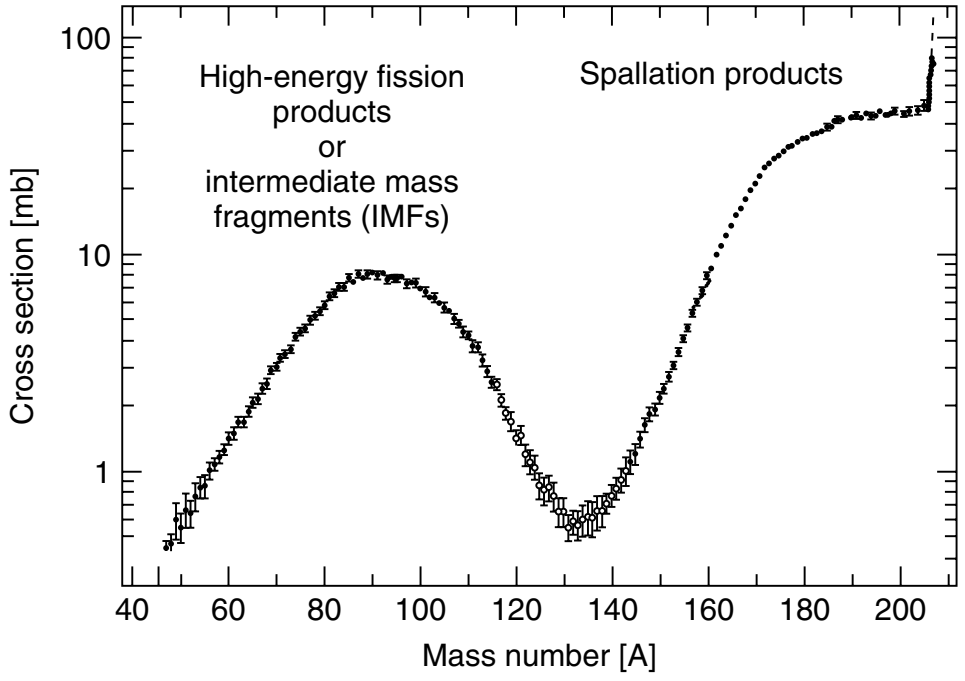

Figure 3.17: Spallation residual mass distributions of 1 A GeV ^{208}Pb + p reactions [108].

Fig. 3.17 shows a typical mass distribution of spallation residuals, for 1-GeV protons on a ^{208}Pb target [108]. On average, and in contrast to what happens in the fission process, nuclei that remain after the evaporation stage are 15 atomic mass units lighter than the target nuclei, since the emitted particles are light particles like neutrons and protons. It is also important to notice that

the fission products in high-energy fission are symmetrically distributed around $A = 90$, while in low-energy fission the nucleus is usually split into asymmetric fragments (a light fragment and a heavy fragment). At high energies, the shell effects are washed out.

Another difference between fission and spallation is the number of released neutrons: while the number of neutrons released per fission event is typically 2–3 (2.42 is the average value for fission induced by thermal neutrons in ^{235}U), a typical spallation event caused by a 1-GeV proton on a heavy target releases 25 to 30 neutrons. Furthermore, approximately 200 MeV of energy are released as kinetic energy in a fission reaction, while a spallation event in a Hg target releases about 55 MeV. Also important is the difference in the spectra of fission and spallation neutrons: as Fig. 3.18 shows, spallation neutrons are, in average, more energetic than fission neutrons, exhibiting a high-energy component which approaches the energy of the incident protons [109]. In spallation, the low energy (< 20 MeV) neutrons from the intranuclear cascade, evaporation and fission processes are emitted isotropically, while the high-energy neutrons have a strong angular dependence – neutrons emitted in the forward direction can have the same energy as the incident protons which caused the spallation event.

An overall scheme of the spallation process is given in Fig. 3.19. The incoming particle transfers part of its energy to the nucleus, increasing the energy of the nucleons inside. The intranuclear cascade occurs within 10^{-22} s after this energy transference. During the intranuclear cascade, energetic particles may leave the nucleus and induce spallation reactions in neighbouring target nuclei, generating internuclear cascades. Following the intranuclear cascade, the excited nucleus enters the evaporation stage, which occurs in a time frame of 10^{-18} s or less. Low-energy particles (mostly neutrons) are emitted isotropically during the evaporation stage. When particle emission is no longer energetically possible, de-excitation through the emission of gamma radiation takes place, if the nucleus is still left in an excited state. In heavy spallation targets, high-energy fission may compete with evaporation [106].

3.3.2 Intranuclear Cascade Models

During the past 30 years, several theoretical Intranuclear cascade (INC) models have been developed. The majority of the models assumes that the interactions between high-energy particles and the nucleus can be represented by collisions between free particles within the nucleus. As mentioned in the previous section, the intranuclear cascade process is followed by various physical processes like evaporation, fission and other de-excitation processes. In the energy range between 0.1 and 5 GeV the most complete models for INC calculations are BERTINI, INCL, ISABEL and CEM, described in the following subsections. Special attention will be given to the BERTINI model, the precursor of all modern INC models, to illustrate the basics of these codes. An extensive description of INCL, ISABEL and CEM, which is beyond the scope of this introduction, can be found in [106].

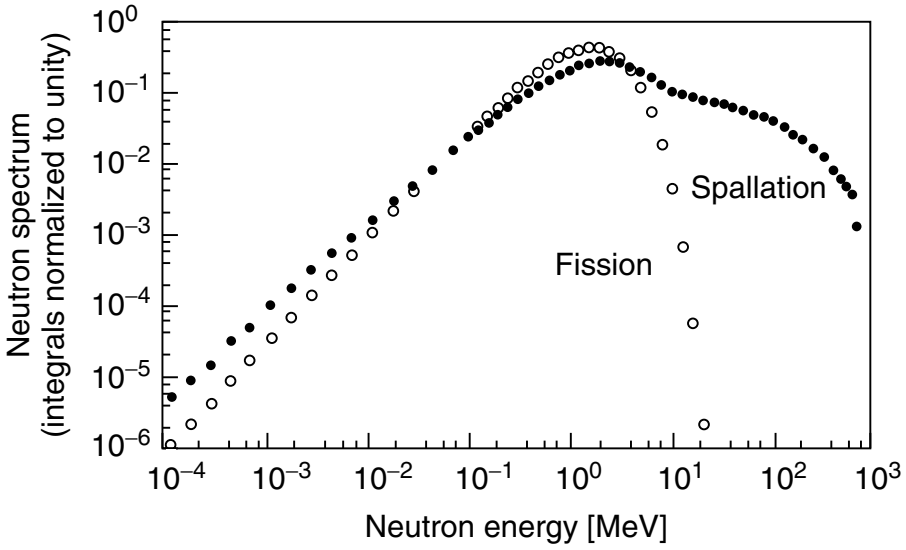

Figure 3.18: Spallation neutron spectrum compared to a typical neutron spectrum from thermal neutron fission of ^{235}U, for a tungsten target bombarded by 800 MeV protons [109].

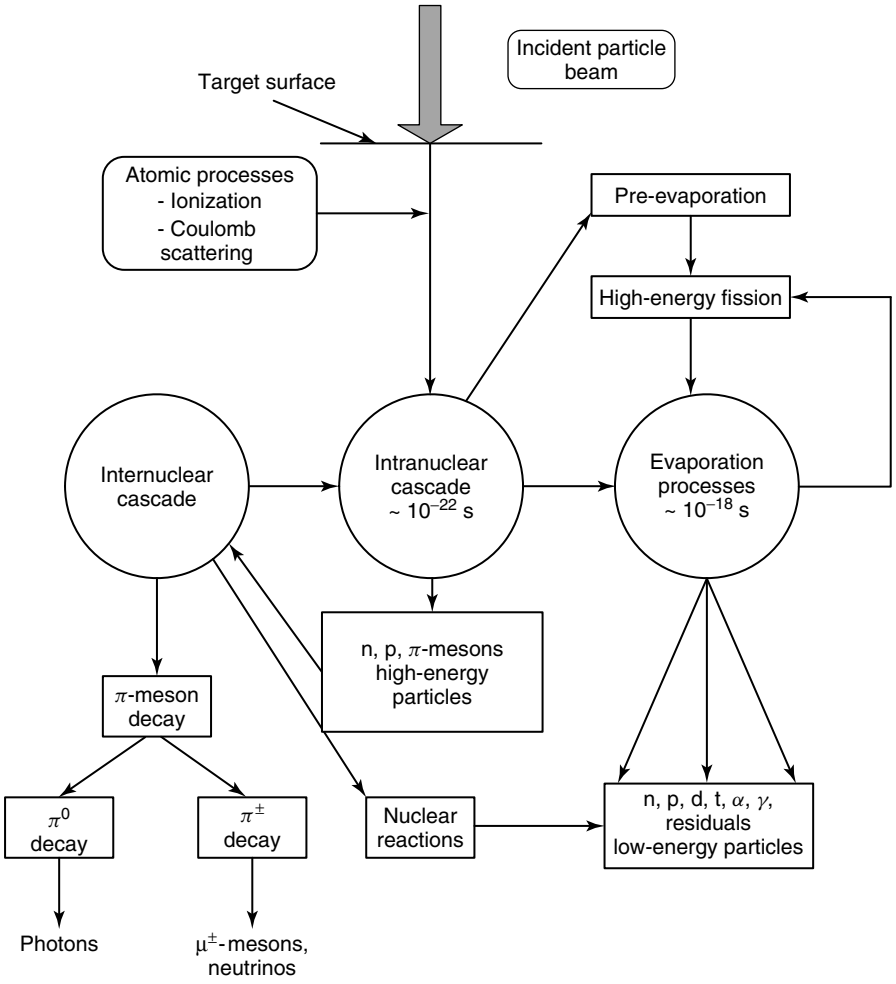

Figure 3.19: Logical scheme of a spallation reaction (obtained from [106]).

3.3.2.1 The BERTINI Nuclear Model

In the BERTINI [110] model, the target nucleus is divided in three regions, as an approximation to the changing density distribution of matter within the nucleus. It uses the Fermi gas model to describe the behaviour of the nucleus inside the nucleus, obeying Fermi-Dirac statistics and the Pauli exclusion principle. When an incident particle (proton, neutron, pion, etc.) hits a nucleon from the target nucleus, the intranuclear cascade process starts and secondary particles are produced. Each secondary particle is followed until it escapes from the nucleus or its energy falls below some predetermined cut-off energy, usually half of the Coulomb barrier of the surface of the nucleus. The BERTINI model uses relativistic kinematics.

Nucleon density distribution inside the nucleus The nucleus in the BERTINI model is made of three concentric spheres, with radii r_1, r_2 and r_3, each with uniform density. The proton density in each region is proportional to the average value of a continuous nonzero Fermi charge distribution obtained from experimental measurements. The charge density inside the nucleus as a function of its radius is then given by

$$\rho(r_i) = \frac{\rho_0}{1 + \exp(\frac{r_i - r_0}{\alpha})}, \tag{3.56}$$

where ρ_0 is a normalisation constant, r_i corresponds to the three zones of the nucleus, $r_0 = 1.07 \cdot A^{1/3} \times 10^{-13}$ cm and $\alpha = 0.545 \times 10^{-13}$ cm. Since the neutrons are assumed to be distributed in the same way as protons, ρ_0 is given by

$$\rho_0 = \frac{4\pi}{A} \int_0^\infty dr \cdot r^2 \cdot \rho(r). \tag{3.57}$$

The density of the nucleus decreases with increasing radius:

$$\begin{aligned} \rho(r_1) &= 0.90 \cdot \rho_0, \\ \rho(r_2) &= 0.20 \cdot \rho_0, \\ \rho(r_3) &= 0.10 \cdot \rho_0. \end{aligned} \tag{3.58}$$

Assuming $r_0 = 0$, the nucleon density in zone i is then given by

$$\rho_i = \frac{4\pi}{V_i} \int_{r_i - 1}^{r_i} dr \cdot r^2 \cdot \rho(r). \tag{3.59}$$

The fraction of the number of protons (p_i) and neutrons (n_i) in each of the three zones is the same as for the nucleus as a whole:

$$\begin{aligned} p_i &= (\rho_i/A) \cdot Z \\ n_i &= (\rho_i/A) \cdot (A - Z) \\ (n_i/p_i)v_i &= ((A - Z)/Z)_{\text{nucleus}} \end{aligned} \tag{3.60}$$

Fig. 3.20 shows a comparison of typical nucleon density distributions for ^{65}Cu and ^{197}Au, plotted against experimental experimental measurements from [111].

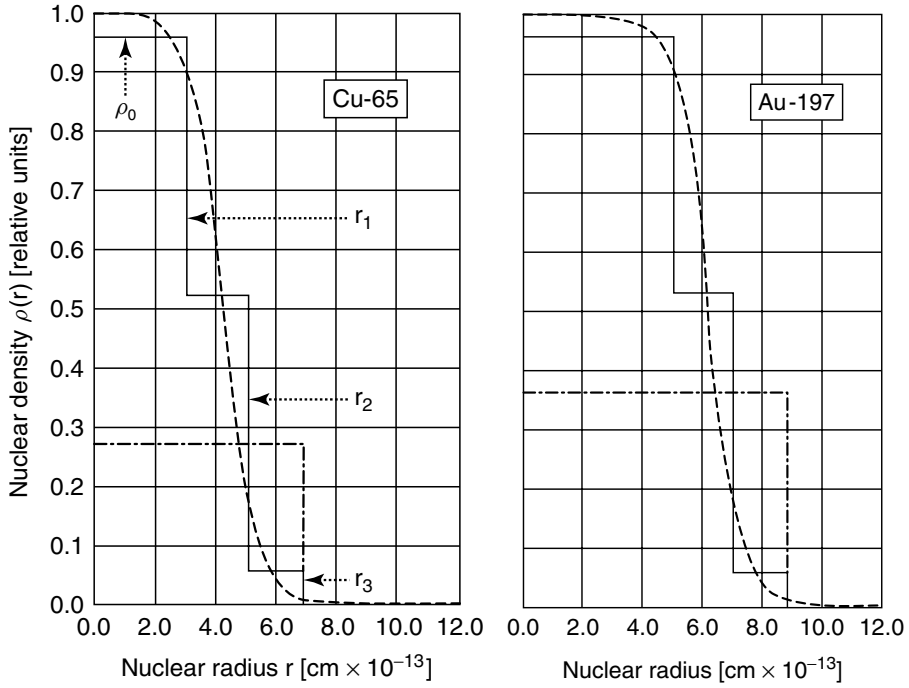

Figure 3.20: Comparison of various nucleon density distributions inside the nucleus, for ^{65}Cu (left) and ^{197}Au (right). Solid lines represent the standard nonuniform nucleon density configuration, for the three standard zones; dashed-doted lines represent the uniform nucleon density distribution, when $\rho(r_1) = \rho(r_2) = \rho(r_3)$; the dashed line refers to experimental measurements from [111] (obtained from [106]).

Momentum distribution of nucleons inside the nucleus In the BERTINI model, the momentum distribution of the nucleons is a approximated as a mixture of degenerated Fermi gases of protons and neutrons, in which the protons and neutrons are treated as free particles enclosed in a sphere. Protons and neutrons are, according to the exclusion principle, identical particles (*fermions*[2]) occupying different quantum states. The number of states corresponding to a momentum smaller than the Fermi momentum P_F for neutrons and protons is, according to [113],

[2]Fermions are particles with half-integer spin – they include all baryons (protons and neutrons are baryons), leptons and quarks [112].

given by

$$N_{states} = \frac{2}{(2\pi\hbar)^3} \cdot \frac{4}{3} \cdot \pi \cdot V \cdot P_F^3. \tag{3.61}$$

At a complete degeneracy of the Fermi gas, the Fermi momenta for protons and neutrons in the ground state are

$$\begin{aligned} P_{F_p} &= (3\pi^2)^{1/3} \cdot \hbar \cdot (Z/V)^{1/3} \\ P_{F_n} &= (3\pi^2)^{1/3} \cdot \hbar \cdot ((A-Z)/V)^{1/3}. \end{aligned} \tag{3.62}$$

With the approximation $Z = N = A/2$ the Fermi momentum is given by

$$P_F = \hbar \cdot \left(\frac{3\pi^2 \cdot A}{2 \cdot V} \right)^{1/3}, \tag{3.63}$$

with the volume of the nucleus given by $V = (4/3)\pi \cdot r_0 \cdot A^{1/3}$ [113].

The momentum distribution in each of the three zones of volume V_i in the BERTINI model follows a Fermi distribution with zero temperature:

$$\int_0^{P_{F_i}(r_i)} f(p)dp = N_p \text{ or } N_n. \tag{3.64}$$

The integral is the total number of protons or neutrons in one of the three zones and

$$P_{F_i} = \hbar \cdot \left(\frac{3\pi^2 \cdot \rho(r_i)}{2} \right)^{1/3} \tag{3.65}$$

is the radius-dependent momentum of a nucleon corresponding to the radius-dependent Fermi energy, given by

$$E_{F_i} = \frac{\hbar^2}{2 \cdot m_N} \cdot (3\pi^2 \cdot \rho_{p,n}(r_i))^{2/3}, \tag{3.66}$$

where the subscripts p, n refer to the proton and neutron densities, m_N is the mass of the nucleon and $\hbar = 1.054 \times 10^{-34}$ J s is the reduced Planck constant ($h/2\pi$). The Fermi energy depends on the value of the nuclear radius r_i and the assumed density. This requires the use of a radius- and density-dependent nuclear model [106].

Potential energy distribution inside the nucleus If $B(A, Z)$ is the binding energy of a nucleon and V_C is the Coulomb potential (energy in the centre of mass system which is needed to overcome the Coulomb repulsion), the potential of a nucleon is given by

$$V(A, Z, r_i) = E_{F_i}(r_i) + B(A, Z) + V_C(A, Z). \tag{3.67}$$

Using equations (3.65) and (3.66), the proton or neutron potential in zone V_i is given by

$$\begin{aligned} V_i(A,Z) &= E_{F_i}(r_i) + B(A,Z) \\ &= \hbar^2 \cdot \frac{(3\pi^2 \cdot \rho_{p,n}(r_i))^{2/3}}{2m_n} + B(A,Z) \\ &= \frac{P_{F_i}(r_i)^2}{2m_N} + B(A,Z). \end{aligned} \tag{3.68}$$

For a nuclear volume of $V \approx (4/3)\pi \cdot r_0^3 \cdot A$, the proton and neutron momenta may be written as

$$\begin{aligned} P_{F_{proton}} &= \hbar/r_0 \cdot (9\pi \cdot Z/4A)^{1/3} \\ P_{F_{neutron}} &= \hbar/r_0 \cdot (9\pi \cdot N/4A)^{1/3}, \end{aligned} \tag{3.69}$$

according to equations (3.62) and (3.63). To estimate the Fermi momenta, the approximation $N = Z = A/2$ can be take once again, giving

$$P_{F_{\text{proton}}} \simeq P_{F_{\text{neutron}}} \simeq \hbar/r_0 \cdot \left(\frac{9\pi}{8}\right)^{1/3} \simeq \frac{297}{r_0}\ \text{MeV}/c. \tag{3.70}$$

The respective kinetic Fermi energy is given by

$$F(E_{max}) = \frac{(P_{F_{\text{proton}}})^2}{2 \cdot m_{\text{proton}}} = \frac{(P_{F_{\text{neutron}}})^2}{2 \cdot m_{\text{neutron}}} \simeq 34\ \text{MeV} \tag{3.71}$$

which corresponds to the kinetic energy of the highest occupied orbit, with the smallest binding energy. If the binding energy is $B = 8$ MeV, as assumed in the BERTINI model, an estimate of the nuclear well depth is given by $E_{max} = F(E_{max}) + B \simeq 42$ MeV. Fig. 3.21 is an example of the potential well for protons and neutrons in a nucleus, $E_{F_{neutron}} = 34$ MeV being the maximum kinetic energy of a neutron bound to the nucleus. The difference in the wells for protons and neutrons is due to the Coulomb well.

Application of the Pauli Exclusion Principle The exclusion principle is the only quantum mechanical effect included in the BERTINI model, through the introduction of the Pauli blocking factor for protons and neutrons. The exclusion principle forbids interactions in which the collision products would be in occupied states. Since for a degenerate Fermi gas the levels are filled starting from the lowest level, collisions are forbidden in which a very large or a very small amount of energy is transferred. In a collision, the minimum energy of the low-energy product is the lowest unfilled level of the system – the Fermi energy in the appropriate zone V_i of the nucleus. In a Monte Carlo calculation using the BERTINI model, the exclusion principle is applied by accepting only secondary nucleons with energies larger than the Fermi energy [106].

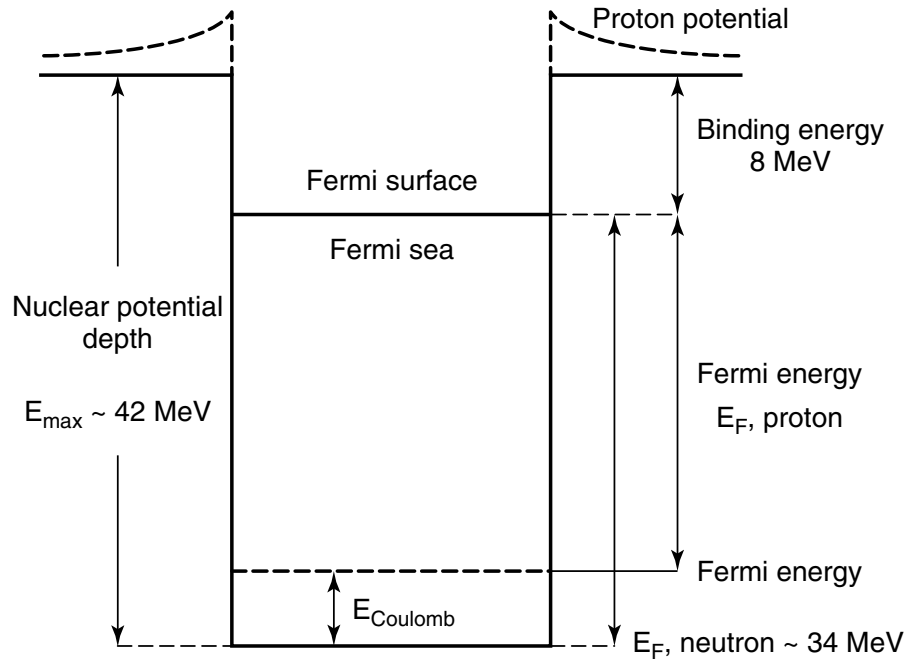

Figure 3.21: Example of the potential well for protons and neutrons in a nucleus (obtained from [106]).

Cross section data The BERTINI model requires cross section data for nucleon-nucleon elastic and inelastic scattering, pion-nucleon elastic scattering, charge exchange and pion production, which are reasonably known from experimental data. The model takes into account neutron and proton reactions up to 3.5 GeV and pion reactions up to 2.5 GeV.

The differential cross sections for p-p scattering $(d\sigma/d\Omega)_{pp}$ are assumed isotropic in the center-of-mass system for protons up to 500 MeV. For energies up to 4.4 GeV, the expression

$$(d\sigma/d\Omega)pp = A + B \cdot \mu^3, \tag{3.72}$$

from semiempirical fits, is used, with μ representing the cosine of the scattering angle in the centre-of-mass system. The differential cross-sections for n-p scattering are treated for forward and backward scattering separately, using various semiempirical fits for different energy ranges. Figs. 3.22 and 3.23 show the total proton-proton and neutron-proton scattering cross sections used in the original BERTINI model. These cross sections exhibit a good agreement with experimental data evaluated by the *Particle Data Group* [106, 114].

Method of computation The BERTINI model uses the Monte Carlo method to simulate the interaction of hadrons with nuclei. The incident particle starts by interacting with a single nucleon inside the nucleus as if the nucleons were in free space, taking into account the exclusion principle to exclude collisions with disallowed momentum transferences. The basic steps for the

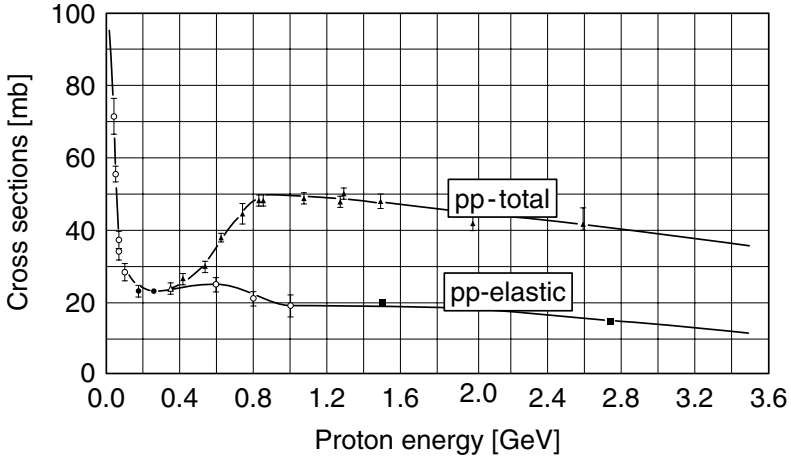

Figure 3.22: Total and elastic proton-proton cross sections used in the BERTINI model (obtained from [106]).

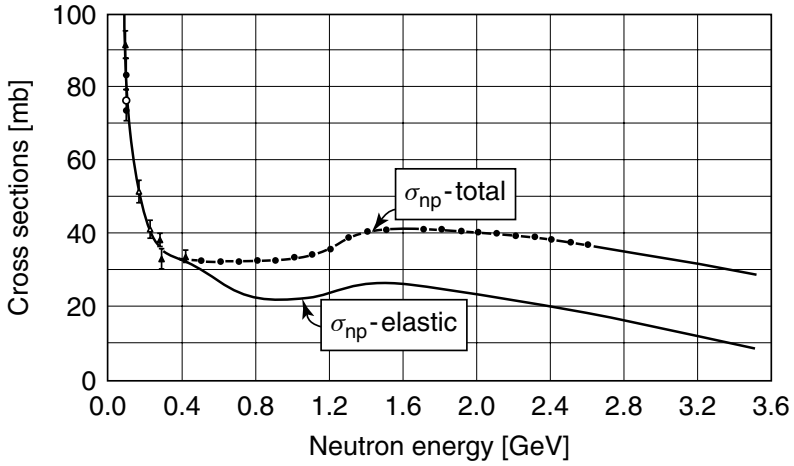

Figure 3.23: Total and elastic neutron-proton cross sections used in the BERTINI model (obtained from [106]).

simulation are:

1. the spatial point where the incident particle enters the nucleus is determined, sampling from a uniform distribution over a circular area representing the projected area of the nucleus;

2. to select the distance travelled by the particle in the nucleus, a path length is sampled using the total cross sections and the nucleon densities;

3. if the particle escapes the nucleus without colliding, there is *nuclear transparency*. If there is a collision inside the nucleus, the momentum of the struck nucleon, the type of reaction and the energy and direction of the reaction products are sampled from the cross sections;

4. if the exclusion principle allows the collision and the kinetic energy of the product is above the cutoff energy, then the simulation goes back to point 2 and the resulting particles are transported further;

5. when the intranuclear cascade caused by an incident particle ends, the mass and charge of the residual nucleus are determined from a particle balance, and the residual energy is determined from an energy balance;

The outcome of the BERTINI model is the double differential particle spectra of cascade particles (in energy and laboratory angle) and a residual nucleus [106].

Assumptions and limitations of the BERTINI model One of the advantages of the BERTINI model is that it requires only fundamental particle-particle cross sections, which are relatively well known. It has shown a reasonable agreement with a wide range of experimental data, for incident protons, neutrons and charged pions with energies between 0.1 and 3 GeV. The model can be applied to all target nuclei with $A \geq 1$, although the approximation of dividing the nucleus in three zones is only valid for heavier nuclei (for light nuclei, other models should be preferred, like the shell model). The BERTINI model is still implemented in a variety of transport models and codes, like FLUKA, MCNPX and GEANT4.

As for its limitations, the model is only valid for incident protons, neutrons and pions and should only be applied above the low-energy limit defined by the de Broglie wavelength. For energies below 150-200 MeV, a pre-equilibrium or evaporation model should be used instead.

3.3.2.2 The INCL Model

The INC-Liège model, or INCL [115], is a more recent alternative to the BERTINI model which is actively developed at the University of Liège in Belgium. The fundamental assumptions of the INCL model are based on the semiclassical microscopic description of a collision between a particle and a nucleus, as described in the BERTINI model: the motions of particles obey the laws of classical mechanics (the only quantum mechanical effect is the Pauli exclusion principle), reaction cross sections are computed when not available, it uses relativistic kinematics, etc. The latest INCL model, INCL4, is probably the most sophisticated INC model currently available, including the latest hadron and meson reaction mechanisms and data.

When compared to other INC models and previous versions of INCL, INCL4 has several new features, including the following:

- it includes a realistic target density distribution, which allows to model a diffuse nuclear surface;

- it has an improved treatment of the Pauli blocking, removing nonphysical features linked with the statistical blocking factors;

- the rest angular momentum is included in the output of the model;

- the history of all particles is followed as a function of time, taking into account the time at which the INC calculated is terminated and allowing the coupling with pre-equilibrium or evaporation models.

The incident particle can be a proton, neutron, deuteron, triton, ^{3}He, ^{4}He, π^+, π^- or π^0, which hits a target nucleus at rest. INCL4 is well validated for projectiles in the energy range from 0.2 to 2.0 GeV. Fig. 3.24 shows a comparison between experimental data and predictions made with INCL coupled to an evaporation model, for 1.2 GeV protons hitting Pb and Th targets [116]. Overall, the agreement between experimental and simulation data shows that the INCL model, coupled to an evaporation code, can reproduce the neutron production cross sections in the whole phase space.

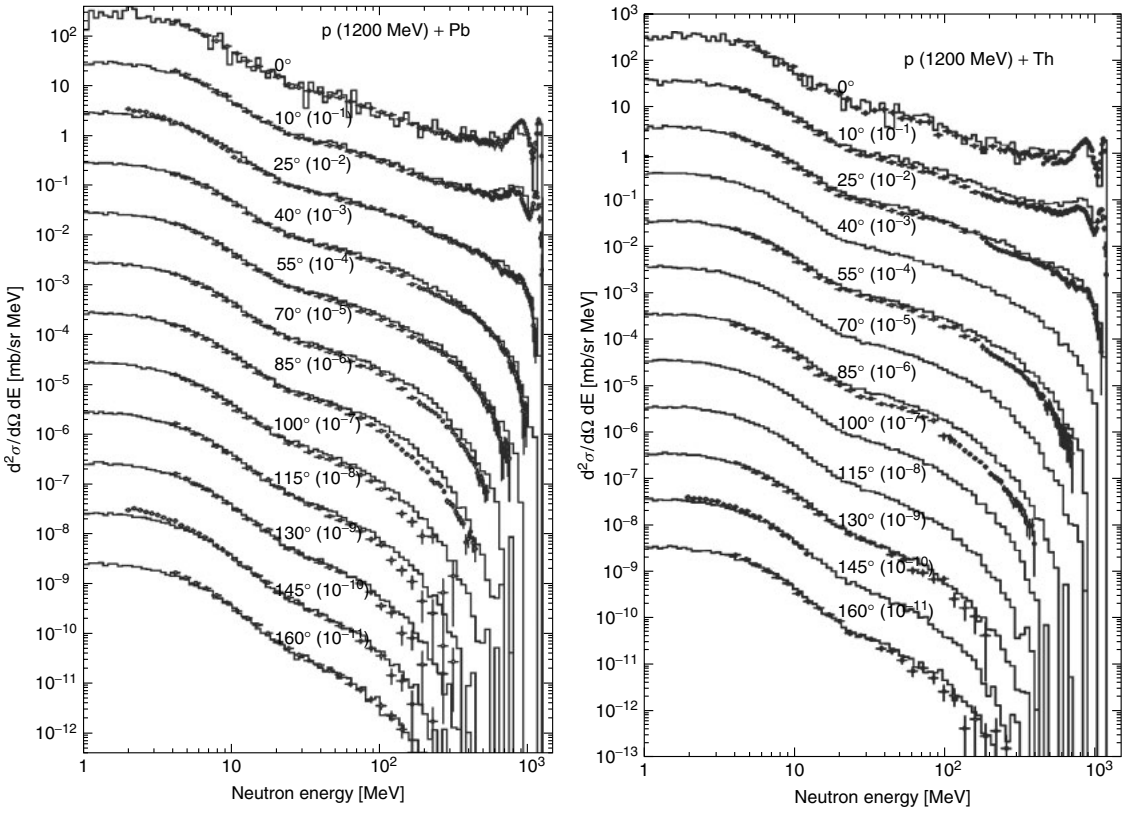

Figure 3.24: Simulated (histogram) and experimental (circles) double differential cross sections for 1.2 GeV proton induced reactions on Pb (left) and Th (right) targets, and detection angles from 0° to 160°. The spectra have been multiplied by decreasing powers of ten, except for 0°. The INCL model was used in the simulations, coupled with an evaporation code (obtained from [106]).

3.3.2.3 The ISABEL Model

The ISABEL model [117] was developed between 1978 and 1981 by Yariv and Frankel, and is implemented in the Monte Carlo codes LAHET and MCNPX. It simulates hadron-nucleus and nucleus-nucleus interactions for energies between 0.1 and 1.5 GeV/particle. The original version included hadrons, pions, kaons and antinucleons as incident particles, and later extensions were added to take into account heavy-ion reactions. The possibility of following intranuclear cascades on a time-like basis and to accommodate nucleus-nucleus interactions are important characteristics of the ISABEL model, which, apart from those features, shares many characteristics with the BERTINI and INCL models [106].

3.3.2.4 The CEM Model

The CEM (Cascade Exciton Model) [118] considers three stages in the spallation reactions: cascade, pre-equilibrium and equilibrium. It is not a pure intranuclear cascade model like BERTINI, INCL or ISABEL; instead, it has many different simulation models in it, including models that simulate different physics processes like evaporation, high-energy fission or photonuclear reactions. It is very well validated and covers a wide energy range, from eV to several TeV. It has the advantage of predicting the production of residual nuclei, fission fragments, low and high energy light particles and product yields from high-energy photonuclear reactions [106].

3.3.3 Evaporation and High-Energy Fission

The intranuclear cascade is the first step of the spallation process, and the calculations performed with the INC models of the previous sections are stopped when equilibrium is achieved. To account for the full process, an evaporation model is usually used after the fast stage of the spallation process, to continue the de-excitation of the highly excited residual nucleus. There are several models to accomplish this task, most of them based on the statistical theory of evaporation from the excited compound nucleus, developed by Weisskopf [119]. Some of the most important models are the Dresner EVAP model [120], the GEM model [121], the abrasion-abla model ABLA [122, 123] and the GEMINI model [124], among others.

For heavy targets, high energy fission competes with evaporation at each step of the de-excitation process. Models like EVAP or GEM are coupled with fission models to take high-energy fission into account, while ABLA and GEMINI have their own high-energy fission models. When the excitation energy falls below some cut-off value, usually close to 7 MeV, further excitation is done by evaporation or gamma emission. A detailed description of the physics models for evaporation and fission can be found in [106].

3.4 FLUKA

FLUKA is a general-purpose Monte Carlo code for particle transport simulation, with applications in several fields of science such as accelerator shielding, target design, activation, dosimetry, detector design, cosmic rays, radiotherapy, etc. FLUKA can simulate the interaction and propagation in matter of about 60 different particles, handling very complex geometries which can be built with various visualisation and debugging tools. It is written in Fortran 77 and, for most applications, requires no programming from the user.

The history of FLUKA can be split into three different generations: a first version in the 1970s, developed by J. Ranft and J. Routti, a second version in the 1980s (P. Aarnio, A. Fassò, H. Mohring, J. Ranft and G. Stevenson) and the current version (A. Fassò, A. Ferrari, J, Ranft and P. Sala). Each generation represented a major upgrade from the previous one – the current version of FLUKA is completely different from the earlier versions, with completely new physical models, rewritten code and different tracking strategies and scoring capabilities.

In the 1980s, FLUKA was a specialised program to calculate shielding of high-energy proton accelerators; today, FLUKA is used worldwide in a wide range of applications, including activation studies, radiation damage, isotope transmutation, dosimetry and medical applications. While radiation damage has always been a field of application of FLUKA, it used to be restricted to hadron damage in accelerator components. With the recent capability of tracking low-energy neutrons, FLUKA has widened its range of applications to include electronics and other sensitive detector parts. Shielding design calculations are no longer restricted to proton accelerators; any kind of radiation sources, artificial or natural, can be simulated with FLUKA. The following sections describe the general capabilities of FLUKA, following reference [75].

3.4.1 Physics of FLUKA

3.4.1.1 Hadron Inelastic Nuclear Interactions

In FLUKA, two models are used in hadron-nucleus interactions. At momenta below 3-5 GeV/c the PEANUT package includes a very detailed Generalised Intranuclear Cascade (GINC) model and a pre-equilibrium stage. At higher energies, between 5 GeV and 20 TeV, a less refined GINC model is used, based on the Gribov-Glauber multiple collision mechanism. Equilibrium processes follow: evaporation, fission, fermi break-up and gamma desexcitation. Inelastic cross sections for hadron-hadron interactions are obtained through parameterised fits based on available experimental data, while for hadron-nucleus interactions a mixture of tabulated data and parameterised fits is used. FLUKA can also simulate photonuclear interactions [75].

The PEANUT model handles interactions of nucleons, pions, kaons and γ rays from a few GeV

down to reaction threshold (or 20 MeV for neutrons). The reaction mechanism is modelled by a GINC model smoothly joined to statistical pre-equilibrium emission. After that, the evaporation of nucleons and light fragments (α, d, ^{3}H, ^{4}He) is performed, according to the Weisskopf statistical treatment. Competition of high-energy fission with evaporation has also been implemented using a statistical approach. The Fermi Break-up model is used for light nuclei. A new evaporation treatment was developed by Ferrari and Sala in 1996-1997 and refined in 2001, with several physics improvements which made the description of the production of residual nuclei much more accurate. The production of fragments up to mass 24 has been included in the meantime as an option to be activated by the user.

Secondary particles are treated in the same way as primary particles, except that they start their trajectory inside the nucleus. They are transported according to their mean nuclear field and to the Coulomb potential, along classical trajectories affected by a few relevant quantum mechanics effects. Binding energies are obtained from mass tables and relativistic kinematics is applied, with conservation of energy and momentum [125].

3.4.1.2 Nucleus-Nucleus Interactions

Nuclear interactions generated by ions are treated through interfaces to external event generators: DPMJET-II or DPMJET-III for energies above 5 GeV per nucleon and a modified version of RQMD for energies between 0.1 and 5 GeV per nucleon.

DPMJET is a high-energy hadron-hadron, hadron-nucleus and nucleus-nucleus model developed by J. Ranft, S. Roesler and R. Engel, which describes interactions from several GeV per nucleon up tho the highest cosmic ray energies. The interface with FLUKA allows to treat arbitrary ion interactions at energies above 5 GeV per nucleon. The excited projectile and target residuals are passed back to the FLUKA evaporation, fission and break-up routines for de-excitation.

RQMD is an interface similar to DPMJET, developed by F. Cerutti, T. Empl, A. Ferrari, M. Garzelli and J. Ranft, using the Relativistic Quantum Molecular Dynamics (RQMD) code of H. Sorge. This interface allows FLUKA to transport ions from roughly 100 MeV per nucleon up to cosmic ray energies. Evaporation and de-excitation of residuals are also performed by FLUKA [75].

3.4.1.3 Transport of Charged Hadrons and Muons.

FLUKA uses an original treatment of multiple Coulomb scattering and ionisation fluctuations to handle some challenging problems such as electron backscattering and energy deposition in thin layers in the few keV energy range. The Bethe-Block theory is used for energy loss, with improved ionisation potential and handling of porous substances. The energy range for the

transport of charged hadrons is 1 keV-20 TeV, but 100 keV is the minimum recommended energy for primary particles [75].

3.4.1.4 Low-Energy Neutrons

FLUKA uses its own neutron cross sections libraries for neutrons with energies below 20 MeV, in 72 or 260 energy groups, derived from the most recent evaluated data from libraries like JEFF, ENDF or JENDL and containing more than 200 materials. Among other capabilities, It uses standard multigroup transport with photon and fission-neutron generation, provides detailed kinematics of elastic scattering on hydrogen nuclei and allows the transport of proton recoils and protons from (n,p) reactions [75].

3.4.1.5 Electron and Photon Transport

For electron transport, FLUKA uses an original algorithm for charged particles which includes a complete Coulomb scattering treatment. Differences between positrons and electrons are taken into account for stopping power and bremsstrahlung. FLUKA is able to transport electrons with energies between 1 KeV and 1000 TeV, although the minimum energy for primary electrons is between 50 and 100 keV for light materials and between 100 and 200 keV for heavy materials. These limitations at low-energies can be overcome by using a single-scattering option, at the price of some increase in CPU time.

As in the case of electrons, the transport of photons can be made at energies between 1 keV and 1000 TeV. It includes pair production with actual angular distribution of electrons and positrons, Compton effect taking into account atomic bonds by using inelastic Hartree-Fock form factors, photoelectric effect with actual photoelectron angular distribution, Rayleigh scattering, etc. For primary photons, the minimum recommended energy is about 5 to 10 keV. Generation and transport of Cherenkov, Scintillation and Transition Radiation are also provided to the user as an option [75].

3.4.2 Geometry

FLUKA uses a Combinatorial Geometry (CG) package, which has been continuously improved to provide efficiency, accuracy, consistency and flexibility. A fast tracking strategy has been developed, with special attention to charged particle transport in magnetic fields. It allows the definition of up to 10000 regions, with the possibility of introducing lattices for repetitive structures. Voxel geometries are also available, completely integrated into CG. FLUKA also includes a geometry debugger and a geometry plotter.

3.4.3 Variance Reduction Techniques

Several variance reduction options are available in FLUKA, including lead particle biasing for electrons and photons, russian roulette and splitting at boundary crossing based on region relative importance, region-dependent weight windows in three energy ranges and biased decay length for increased daughter production.

3.4.4 Scoring

FLUKA provides generalised scoring options with sophisticated scoring algorithms that would be too complex for a generic user to program. Among other options, it allows the user to score fluence and current as a function of energy and angle, dose-equivalent, track-length fluence or dose equivalent in a binning structure, residual nuclei, fission density, momentum transfer density, etc [75].

3.4.5 FLAIR

FLAIR (FLUKA Advanced Interface) [126] is an advanced user-friendly interface for FLUKA which makes it easy to create and edit input files, execute the code and visualise the results. Besides editing input files, it has a powerful interactive geometry editor that allows the user to edit the geometry and visualise it in real time. It also includes a library of pre-defined materials that can easily be added to the input file by the user. FLAIR is used to debug the input file, compile the code, start the runs (and split them in several parallel runs, for multiprocessor architectures) and monitor their status. Post-processing of the simulation data can also be done inside FLAIR, which has an interface to Gnuplot to visualise the results.

Nuclear data have both fundamental and practical importance. They are produced and intensively used in the experimental and theoretical studies of nuclear reactions and structure of excited nuclei. In practical applications, assessed and verified nuclear data are of extreme importance since they are used in the performance and safety analyses of nuclear facilities. The large variety of applications such as fission and fusion energy generation, particle acceleration, use of radiation in medicine, analytical techniques for material properties analysis, management and safeguards of spent fuel and radioactive wastes dictate the needs for variety of basic nuclear data.

3.5 Nuclear Data Libraries

Nuclear data libraries are extremely important for fundamental science and its applications. The accurate knowledge of nuclear interaction cross-sections and decay data is the basis for experimental and theoretical studies in several fields, such as fission and fusion energy generation, particle accelerators, medical applications of ionising radiation, material analysis and management of radioactive waste [127]. There are several steps involved in the production of data libraries for applications, which include measurements, model calculations, production of files in suitable formats to be used by different programs and benchmark testing.

The most important libraries are referred to as *General Purpose Libraries*, and contain descriptions of all sorts of reactions with different kinds of incident particles in the form of cross sections at a range of energies which, for incoming neutrons, for example, goes from 10^{-5} eV to 20 MeV (modern files may extend to 200 MeV). The accuracy of the cross sections is crucial, since they will be used by particle transport codes to calculate physical quantities such as dose rates, heat production, activation and material damage, and the validity of the results is highly dependent on the quality of the cross section data.

There are several general purpose libraries available worldwide: The ENDF/B-VII.1 [128] file is developed in the USA, the JEFF-3.1.2 [129] file is produced by the OECD countries (mostly European countries), JENDL-4 [130] is the Japanese library, CENDL-3.1 [131] is from China and ROSFOND 2010 [132] is from Russia. Additionally, FENDL-2.1 [133] is a comprehensive data library which aims at collecting the best data from the general purpose files for fusion applications. Besides these evaluated files, which are based on evaluations made at different times with various methodologies, there are libraries such as TENDL-2012 [134] which are complete but are based on calculations and do not take into account all available experimental data. Evaluations of the nuclear data libraries are typically performed every 5-10 years [135].

Besides nuclear reaction data, most applications need information on the decay properties of nuclides produced through activation of the materials, which is stored in *Special Purpose Libraries* of decay data, such as the JEFF-3.1.1 radioactive decay data library, which gives information on half-lives, decay modes and energy release, using the ENDF-6 format. Also important are dosimetry libraries such as IRDFF1.02 [136], the International Reactor Dosimetry and Fusion File, a standardised evaluated cross section library of neutron dosimetry reactions, and activation libraries like the European Activation File EAF-2010 [**?**], an extensive data library prepared for the European Activation System (EASY) with activation-transmutation neutron data including 816 target isotopes and energies ranging from 10^{-5} eV to 60 MeV.

The Nuclear Energy Agency (NEA) is a specialised agency within the Organisation for Economic Co-operation and Development (OECD) with the mission of assisting " its member countries in maintaining and further developing, through international co-operation, the scientific, tech-

nological and legal bases required for a safe, environmentally friendly and economical use of nuclear energy for peaceful purposes" [137]. The NEA offers access to a number of databases containing:

Evaluated Data Evaluated sets are produced by a selection of experimental data complemented by nuclear model calculations. These evaluated libraries are stored in a computer readable format called ENDF format, which divides the data set for each material by data type (reaction cross section, angular and energy distributions, etc.) and reactions type (total cross section, fission cross section, etc.). The NEA evaluated database contains a large number of evaluated data libraries, including all the libraries mentioned in the previous paragraphs.

Experimental Data The database containing experimental data is called EXFOR [138]. It includes a complete compilation of experimental neutron-induced reaction data and selected compilations of charged-particle and photon induced reaction data.

Bibliographic Information The experimental and evaluated information stored in EXFOR has been based on data published in scientific journals and reports. The bibliographic databases contain cross references between the numerical databases and the articles from which that information was taken. The CINDA (Computer Index of Neutron Data) [139] database contains references to measurements, calculations, reviews and evaluations of neutron cross-sections and other microscopic neutron data.

These databases can be accessed using the JANIS (Java-based Nuclear Information Software) application [140], a display program designed to facilitate the visualisation and manipulation of nuclear data.

3.6 Cross Section Codes

In this section, two cross section codes will be introduced: TALYS and ABRABLA. The importance of these codes for this work will be seen in later chapters, since they were used, in conjunction with FLUKA, to estimate the production of residuals in the target system of the ISOLDE facility.

3.6.1 TALYS

TALYS [141] is a computer code which simulates nuclear reactions involving neutrons, photons, protons, deuterons, tritons, ^{3}He and alpha particles in the energy range between 1 KeV and 200 MeV, for target nuclides of mass 12 and heavier. A suite of nuclear reaction models is integrated in TALYS, allowing the evaluation of nuclear reactions from the unresolved resonance

range up to intermediate energies. TALYS has been extensively used in various application areas such as innovative nuclear power reactors , transmutation of radioactive waste, medical isotope production, radiotherapy and astrophysics. The idea behind TALYS was to develop a computer code that predicts many reaction channels simultaneously, rather than devoting several years of theoretical research to perfect one or a few particular reaction channels.

Some important features of the code are:

- an exact implementation of many of the latest nuclear models for direct, compound, pre-equilibrium and fission reactions;
- a continuous description of reaction mechanisms in the 1 keV – 200 MeV range for target mass numbers between 12 and 339;
- Total and partial cross sections, energy spectra, angular distributions, double-differential spectra and recoils;
- discrete and continuous photon production cross sections;
- excitation functions for residual nuclide production, including isomeric cross sections;
- several fission models to predict fission cross sections and product yields;
- models for pre-equilibrium reactions;
- user-friendly input/output capabilities;
- a large collection of examples and sample cases.

TALYS provides a complete set of answer for each nuclear reaction, for all open channels and associated cross sections, spectra and angular distributions [141].

Fig. 3.25 shows the residual production cross sections for protons incident on Fe. There is in general a good agreement between the TALYS cross sections (solid lines) and the experimental data [142], for the energy range 0 –100 MeV. A good agreement between TALYS and experimental data [143] is also seen in Fig. 3.26, which shows the fission fragment mass yield curves as a function of the mass number, produced by 5.5 MeV neutrons on ^{238}U.

3.6.2 ABRABLA

The abrasion-ablation code system ABRABLA [122, 123], developed at GSI, is able to simulate the competition between evaporation and high-energy fission in the decay of excited nuclei. In recent years, ABRABLA was improved through the inclusion of a time-dependent fission decay width and the emission of composite light-charged particles and intermediate mass fragments.

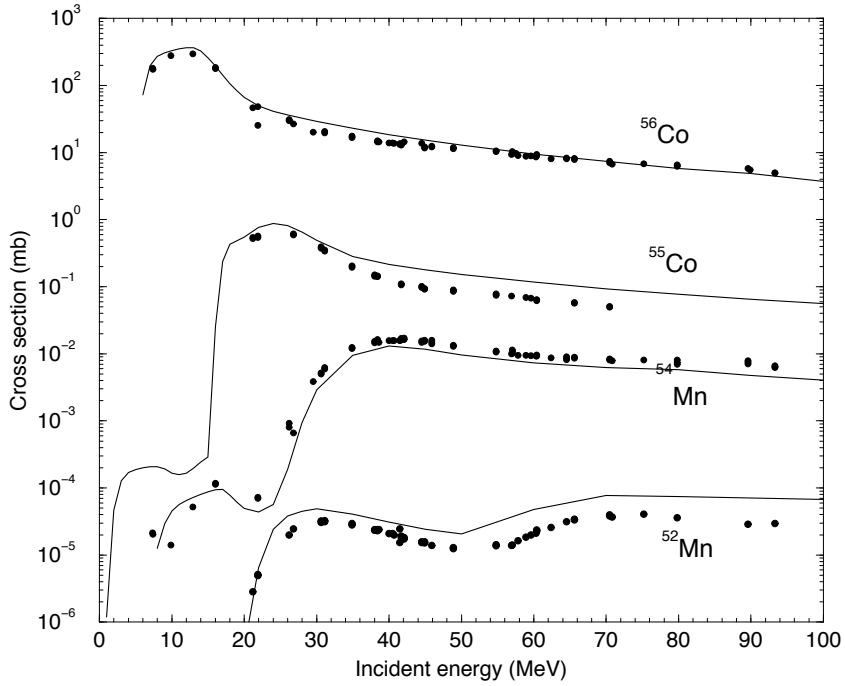

Figure 3.25: Residual production cross sections for protons incident on Fe. Comparison between TALYS (solid lines) and experimental data from [142] (obtained from [141]).

.

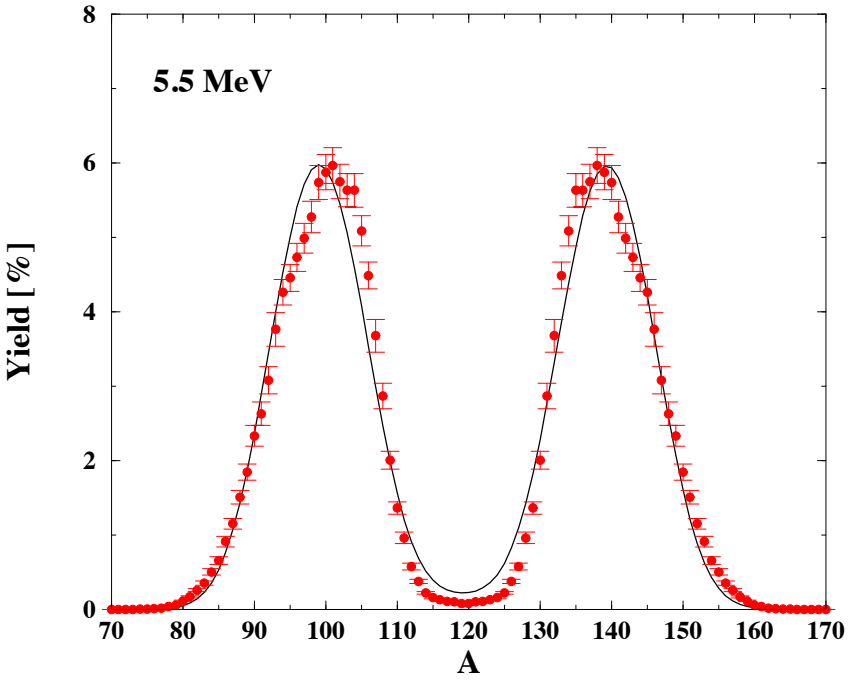

Figure 3.26: Fission fragment mass yield curves as a function of the mass number, produced by 5.5 MeV neutrons on ^{238}U. Comparison between TALYS (solid line) and experimental results from [143] (obtained from [141]).

The coupling of ABRABLA to intranuclear cascade codes has shown to give a satisfying agreement with the isotopic distribution of spallation residues in the region of fission and heavy evaporation products. For the de-excitation stage of the spallation reaction, ABRABLA has been able to give a much better reproduction of isotopic distributions and fission yields than other well known models [106].

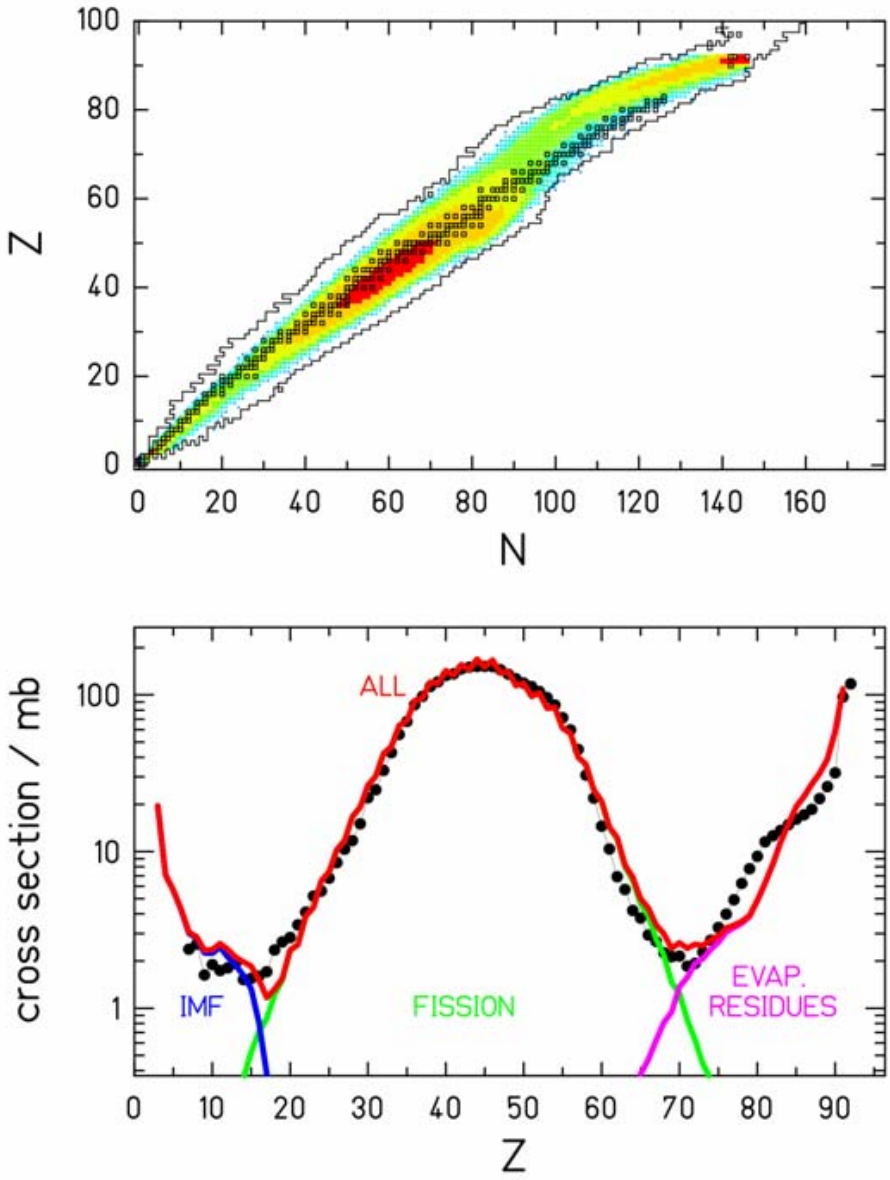

Figure 3.27: Cross sections for the nuclei produced in ^{238}U by 1 GeV protons. Top – Predictions of ABRABLA on the chart of the nuclides. Bottom – ABRABLA (solid lines) *vs* experimental data from [144–146]. The solid red line represents the sum of three components: intermediate-mass fragments, fission fragments and heavy evaporation residues (obtained from [144]).

Fig. 3.27 shows the production of residuals by 1 GeV protons on ^{238}U, as predicted by ABRABLA. On the top, the entire production range is shown, in the chart of the nuclides. On the bottom,

the predicted results are compared with experimental data [144–146]. In general, there is a very good agreement between predicted and experimental data (more comparisons can be found in [144]).

Part II

Radiation Protection and Safety of the EURISOL Facility

Chapter 4

EURISOL

4.1 The EURISOL Project

In its document entitled "Roadmap for Construction of Nuclear Physics Research Infrastructures in Europe" [147], the European Expert Committee NuPECC (Nuclear Physics European Collaboration Committee) has recommended the construction of EURISOL (using the ISOL method) as one of two next-generation facilities for the production of Radioactive Ion Beams in the European Union. The other project, FAIR (currently under construction at GSI, Germany), will use the Projectile Fragmentation technique. Since FAIR is based on in-flight separation of isotopes, using heavy ion beams, the range and yields of produced nuclides will be complementary to those produced at EURISOL.

The EURISOL facility will produce RIBs with intensities two to three orders of magnitude higher than those currently available, for studies of relevance in several fields of research, such as Nuclear Physics and Nuclear Structure (neutron halos, shell structure, superheavy elements, exotic radioactivity), Nuclear Astrophysics (neutron stars, the r-process, X-ray bursts), Fundamental Interactions (beyond the Standard Model, beta beams), Solid State Physics and Medicine.

The design of the EURISOL facility and associated infrastructures involves the consideration of scientific, technological and engineering leading edge and multidisciplinary topics such as extremely high neutrons fluences and dose rates (and its consequences for Radiological Protection and Safety), the thermal and mechanic properties of structural materials undergoing intense neutron irradiation, accelerator and targets technology, coupled neutronics and thermal-hydraulics calculations, remote handling and maintenance of critical components (targets), in-Service Inspection & Repair (ISI&R), automation, robotics, etc.

4.1.1 The Feasibility Study (2000-2003)

The first phase of the EURISOL Project was a Feasibility Study, undertaken by a collaboration of European institutions coordinated by GANIL, funded by the European Commission as a Research & Technical Development (RTD) study under its Fifth Framework Programme (FP5). The study spanned 4 years, from 2000 to the publication of The EURISOL Report in 2003 [3]. This report included:

- the scientific case for the construction of EURISOL;
- the proposed scheme for the future EURISOL facility, with emphasis on its main components: driver-accelerator, target/ion-source assembly, mass-selection system, post-accelerator and scientific instrumentation;
- the expected performance of the EURISOL facility;
- the identification of the neccessary R&D studies before the final design;
- the identification of possible synergies between the EURISOL facility and other European projects;
- the expected costs.

During the EURISOL Feasibility Study it was proposed that a 1 GeV proton beam would be suitable to produce the desired RIB intensities, having advantages over heavier ion beams with respect to target cooling, since the beam energy would be distributed over a greater depth in the target material. A beam power of up to 4 MW was considered, in order to achieve the desired fission rate of 10^{15} fissions per second in the target. A liquid metal target, such as mercury or lead-bismuth eutectic, was deemed necessary to effectively remove the heat load that such an intense beam would produce in the target. In the original concept, a Hg "jet" was surrounded by a cylinder of uranium carbide. The proton beam would hit the spallation target, generating neutrons that would induce fission in the surrounding uranium carbide target and produce the desired radioactive isotopes.

Three complementary 100 kW "direct targets" were also studied, using specific target materials to produce selected isotopes. A fraction of the proton beam intensity would be directed to each of these targets, to produce (mostly neutron-deficient) nuclides not available in the fission of uranium.

It was suggested that this first phase should be followed by two sequent phases: a number of RTD investigations on the crucial technical points – a Design Study –, followed by a full engineering design of the facility.

4.1.2 The Design Study (2005-2009)

The EURISOL Design Study started in 2005, supported by the European Commission under its Sixth Framework Programme (FP6). GANIL was the Coordinating Institution of a consortium of 20 institutions, with 21 additional collaborators from Europe, Asia and America. The main objective of the EURISOL Design Study was to address the main technological challenges identified in the Feasibility Study. The work of the Design Study was divided in 12 Tasks:

- Task 1: Management
- Task 2: Multi-MW target station
- Task 3: Direct (100 kW targets)
- Task 4: Fission target
- Task 5: Safety and radio protection
- Task 6: Heavy-ion accelerator
- Task 7: Proton Accelerator
- Task 8: Superconducting cavity development
- Task 9: Beam preparation
- Task 10: Physics and instrumentation
- Task 11: Beam intensity calculations
- Task 12: Beta-beam aspects.

The results of these studies were summarised in the Final Report of the EURISOL Design Study, issued in November 2009 [148].

One of the important developments in the early stages of the EURISOL Design Study was the realisation that a single large-volume uranium carbide target surrounding the proton-to-neutron converter[1] would not be efficient to extract the short-lived nuclides, due to the long effusion and diffusion times. The fission target geometry was re-evaluated and an alternative configuration was proposed. In this configuration, six small fission targets are located close to the mercury spallation target, each with an adjacent ion-source, described in detail in the next sections.

[1] The spallation target is often referred to as *proton-to-neutron converter*, or simply *converter*.

4.2 The EURISOL Facility

4.2.1 Layout

The proposed scheme for the EURISOL facility is represented in Fig. 4.1. A 4 mA proton beam is accelerated to 1 GeV (4 MW) in a linear accelerator (driver-accelerator). The proton beam hits a spallation target of liquid mercury, and the induced neutron fluences produce fission in the surrounding actinide targets, composed of ^{235}U dispersed in a matrix of graphite. The fission products are extracted from the target, mass separated and accelerated in a post-accelerator to the energies required in the different experimental areas [3, 149, 150].

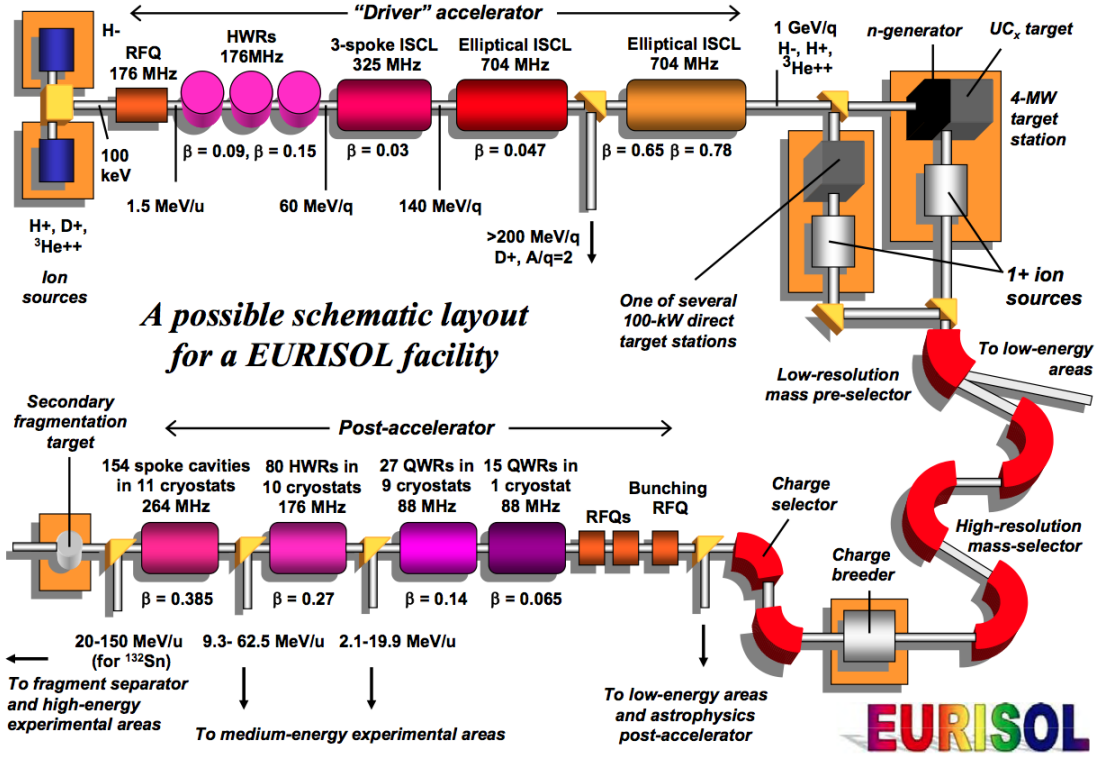

Figure 4.1: A schematic diagram of the EURISOL facility [148].

Fig. 4.2 shows the plan view of the EURISOL facility, with its major components, including:

- the injector building for the driver-accelerator, with ion sources for protons, dueterons and ^{3}He ions;
- a driver-accelerator tunnel (240 m);
- a power building adjacent to driver-accelerator;
- a building for liquid helium and nitrogen supplies;

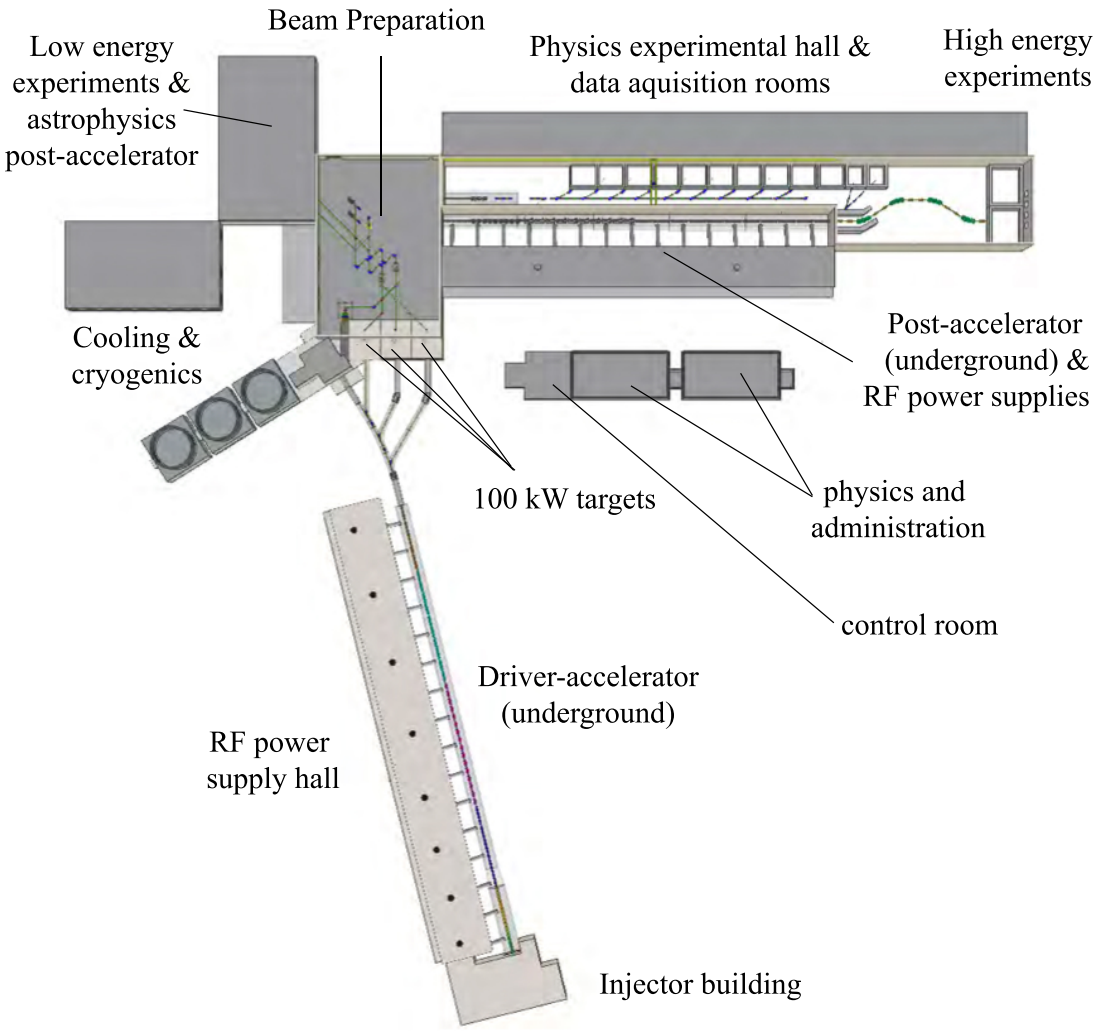

Figure 4.2: General View of the EURISOL facility. The driver is 240 m long and the post-accelerator linac is 207 m long [148].

- beam lines to the ISOL target stations;
- a multi-MW target station with target-handling facilities;
- six fission target stations with target-handling facilities;
- three 100 kW target stations with target-handling facilities;
- a beam-preparation area, which includes a beam-merging station, a high-resolution mass-separator, beam coolers and charge breeders;
- a low-energy post-accelerator
- a high-energy post-accelerator (207 m);

- separate experimental areas for low, medium and high energy beam lines.

4.2.2 Site

The location of the EURISOL facility is not yet specified. Three types of generic sites were accounted for in the EURISOL Design Study:

1. an international European laboratory with accelerator facilities that serve a wide scientific user base;
2. a national accelerator-based laboratory;
3. a "green-field" site.

The first and second options could have several advantages: experienced staff in accelerator technologies, accumulated experience in dealing with national and international nuclear facility regulations, existing infrastructures, etc. In a green-field site, the facility and infrastructures could be built to meet the specific requirements of EURISOL. Such a site could be located in a place with no large multinational facilities, thus driving forward the development of a local high-tech industry, a scenario which could attract EU funding. The downside of the green-field option is the cost, since the absence of local infrastructures would probably make it the most expensive alternative.

CERN (Switzerland/France), LNL (Italy), GANIL (France), Rutherford Appleton Laboratory (United Kingdom) and a generic green-field site have been pointed as suitable options to host the EURISOL facility [148].

4.3 Multi-MW Target System - MAFF Configuration

A possible layout for the EURISOL target complex is shown in Fig. 4.3. The multi-MW target station lies at the centre of the facility, receiving a 4 MW proton beam from the driver-accelerator. The three 100 kW direct targets are placed in an adjacent building on the opposite side of the multi-MW target handling rooms, to minimise the interference between the two types of targets with different operational modes. The direct targets have their own systems for target handling, data retrieval and isotopic separation.

The operation of a liquid-metal target requires a rapid flow of liquid metal in the impact point of the proton beam. The proton beam hits the flowing mercury and generates intense neutron fluxes, which have an approximate isotropic distribution around the impact point. The heat is thus efficiently removed from the area in which the incoming protons deposit the greatest portion of their energy. Figs. 4.4 and 4.5 show conceptual layouts for the integration of converter

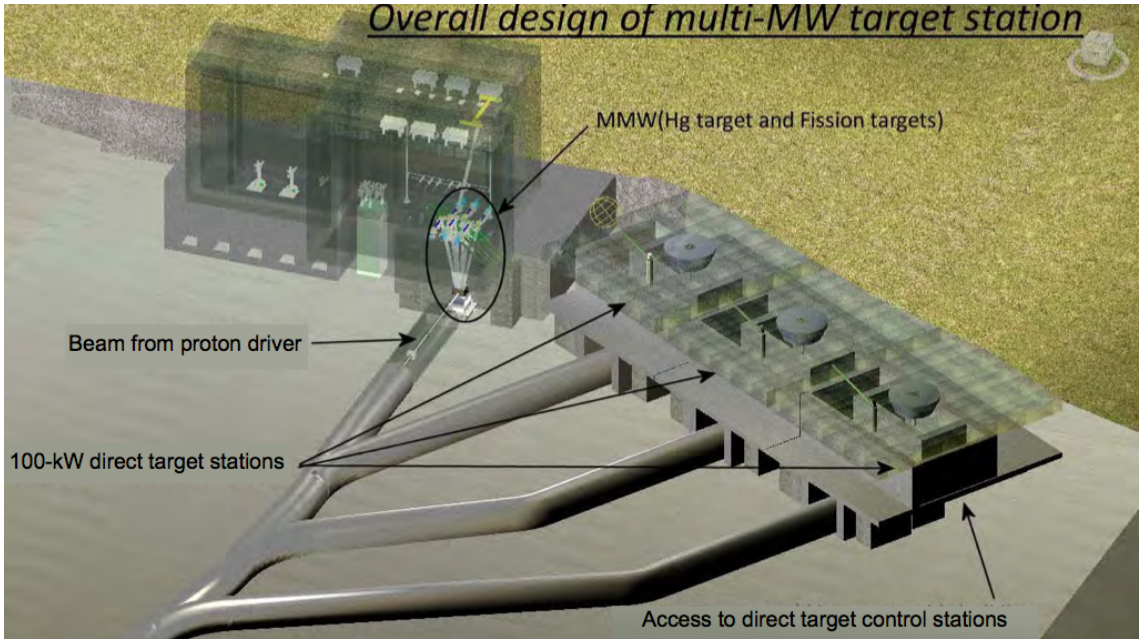

Figure 4.3: Multi-MW target area and three 100 kW target vaults [148].

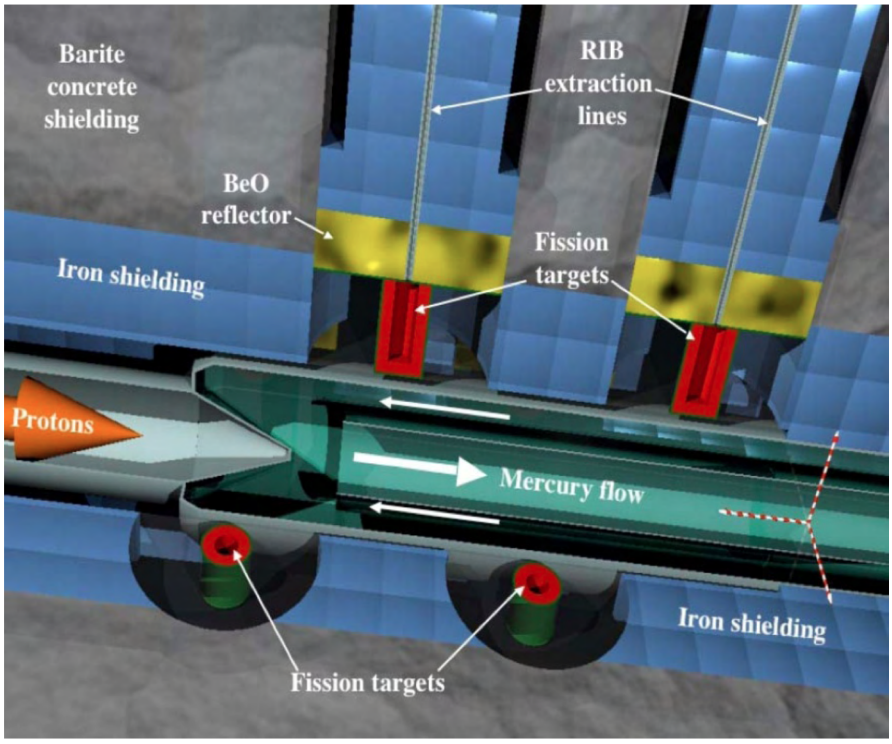

Figure 4.4: Scheme of the converter and target integration [148].

and fission targets. Each of these targets is designed in a modular way, so that individual parts can be easily replaced through remote handling.

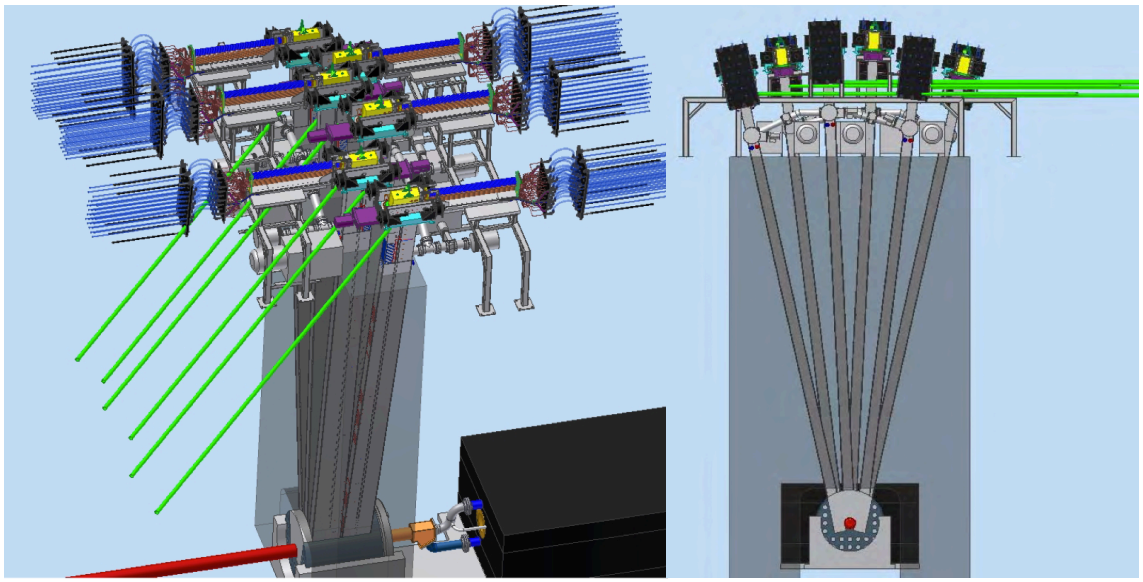

Figure 4.5: Scheme of the converter and target integration [148].

The design of the targets assembly is inspired by the concept proposed in the PIAFE (*Projet d'Ionisation et d'Acceleration de Faisceaux Exotiques*) and MAFF (*Munich Accelerator for Fission Fragments*) projects [151, 152]. Each fission target is filled with ^{235}U or other actinide and inserted through a channel created in the shielding in a position of maximum neutron flux, close to the neutron converter. The fission targets are placed inside $\sim$ 7 m long double-walled vacuum tubes, which are easily removed and allow remote handling for fission target maintenance and replacement. Each tube has a water cooling system, to evacuate the $\sim$30 kW of heat released from the expected 10^{15} fissions per second.

Up to six fission target extraction tubes are foreseen, each with a MAFF-like production system, and the RIB lines from the each tube (green lines in Fig. 4.5) are joined in a beam merging device. When a tube is removed, it is taken to a fission target handling room, located above the spallation target room, and then moved to a hot-cell where remote handling can be performed under visual control. A 6-7 meter long concrete wall separates the targets from the fission targets handling room. There is an additional carbon moderator surrounding the mercury target, to moderate the spallation neutrons.

The next chapter summarises the work done at CERN for Tasks 2, 4 and 5 of the EURISOL Design Study, concerning the neutronics and radiation protection aspects of the multi-MW target station and respective spallation and fission targets. The nominal parameters of operation foreseen for the multi-MW target unit are presented in Table 4.1 [148].

Table 4.1: Essential parameters for the multi-MW converter and fission target system.

Parameter	**Units**	**Nval**	**Range**
Converter target material	–	Hg (liquid)	LBE
Secondary target material	–	UC_x, BeO	
Beam particles	–	Proton	
Beam particle energy	GeV	1	≤ 2
Beam current	mA	4	2–5
Beam time structure	–	dc	ac 50 Hz 1ms pulse
Gaussian beam geometry	mm	15	≤ 25, parabolic
Beam power	MW	4	≤ 5
Converter length	cm	45	≤ 85
Converter radius	cm	15	8–20
Hg temperature	°C	150 (tbc)	$\ll 357$
Hg flow rate	ton/s	1 (tbc)	$\ll 3$
Hg speed	m/s	5 (tbc)	$\ll 15$
Hg pressure drop	bar	tbc	$\ll 100$
Hg overpressure	bar	tbc	$\ll 100$
UC_x temperature	°C	2000	500–2500

Chapter 5

Simulations for Neutronics, Dosimetry and Activation

There were two distinct objectives for the studies presented in this chapter, namely:

1. To perform a complete neutronics study of the MAFF configuration proposed for the multi-MW station of the EURISOL facility. This task included
   - the implementation of the complex target station geometry in FLUKA;
   - calculations of neutron fluxes and fission rates;
   - the optimisation of the materials used in the fuel and reflector elements of the system, in order to achieve the highest fission rates possible.
2. To undertake extensive computational studies assessing key topics related to radiological protection and safety, which included:
   - dose rate calculations to identify the necessary shielding and access restrictions for each section of the entire facility, including maintenance, storage and remote control spaces, during operation;
   - activation calculations for every material used in the multi-MW target station;
   - assessment of the dose rates in the shutdown periods, when the facility stops for maintenance, arising from the decay of radioactive products formed due to activation of the structural materials;
   - optimisation of the target station materials, in order to to reduce activation.

In the first task, the aimed fission rate for the total six fission targets was 1×10^{15} fissions/s, a fission rate deemed necessary to make the desired intensity for the ion beams possible [148, 153,

154]. For the radiological protection studies the objective was to minimise the dose rates due to activation in the system without compromising its performance. The results presented in this chapter are part of a broader work presented in a CERN report entitled "EURISOL Multi-MW Target MAFF Configuration: Radiological Protection, Radiation Safety and Shielding Aspects" [155].

5.1 Geometry Implementation in FLUKA

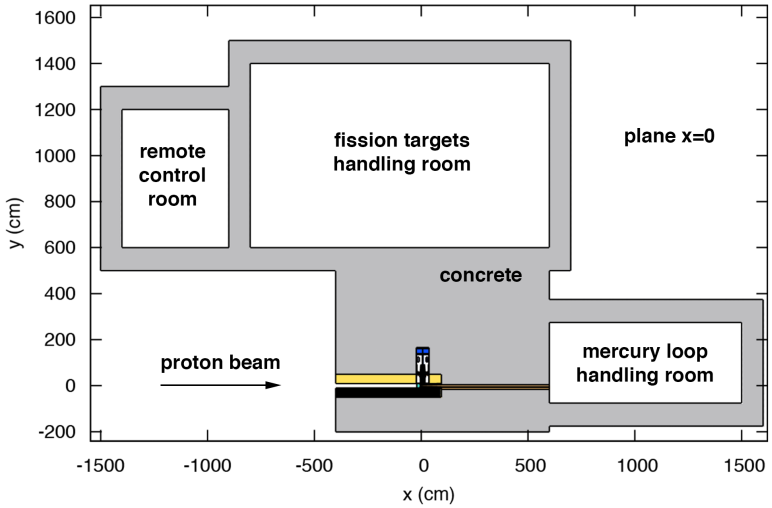

Figure 5.1: Longitudinal view of the multi-MW target station as implemented in FLUKA, plane $x = 0$.

Figs. 5.1 and 5.2 show the global view of the multi-MW target station as implemented in the Monte Carlo code FLUKA. The initial step in this work consisted in the implementation of this complex geometry, based on a previous MCNPX [77] model. The various rooms in the target station are shown in two perpendicular planes, $x = 0$ and $z = 0$, and include the fission targets handling room, the remote control room and the mercury loop handling room.

Figs. 5.3 and 5.4 are zoomed versions of the previous figures, showing in detail the spallation and fission targets region for the planes $x = 0$ and $z = 0$, respectively. There are six fission targets, with 15 g of ^{235}U each (in the standard configuration), located close to the liquid mercury spallation target, inside 7 m long tubes, the fission products extraction tubes (which contain the RIB extraction lines). The extraction tubes are easily removable and allow a versatile manipulation of the fission targets. There is also a water-cooled carbon neutron moderator surrounding the spallation target and the fission targets.

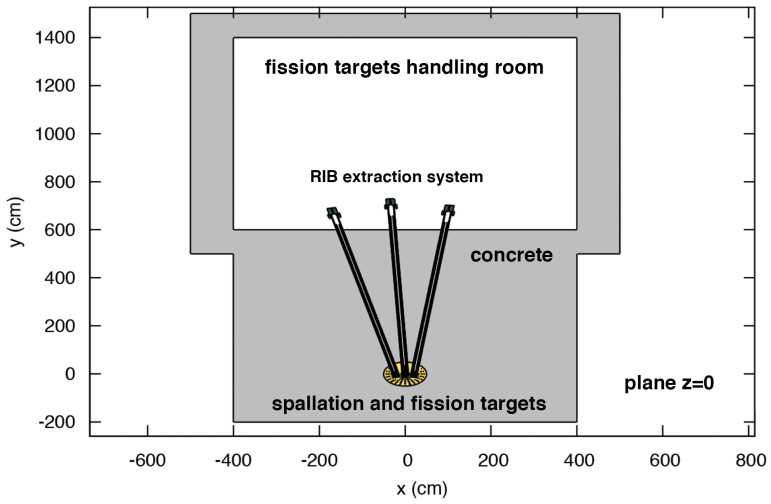

Figure 5.2: Transverse plane of the multi-MW target station as implemented in FLUKA, plane $z = 0$.

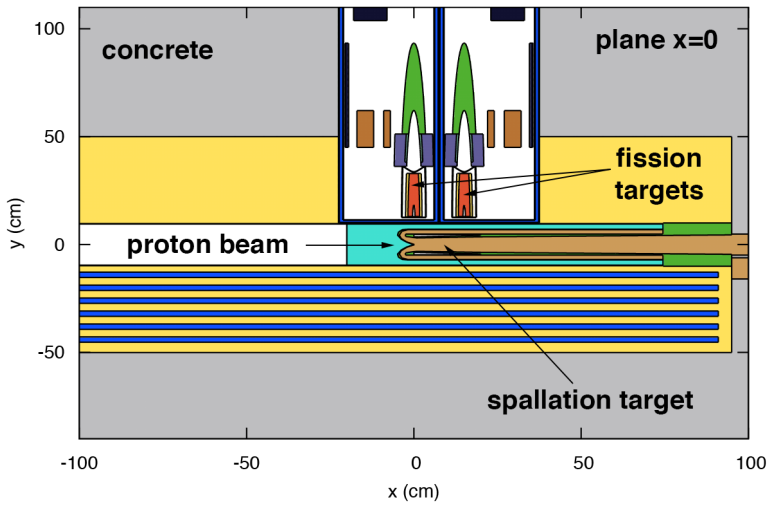

Figure 5.3: Zoomed view of the spallation and fission targets as implemented in FLUKA, plane $x = 0$.

5.1.1 Fission Target Extraction Tubes

The geometry of the extraction tubes and their main components is shown in Fig. 5.5, as implemented in FLUKA. The most important element is the fission target itself, which is placed at the bottom of the tube inside the fission target container (both the container and the target can be made of different materials). There are also two neutron reflectors, a carbon reflector around the fissile material and a beryllium oxide reflector in the exit tube, the region from which the ions are extracted. Cooling water is continuously circulating between the internal and the external walls.

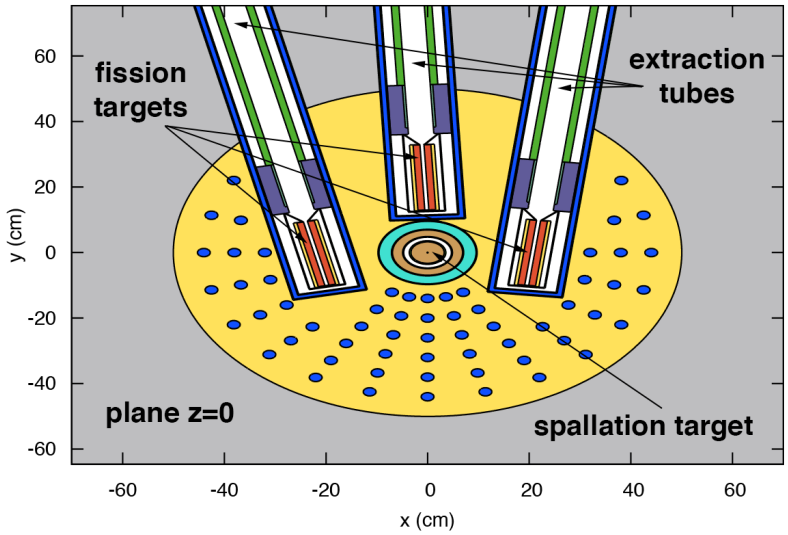

Figure 5.4: Zoomed view of the spallation and fission targets as implemented in FLUKA, plane $z = 0$.

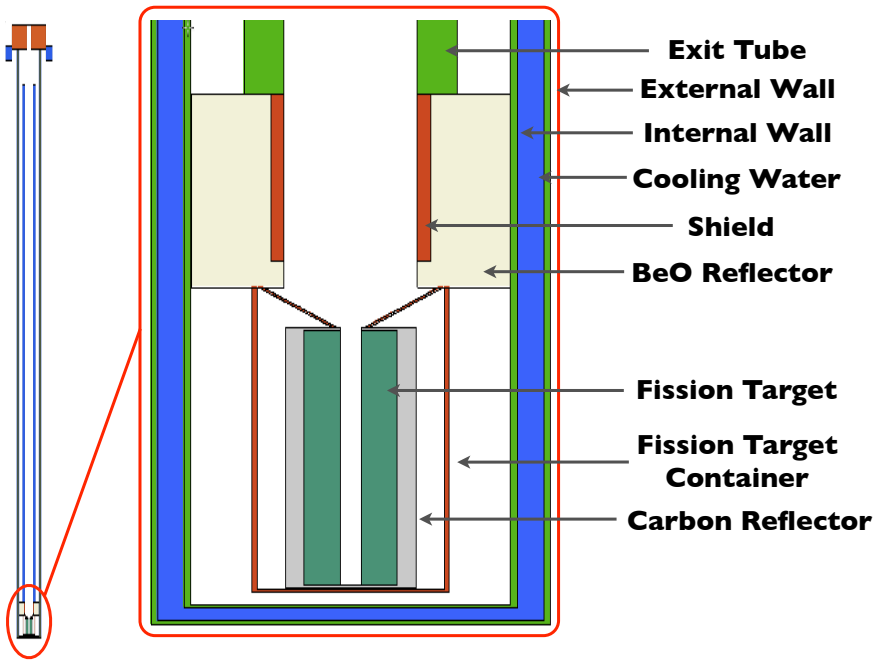

Figure 5.5: Extraction tube geometry as implemented in FLUKA.

5.1.2 Alternative Configurations

Two alternative configurations were tested in the simulations, here referred to as *Option-1* and *Option-2*. In fact, the second option evolved from the first, to address problems raised during the first phase of this work. For convenience, the results will be presented side-by-side, as if these were two independent alternative configurations, to allow a direct comparison between

designs and materials. The main differences between the two configurations are summarised in Table 5.1. In Option-1, the fission target container is made of tantalum, and aluminium is the material chosen for the structural components – internal wall, external wall and exit tube – and the spallation target is surrounded by an iron cylinder with a 20 cm radius. In Option-2, the material of the fission target container was changed to molybdenum and the structural components material was changed to aluminium, for reasons that will become apparent in the next sections. The material surrounding the spallation source was changed to carbon, water-cooled, and its radius was increased to 50 cm. There were some additional minor differences in the extraction tubes, the most important example being an additional water moderator in Option-1 that was removed in Option-2, due to the presence of the carbon moderator around the spallation target. Further details regarding the materials of each component will be provided later in this chapter.

Table 5.1: Main differences between the two alternative configurations.

	Option-1	**Option-2**
Fission target container material	tantalum	molybdenum
Structural components material	L316 stainless steel	aluminium
Spallation target reflector material	iron	carbon
Spallation target reflector radius	20 cm	50 cm

5.2 Neutronics Study of the MAFF Configuration

5.2.1 Fluxes in the Targets

The neutron flux map in the region of the impact point of the proton beam in the mercury target is represented in Figs. 5.6 and 5.7, in two perpendicular planes. The neutron fluxes are very intense, with peak values of the order of 10^{15} neutrons/cm^2/s, in the impact point of the proton beam in the spallation target. The fission targets are located close to the spallation target, to get the highest possible neutron fluxes, which decrease gradually when the distance to the impact point of the proton beam increases.

A 4 MW proton beam in the positive z direction was assumed, with 1 GeV and 4 mA and spatial gaussian distributions in the x and y directions, with $\sigma = 1.5$ cm. Such unprecedentedly high neutron and proton fluxes in the targets region, though necessary in order to reach the aimed fission rates for the multi-MW target station, will activate the targets and structural materials,

as will become apparent in later sections.

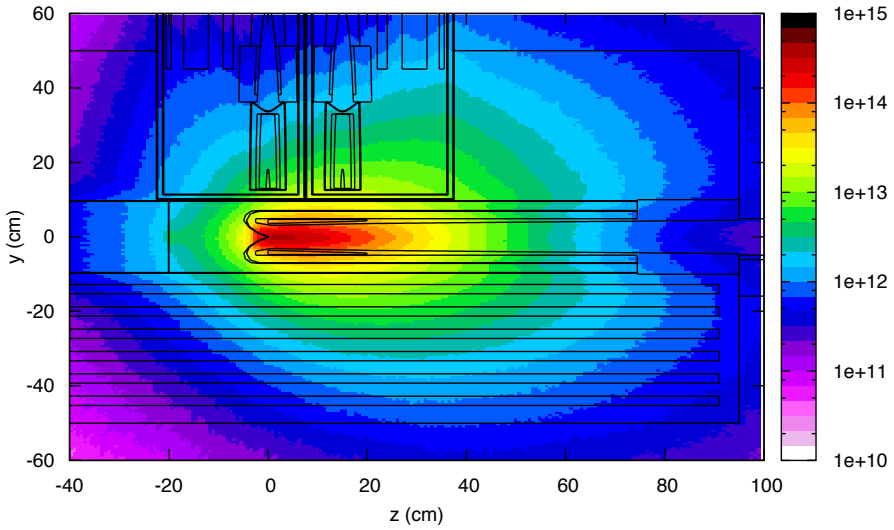

Figure 5.6: Neutron fluxes (neutrons/cm^2/s) in the spallation and fission targets region (average values for a 10 cm thickness in the x axis).

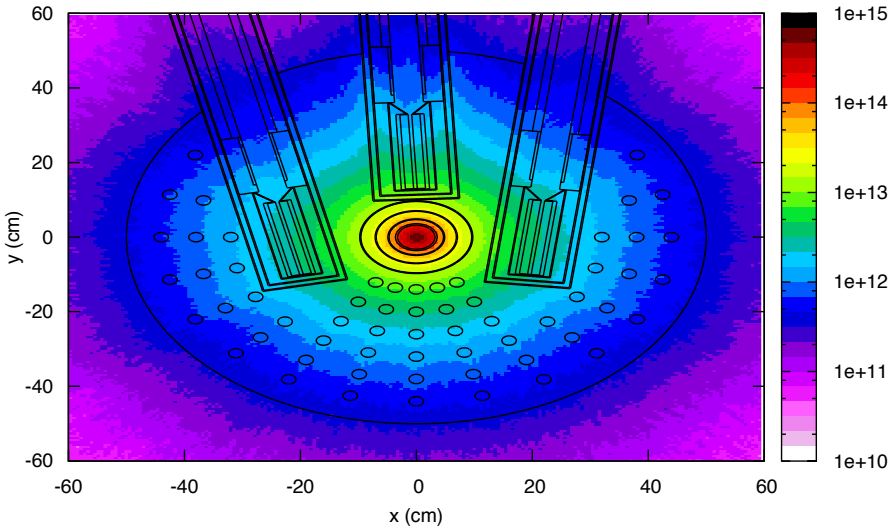

Figure 5.7: Neutron fluxes (neutrons/cm^2/s) in the spallation and fission targets region (average values for a 5 cm thickness in the z axis).

5.2.2 Fission Rates

The aforementioned differences between Option-1 and Option-2 configurations will result in different fission rates. The fission rates were calculated for the two configurations, with different fissile materials in the fission target, in order to measure the effects of the geometry changes. The fissile materials are described in Table 5.2.

Table 5.2: Fissile materials used in the fission target.

Material ID	Density (g/cm^3)	Composition
MAT-1	1.883	Carbon (95.6%) ^{235}U (4.4%)
MAT-2	4.4	Carbon (4.7%) ^{235}U (1.9%) ^{238}U (93.4%)
MAT-3	9.86	ThO_2

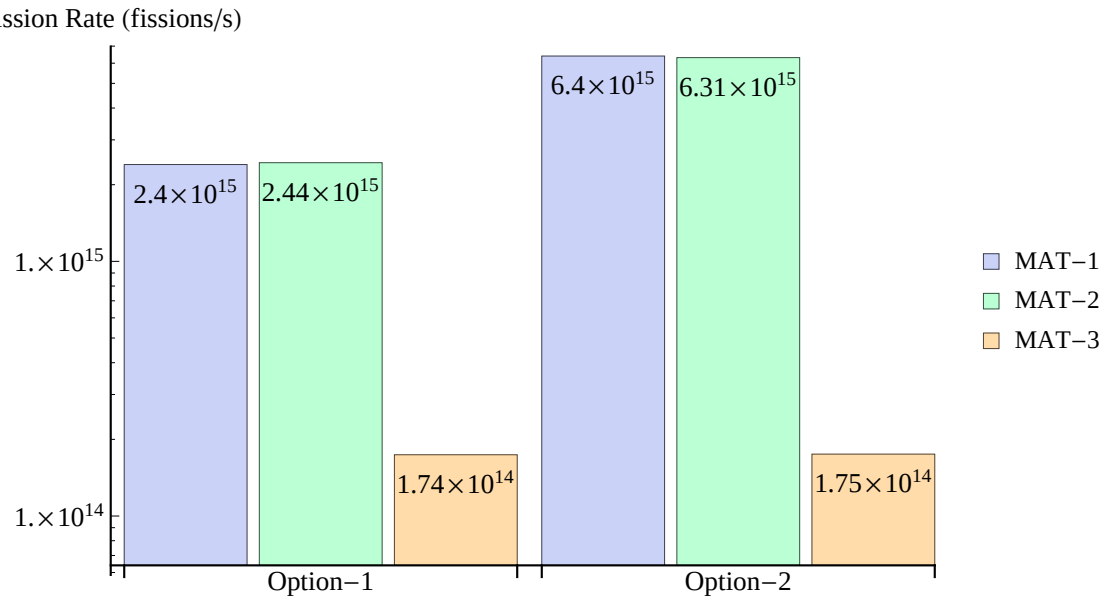

Figure 5.8: Comparison of the total fission rates obtained with the two geometries and with different fissile materials.

Both MAT-1 and MAT-2 have approximately 15 g of ^{235}U in each of the six targets. The total fission rates obtained with these materials in both geometries (for the total six targets) are summarised in Fig. 5.8. The introduction of carbon around the spallation target in Option-2 leads to an increase in the fission rates when compared to those obtained with Option-1, since the neutrons are moderated more effectively and ^{235}U is the only fissile material in MAT-1. For this reason, the fission rate increases by a factor of 2.7. With MAT-2, the fission rate also increases, by a factor of 2.6. By comparison with the results obtained with MAT-1, it is possible to see that the fissions in MAT-2 are essentially ^{235}U fissions, while ^{238}U has a very small contribution to the total fission rate. With MAT-3 the fission rates are much lower than with the other materials, since a harder neutron spectrum is required in order to achieve higher fission rates in ^{232}Th. The same is valid for ^{238}U, as shown in Fig. 5.9 [94].

These results indicate that the aimed fission rate for the EURISOL multi-MW target station,

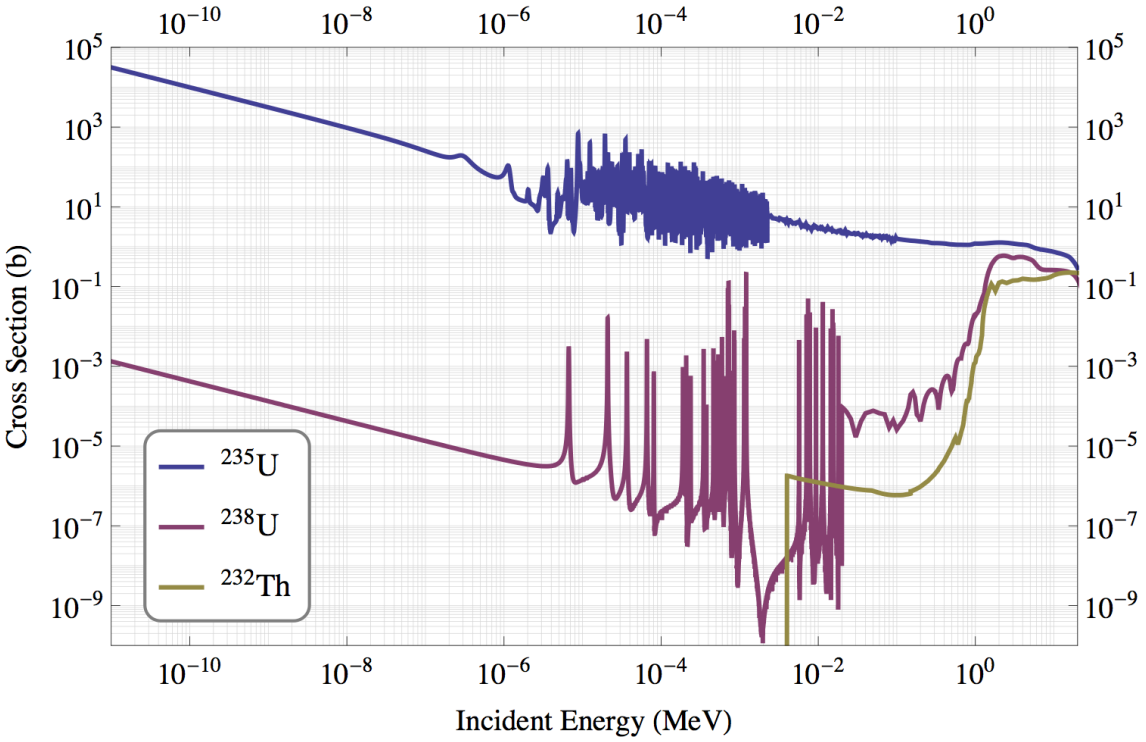

Figure 5.9: Fission cross sections of ^{235}U, ^{238}U and ^{232}Th [94].

1×10^{15} fissions/s, can be achieved. A fission rate of 6.4×10^{15} fissions/s, well above the targeted value, was predicted with the configuration Option-2 and MAT-1 as fissile material.

5.3 Dosimetry and Activation Studies

In this section the activation in the extraction tubes containing the fission targets is studied in detail. The fact that the extraction tubes need to be replaced periodically (typically every 6 months [1]), due to the burnup of the fissile material, implies that the activities in each component must be known for different cooling times after the stoppage of the primary beam, in order to determine how long they need to cool down before they can be handled and disposed. For the activation calculations, it was considered that the facility operates continuously during 200 days before stopping for target replacement and waste disposal.

[1]Assuming a fission rate of 10^{15} fissions/s, after 1000 hours of work $10^3 \times 3600 \times 10^{15} = 3.6 \times 10^{21}$ atoms of ^{235}U will be consumed, or $\frac{3.6 \times 10^{21}}{6.022 \times 10^{23}} \times 235$ g $= 1.4$ g. This is approximately 10% of the ^{235}U atoms,.after 40 days of continuous operation.

5.3.1 Spallation Target, Fission Target and Carbon Reflector

Fig. 5.10 shows the time evolution of the specific activity in the spallation target, fission target (the fission target with the greatest fission rate was chosen for this comparison) and carbon reflector surrounding the spallation target (Option-2 geometry was used in these calculations), for a period ranging from the moment when the proton beam is shut-off until ten years after. The fissile material is the most activated, even more than the mercury in the spallation target. Its specific activity ranges from 3×10^{12} Bq/g when the beam is stopped to 6×10^{9} Bq/g ten years after shutdown. These activities will result in high dose rates during the cooling periods.

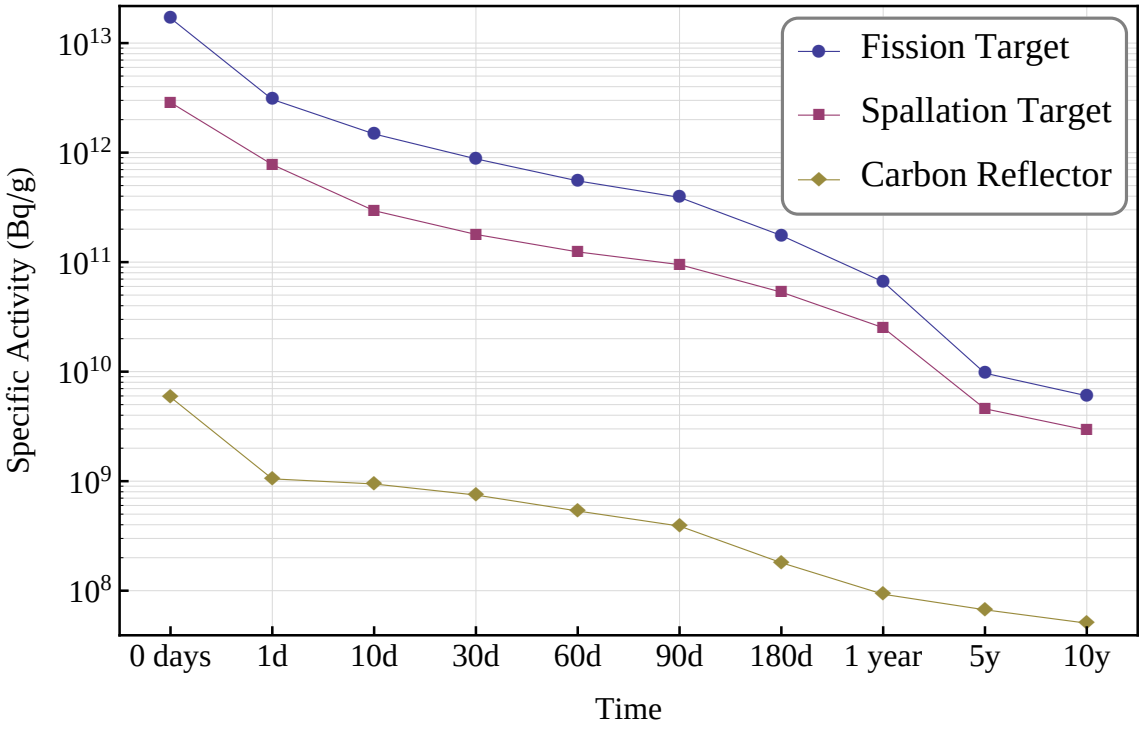

Figure 5.10: Specific activity (Bq/g) evolution: fission target, spallation target and carbon reflector.

5.3.2 Activation of the Extraction Tubes

A similar analysis was performed individually for all the elements of the fission target structures, which include the fission targets, moderators, connectors and cables, cooling water, cryogenic panels, etc. As mentioned before, the extraction tubes need to be exchanged periodically and the conditions in which they are going to be handled must be known. The results presented in this section refer to the most activated of the six extraction tubes, the central tube on the plane $z = 0$ (MAT-1 was chosen as fissile material). The calculations were performed for every component in both configurations, listed in Table 5.3 with the corresponding volume. This information is relevant since the activities presented in this section represent the total activities in each region,

not the specific activities.

Table 5.3: Extraction tube components, volumes (cm^3) and materials.

Region	Material		Volume (cm^3)
	Option-1	Option-2	
External Wall	Aluminum	L316	15419
External Wall	Aluminum	L316	13748
Exit Tube	Aluminum	L316	18657
Shield	Tantalum	Molybdenum	112
Fission Target Container	Tantalum	Molybdenum	114
Fission Target	MAT-1 (Table 5.2)		181
Cooling Water	Water		58556
Carbon surrounding Fission Target	Carbon		189
BeO Insulator	Beryllium Oxide		1284
Connectors and Cables	Copper		23030
Cryogenic Panels	Liquid Helium		18424

5.3.2.1 Fission Target (Fissile Material)

The first region in the calculations was the fission target itself, composed by MAT-1. Fig. 5.11 shows the activities obtained with both geometries, for several cooling periods after the shutdown of the facility. The activities are higher with the Option-2 geometry, as expected, since the fission rate is higher in this case, as shown in the previous section. The activity in the fission target in Option-2 ranges from 5.8×10^{15} Bq for $t = 0$ days (shutdown time) to 2.1×10^{12} Bq ten years after shutdown.

Extensive lists with the nuclides formed by activation in the target were also created, for the same periods after the shutdown. Tables 5.4 and 5.5 list the nuclides with the biggest contributions to the total activities in the fission targets, along with the respective percentages to the total activity, for Option-1 and Option-2 configurations.

A column with the multiple of the exemption limit (MEL), according to the Swiss legislation [156], is also provided. In these terms, components are considered wastes if the activity concentration a (specific activity) of an isotope exceeds the exemption limit EL and the total activity A of that isotope exceeds 100 EL. The values of EL are defined isotope-specifically. In the case of

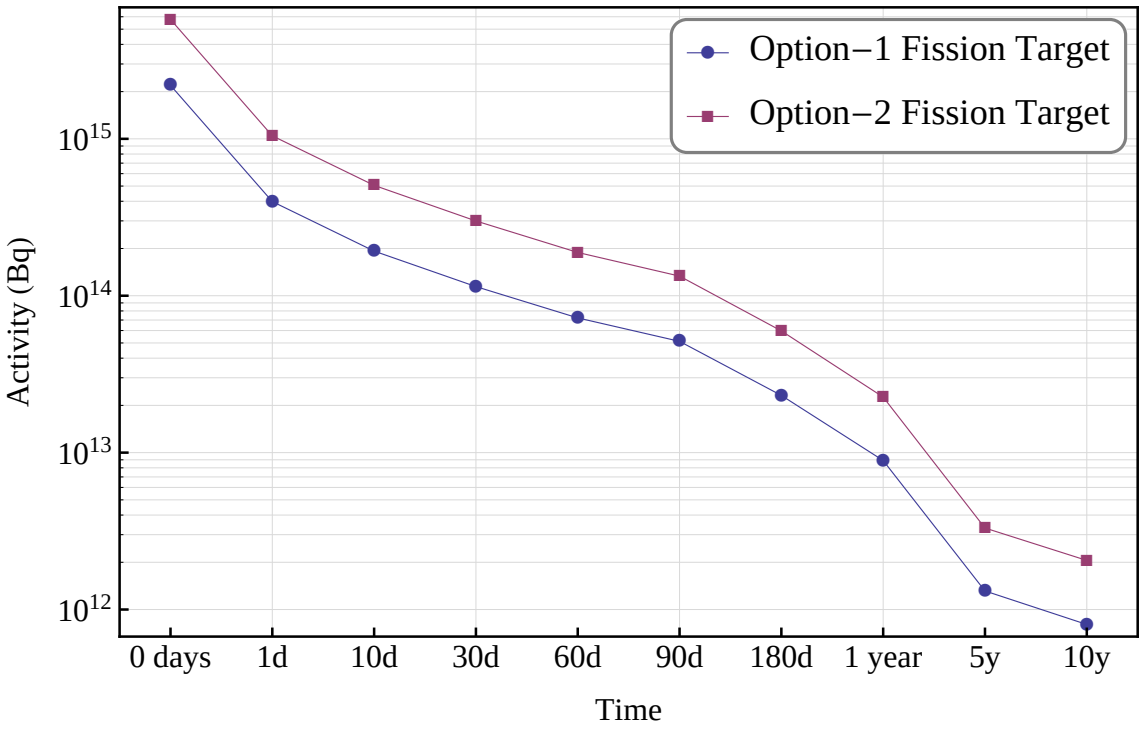

Figure 5.11: Activity (Bq) time evolution in the fission target.

components containing a multitude of isotopes, they must fulfil the following conditions to be considered wastes [157]:

$$\sum \frac{a_i}{EL_i} > 1 \tag{5.1}$$

and

$$\sum \frac{A_i}{EL_i} > 100. \tag{5.2}$$

It is seen in Tables 5.4 and 5.5 that the MEL values for the fission targets exceed the limit defined in (5.2) by nine orders of magnitude after the stoppage of the beam, and by seven orders of magnitude after ten years. This confirms that radioactive waste is indeed an important issue to be considered in the design of the multi-MW target station of the EURISOL facility.

The half-lives of the most relevant nuclides accumulated in the fission targets are displayed in Table 7.5 [158]. These are mostly fission products commonly found in nuclear reactors, such as ^{131}I, which has a specific activity of 8.3×10^{10} Bq/g in the Option-2 configuration after the stoppage of the proton beam. Ten years after shutdown, only the longest-lived isotopes remain: ^{147}Pm (2.6 years), ^{90}Sr (28.8 years), ^{137}Cs (30.1 years) and ^{232}U (68.9 years). The exception is ^{90}Y, a decay product of ^{90}Sr with a half-life of 60 hours. The production of ^{232}U follows the following chain of reactions [159]:

$$^{235}\mathrm{U}(n,\gamma) \rightarrow {}^{236}\mathrm{U}(n,\gamma) \rightarrow {}^{237}\mathrm{U}(\beta^-) \rightarrow {}^{237}\mathrm{Np}(n,2n) \rightarrow {}^{236\mathrm{m}}\mathrm{Np}(\beta^-) \rightarrow {}^{236}\mathrm{Pu}(\alpha) \rightarrow {}^{232}\mathrm{U}$$

Table 5.4: Nuclides formed by activation in the fission target, for configuration Option-1.

Option-1 – Fission Target					
Time	**Multiple of EL**	**Main Contributors to MEL**			
0d	3.01E+11	^{131}I (20.3%)	^{133}I (12.5%)	^{140}Ba (5.9%)	^{132}Te (5.4%)
1d	2.16E+11	^{131}I (26.3%)	^{133}I (8.1%)	^{140}Ba (7.8%)	^{91}Y (6.8%)
10d	1.14E+11	^{131}I (23.4%)	^{91}Y (11.6%)	^{144}Ce (10.1%)	^{89}Sr (9.5%)
30d	6.11E+10	^{144}Ce (17.9%)	^{91}Y (17.0%)	^{89}Sr (13.4%)	^{131}I (7.8%)
60d	3.84E+10	^{144}Ce (26.5%)	^{91}Y (18.9%)	^{89}Sr (14.1%)	^{95}Zr (8.6%)
90d	2.92E+10	^{144}Ce (32.4%)	^{91}Y (17.4%)	^{89}Sr (12.3%)	^{95}Zr (8.2%)
180d	1.71E+10	^{144}Ce (44.5%)	^{90}Sr (11.8%)	^{91}Y (10.3%)	^{137}Cs (6.5%)
360d	9.80E+09	^{144}Ce (50%)	^{90}Sr (20.4%)	^{137}Cs (11.1%)	^{106}Ru (7.2%)
5y	3.15E+09	^{90}Sr (61.8%)	^{137}Cs (34.1%)	^{144}Ce (2.8%)	^{90}Y (2.6%)
10y	2.60E+09	^{90}Sr (64.3%)	^{137}Cs (32.4%)	^{90}Y (2.9%)	^{232}U (0.5%)

Table 5.5: Nuclides formed by activation in the fission target, for configuration Option-2.

Option-2 – Fission Target					
Time	**Multiple of EL**	**Main contributors to MEL**			
0d	7.93E+11	^{131}I (20.9%)	^{133}I (12.3%)	^{140}Ba (5.8%)	^{132}Te (5.6%)
1d	5.71E+11	^{131}I (27.0%)	^{133}I (8.0%)	^{140}Ba (7.7%)	^{91}Y (6.7%)
10d	3.00E+11	^{131}I (24.1%)	^{91}Y (11.4%)	^{144}Ce (9.7%)	^{89}Sr (9.5%)
30d	1.60E+11	^{144}Ce (17.4%)	^{91}Y (16.9%)	^{89}Sr (13.5%)	^{131}I (8.1%)
60d	1.00E+11	^{144}Ce (25.8%)	^{91}Y (18.9%)	^{89}Sr (14.3%)	^{95}Zr (8.7%)
90d	7.59E+10	^{144}Ce (31.6%)	^{91}Y (17.5%)	^{89}Sr (12.5%)	^{95}Zr (8.3%)
180d	4.42E+10	^{144}Ce (43.7%)	^{90}Sr (12.7%)	^{91}Y (10.3%)	^{137}Cs (6.3%)
360d	2.54E+10	^{144}Ce (49.1%)	^{90}Sr (21.9%)	^{137}Cs (10.9%)	^{106}Ru (7.1%)
5y	8.39E+09	^{90}Sr (60.1%)	^{137}Cs (30.1%)	^{144}Ce (4.2%)	^{90}Y (2.7%)
10y	6.95E+09	^{90}Sr (64.3%)	^{137}Cs (32.4%)	^{90}Y (2.9%)	^{147}Pm (0.2%)

5.3.2.2 Structural Components

One of the differences between the two configurations is the material of the structural components of the extraction tubes. In Option-1, aluminium was used for the external wall, internal wall and exit tube. In Option-2, L316 stainless steel was tested, due to its favourable characteristics from the structural point of view. The activities in these components are shown in Fig. 5.12, for both configurations. Stainless steel proved to be much more activated than aluminium,

Table 5.6: Half-lives of the most relevant nuclides accumulated in the fission targets.

Isotope	Half-Life	Isotope	Half-Life
^{133}I	20.8 h	^{95}Zr	64.0 d
^{90}Y	60.0 h	^{144}Ce	284.9 d
^{132}Te	3.2 d	^{106}Ru	373.6 d
^{131}I	8.0 d	^{147}Pm	2.6 y
^{140}Ba	12.8 d	^{90}Sr	28.8 y
^{89}Sr	50.5 d	^{137}Cs	30.1 y
^{91}Y	58.5 d	^{232}U	68.9 y

the differences in the total activities ranging from one to three orders of magnitude. Table 5.7 lists the main nuclides responsible for the activities in the external wall, which are basically the same for the internal wall and exit tube. ^{60}Co, produced through neutron activation (n, γ) of the stable ^{59}Co [160], present in the steel alloy, is the nuclide with the greatest contribution to the total activity of stainless steel. Other contributors include ^{58}Co, produced from the stable ^{58}Ni through the reaction $^{58}\mathrm{Ni} + n \rightarrow {}^{58}\mathrm{Co} + p$ [161], and ^{55}Fe, produced through neutron activation of iron.

In aluminium, the greatest contributor to the activity is ^{22}Na, which can be produced by (n, x) or (p, x) reactions with ^{27}Al [162, 163]. Other relevant contributors include ^{28}Al, produced trough radiative capture, and ^{24}Na, produced through (n, α) or (p, x) reactions [164].

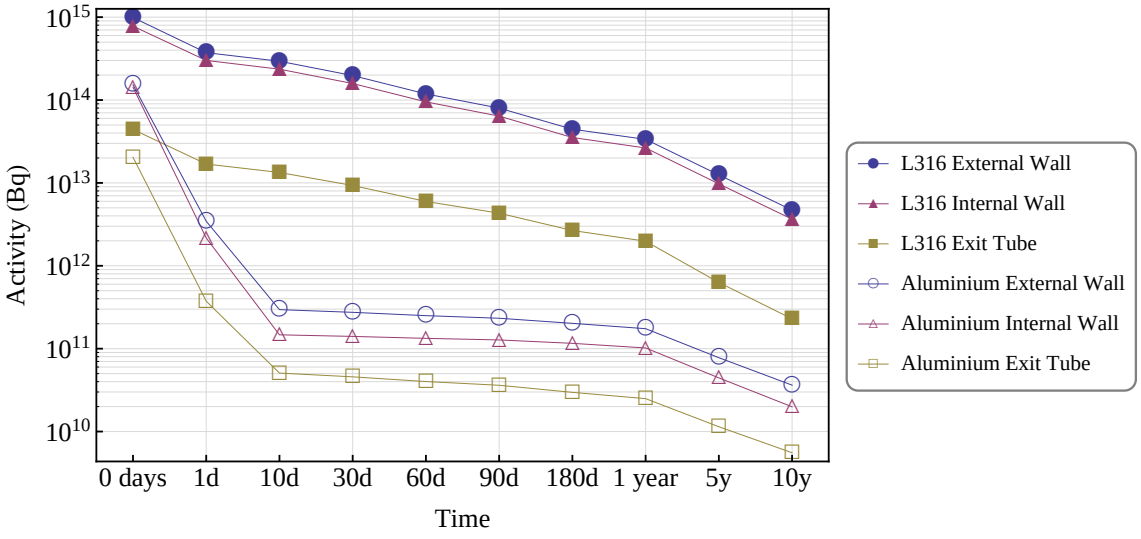

Figure 5.12: Comparison between activities obtained with the two configurations in the external wall, internal wall and exit tube. Aluminium was used in Option-1 and L316 was used in Option-2.

Table 5.7: Nuclides formed by activation in the external wall.

	External Wall					
	Option-2 (L316)			Option-1 (Aluminium)		
Time	Multiple of EL	Main contributors to the activity		Multiple of EL	Main contributors to the activity	
0d	4.59E+08	^{56}Mn (45.3%)	^{60}Co (24.9%)	6.89E+08	^{28}Al (97.8%)	^{24}Na (2.0%)
1d	2.14E+08	^{60}Co (53.4%)	^{58}Co (9.7%)	6.06E+06	^{24}Na (73.0%)	^{22}Na (26.8%)
10d	1.92E+08	^{60}Co (59.5%)	^{58}Co (10.0%)	1.63E+06	^{22}Na (99.3%)	^{3}H (0.4%)
30d	1.75E+08	^{60}Co (64.9%)	^{58}Co (9.0%)	1.60E+06	^{22}Na (99.4%)	^{3}H (0.4%)
60d	1.59E+08	^{60}Co (70.3%)	^{55}Fe(9.6%)	1.57E+06	^{22}Na (99.4%)	^{3}H (0.4%)
90d	1.49E+08	^{60}Co (74.2%)	^{55}Fe(10.0%)	1.53E+06	^{22}Na (99.5%)	^{3}H (0.4%)
180d	1.33E+08	^{60}Co (80.7%)	^{55}Fe(10.5%)	1.43E+06	^{22}Na (99.5%)	^{3}H (0.4%)
360d	1.18E+08	^{60}Co (85.3%)	^{55}Fe(10.5%)	1.26E+06	^{22}Na (99.5%)	^{3}H (0.5%)
5y	6.40E+07	^{60}Co (92.6%)	^{55}Fe(7.0%)	4.34E+05	^{22}Na (99.0%)	^{3}H (1.0%)
10y	3.21E+07	^{60}Co (95.7%)	^{55}Fe(3.9%)	1.17E+05	^{22}Na (97.0%)	^{3}H (2.9%)

5.3.2.3 Fission Target Container

Fig. 5.13 shows the activities in the fission target container and in the shield. In Option-1 tantalum was used for these components, while molybdenum was tested in Option-2. It can be seen that tantalum is much more activated than molybdenum.

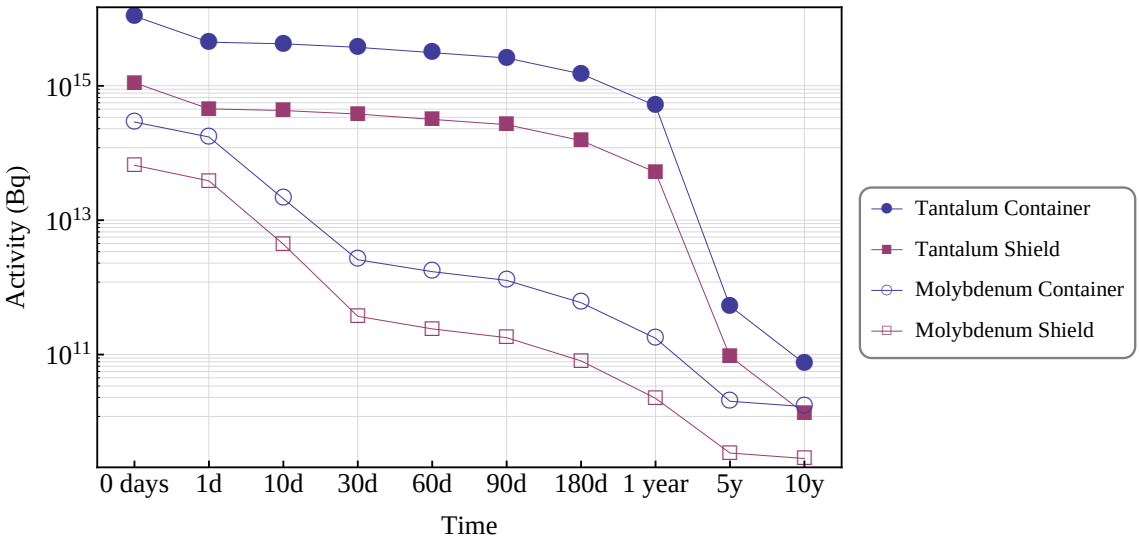

Figure 5.13: Comparison between the activities obtained in the fission target container and shield. Tantalum was used in Option-1 and molybdenum was used in Option-2.

The fission target container is one of the most critical regions in the extraction tubes. It is

subject to extremely high neutron fluxes, and therefore its material has to be very resistant from a thermo-mechanical point of view. This is especially important since the container holds the fissile material and acts as a first barrier against the release of the fission products. Both tantalum and molybdenum have high melting points, an important characteristic given the high temperatures the container will be subject to. However, the activities obtained with tantalum in Option-1, even higher than the activities in the fissile material, could rule it out as a choice for the fission target container. It is clear that, despite its more favourable thermo-mechanical properties, the high activation registered in tantalum makes molybdenum a better solution for the container.

Table 5.8 lists the main nuclides responsible for the activities found for tantalum and molybdenum in the two configurations. In tantalum, ^{182}Ta, produced through the (n,γ) reaction with ^{181}Ta (99.988% of natural tantalum), is responsible for over 99.9% of the activities for all cooling periods below 1 year.

Table 5.8: Nuclides formed by activation in the fission target container.

	Fission Target Container					
	Option-2 (Molybdenum)			**Option-1 (Tantalum)**		
Time	**Multiple of EL**	**Main contributors to MEL**		**Multiple of EL**	**Main contributors to MEL**	
0d	1.19E+10	^{99}Mo (94.1%)	^{90}Nb (1.2%)	3.28E+11	^{182}Ta (99.7%)	^{180}Ta (0.3%)
1d	9.03E+09	^{99}Mo (96.2%)	^{89}Zr (0.8%)	3.25E+11	^{182}Ta (99.9%)	^{180}Ta (0.03%)
10d	1.04E+09	^{99}Mo (86.2%)	^{88}Y (3.7%)	3.08E+11	^{182}Ta (99.9%)	^{175}Hf (0.02%)
30d	1.07E+08	^{88}Y (35.4%)	^{95}Nb (18.3%)	2.72E+11	^{182}Ta (99.9%)	^{175}Hf (0.02%)
60d	7.36E+07	^{88}Y (48.4%)	^{83}Rb (14.6%)	2.27E+11	^{182}Ta (99.9%)	^{175}Hf (0.02%)
90d	5.70E+07	^{88}Y (57.7%)	^{88}Zr (12.9%)	1.89E+11	^{182}Ta (99.9%)	^{175}Hf (0.01%)
180d	3.17E+07	^{88}Y (74.9%)	^{88}Zr (11.0%)	1.10E+11	^{182}Ta (99.9%)	^{175}Hf (0.01%)
360d	1.17E+07	^{88}Y (85.7%)	^{88}Zr (6.7%)	3.69E+10	^{182}Ta (99.9%)	^{179}Ta (0.01%)
5y	3.91E+05	^{93}Mo (85.4%)	^{3}H (7.5%)	7.90E+06	^{182}Ta (65.4%)	^{179}Ta (12.6%)
10y	3.82E+05	^{93}Mo (87.3%)	^{3}H (5.8%)	4.19E+05	^{179}Ta (34.4%)	^{172}Hf (32.4%)

5.3.2.4 Cooling Water, Moderators/Reflectors, Cryogenic Panels and Cables

Fig. 5.14 shows the activities, for both configurations, in the carbon moderator surrounding the fission target, the beryllium oxide reflector and the cooling water. The materials were grouped in this way due to the fact that they are all neutron moderator/reflector materials, and therefore their levels of radioactivity can be compared (although the water is used as coolant in this case). Looking at the two geometries, it can be seen that in all three cases the activities are slightly

higher in Option-2, since the fission rate is higher in that case. Carbon has a smaller contribution to the total activity than the other materials, despite being so close to the fission target (although its specific activity, because it has a smaller volume, is higher than those of the other materials).

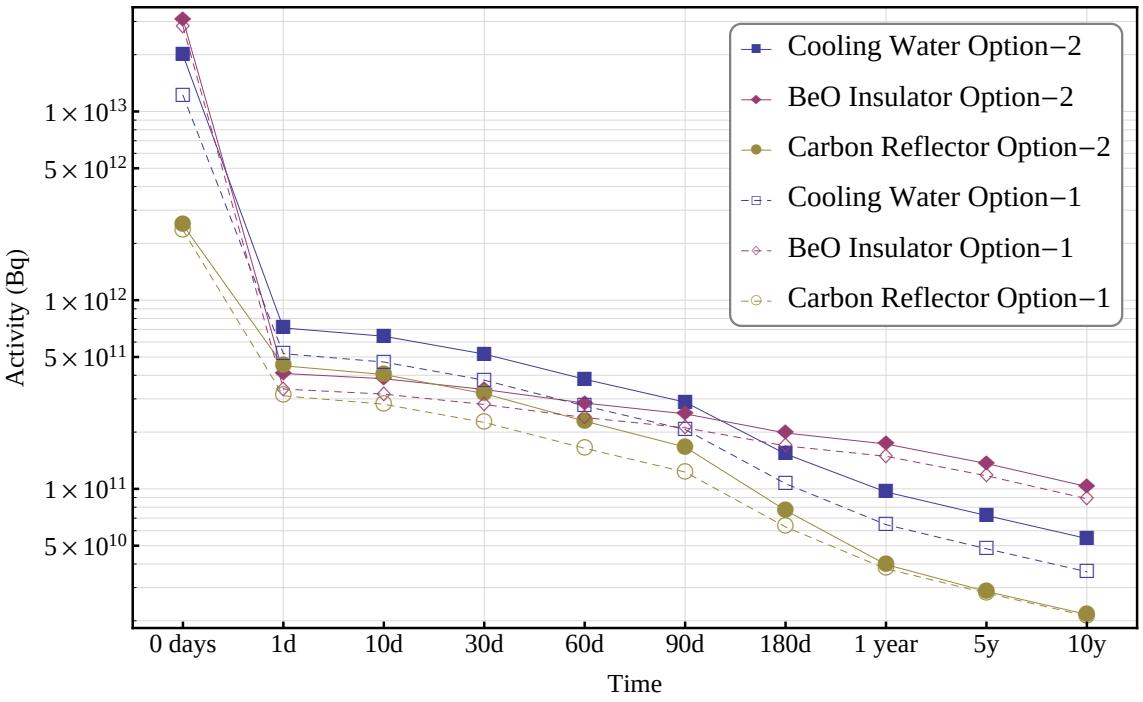

Figure 5.14: Comparison between the activities obtained in the cooling water, carbon reflector and BeO insulator.

The main nuclides responsible for the activities in the cooling water are listed in Table 5.9. The activities in the water come mainly from the formation of ^{7}Be and ^{3}H, spallation products of oxygen [165], and the same is true for the activation of Carbon and Beryllium Oxide. The long half-life of tritium (12.3 years) is a problem – the activities represented in Fig. 5.14 drop less than 50% from one year after shutdown to ten years after shutdown, when tritium is responsible for more than 95% of the total activity.

Finally, the activities in the cryogenic panels and connectors and cables are shown in Fig. 5.15. The region of the connectors and cables shows very high activities for the first 10 days after shutdown, but the decay of ^{66}Cu and ^{64}Cu lowers the activities after 10 days. From then on, ^{60}Co and ^{58}Co are the main contributors to the total activity. In the cryogenic panels, the activity is only due to the formation of the long-lived ^{3}H, and therefore it is almost constant throughout the different cooling times.

Table 5.9: Nuclides formed by activation in the cooling water.

	Cooling Water					
	Option-2			Option-1		
Time	Multiple of EL	Main contributors to MEL		Multiple of EL	Main contributors to MEL	
0d	1.28E+05	^{11}C (72.7%)	^{7}Be (20.9%)	1.18E+05	^{11}C (74.7%)	^{7}Be (19.8%)
1d	3.46E+04	^{7}Be (76.1%)	^{3}H (23.6%)	2.95E+04	^{7}Be (78.0%)	^{3}H (21.7%)
10d	3.17E+04	^{7}Be (74.0%)	^{3}H (25.7%)	2.70E+04	^{7}Be (75.9%)	^{3}H (23.8%)
30d	2.63E+04	^{7}Be (68.7%)	^{3}H (30.9%)	2.23E+04	^{7}Be (70.9%)	^{3}H (28.7%)
60d	2.04E+04	^{7}Be (59.9%)	^{3}H (39.6%)	1.71E+04	^{7}Be (62.4%)	^{3}H (37.1%)
90d	1.64E+04	^{7}Be (50.4%)	^{3}H (49.0%)	1.37E+04	^{7}Be (53.0%)	^{3}H (46.4%)
180d	1.06E+04	^{3}H (74.8%)	^{7}Be (24.2%)	8.57E+03	^{3}H (72.8%)	^{7}Be (26.2%)
360d	8.07E+03	^{3}H (95.7%)	^{7}Be (3.1%)	6.37E+03	^{3}H (95.3%)	^{7}Be (3.4%)
5y	6.26E+03	^{3}H (98.4%)	^{14}C (1.6%)	4.93E+03	^{3}H (98.3%)	^{14}C (1.7%)
10y	4.75E+03	^{3}H (97.9%)	^{14}C (2.1%)	3.74E+03	^{3}H (97.7%)	^{14}C (2.3%)

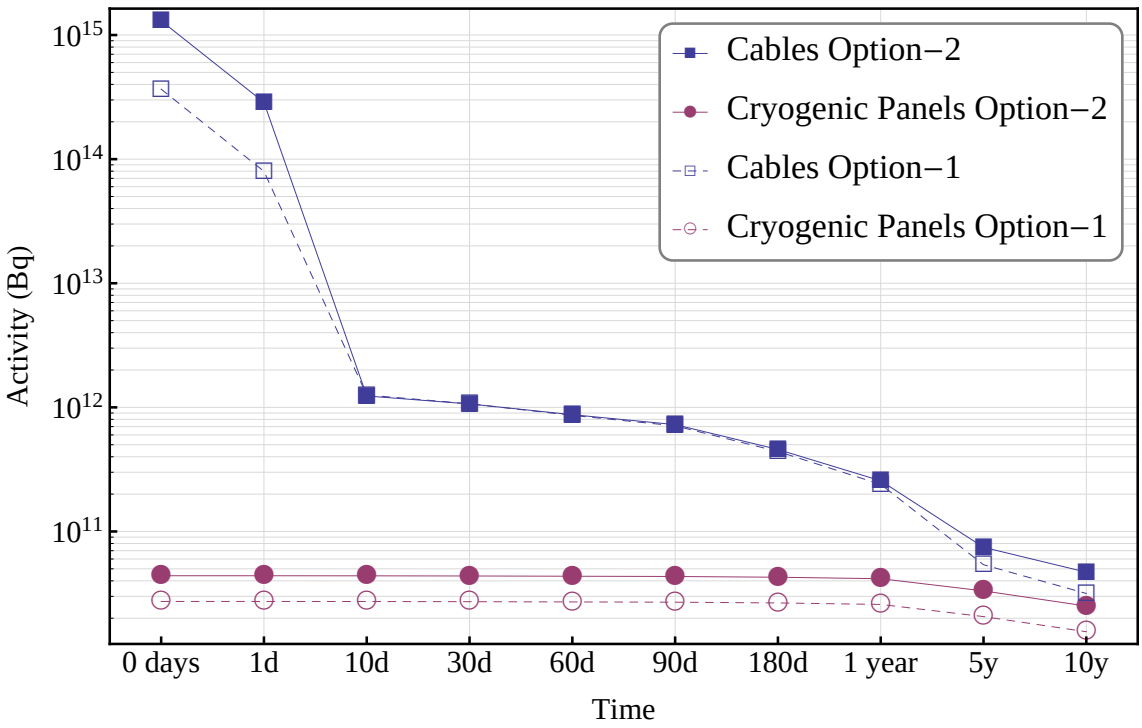

Figure 5.15: Comparison between the activities obtained in the cryogenic panels and connectors and cables.

5.3.3 Equivalent Dose Results

The time evolution of the dose rate was also calculated for three regions of the extraction tubes, considered to be critical from the radioprotection point of view. These were the fission target (fissile material), the fission target container and the cooling water. The fission target and the fission target container were the most activated regions, and the cooling water is also important since the design of its circulation system depends on the activities registered in the water and the doses that result from those activities. The dose rates in these three regions after shutdown are shown in Fig. 5.16 (conversion factors obtained from [166]). Once again, the facility is considered to be continuously operating during 200 days before the beam stops ($t = 0$ days, in the decay time scale). The dose rates after shutdown are due to the decay of the radioactive products formed in these regions by activation. During operation, the highest dose rate is registered in the water, an expected result since the neutrons deposit more energy in the water than in any of the other materials. The doses are higher in the fissile material than in the fission target container. In Option-2, the residual dose immediately after shutdown in the fissile material is still 2.4×10^6 Sv/h (4 orders of magnitude lower than during operation). It is important to notice that when the fission target container is made of tantalum (dashed line), the dose rate in this element, for several times elapsed after shutdown, is even higher than in the fissile material (molybdenum is clearly less activated than tantalum). Water is the least activated material.

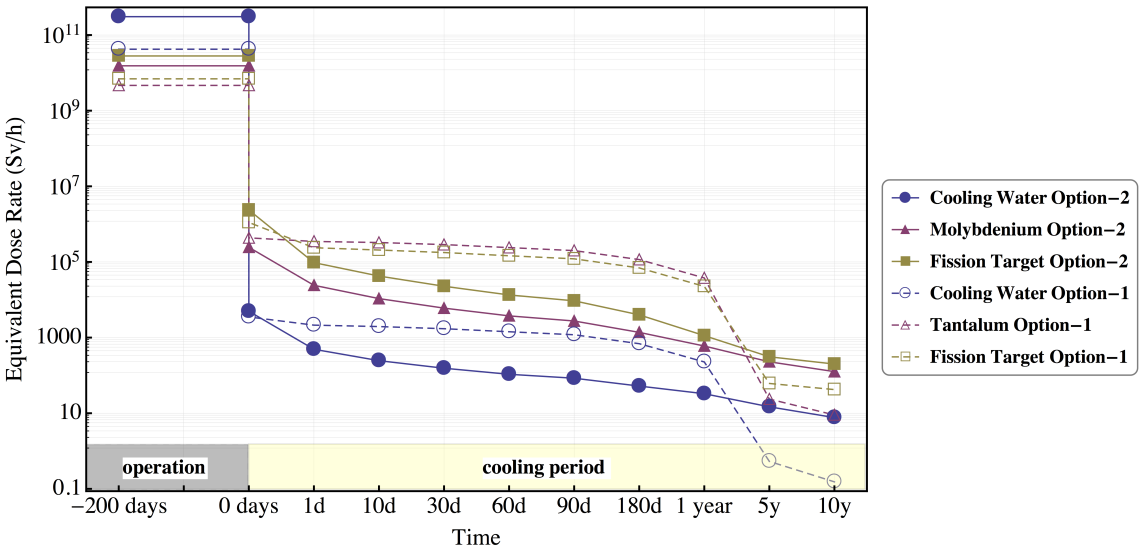

Figure 5.16: Equivalent dose rate (Sv/h) evolution in different regions of the fission targets extraction tubes.

The doses after shutdown are in general higher for the Option-1 configuration, and this is in due to the high activation of tantalum. The radioactivity of the nuclides formed in tantalum by activation is responsible for the higher doses in the other materials (even though Option-2 has the highest prompt fission rates). It can be seen that the tantalum fission target container is

subject to very high doses, superior to 10^5 Sv/h/cm^3, for cooling times inferior to one year. When molybdenum is used, the doses in the container and surrounding components are lower.

5.4 Conclusions

In this chapter, two different configurations for the EURISOL multi-MW target station were simulated: Option-1 and Option-2. The main differences between those geometries can be summarised as follows:

Option-1 the spallation target was surrounded by a cylindrical iron shielding with radius 20 cm; there was a water moderator near the fission target; the fission target container was made of tantalum; the structural components of the extraction tube were made of aluminium.

Option-2 the spallation target was surrounded a cylindrical carbon reflector radius 50 cm; there was no water moderator for the fission targets; molybdenum was used for the fission target container instead of tantalum; L316 stainless steel was used for the structural components of the extraction tube instead of aluminium.

The highest fission rate value (6.4×10^{15} fissions/s) of all the geometry combinations was achieved with Option-2 geometry and ^{235}U as fissile material. This result was expected since in this configuration the neutrons are moderated more efficiently, due to the presence of the carbon around the spallation target. For this reason, it can be concluded that this configuration is well optimised for fission in ^{235}U. A harder neutron spectrum is required if the objective is to increase the fission rates in other fissile nuclei, like ^{238}U and ^{232}Th. In that case, no significant moderation should occur and the reflector material should be suitable for fast neutrons. It is important to underline that the current configuration of the multi-MW target station, with removable extraction tubes, facilitates the integration of several fissile materials with custom moderators and reflectors, to maximise the performance for each situation, an essential characteristic for a facility which aims at producing a wide range of radioactive ion beams.

The activation in the extraction tubes containing the fission targets was studied in detail. This study was particularly important since the extraction tubes need to be exchanged periodically, due to the burn-up of the fission target material, and therefore the activities in its different components, as well as the main nuclides responsible for those activities, must be predicted for several cooling periods, in order to properly project the extraction tubes handling system. This analysis was done for the two configurations. For all the activation calculations, 200 days of irradiation (4MW proton beam) were assumed, and the cooling periods ranged from 0 days (shutdown time) to ten years after shutdown.

The activities in the fission target, one of the most activated regions of the extraction tubes, were higher in Option-2, as in this case the obtained fission rates were also higher. Also for this

reason, the activities were higher in the other components in Option-2 than in Option-1, except when different materials were tested. In the structural components (external and internal walls and exit tube), aluminium (Option-1) was much less activated than L316 stainless steel (Option-2). From the radioprotection point of view, aluminium is clearly the better choice. Nevertheless, structural requirements may force the option for stainless steel.

Regarding the fission target container material, tantalum was tested in Option-1 and molybdenum in Option-2. In this case, the activation of tantalum was huge compared to the activation of molybdenum. The activities in the tantalum container in Option-1 were even higher than the activities in the fission target. For this reason, molybdenum should definitely be preferred to tantalum in the fission target container.

The dose equivalent for the same cooling periods was also calculated for four important regions: the cooling water, the internal wall, the fission target and the fission target container. The doses were in general higher in Option-1, due to the contribution of the high activation of tantalum. The radioactivity of the nuclides formed in tantalum by activation is responsible for the higher doses in the other materials. When molybdenum is used, the doses in all the other regions are lower.

Option-2 was a good improvement over Option-1. It allows to obtain higher neutron fluxes and fission rates, and, at the same time, lower doses in the different regions of the extraction tubes due to the activation. A further improvement can be considered to Option-2 geometry if aluminium can be used in the structural components instead of L316 stainless steel.

Part III

Optimization Studies for the CERN-ISOLDE Facility

Chapter 6

The CERN-ISOLDE Facility

The ISOLDE facility at CERN has been one of the premier ISOL facilities worldwide since it started operating in 1967 [167, 168]. The decision to build ISOLDE at the 600 MeV Proton-Synchro-Cyclotron (SC) at CERN was taken in 1964, three years before the first ISOLDE experiments. Several upgrades took place at ISOLDE during the following 25 years, before it was moved, in 1992, to a new building complex fed by a 1 GeV proton beam from the injector synchrotron, called the PS-Booster (PSB) [169, 170]. Fig. 6.1 shows the integration of the PSB in the accelerator complex at CERN [171]. ISOLDE, the heaviest user of the PSB, is able to take beam from the accelerator complex while the Proton Synchrotron (PS) is ramping and accelerating beams destined to other experimental areas [172]. It receives 30–40% of the protons accelerated at CERN.

Table 6.1: Key dates in the history of ISOLDE [169, 170].

1964, December	Decision to build ISOLDE at SC
1967, October 23	First experiments at ISOLDE
1973	Shut down and reconstruction of ISOLDE at SC
	Increase of the external SC beam to 4 μA
1974	Start of ISOLDE 2 at SC
1987	Installation of a high-resolution separator in the SC proton hall
1989	Start of the civil engineering work on the new ISOLDE site
1990, December	Final shut-down of the SC which had started operation in 1957
1992, June	First experiment at the PSB
2001, October	First accelerated beams in REX-ISOLDE
2009, December	Approval of the HIE-ISOLDE Project

Operational since 2001, the facility for accelerated radioactive ion beams (RIBs) at ISOLDE, REX-ISOLDE (REX-Radioactive beam Experiment) [173–176], consists of a normal conducting linear accelerator with the potential to accelerate up to 3 MeV/u most of the 1000+ radioactive isotopes produced at ISOLDE, following the bombardment of various primary targets with a 1.4 GeV

pulsed proton beam (with an average intensity of 2 μA) [177–179]. Table 6.1 presents some key dates in the history of ISOLDE.

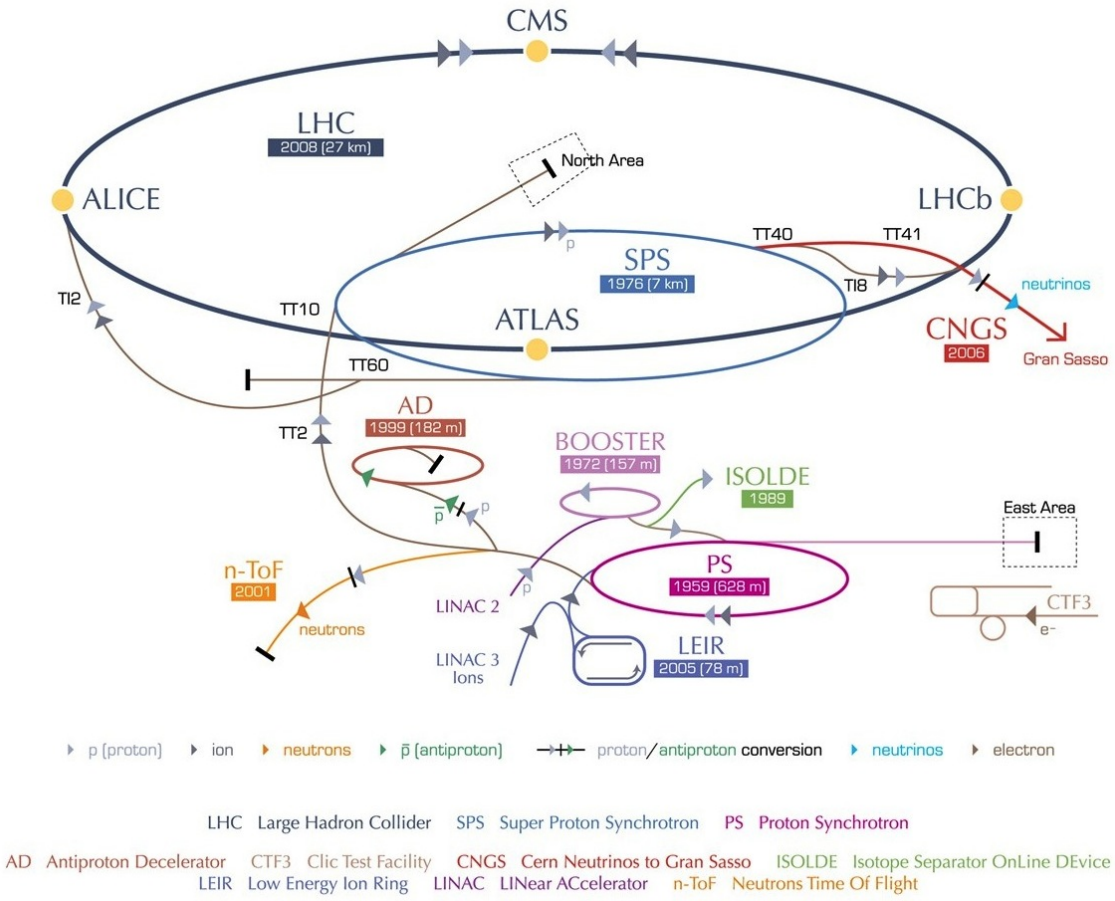

Figure 6.1: Integration of the PS-Booster and ISOLDE in the accelerator complex at CERN.

6.1 Layout of the ISOLDE Facility

The current layout of the ISOLDE facility is shown in Fig. 6.2 [180]. Beam pulses with approximately 3×10^{13} protons per bunch with energies in the range 1–1.4 GeV are delivered to two separate ISOLDE target stations every 1.2 seconds, or multiples of this period, resulting in an average beam intensity of 2 μA. Various solid and liquid target materials are used to produce a wide spectrum of radioactive isotopes covering essentially the whole nuclear chart below uranium (Z = 92). UC_x is the most frequently used target material, having accounted for 67% of the beam time in 2007, followed by SiC (9%) and liquid lead (6%) [180].

When the beam hits a target, radioactive isotopes are produced via fragmentation, spallation and fission reactions. The radioactive products are then thermalised in the target material and diffuse out of it, in a process governed by the diffusion properties of the atoms of interest and

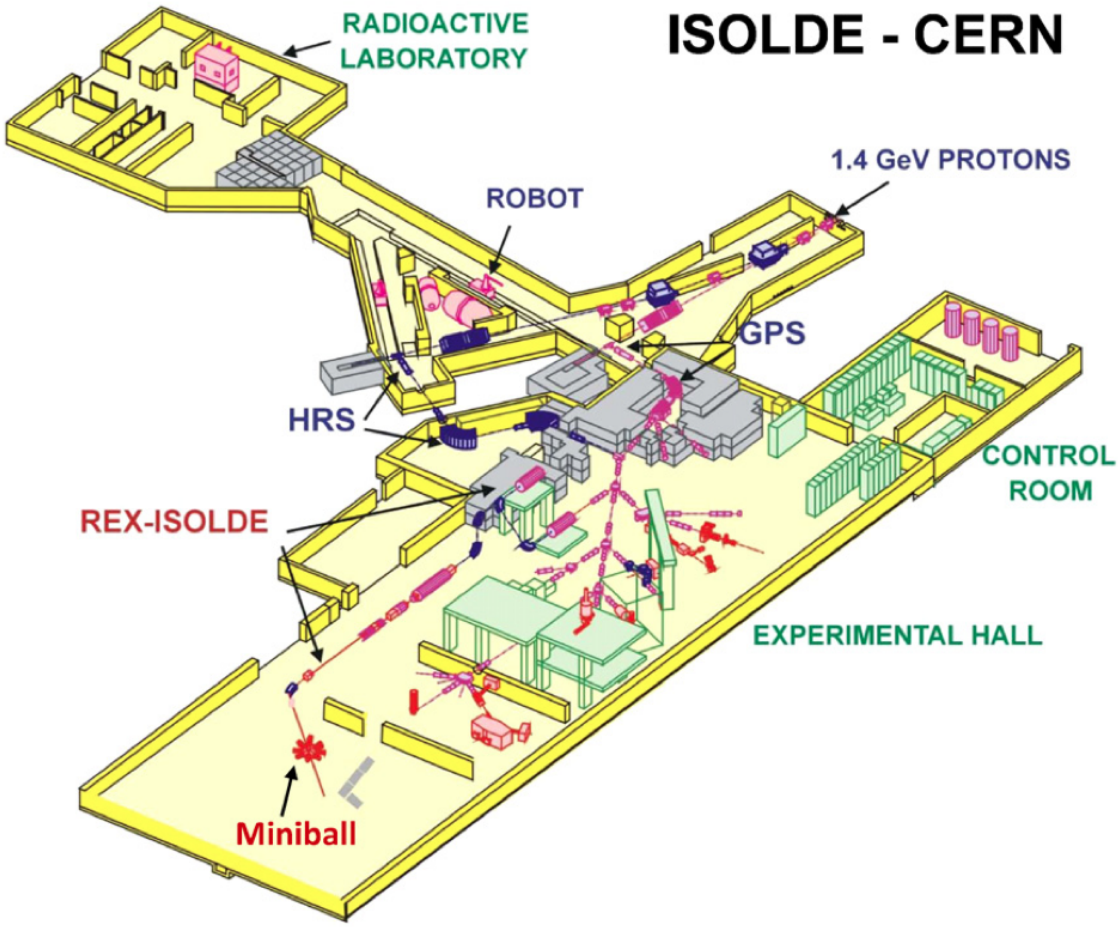

Figure 6.2: ISOLDE facility layout. REX-ISOLDE receives RIBs from both mass separators, GPS and HRS.

the target matrix. This diffusion process is followed by effusion towards the ion source, through the transfer line. When the nuclides reach the ion source, a large fraction is ionised via one of several possible ionisation mechanisms, generally to a singly-charged positive or negative state (in a few cases, multiply-charged ions are produced as well). The target, transfer line and ion source are commonly referred to as target-ion source system or target unit. The target unit is heated to speed up the diffusion and effusion processes, typically to 2000 °C when the target material is UC_x [180, 181].

The target units are coupled to the ISOLDE target stations, also called front-ends. After extraction from the ion source and acceleration to 60 keV, the ions are sent to the magnetic mass separators, where they are mass-separated according to the mass-over-charge ratio using a dipole magnet. Here, ISOLDE uses two different systems, the General Purpose Separator (GPS) and the High Resolution Separator (HRS), arranged to allow that a beam from either machine can be fed into a common beam distribution system before being sent to the experimental set-ups, for nuclear spectroscopy, laser spectroscopy, mass measurements, solid state and surface studies [170].

HRS is a more complex system which allows greater resolution than GPS, but GPS can distribute three beams of different masses, within the mass range of $\pm 15\%$ from the central mass, to three experiments at the same time [182, 183].

Some experiments get the beam from the mass separators directly, while for others further treatment is needed. A cooler device is used to reduce the axial and radial energy spread of the beam, to improve its optical properties. Bunching is also often required to increase the peak to background ratio for some experiments, or to inject the beam into a charge-state breeder. Penning traps (a combination of magnetic and electrical fields) [184] and radio frequency (RF) coolers (using electrical DC and RF fields) [185] are used for cooling and bunching the beam. Buffer gas like helium or argon is introduced and the radioactive ions loose energy through collisions with the buffer gas [181].

To allow for an efficient post-acceleration, a charge-state breeder [186], in which the ions are bombarded with energetic electrons, is used to change the singly-charged state of the ion beam to a multiply-charged state. The highly-ionised beam is then accelerated and delivered to the experimental areas. REX-ISOLDE can accelerate ion beams up to 3 MeV/u.

The target area is a place with high radiation levels, not only during operation but also due to the activation of the targets and surrounding materials. There is also a potential risk of accidental release of radioactivity. For these reasons, the target area is shielded by concrete and steel blocks and buried under 8 m of soil, with an adequate ventilation system. The manipulation of the radioactive target units is done by industrial robots, with no direct human intervention. Attached to the primary radiation zone is a class A radioactive laboratory, where radioactive materials are handled. After a suitable cooling period, irradiated targets can be inspected in an adapted hot cell. Radioactive material does not leave this zone except for disposal [182, 187].

Access to the experimental hall, which is completely separated from the targets area, requires authorisation, and the use of a dosemeter is mandatory. Most of the operation of the ISOLDE facility is is done in the control room, through a computer-based control system.

6.2 Target Unit

6.2.1 Direct Configuration

Several different combinations of target materials and ion sources can be used at ISOLDE. Fig. 6.3 [183] shows a representation of an ISOLDE target unit, containing the target, a transfer line and an ion source. The target container is a 200 mm long tantalum cylinder with 20 mm of diameter. As mentioned before, it can be filled with different materials. In the standard ISOLDE

configuration this target is hit directly by the proton beam, producing the radioactive isotopes through fission, spallation and fragmentation reactions. This configuration will be called "direct configuration" in this work.

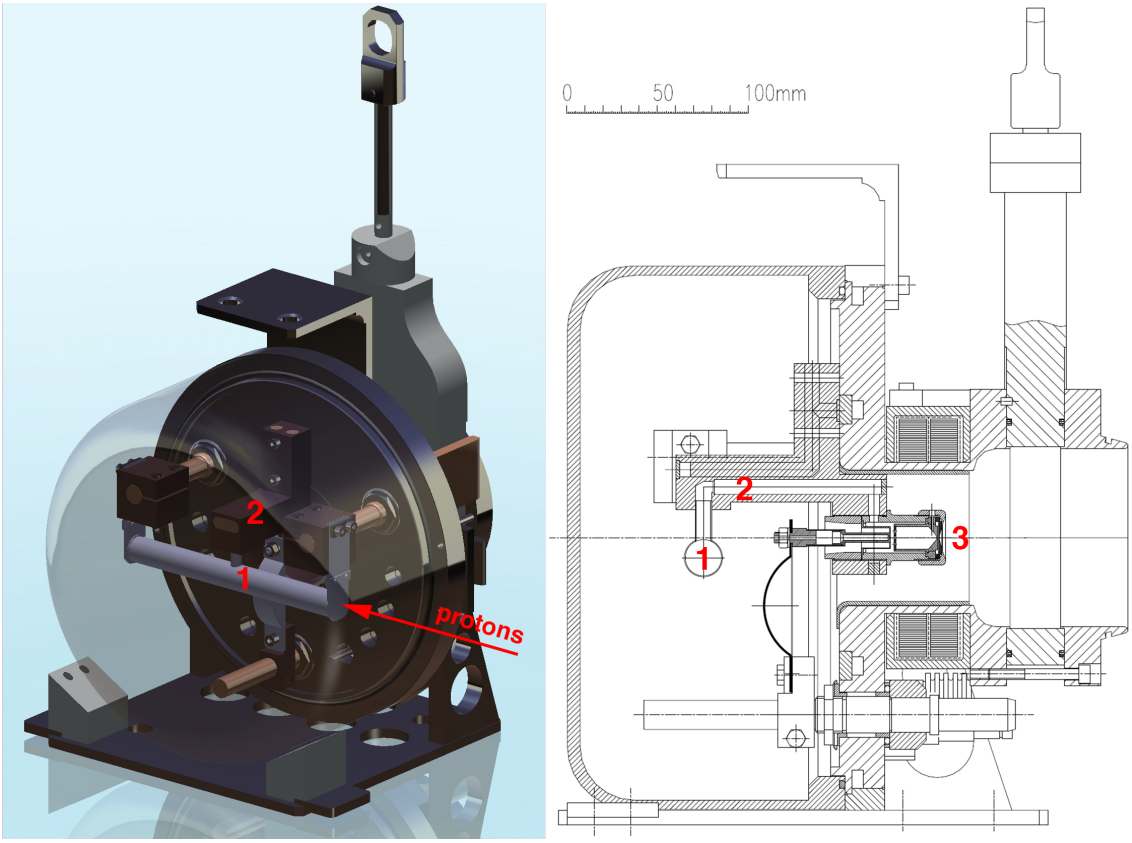

Figure 6.3: Left – ISOLDE target unit in 3D. Right – cut perpendicular to the direction of incidence of the proton beam. The numbers indicate the target container (1), the transfer line (2) and the ion source (3). These images are courtesy of João Pedro Fernandes Ramos and Stefano Marzari.

When the direct configuration is used, fission is induced mainly by GeV protons and there is a strong contribution of spallation-fission, meaning that many of the target nuclei will first evaporate a significant number of neutrons and protons and then fission at a later stage. This leads to a shift of the fission yields towards neutron-deficient species, which means that there will be a background of neutron-deficient isobars when the aim is to produce neutron-rich species. To avoid this background, low-energy fission can be used [180, 188].

6.2.2 Converter Configuration

At ISOLDE, a solid neutron converter has been used for several years to obtain MeV neutrons from the incident proton beam, which then induce fission in the UC_x target ("converter configuration"). Fig. 6.4 shows a picture of a target unit with a UC_x target and a tantalum neutron

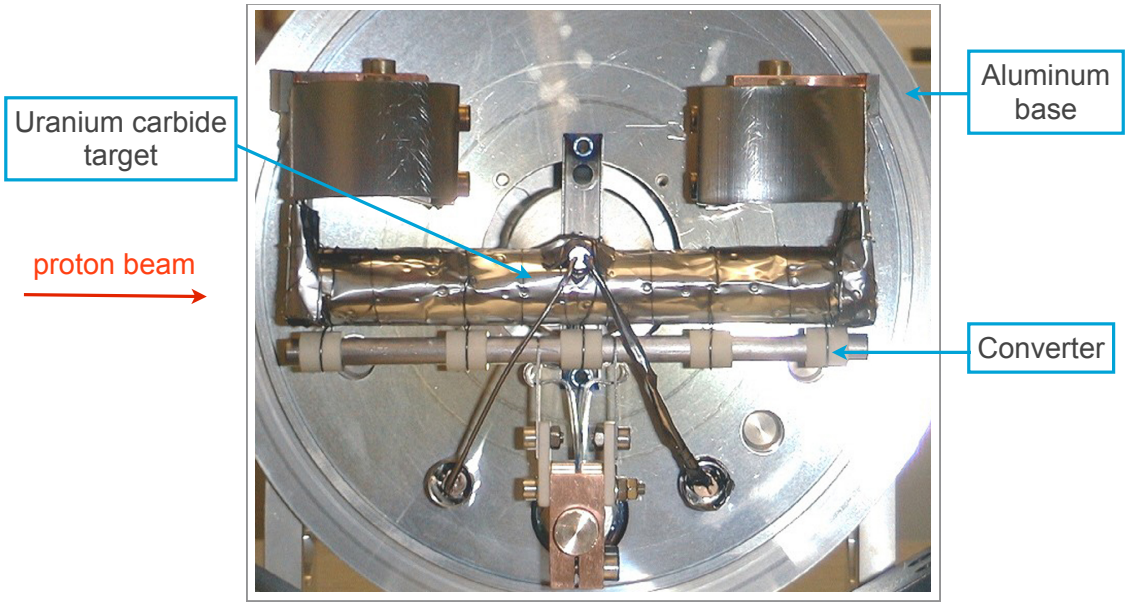

Figure 6.4: ISOLDE target unit with a tantalum converter.

converter placed close to the target. In this configuration, the protons are directed to the converter, producing intense neutron fluences through spallation processes. The spallation neutrons, in turn, induce fission in the UC_x target, producing a great variety of radioactive nuclides. These nuclides, when compared to the the ones produced with the direct configuration, will be shifted towards the neutron-rich part of the nuclide chart, with less contaminations from neutron-deficient nuclei. However, reduced beam intensities result from the present layout of the converter configuration, in comparison with the yields obtained with the direct beam configuration [189].

6.3 HIE-ISOLDE

The HIE-ISOLDE project foresees a major upgrade to the ISOLDE facility [190, 191], aiming to expand the physics program of REX-ISOLDE by using higher beam energies and intensities with improved quality and flexibility. New improvements in radioisotope selection, charge-breeding and target-ion source development are therefore required in order to take advantage of the higher intensities provided by LINAC4, the new injector for the PS-Booster. The existing REX accelerating structure will be replaced by a superconducting (SC) linear accelerator that can deliver a maximum energy of 10 MeV/u for a mass-to-charge ratio of A/Q=4.5, an improvement that will open a broad programme of nuclear structure and nuclear astrophysics studies using different classes of nuclear reactions. HIE-ISOLDE will represent, along with SPES at INFN-LNL (Italy) and SPIRAL2 at GANIL (France), a step forward towards the ultimate European ISOL facility, EURISOL.

The HIE-ISOLDE project includes a design study of improved production targets and front-ends taking into account the increase of proton beam intensity delivered by the new proton driver. With the installation of LINAC4 at CERN, the average primary beam current can be increased by a factor 3, up to 6 μA [191]. There is also the possibility of further gains in intensity through an upgrade in energy of the PS-Booster, from the present 1.4 GeV to 2 GeV [192, 193].

Presently, civil engineering works are in progress for the construction of new buildings adjacent to the existing ISOLDE experimental hall. To guarantee a minimum of perturbation to the operation of the facility, works in the experimental hall related to the HIE-ISOLDE upgrade will take place during the CERN Long Shutdown, which started in December 2012 and will last until April 2014. It is foreseen that physics with 5.5 MeV/u beams should start in early 2015 [192].

Chapter 7

Optimisation Studies of the ISOLDE Target System

7.1 Introduction

The current configuration of the ISOLDE neutron converter and fission target system, which has been used for ten years at ISOLDE to produce neutron-rich fission fragments, was studied in detail, using the state-of-the-art Monte Carlo code FLUKA [74, 75] and the cross section codes TALYS [141] and ABRABLA [122, 123]. An optimisation of the existing system is here proposed, to maximise the production of important neutron-rich isotopes while reducing undesired backgrounds of neutron-deficient isobars. The optimisations proposed in this chapter can already be applied to ISOLDE and will be of special relevance for HIE-ISOLDE, since the planned increase in proton beam energy (from 1.4 to 2 GeV) will result in larger fractions of produced backgrounds [194].

7.1.1 Radioactive Ion Beam Intensity

Two of the main figures of merit for a RIB facility are the intensity and the purity of the beams. The intensity of the RIBs delivered to the experimental areas of an ISOL facility is given by

$$i = \Phi \cdot \sigma \cdot N \cdot \epsilon_{target} \cdot \epsilon_{source} \cdot \epsilon_{sep} \cdot \epsilon_{transport}. \tag{7.1}$$

The in-target production (number on nuclides of a given isotope produced in the target per unit time) is $\Phi \cdot \sigma \cdot N$, the product of the flux of primary particles (per unit time and area), the cross-section for the production of the desired isotope and the number of target atoms exposed to the

primary beam. The final RIB intensity is obtained by multiplying the in-target production by the target release efficiency (ϵ_{target}), the ion source efficiency (ϵ_{source}), the transmission of the mass-separator (ϵ_{sep}) and the transmission to the detection system ($\epsilon_{transport}$) [195].

Higher proton beam intensities lead to direct gains in RIB intensity, without affecting the remaining parameters of Equation (1) [196]. For the ISOLDE facility, this is foreseen in the HIE-ISOLDE upgrade, described in Section 6.3, with an increase in the proton beam intensity from 2 μA to 6 μA. The in-target production can also be increased by expanding the target dimensions, to increase the number of target atoms exposed to the primary beam. However, larger target dimensions will affect the release efficiency from the target [197], ϵ_{target}, since the produced radionuclides will have to cover longer paths in the effusion process, increasing the number of collisions with the target container and, consequently, increasing the losses through radioactive decay. These losses are particularly relevant for short-lived exotic species.

7.2 Objectives and Methods

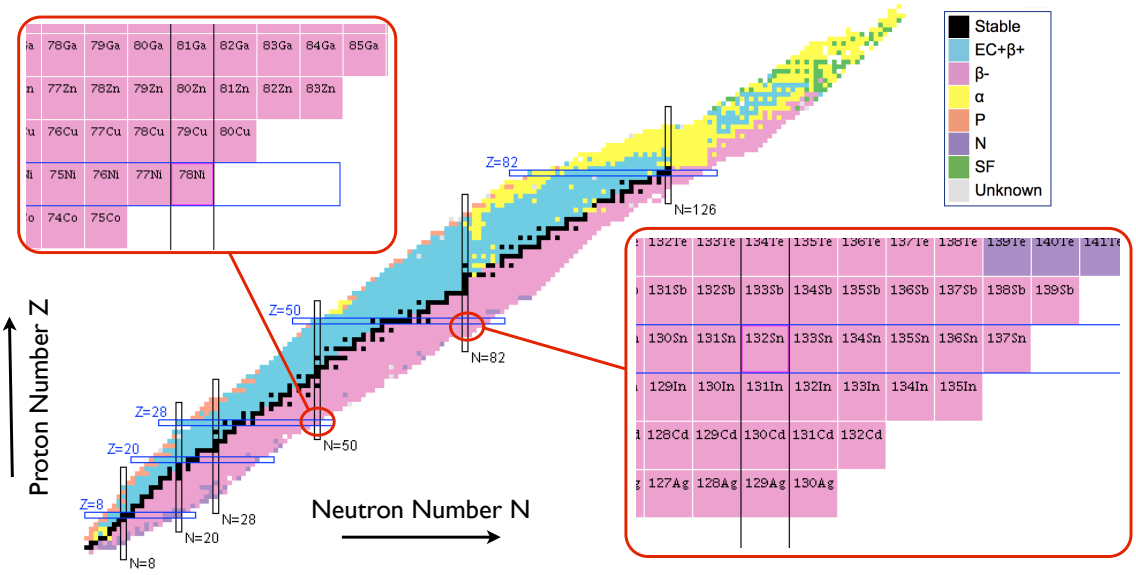

Figure 7.1: Nuclear Landscape and main regions of interest for this work.

The nuclear landscape is represented in Fig. 7.1. Emphasis is given to the regions around the double shell closures of ^{78}Ni and ^{132}Sn, the main regions of interest for this study. Knowledge of the properties of nuclides beyond the nuclear shell closures in exotic nuclei is very important for a fundamental understanding of nuclear structure or to determine the path of the r-process, responsible for the nucleosynthesis of about half of the heavy elements [198, 199]. In these regions, Zn, Ga, Cu, and Cd isotopes are preferred since they have the most appropriate release

properties for the target materials currently used at ISOLDE. In this study, focus is given to zinc and cadmium isotopes, namely ^{80}Zn and ^{130}Cd, which lie in the neutron shell closures N=50 and N=82, respectively.

The first objective of this work was to calculate in-target yields of neutron-rich isotopes of zinc and cadmium using FLUKA, after a detailed implementation of the geometry and constituent materials of the production layout, including the target-ion source system and surrounding structures. This was done for two different configurations currently used at ISOLDE, shown in Fig. 7.2 (as implemented in FLUKA):

- In the first configuration (left), the 1.4 GeV proton beam hits a UC_x target, producing, by fission, spallation and fragmentation reactions, a large variety of radioactive products, to be ionized, mass-separated and accelerated at a later stage;
- In the second configuration (right), the proton beam hits a solid tungsten converter, generating intense neutron fluences through spallation processes. These neutrons induce fission in the UC_x target, placed close to the spallation target, generating the desired radioactive products.

As stated before, the converter configuration produces ion beams with less neutron-deficient contaminants, but with reduced intensities when compared to the direct configuration.

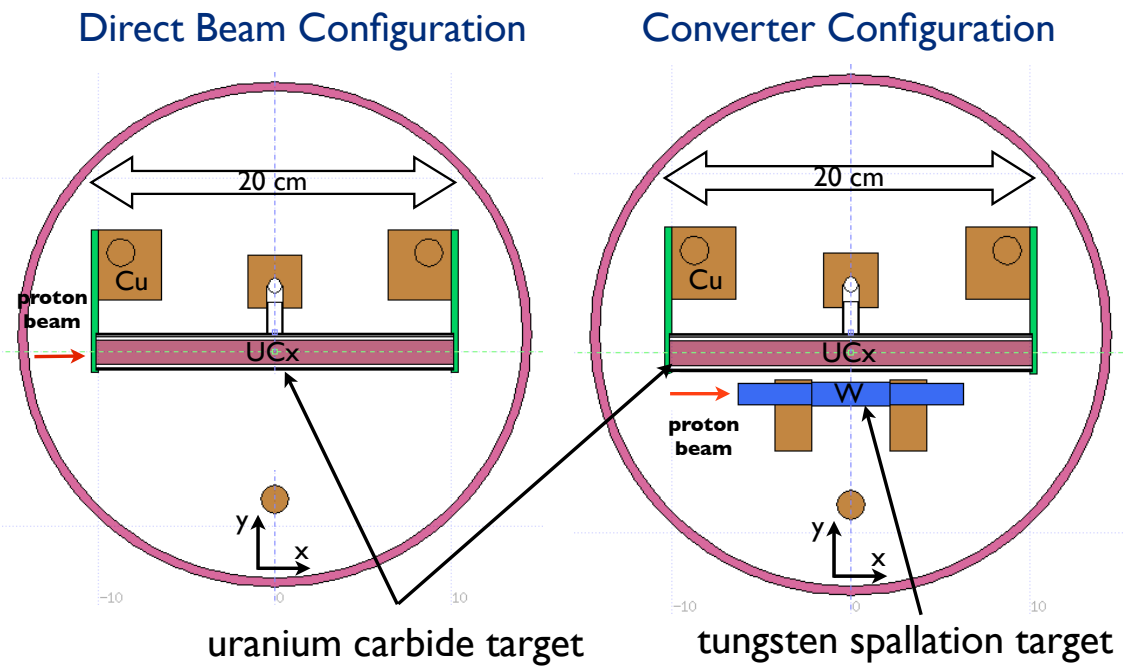

Figure 7.2: Direct beam configuration (left) and converter configuration (right) of the ISOLDE target system.

The uranium carbide target is 20 cm long and has a radius of 0.7 cm (approximate volume of 31

cm^3), while the tungsten converter is 12.5 cm long and has a 0.6 cm radius. The UC_x target is composed of several pellets, each made of depleted uranium carbide phases dispersed in a matrix of graphite, packed tightly inside a tantalum container. For the simulations the fissile material was described as approximately homogeneous, with a density of 3.5 g/cm^3 (average density of the real target). A radial Gaussian distribution with σ=3.5 mm was assumed for the proton beam, to match the experimental conditions.

After validation of the computational yields against experimental data, an optimisation of the target system layout was carried out to increase the production of the neutron-rich isotopes ^{80}Zn and ^{130}Cd while reducing the contamination by the respective neutron-deficient isobars, ^{80}Rb and ^{130}Cs.

7.3 Results and Discussion

7.3.1 Comparison Between Experimental and Computational Yields

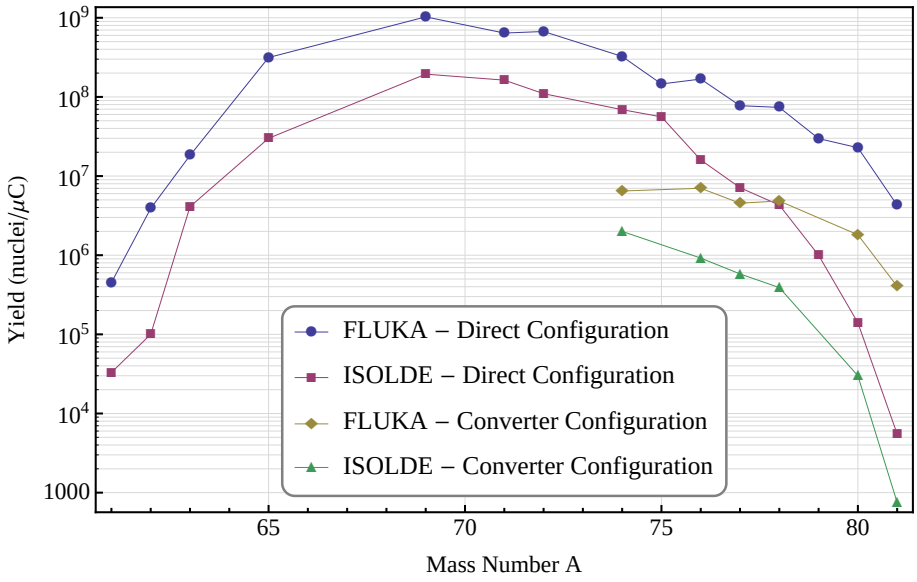

Figure 7.3: Comparison between computational (FLUKA) and experimental (ISOLDE) yields (nuclei/μC) for several zinc isotopes, for both direct and converter configurations.

The comparison between the computational yields calculated with FLUKA and the yields obtained experimentally at ISOLDE, for all zinc isotopes for which there is experimental data available (from A=61 to A=81) is displayed in Fig. 7.3. The experimental results are always lower than the computational results, by approximately one order of magnitude for the isotopes up to mass number 77. For the most exotic isotopes, with mass numbers 78, 79, 80 and 81, the deviation between calculated and measured yields becomes even greater.

These deviations were expected, since FLUKA computes the in-target yields of zinc isotopes, while the experimental yields are obtained after the nuclei formed in the target diffuse out of the target and effuse to the ion source, are ionized, mass-separated and transported to the detection system, each of these processes having an associated efficiency, as stated in Eq. 7.1. This also explains the fact that the largest deviations correspond to the most exotic nuclides, since these have very short half-lives and, therefore, a large fraction of them decay before reaching the detection system.

The in-target yields computed with FLUKA can be compared with the experimental yields measured at ISOLDE by multiplying the computational results with known efficiencies. However, it is difficult to assess these efficiencies experimentally. As a first step in this analysis, an alternative approach was followed, that consisted in comparing the ratios

$$ISOLDE_{direct}/ISOLDE_{converter}$$
$$FLUKA_{direct}/FLUKA_{converter}$$

instead, with:

- $ISOLDE_{direct}$ – RIB intensity measured at ISOLDE, direct beam configuration;
- $ISOLDE_{converter}$ – RIB intensity measured at ISOLDE, converter configuration;
- $FLUKA_{direct}$ – in-target production calculated with FLUKA, direct beam configuration;
- $FLUKA_{converter}$ – in-target production calculated with FLUKA, converter configuration.

When these ratios are computed, the efficiencies, which are (as a first approximation) the same for both direct and converter configurations, cancel-out, and the comparison is made between the ratios of the in-target yields obtained with FLUKA and the ratios of the yields obtained experimentally. The comparison between these ratios is shown in Fig. 7.4 (top), for the mass numbers for which there is data available for both configurations. The relative deviations between the two curves are shown in Fig. 7.4 (bottom). For mass numbers 74, 76, 77, 78 and 81 the relative deviation between the two curves is of approximately 40%. ^{80}Zn is the exception, exhibiting a relative deviation of 170%. These relative deviations have to be taken and understood in the appropriate context, considering that benchmarks of this kind are always difficult, and even more in this case, due to the difficulties imposed by the (so far) neglected efficiencies.

The next step consisted in the direct comparison between the computational yields and the experimental ones, by combining the computational yields with the efficiencies of Eq. 7.1, obtained experimentally. Fig. 7.5 shows the release efficiency curves measured at the ISOLDE tape station [200] for zinc isotopes as a function of their half-lives, for both direct and converter configurations. The release efficiencies are very close to unity for longer-lived isotopes, from ^{61}Zn to ^{74}Zn. As expected, from ^{74}Zn to ^{81}Zn the efficiencies decrease from 1 to 0.48, since more nuclei decay

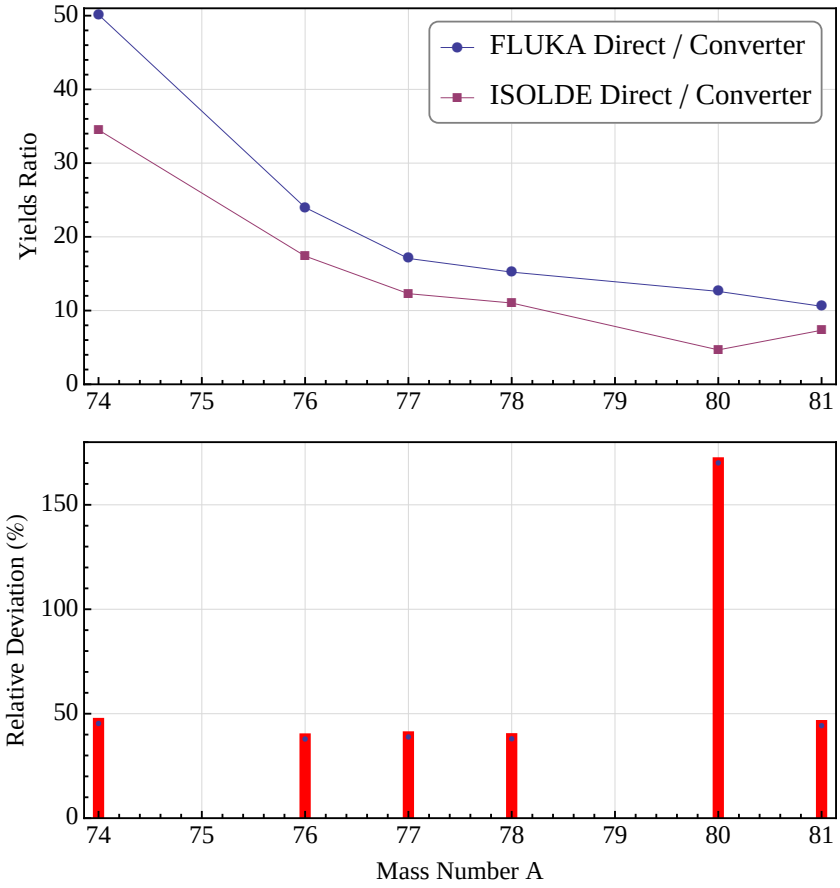

Figure 7.4: Top - ratio between direct and converter configuration yields, for computational (FLUKA) and experimental (ISOLDE) yield ratios. Bottom - relative deviations between computational and experimental yield ratios.

during the diffusion process.

Fig. 7.6 shows the effect of multiplying the computational yields by the release efficiencies. It is seen that the release efficiencies only affect the yields of neutron-rich nuclei, as expected from the previous discussion. Two additional curves are shown in Fig. 7.6, each obtained by multiplying the simulation yields by the release efficiencies and an ionisation efficiency. Since no accurate experimental value for the ionisation efficiency was available, two reasonable values were tested: 5% and 10%. Although an efficiency of the order of 10% seems to be the most appropriate for matching the computational and experimental results for most nuclides, it can be seen that there is still a big discrepancy for the neutron-rich isotopes ^{79}Zn, ^{80}Zn and ^{81}Zn. Since the ionisation efficiency is isotope-independent, these discrepancies can be attributed to inaccuracies in the release efficiencies, cross sections or experimental results.

The next step was to check the cross sections. To this effect, two codes were used: TALYS and ABRABLA (described in Chapter 3). TALYS was used to compute cross sections for energies up to 200 MeV and ABRABLA to calculate cross sections from 200 MeV to 2 GeV. FLUKA was

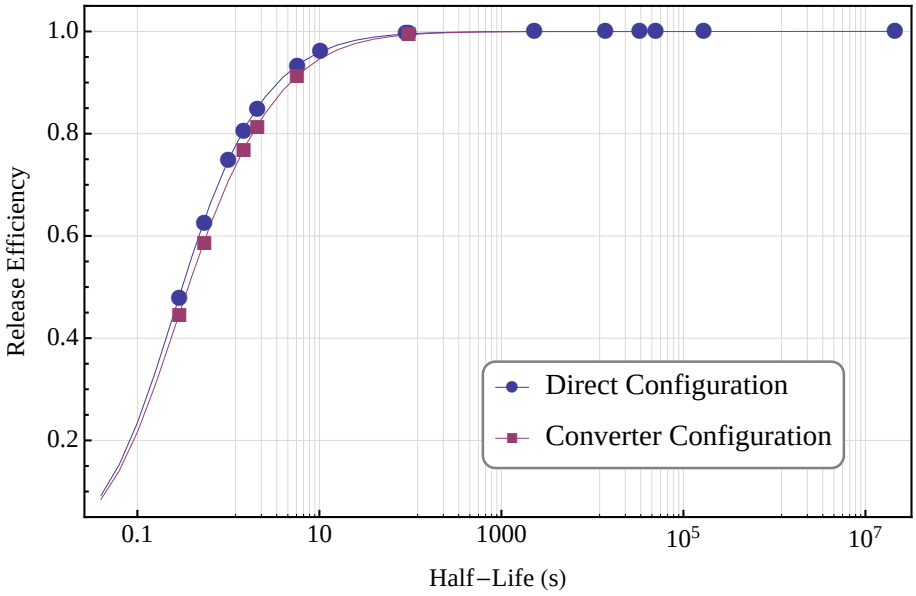

Figure 7.5: Release efficiency curves (direct and converter configurations) for zinc isotopes, as a function of the isotope half-lives.

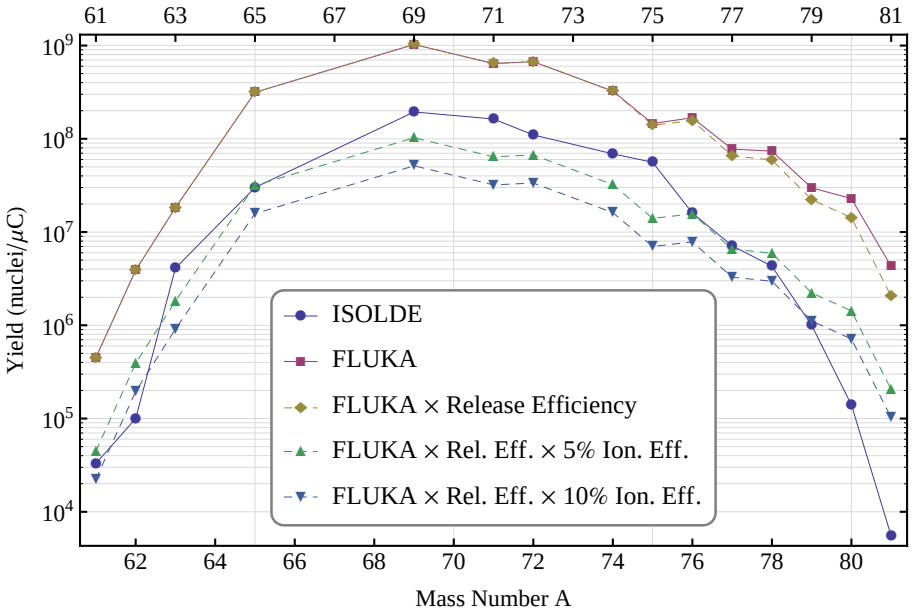

Figure 7.6: Comparison between simulated and experimental yields of Zinc isotopes for the direct configuration. The computational results are multiplied by the release efficiencies, and two ionisation efficiencies are tested.

used to obtain the proton and neutron track-length fluence spectra in the UC_x target (average fluences over the target volume), and these fluences were later multiplied by the cross-sections and number of target atoms, to obtain the in-target yields.

Figs. 7.7 and 7.8 show the comparison between the yields obtained with FLUKA and the yields

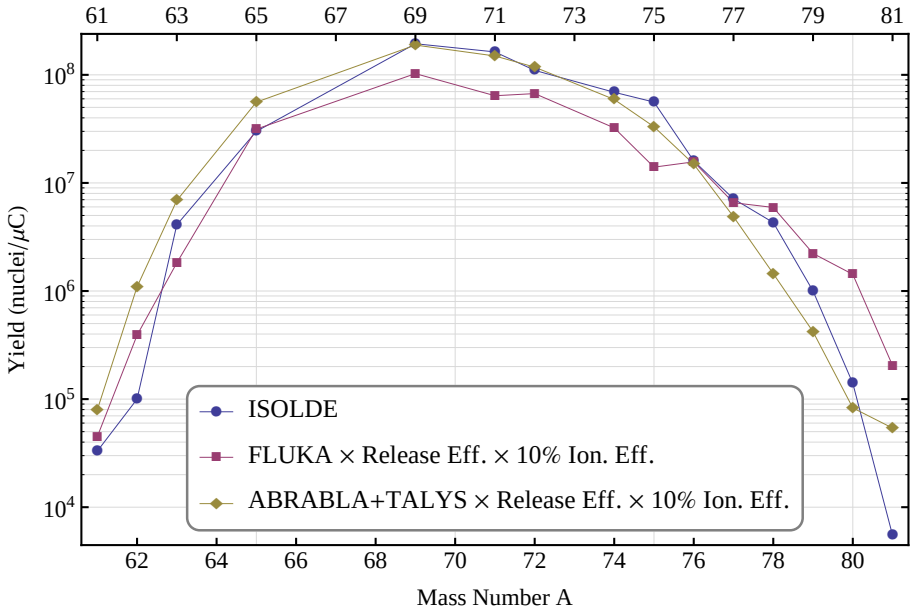

Figure 7.7: Comparison between Zinc isotope yields obtained with FLUKA and ABRABLA + TALYS cross sections, for the direct configuration.

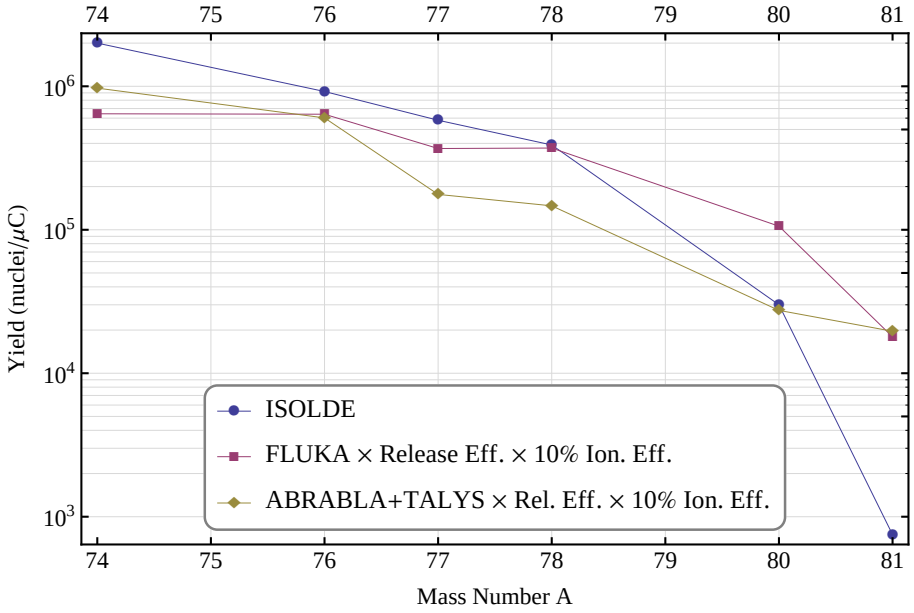

Figure 7.8: Comparison between Zinc isotope yields obtained with FLUKA and ABRABLA + TALYS cross sections, for the converter configuration.

obtained with the TALYS + ABRABLA combination, for direct and converter configurations, respectively. The results are multiplied by the release efficiencies and an assumed ionisation efficiency of 10%, and plotted against the experimental data. For most isotopes, the yields obtained with TALYS + ABRABLA cross sections are closer to the experimental yields than the ones obtained with FLUKA. In spite of this better agreement, there are still sizable discrepancies

for ^{62}Zn and ^{81}Zn. These discrepancies might be related to uncertainties in the production cross sections and yield measurements.

Since a better agreement was achieved with the ABRABLA + TALYS cross-sections, these were chosen for most of the calculations presented in this chapter. Nevertheless, all calculations were also done using FLUKA cross sections, and these results will be shown or mentioned when appropriate.

To further determine an ionisation efficiency that better matches the experimental and computational results, the sum of the squared relative differences between the experimental and calculated yields was minimized, with the ionisation efficiency as the free parameter [201]. For this calculation, the results for ^{62}Zn and ^{81}Zn were excluded, due to the already mentioned discrepancies. An ionisation efficiency of 8.1% was thus determined, close to the efficiency values obtained in typical "offline" efficiency measurements. Fig. 7.9 shows the relative deviations between computational and experimental results for direct and converter configurations with this ionisation efficiency. In the direct configuration there is a maximum in the ratio experimental/computational results of 3.7, for ^{78}Zn. For ^{79}Zn this ratio has a value of 2.9, and for the remaining isotopes the experimental and computational results differ by less than a factor of 2. In the converter configuration the ratio experimental/computational reaches 4.1 for ^{77}Zn , 3.3 for ^{78}Zn and 2.5 for ^{74}Zn (below 2 for the remaining isotopes). For the excluded isotopes, ^{62}Zn and ^{81}Zn, these ratios would be 8.7 and 7.8, respectively.

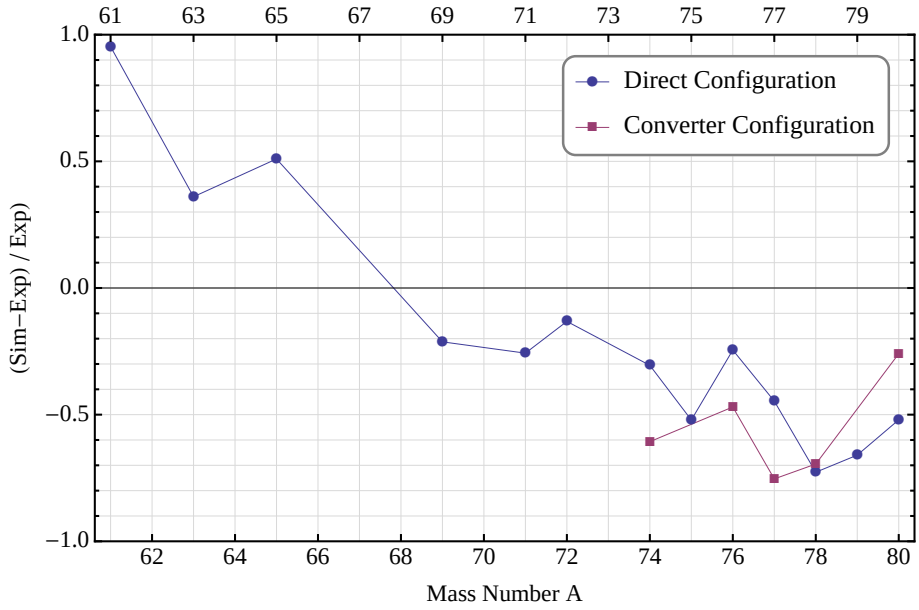

Figure 7.9: Relative deviations between computational and experimental yields – direct and converter configurations.

Even though there are still significant deviations between the experimental and computational results for some isotopes, this can be considered an acceptable benchmark, if the difficulties

imposed by the uncertainties in the efficiencies, cross sections and experimental yields are taken into account.

7.4 Optimisation Studies

7.4.1 Particle Fluences and Isotope Yields in the UC_x Target – Standard Converter Configuration

As previously stated, the main objective of the optimisation studies described in this chapter was to propose a new geometry for the converter configuration of the ISOLDE target system, that maximised the in-target production rates of the neutron-rich isotopes ^{80}Zn and ^{130}Cd (and beyond, towards more neutron-rich nuclides, if possible) while reducing as much as possible the production rates of the neutron-deficient contaminants ^{80}Rb and ^{130}Cs. The first step consisted in calculating the production rates of several isotopes of zinc, rubidium, cadmium and cesium for the standard converter configuration. The results are represented in Fig. 7.10. There are

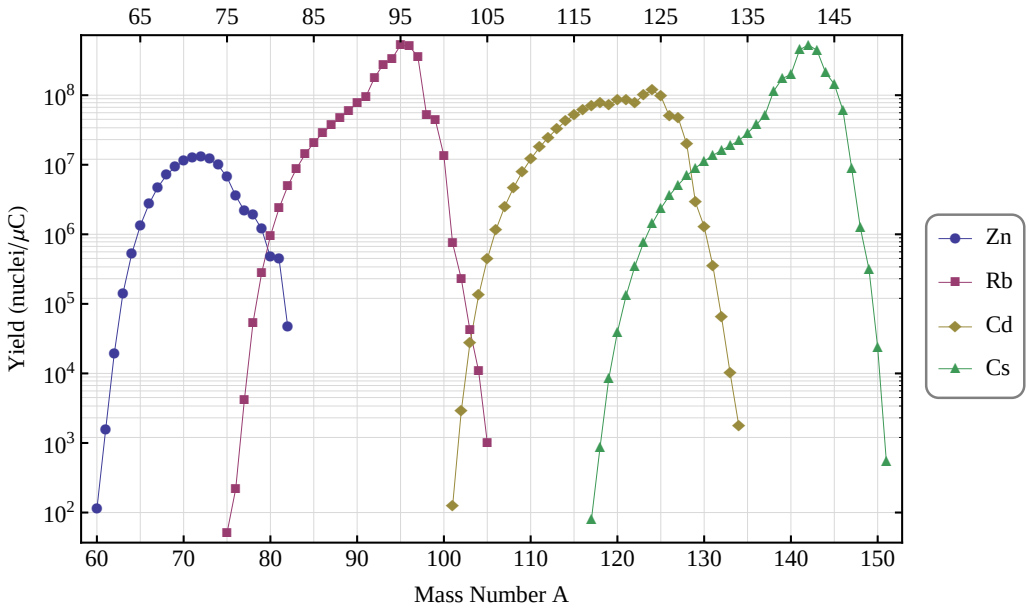

Figure 7.10: In-target production rates (nuclei/μC) of several isotopes of zinc, rubidium, cadmium and cesium (standard converter configuration).

4.69×10^5 nuclei of ^{80}Zn formed in the UC_x target for each μC of protons hitting the converter, while the production rate of ^{80}Rb is approximately the double of that value (9.5×10^5 nuclei/μC). For ^{130}Cd, there are 1.3×10^6 nuclei/μC formed in the target, against 1.1×10^7 nuclei/μC of ^{130}Cs, the neutron-deficient contaminant. For comparison, it is worth mentioning that, for the direct configuration, the ratio ^{80}Rb/^{80}Zn is 175 and the ratio ^{130}Cs/^{130}Cd is 340, which means that a great improvement in these ratios is already achieved by using the converter. In spite of

this improvement, the production rates of the contaminants in the converter configuration are higher than the production rates of the desired nuclides. For isotopes like ^{81}Zn and ^{82}Zn or ^{131}Cd and ^{132}Cd the contamination by neutron-deficient isobars is even greater. It is the objective of this work to reduce as much as possible the production of the mentioned contaminants while maximising the production of the desired species.

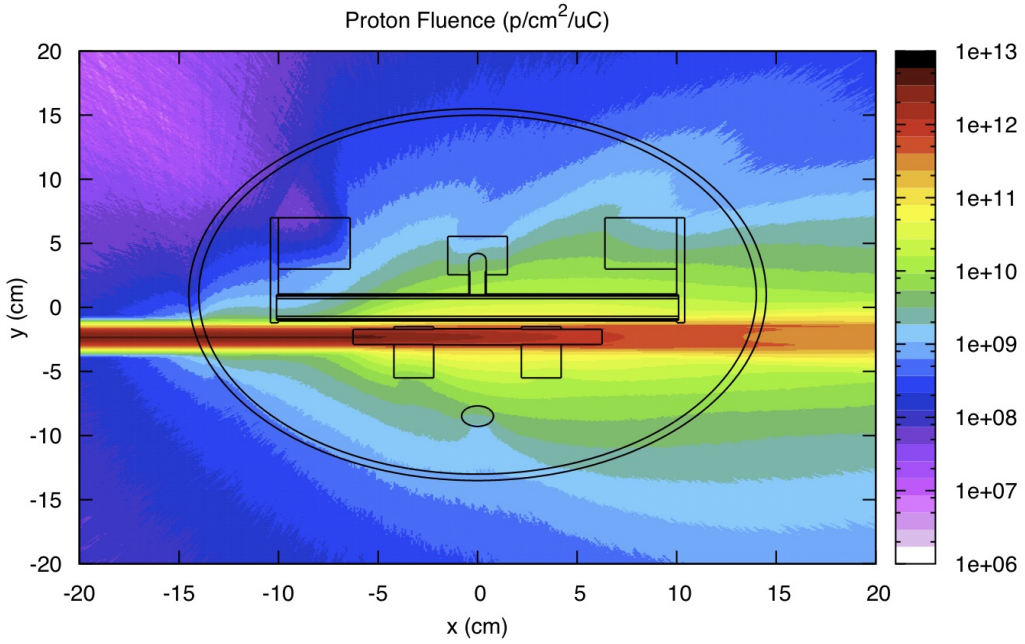

Figure 7.11: Proton fluence map ($1/\mathrm{cm}^2/\mu\mathrm{C}$) obtained with FLUKA (converter configuration).

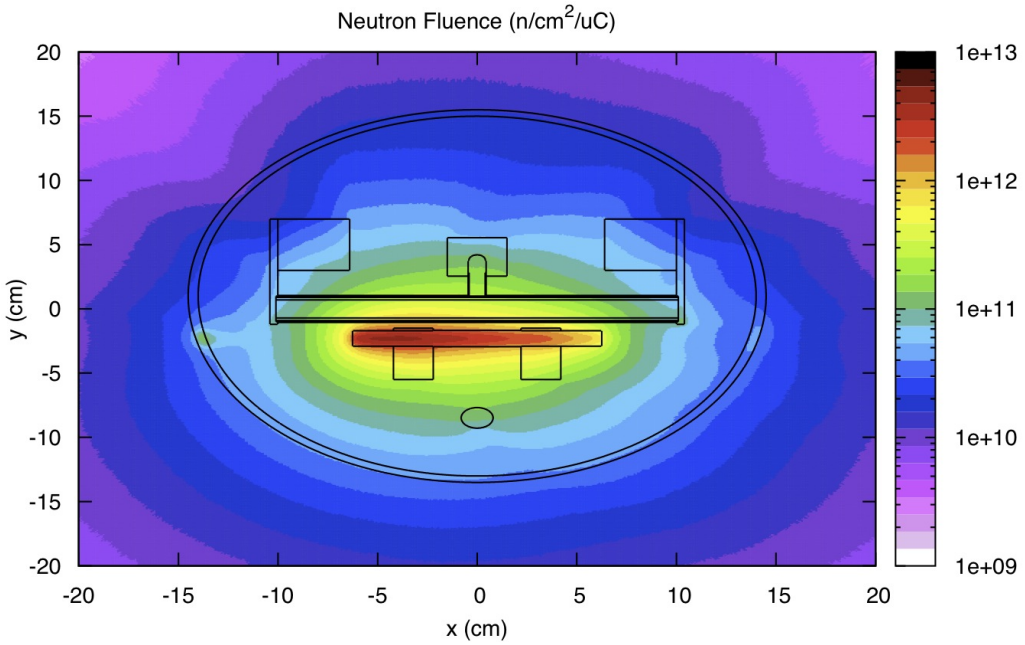

Figure 7.12: Neutron fluence map ($1/\mathrm{cm}^2/\mu\mathrm{C}$) obtained with FLUKA (converter configuration).

In Section 6.3 it was mentioned that the converter is used so that fission is induced by neutrons in the MeV region and not by GeV protons, thus reducing the number of neutron-deficient nuclei (contaminants) formed through spallation-fission. Figs. 7.11 and 7.12 show the proton and neutron fluence maps computed with FLUKA in the targets zone of the converter configuration. It is clearly seen that the proton fluences in the UC_x target are still considerable, especially in the rightmost part of the target. These are very energetic protons that were scattered off the converter, spreading with an approximate "conical shape" in the direction of incidence of the proton beam. The spallation neutrons spread with an approximate isotropic distribution around the converter.

7.4.2 Testing Different Converter and UC_x Target Dimensions

Fig. 7.13 shows the neutron and proton differential fluences as a function of energy in the UC_x target. It confirms that, even though a converter is being used, a significant amount of protons is still reaching the uranium carbide target, specially in the GeV region. The optimisation studies were undertaken with the goal of minimising the indirect proton fluences in the GeV region while maximising the neutron fluences at lower energies.

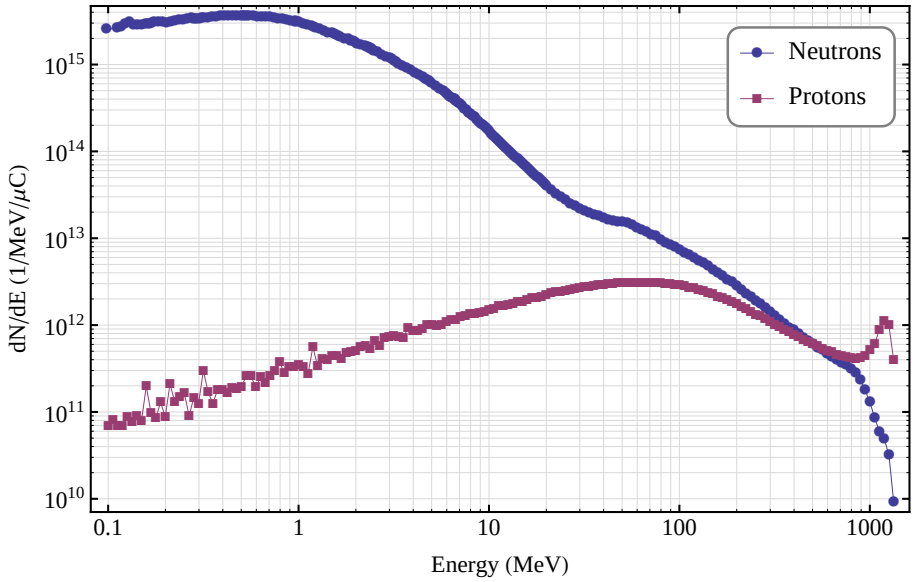

Figure 7.13: Neutron and proton differential fluences (1/MeV/μC) entering the UC_x target, for a 1.4 GeV proton beam on the converter configuration.

7.4.2.1 Optimisation of the UC_x Target Length

The first investigation on the target geometry consisted in the assessment of the impact of the UC_x target length on the proton and neutron fluences. Since the protons spread out with an ap-

proximate "conical shape" around the direction of incidence of the proton beam and the neutrons spread roughly isotropically around the converter (as shown in Figs. 7.11 and 7.12), a logical first step to reduce the ratio protons/neutrons that reach the target is to reduce the target length, to remove the region exposed to higher proton fluences. Four lengths were tested: 20 cm (present layout), 10 cm, 8 cm and 5 cm. The influence on the proton and neutron differential fluences can be seen in Fig. 7.14. It is clear that reducing the length has more effect on the proton fluences at high energies than in neutron (and proton) fluences at lower energies. There is a significant decrease in the proton fluence in the GeV region when the target length is reduced to 10 cm, half of its original length, while the neutron fluences at low energies are much less affected.

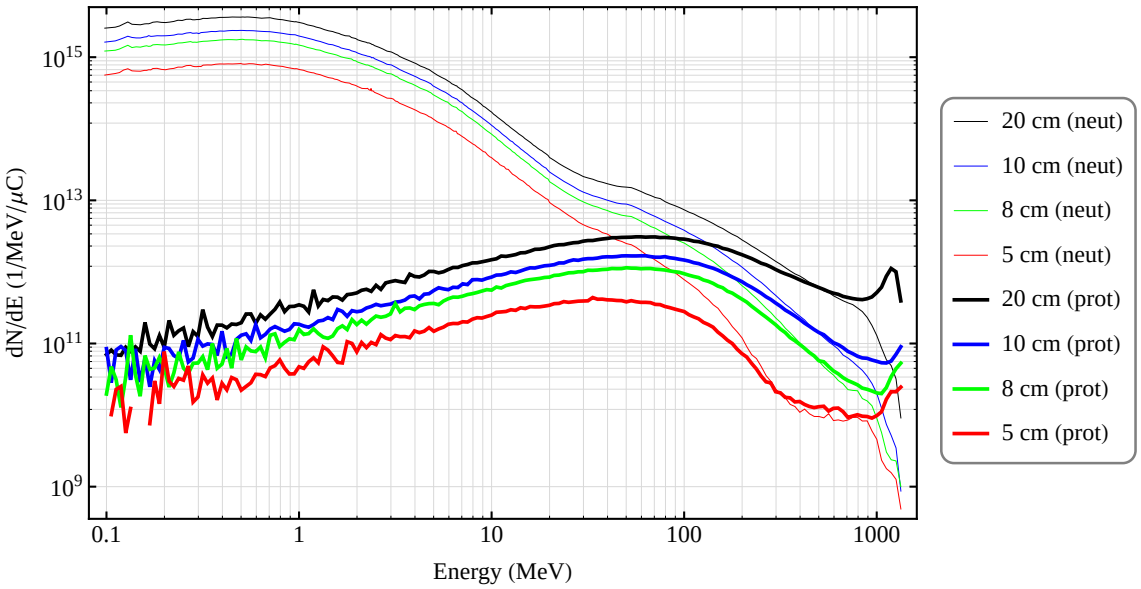

Figure 7.14: Neutron and proton differential fluences (1/MeV/μC) in the UC_x target, for UC_x target lengths ranging from the default value of 20 cm to 5 cm.

7.4.2.2 Optimisation of the Tungsten Converter Radius

Different radii of the tungsten converter were then investigated. Tungsten is almost transparent to neutrons and, as it is a heavy material ($Z = 74$), it is efficient to stop protons. A thicker converter will have several advantages, since it will stop more protons while being a brighter neutron source. To estimate the effect of the converter thickness in the proton and neutron fluences reaching the UC_x target, four radii were tested: 0.3 cm, 0.6 cm (present layout) 1.0 cm and 1.4 cm (Fig. 7.15). Increasing the converter radius to 1.4 cm is indeed a good option to reduce the fluence of energetic protons reaching the UC_x target. The neutron fluences are little affected, as expected, and are even increased for lower energies, relative to the neutron fluences for the standard 0.6 cm target. The neutron fluences would be optimised for a 1.0 cm radius, since it would have a higher neutron production than the 0.6 cm target and less attenuation than the

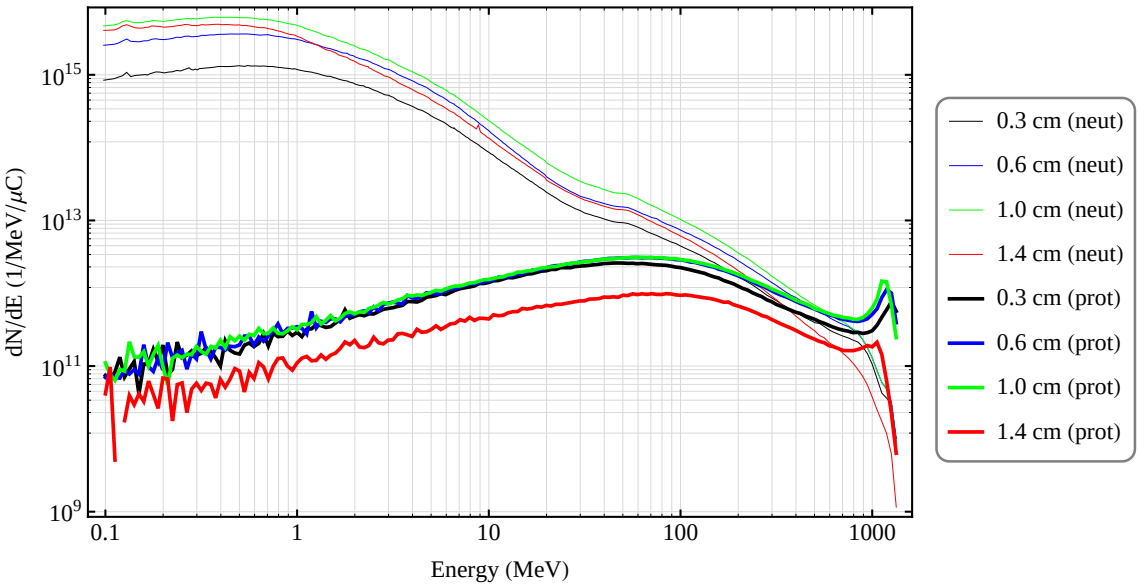

Figure 7.15: Neutron and proton differential fluences (1/MeV/μC) in the UC_x target, for converter radii ranging from 0.3 cm (0.6 cm is the default value) to 1.4 cm.

1.4 cm target, but the fluences of energetic protons would not decrease, which was the main objective of these optimisation studies.

7.4.3 First Optimised Configuration

After evaluating the effect of UC_x target length and W converter radius on the neutron and proton fluences in the UC_x target, several combinations were tested, to reduce as much as possible the fluence of energetic protons in the target. It was found that the best compromise would be a 10 cm long UC_x target and a converter with a 1.4 cm radius. An additional diagonal cut was made to the uranium carbide target, to remove the region with the highest proton fluences. The result can be seen in Fig. 7.16. To compensate for the loss of ^{238}U resulting from the cuts in the target dimensions, the UC_x target radius was also increased from 0.7 cm to 1.5 cm, approximately doubling the mass of uranium of the standard configuration. The effect of this optimisation in the neutron and proton fluences reaching the UC_x target can be seen in Fig. 7.17. Clearly, there is a drastic reduction in the proton fluences, especially for energies in the GeV region, while the neutron fluences at lower energies are less affected. Having increased the number of ^{238}U atoms exposed to these neutrons, it could be anticipated that the yields of the neutron-rich isotopes would be much less affected than the yields of neutron-deficient contaminants.

Fig. 7.18 shows the yields of zinc and rubidium isotopes in the UC_x target before and after optimisation. The ratios between optimised and default yields are presented in Fig. 7.19, along with the improvement in the zinc/rubidium ratio. The yield of ^{80}Zn, one of the reference nuclides

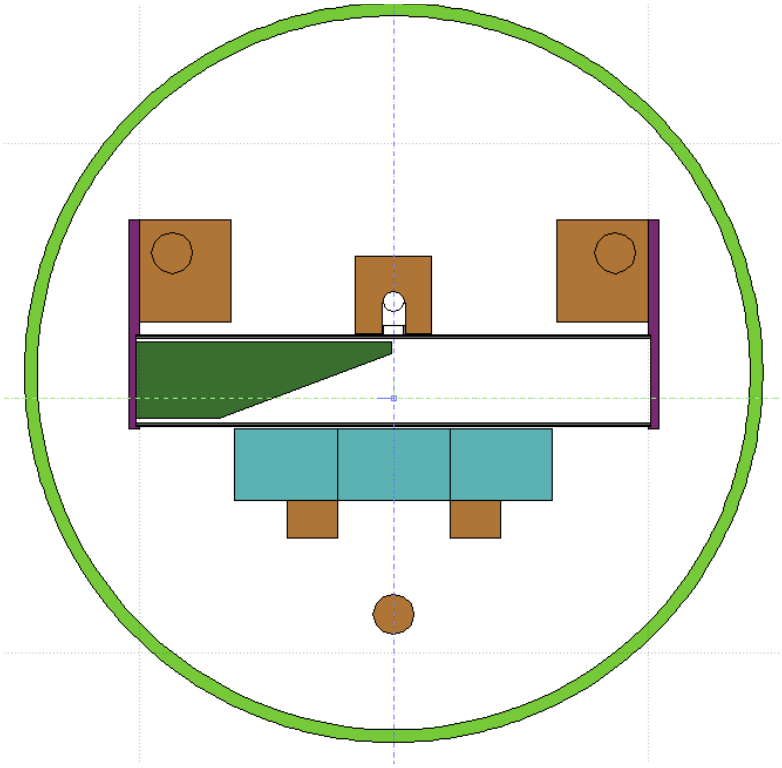

Figure 7.16: Optimised configuration (FLUKA).

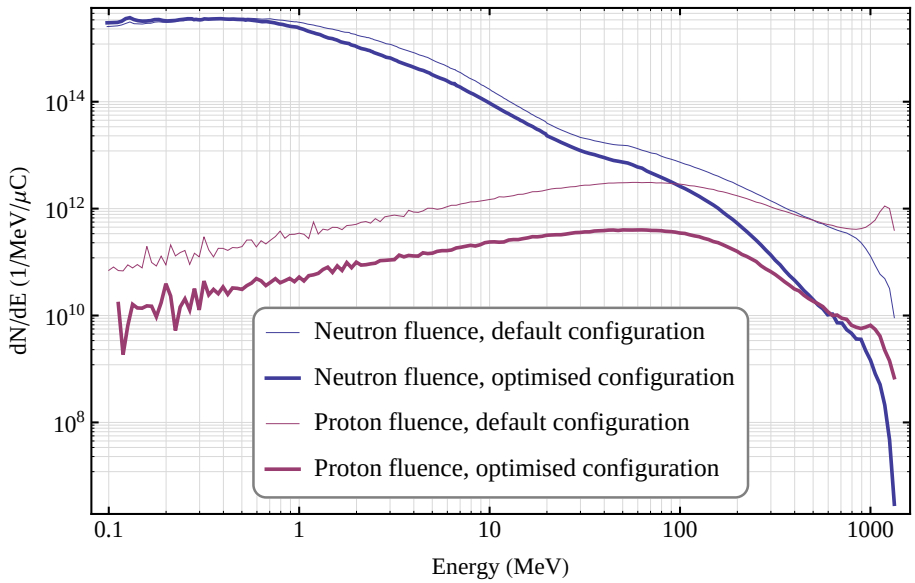

Figure 7.17: Neutron and proton differential fluences (1/MeV/μC) in the UC_x target, for the optimised configuration.

for this work, is reduced to 54% of its original value, while the yield of the contaminant ^{80}Rb is decreased to 1.4% of its value in the current configuration. Overall, the ^{80}Zn/^{80}Rb ratio is

increased by a factor of 39, a result that gives good indications that it is possible to produce purer and more intense beams of neutron-rich zinc isotopes with simple changes in the targets layout. This ratio will of course be maintained in the radioactive ion beam, as can be seen in Eq. 7.1.

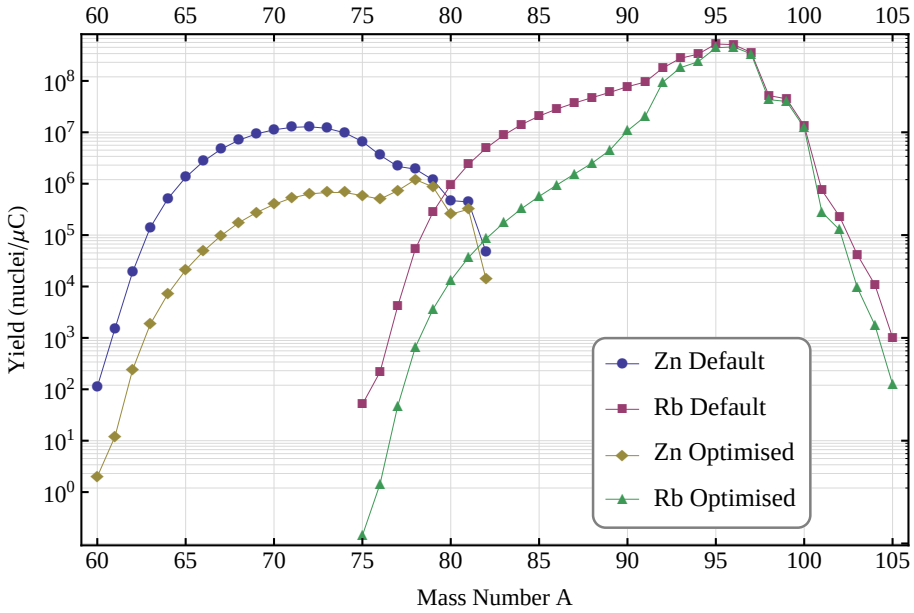

Figure 7.18: Zinc and rubidium yields (nuclei/ μC) before and after optimisation.

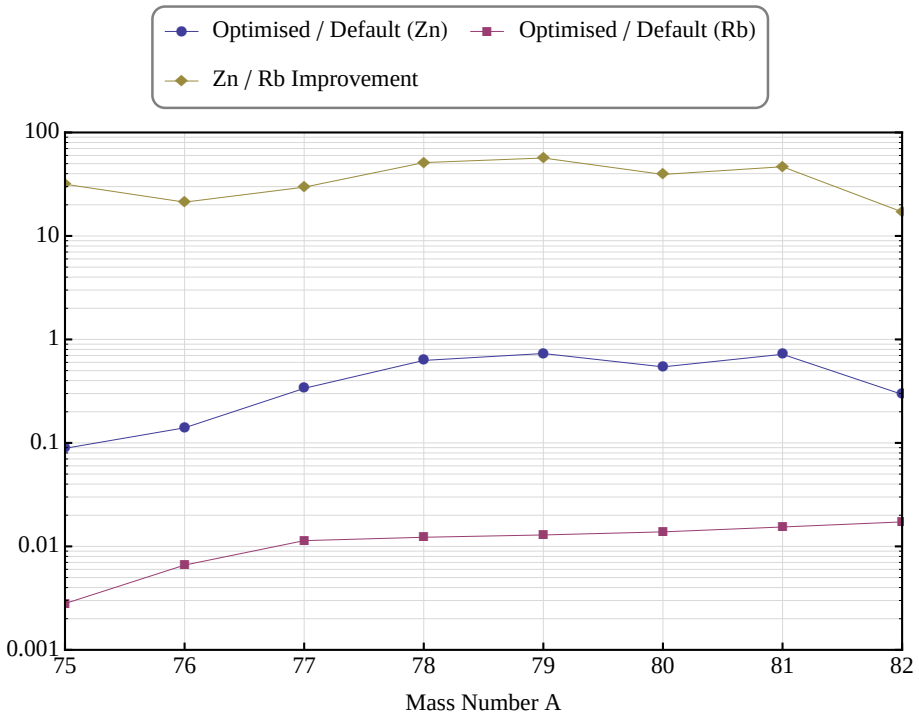

Figure 7.19: Improvement in the zinc/rubidium ratios.

The same results are presented in Figs. 7.20 and 7.21 for cadmium and cesium isotopes. The yield of ^{130}Cd is reduced by 40% while the yield of ^{130}Cs is reduced to 3.3% of its original value. The ratio ^{130}Cd/^{130}Cs is increased 18 times after optimisation, which also represents an important improvement.

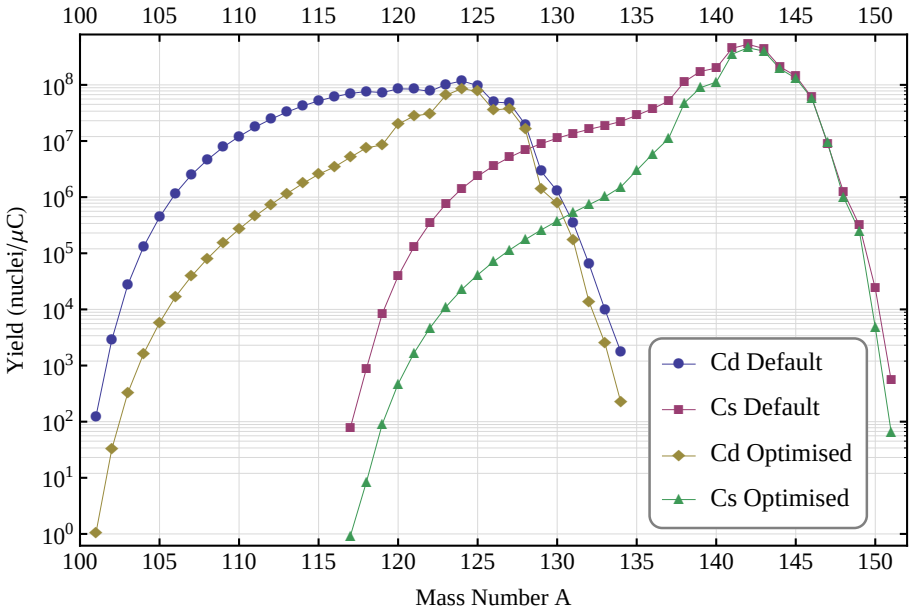

Figure 7.20: Cadmium and cesium yields (nuclei/ μC) before and after optimisation.

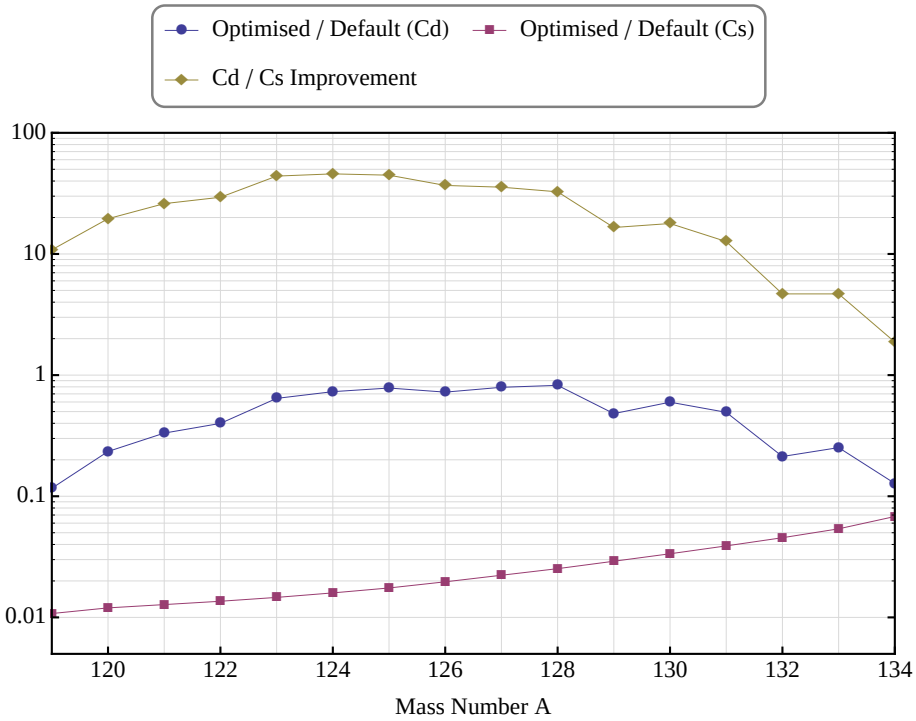

Figure 7.21: Improvement in the cadmium/cesium ratios.

Although the proposed optimisation looks promising, there is a possible drawback, related to the release efficiency of the produced isotopes from the target. The UC_x target radius was increased to compensate for the reduction in target length, and the result was an increased target volume in the proposed configuration. Therefore, the release efficiency will probably be reduced, affecting the intensity of the final RIB.

7.4.4 Further Optimisations – UC_x target concentric to W converter

Fig. 7.22 shows two perpendicular planes of another possible configuration for the ISOLDE targets, based on the previous optimisation. The UC_x target in this configuration is thinner, to enhance the release efficiency, but now it encloses the W converter completely (like a solid of revolution made with a section cut from the previous target). With this design, it is possible to increase the mass of ^{238}U with a thinner target, taking advantage of intercepting more neutrons than in the previous configuration. To keep the design realistic, the assumed UC_x density was

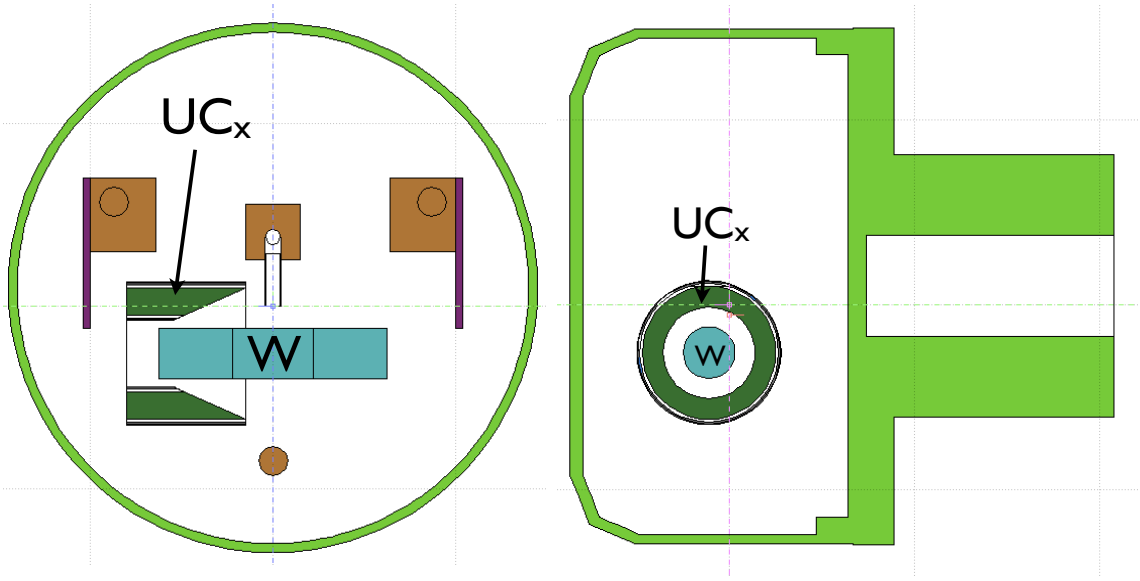

Figure 7.22: Perpendicular planes of an alternative configuration for the UC_x target and W converter, with the UC_x target concentric with the converter and surrounding it completely.

decreased, from an initial value of 3.5 g/cm^3 to 2 g/cm^3, since with such an exotic target it will be difficult in practice to accommodate the UC_x pellets as tightly as in the current configuration. This means that the UC_x target density will be reduced to 57% of its current value, a reduction that was assumed to account for possible compromises which may be required in the construction of the target. In this way, the uranium mass is approximately 2.3 times higher than in the original configuration (for a target with approximately 4 times the volume of the initial target). The same parameters of the previous optimisation were considered for the W converter.

In this alternative configuration, the production of ^{80}Zn is increased by a factor of 2 while the

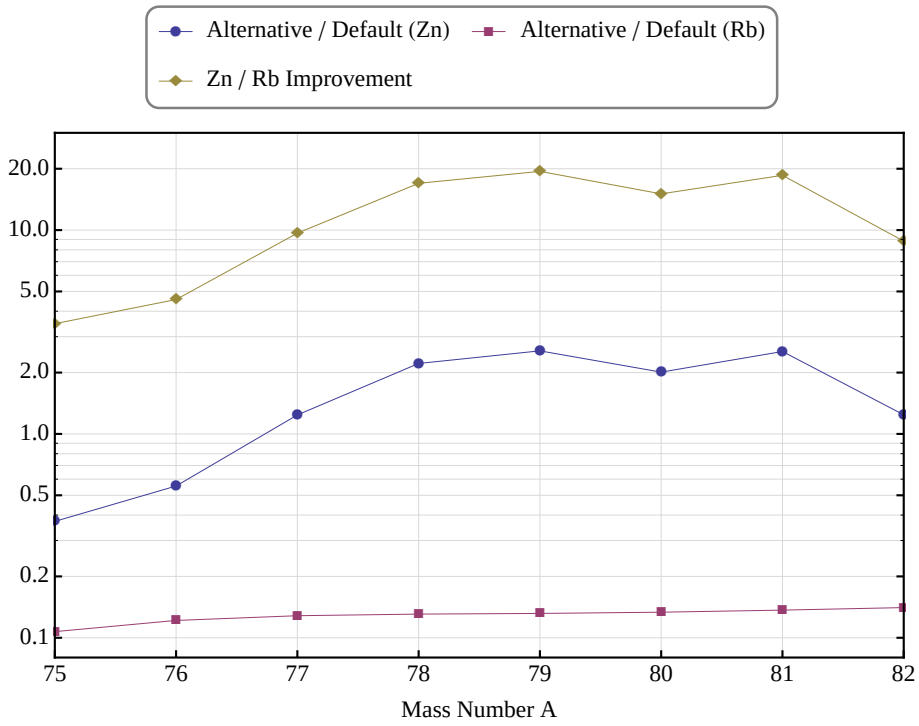

Figure 7.23: Improvements in the ratios Zn/Rb for several isotopes, with the alternative configuration.

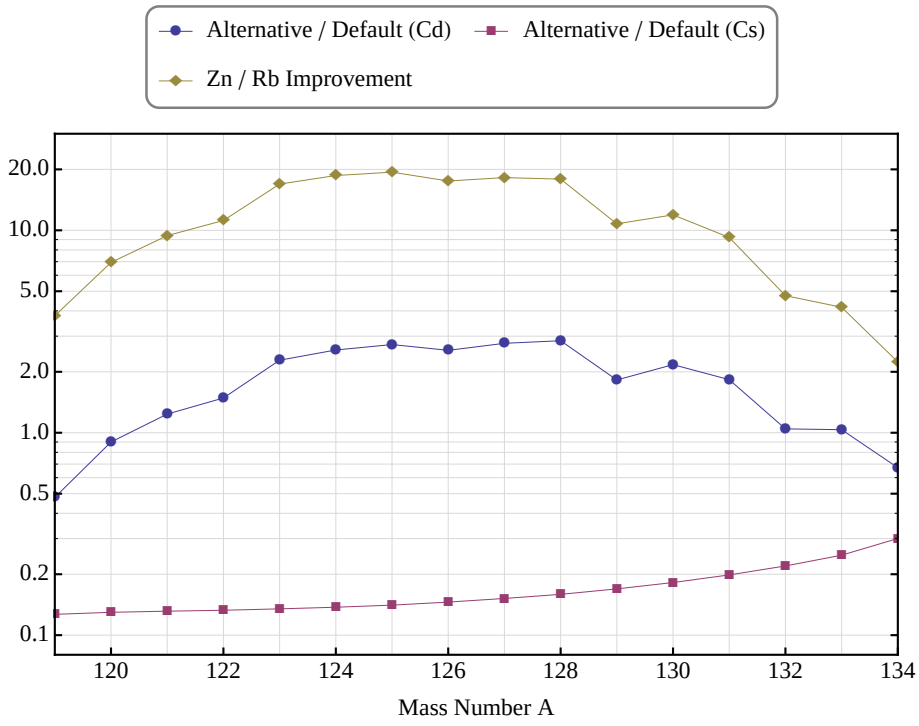

Figure 7.24: Improvements in the ratios Cd/Cs for several isotopes, with the alternative configuration.

production of ^{80}Rb is reduced to approximately 13% of the production obtained with the standard configuration (Fig. 7.23). The result is an improvement in the ^{80}Zn/^{80}Rb ratio by a factor of 15. The ratio ^{130}Cd/^{130}Cs is improved by a factor of 12, with the production of ^{130}Cd being increased by a factor of 2 (Fig. 7.24). The effect of increasing the target volume on the release efficiency, particularly important for short-lived nuclei, will only be assessed through experimental tests, which will be undertaken after a prototype is built. It is also important to notice that with this optimisation the yields on Zn and Cd are increased when compared with the current ISOLDE targets configuration, contrasting with what is predicted with the previous optimisation (even though the final ratios were higher in the previous optimisation). Furthermore, if the density can be increased (a conservative value was used, as mentioned before), the yields of Zn and Cd will be further increased in absolute value, although the relative amount of contaminants will be the same.

These calculations were also performed with FLUKA, and similar improvements in the ratios were predicted. It is interesting to see the effect of the optimisation on the whole nuclear landscape, as shown in Fig. 7.25, in which the ratios between the yields before and after optimisation are plotted, for all nuclides produced in the target (obtained with FLUKA cross sections). It

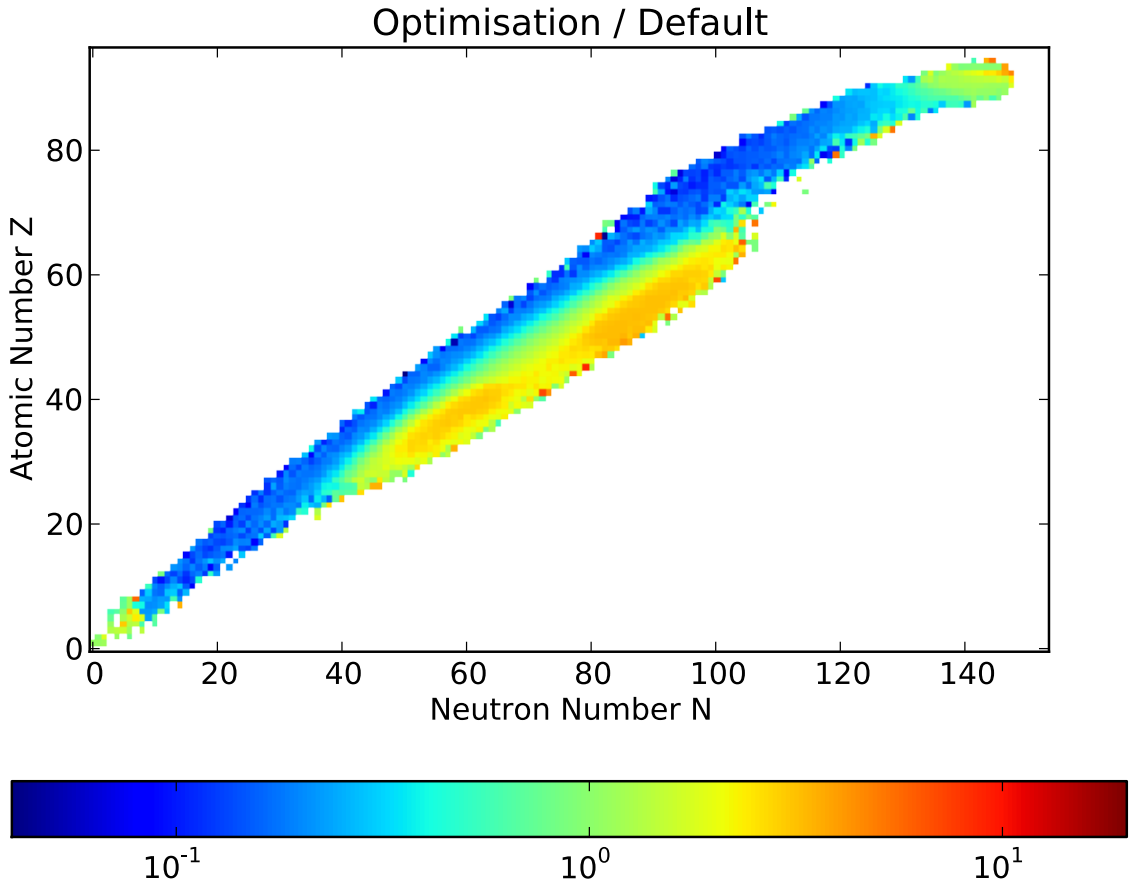

Figure 7.25: Nuclear landscape - ratio optimised yields / default yields (obtained with FLUKA).

is evident that the initial objectives are accomplished with this optimisation, according to this prediction, since a clear shift in fission towards neutron-rich species is observed. The yield improvements in the neutron-rich part of the chart vary from a factor of 2 to a factor of approximately 10. In the neutron-deficient region, the yields are lowered by a factor that ranges from 2 to approximately 50. The predicted improvements in the ratios ^{80}Zn/^{80}Rb and ^{130}Cd/^{130}Cs are similar to those predicted by ABRABLA+TALYS.

7.4.5 HIE-ISOLDE Predictions – 2 GeV Proton Beam

To assess the effect of the proposed optimisation after ISOLDE is upgraded to HIE-ISOLDE, the calculations shown in the previous section were repeated assuming a 2 GeV proton beam (Figs. 7.26 and 7.27). It is seen that for a 2 GeV proton beam the proposed optimisation can lead to a further reduction in the production of contaminants (a dramatic reduction in the production of ^{80}Rb is predicted with both ABRABLA+TALYS and FLUKA cross sections). This happens because the proton beam is more energetic and therefore it is less spread in relation to the direction of incidence (less energetic protons hit the UC_x target). This indicates that the proposed optimisation will be of increased importance for HIE-ISOLDE.

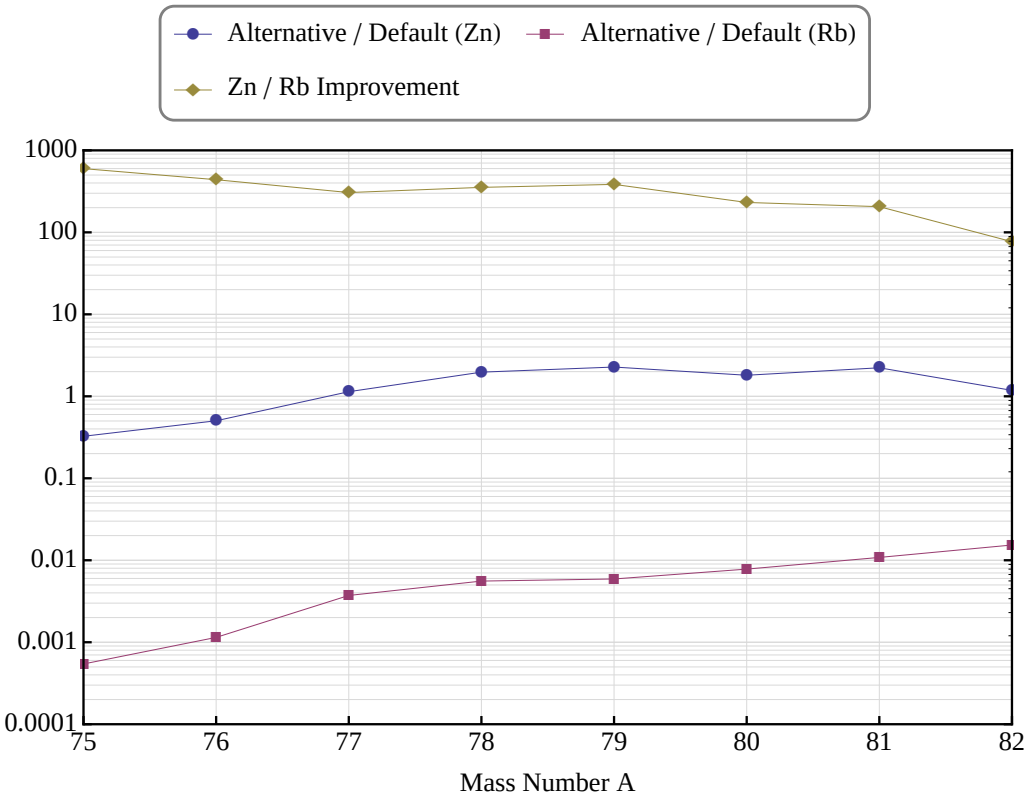

Figure 7.26: Improvements in the ratios Zn/Rb for several isotopes, with the alternative configuration and a 2 GeV proton beam.

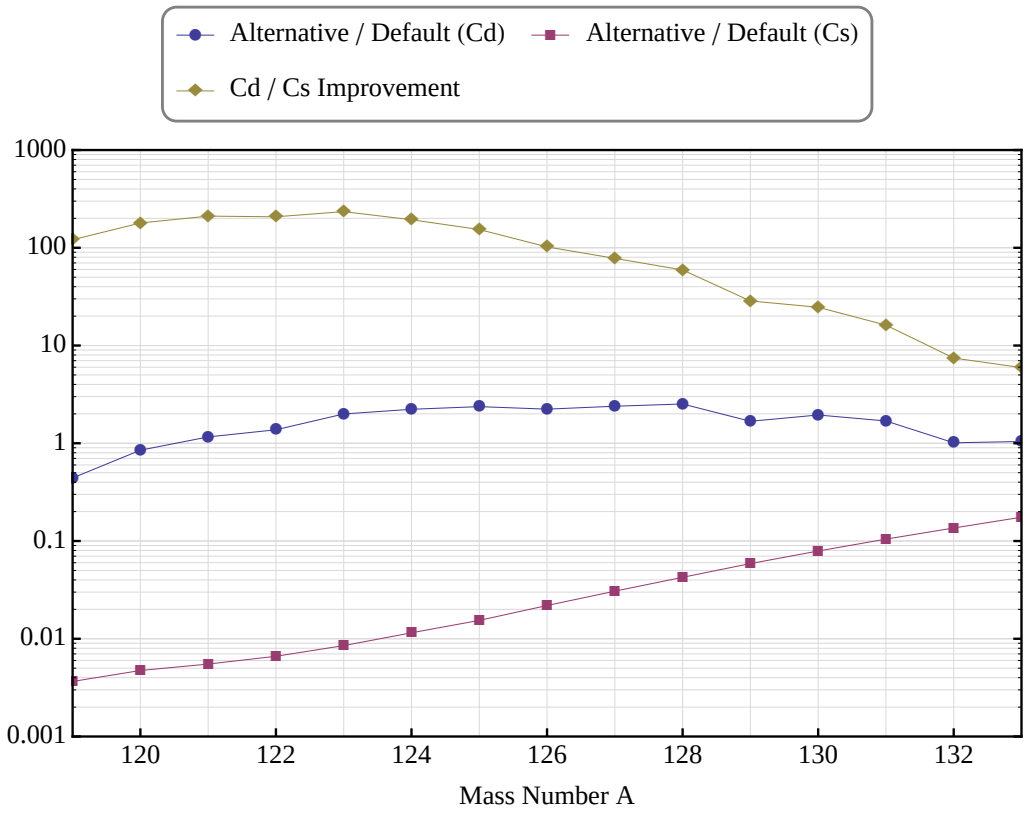

Figure 7.27: Improvements in the ratios Cd/Cs for several isotopes, with the alternative configuration and a 2 GeV proton beam.

7.5 Conclusions

In this chapter, the current configuration of the ISOLDE neutron converter and fission target system was studied in detail using the Monte Carlo code FLUKA and the cross section codes ABRABLA and TALYS, with the objective of understanding the neutronics properties of the system and optimise it for the production of neutron-rich nuclides. Using the experimental yields of the ISOLDE database, a methodology was developed to perform an optimisation of the targets layout in order to enhance the production of the neutron-rich isotopes ^{80}Zn and ^{130}Cd while reducing the production of their contaminating isobars, ^{80}Rb and ^{130}Cs.

The results reported in this study for two alternative optimised configurations indicate that the ratios of ^{80}Zn/^{80}Rb and ^{130}Cd/^{130}Cs can be increased by more than one order of magnitude with respect to the present layout, by increasing the production of ^{80}Zn and ^{130}Cd while reducing the production of ^{80}Rb and ^{130}Cs. Additional results here reported indicate that these gains will be preserved or increased as ISOLDE moves towards higher proton beam energies, as foreseen in the HIE-ISOLDE upgrade. The next chapter will deal with the experimental verification of the validity of the proposed optimisation methodologies.

Chapter 8

Prototype Configuration - Experimental Tests

A prototype target system was built at ISOLDE and tested during the week of October 22-26, 2012. This chapter presents the results obtained with the prototype configuration, after a detailed description of how this configuration evolved from the two configurations proposed in the previous chapter. Simulation and experimental results are presented and compared.

8.1 Prototype Configuration

To test the optimisation concepts of the previous chapter, a prototype target was designed and built at ISOLDE. The main objective was to build a simpler configuration that could prove the main points on which the two previous configurations were founded: that a shorter UC_x target and a thicker converter would produce more neutron-rich and less neutron-deficient fission fragments, since fission will be mainly induced by neutrons with energies in the MeV region.

The first step, therefore, was to simplify the first optimised configuration, far easier to build than the second one. Several variations of the first optimised configuration were simulated before the final prototype configuration, presented in Fig. 8.1, was reached. Fig. 8.2 shows a picture of the prototype target system before irradiation, and Fig. 8.3 shows its engineering project in 2D and 3D.

Several compromises had to be assumed to simplify the construction of the prototype target system, the most important of which was the removal of the diagonal cut in the UC_x target (see Fig. 7.16). The radius of the UC_x target pellets was reduced from 1.5 cm to 1.3 cm and the target length was set to 7.2 cm, with a density of 2.7 g/cm^3 instead of 3.5 g/cm^3. The converter radius was increased from 1.4 cm to 1.5 cm and its length was reduced from 12.5 cm to 9.7 cm. In order

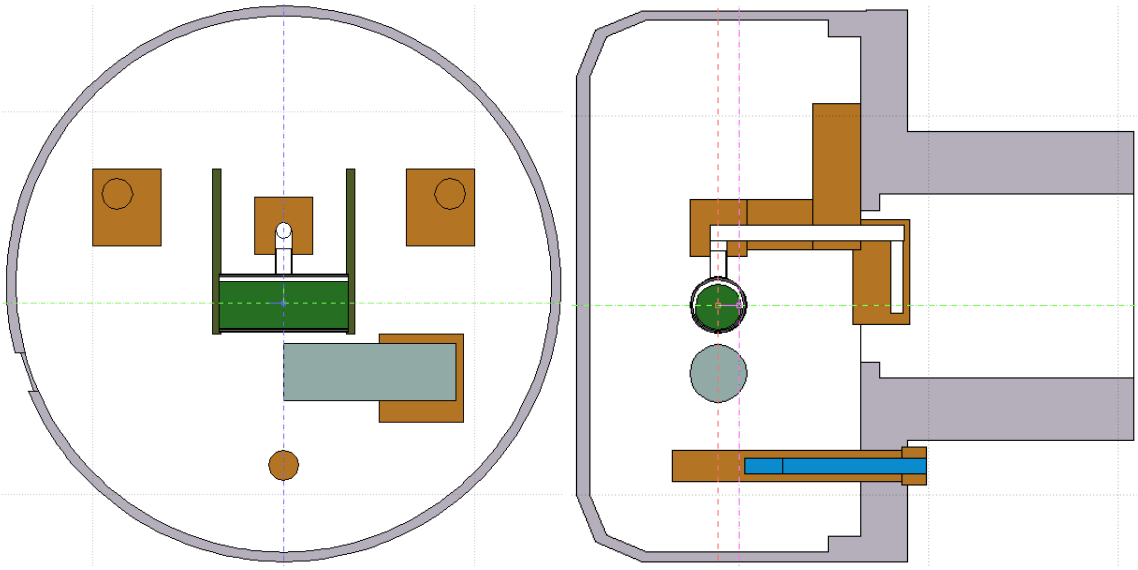

Figure 8.1: Prototype configuration, as implemented in FLUKA.

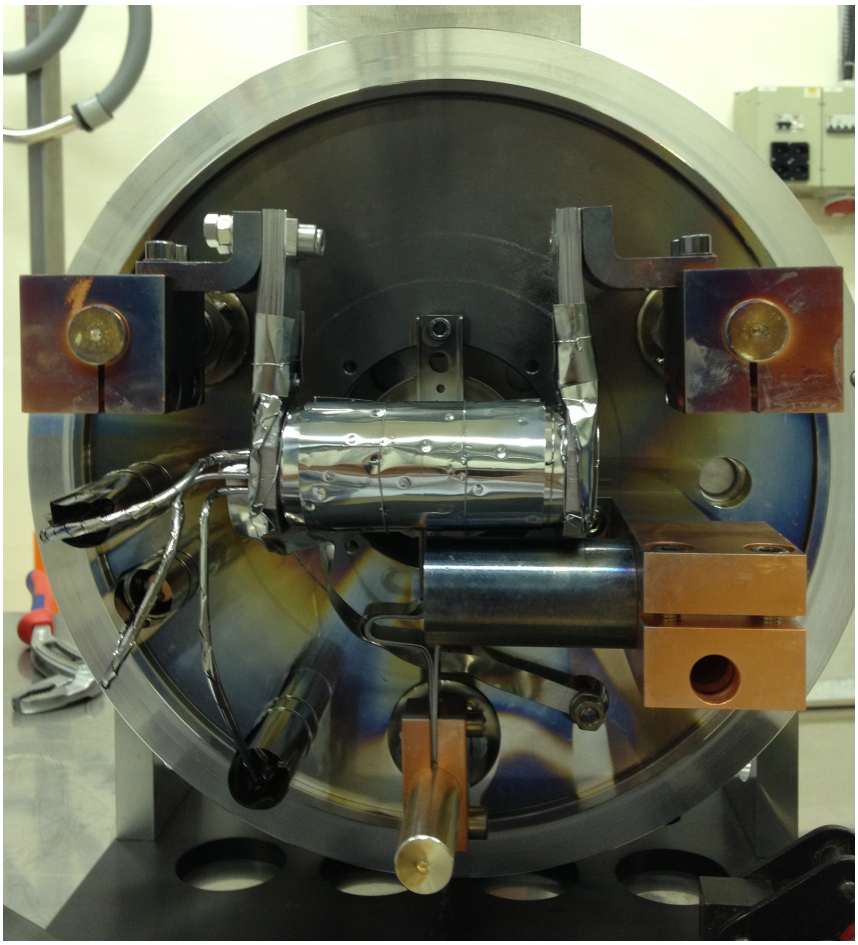

Figure 8.2: Prototype target configuration (courtesy of Alexander Gottberg).

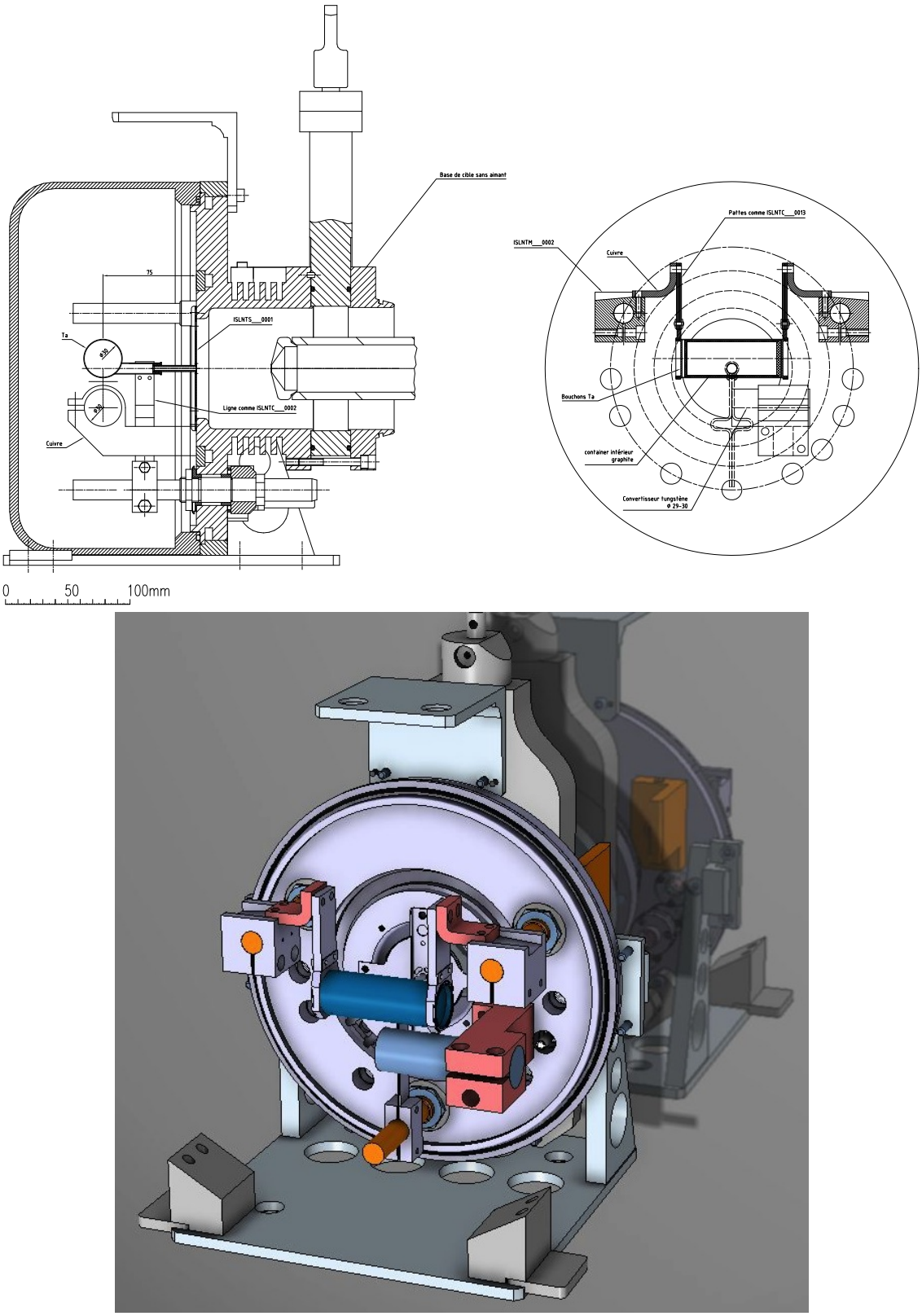

Figure 8.3: Top – Prototype configuration project, perpendicular planes. Bottom – 3D representation (courtesy of Stefano Marzari).

to fix the converter, is diameter was reduced on the side of the copper fitting. Furthermore, the UC_x target was centred in the target container and the converter was shifted to the right, since this made it easier to accommodate the new targets in the container.

Some of these adjustments were made during the design process while others were forced by issues which arose during the construction phase. In parallel, simulations were done to address the effect of these changes in the yields of the neutron-rich and neutron-deficient nuclides of interest for this work. As an example of this iterative process, when the decision was made to shift the UC_x target to the centre of the container, simulations showed that this simple translation would increase the yield of neutron-deficient contaminants. It was found that this was due to the spread of the proton beam in the aluminium of the container, an effect which can be seen in Fig. 7.11. The high-energy protons scattered in the container have a small contribution to the total production of neutron-deficient nuclides in the default configuration, but in the prototype configuration the total production of neutron-deficient nuclides is greatly decreased, and therefore the fraction produced by the mentioned protons increases. This effect was not seen in the first optimised configuration, since in that case the target was closer to the container. The proposed solution for this problem was to decrease the thickness of the container in the entrance point of the proton beam, as shown in Fig. 8.1. The thickness of the target container in this region was reduced from 5 mm to 2 mm, thus reducing the number of protons scattered off the container.

8.1.1 Thermo-electrical Simulations

In the standard ISOLDE target units, the target container is heated by a DC current coupled from the copper connection blocks to the tantalum container via tantalum sheets connected with stainless steel M5 screws. To investigate the thermal behaviour of the target unit, thermo-electrical simulations using the ANSYS code [202] were carried out by Stefano Marzari from the RBS (Radioactive Beam Sources) section of the EN-STI (Sources, Targets & Interactions, Engineering Department) group at CERN. Figure 8.4 shows the results from two thermo-electrical ANSYS simulations. The simulation from the upper panel is related to the normal operation conditions, where no faulty contacts are found and both thermal and electrical resistance are low. The temperatures are variable along the container axis, since the terminals act as cold sinks, with the maximum temperature observed at the center of the container. The simulation from the lower panel shows the situation where both electrical and thermal contacts are defective and present a high thermal and electric resistance. In the latter case, a significative increase of the temperature of the copper blocks and tantalum sheets is observed, which can promote the formation of an inter-metallic compound of stainless steel with copper and change the temperature of the target cylinder.

When the prototype target unit was heated for the first time, the stainless steel M5 screws

melted, due to a chemical reaction between copper and stainless steel. This was later found to be a consequence of the different heat profile of the prototype when compared to conventional ISOLDE target units. For the prototype unit, the stainless steel screws had to be replaced by tungsten screws.

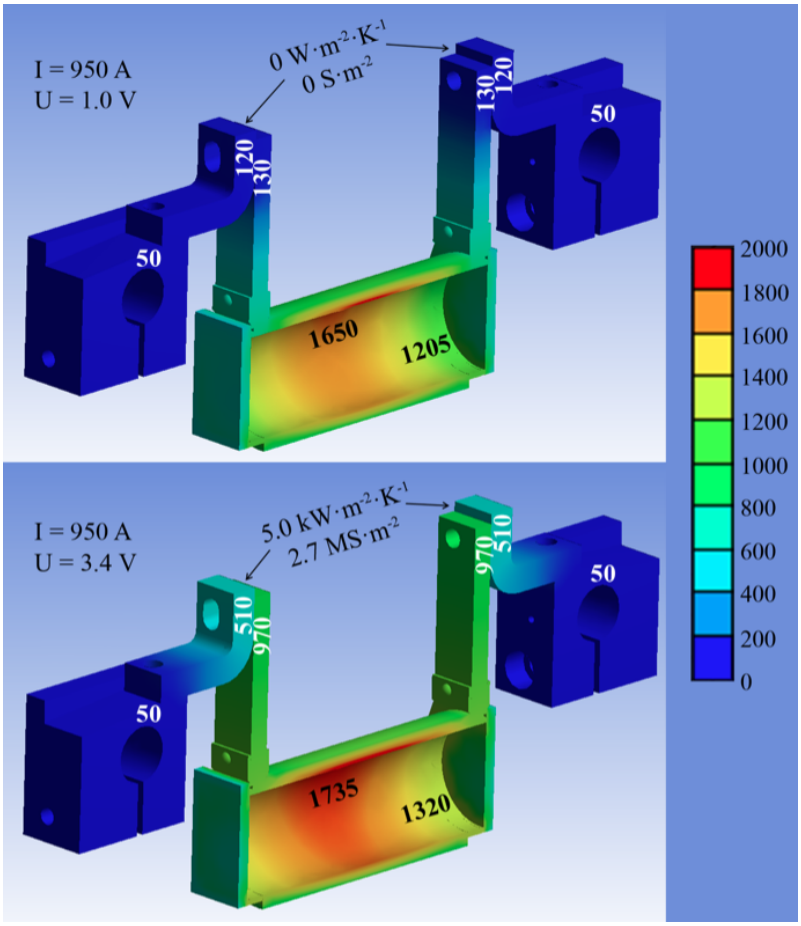

Figure 8.4: Thermo-electrical calculations for a heating current of 950 A and a set of two different thermal and electrical resistances at the contact between the Ta sandwich and the Cu angle piece. Temperatures are given in °C (courtesy of Stefano Marzari).

8.1.2 Synthesis of the Uranium Carbide UC_x Target Material

The uranium carbide target material was synthesized by adjusting the standard ISOLDE procedure in order to obtain material pellets according to the non-standard geometry. Depleted uranium dioxide powder was mixed with high-purity synthetic graphite powder in the molar ratio of 1:6. The mixture was blended in a vibratory grinder for 20 minutes and pressed into pellets by employing a force of 26 tons in a stainless steel dye. Fourty-one of the resulting pellets, with 25 mm diameter, 1.7 mm thickness and 3.0 g each, were piled up and inserted into a cylindrical graphite container. Carbo-thermal reduction of UO_2 was performed in vacuum of

base pressure 10^{-6} mbar at temperatures up to 1820 °C, where no more degassing (and, thus, no more production of CO_2) was observed. The mass of the final load of 102.4 g indicates a complete chemical transition into UC_2 + 2C. Finally, the material was transferred from the vacuum oven to the target unit #493, where it was inserted and sealed inside the tantalum container of the final unit, shown in Fig. 8.2. The synthesis of the UC_x target material was done by Alexander Gottberg, from the RBS section of the EN-STI group.

8.2 Results and Discussion

8.2.1 Simulation Predictions

The proton and neutron fluences in the UC_x target in the standard and prototype configurations are compared in Fig. 8.5. As with the previous optimised configurations, it is seen that the neutron and proton fluences are greatly reduced for high energies, while for lower energies the neutron fluences are much less affected, and even increased in the 0.1-1 MeV range. This means that the bases on which those optimisations were founded are preserved, at least to some extent, in the prototype configuration.

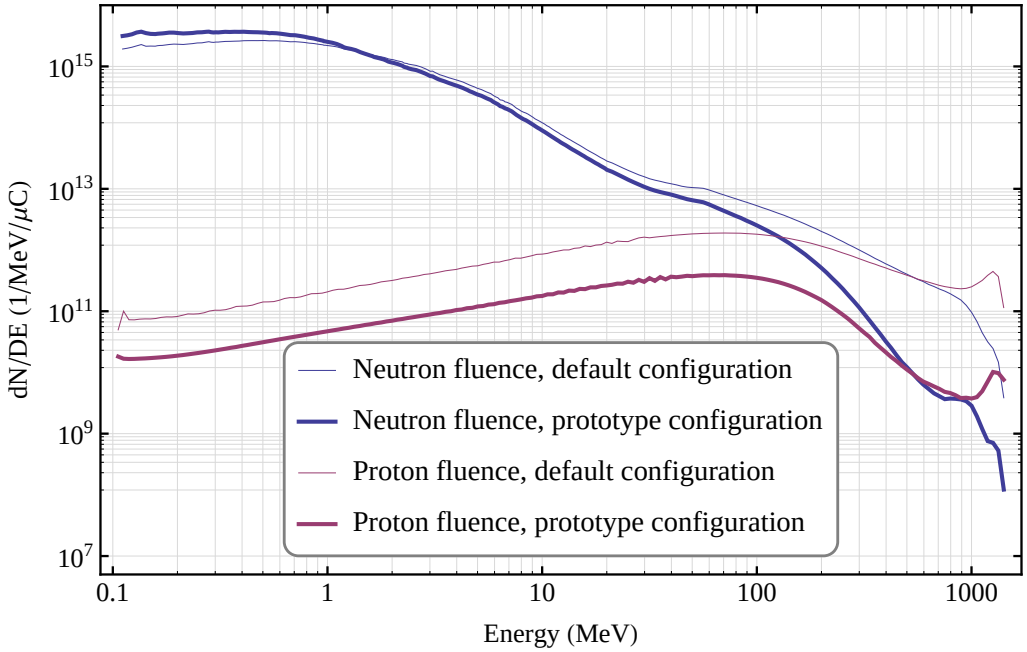

Figure 8.5: Neutron and proton differential fluences (1/MeV/μC) in the UC_x target, for the default and prototype configurations.

Figs. 8.6 and 8.7 show the predictions of the in-target yields of Zn and Rb isotopes in the prototype configuration, using FLUKA and ABRABLA+TALYS cross sections, respectively. With

FLUKA cross sections, an improvement in the ratio ^{80}Zn/^{80}Rb by a factor of 44 is foreseen, while with ABRABLA+TALYS cross sections the prediction is an improvement by a factor of 22. The

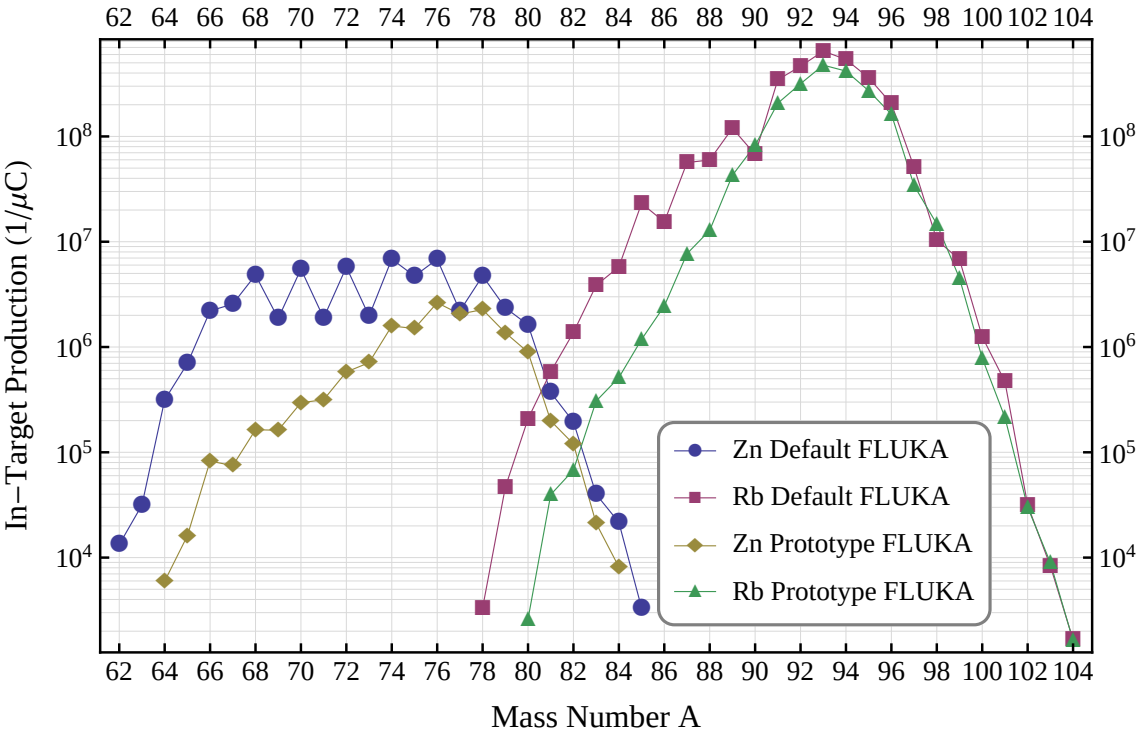

Figure 8.6: Prediction of in-target yields of Zn and Rb isotopes in the prototype configuration, calculated with FLUKA cross sections.

predictions for Cd and Cs isotopes are not shown in this section since it was not possible to measure their yields experimentally; the lasers to ionise Cd isotopes were not available during the experiment and there were contaminations in the measurements of Cs yields which cannot be discriminated offline (more details will be provided in the following sections).

Finally, the effect of the prototype configuration on the yields of all isotopes in the nuclear landscape can be seen in Fig. 8.8, as predicted by FLUKA. The yields are lower for practically all isotopes, but are much more reduced in the neutron-deficient region than in the neutron-rich region. This further confirms that, in spite of the compromises which had to be made in order to build it, the prototype configuration is perfectly suitable to test the validity of the optimisations proposed in Chapter 7, even if the final beams of neutron-rich isotopes have lower intensities when compared to the ones obtained with the standard configuration.

8.2.2 Experimental Results

The isotopes of Copper, Zinc, Gallium, Rubidium and Indium were measured either by using the ISOLDE tape station, equipped with a 4π-beta detector and a high-purity germanium detector for

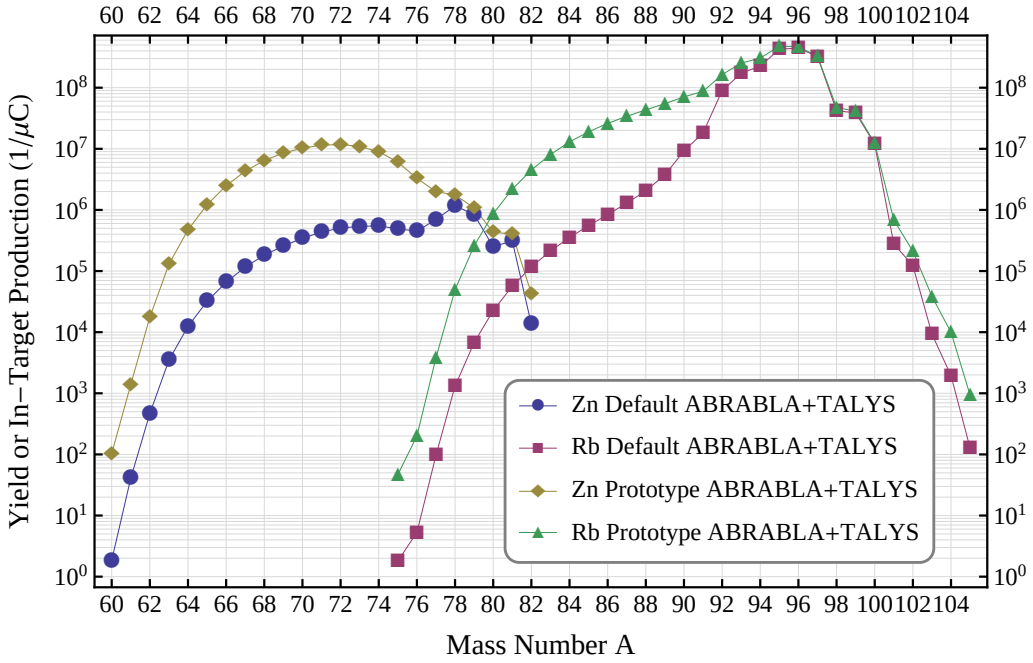

Figure 8.7: Prediction of in-target yields of Zn and Rb isotopes in the prototype configuration, calculated with ABRABLA+TALYS cross sections.

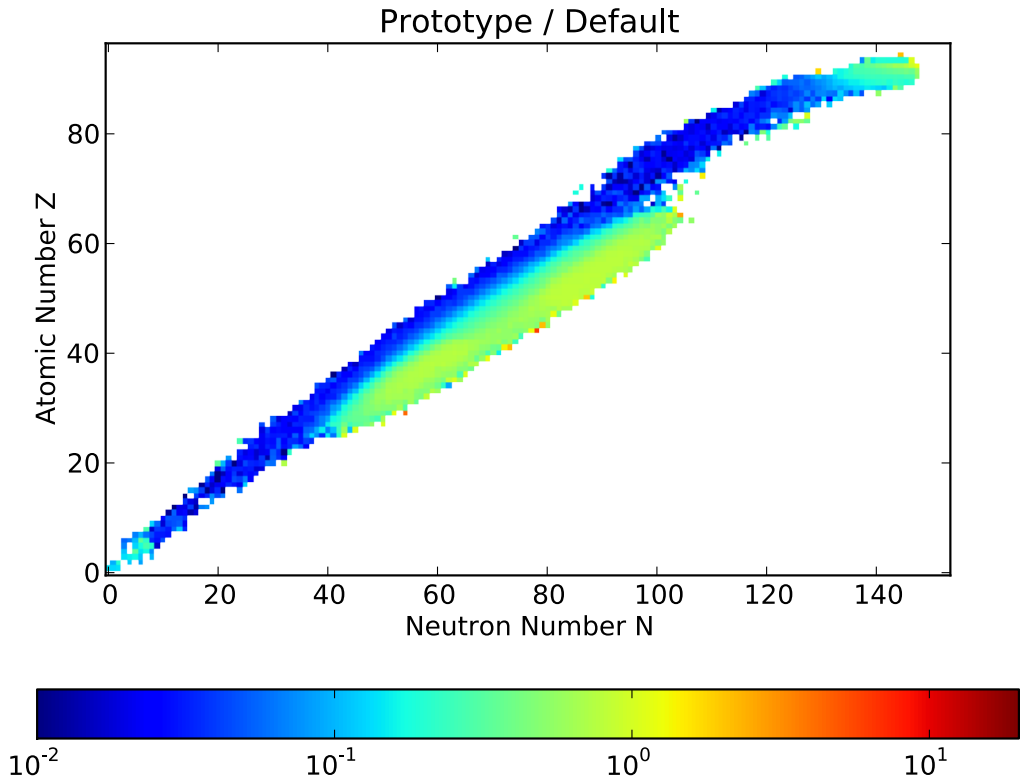

Figure 8.8: Nuclear landscape - ratio prototype yields / default yields (obtained with FLUKA).

gamma spectroscopy or by using the ISOLTRAP multi-reflection time-of-flight mass separator MR-ToF [203]. Ga, Rb and In are ionised inside the hot tungsten cavity by surface ionisation, while Cu and Zn are ionised by the laser ionisation source RILIS [178].

Table 8.1 summarises the results, grouping the experimental RIB intensities with the in-target yields calculated with FLUKA and ABRABLA+TALYS. The results are normalised to the primary proton current, which, in the experimental case, varied between 1×10^{13} and 2×10^{13} protons per pulse. Overall, the release efficiencies seem to be low for most isotopes investigated from this unit, a fact which can be explained by the conservative temperatures adopted during operation.

Isotope	$\mathbf{T}_{1/2}$ (s)	**Experimental Intensity** ($1/\mu$C)	**Calculated in-Target Yield** FLUKA ($1/\mu$C)	ABRABLA+TALYS ($1/\mu$C)
^{80}Rb	30	$\leq 9.00 \times 10^{1}$ $^{\gamma}$	2.60×10^{3}	2.26×10^{4}
^{82}Rb	76.2	3.00×10^{3} $^{\beta}$	6.78×10^{4}	1.17×10^{5}
^{84}Rb	1230	4.14×10^{4} ^{I}	5.12×10^{5}	3.54×10^{5}
^{86}Rb	62	1.54×10^{5} ^{I}	2.45×10^{6}	8.38×10^{5}
^{88}Rb	1038	1.28×10^{6} $^{\beta}$	1.28×10^{7}	2.05×10^{6}
^{91}Rb	58	3.60×10^{6} $^{\beta}$	2.07×10^{8}	1.81×10^{7}
^{92}Rb	4.5	3.63×10^{6} $^{\beta}$	3.17×10^{8}	8.97×10^{7}
^{93}Rb	5.8	3.48×10^{6} $^{\beta}$	4.75×10^{8}	1.72×10^{8}
^{94}Rb	2.69	5.81×10^{6} $^{\beta}$	4.18×10^{8}	2.26×10^{8}
^{95}Rb	0.377	5.85×10^{6} $^{\beta,\gamma}$	2.72×10^{8}	4.26×10^{8}
^{98}Rb	0.114	5.80×10^{3} $^{\beta}$	1.47×10^{7}	4.20×10^{7}
^{74}Zn	96	1.07×10^{4} $^{\beta}$	1.58×10^{6}	5.49×10^{5}
^{75}Zn	10.2	1.98×10^{4} $^{\gamma}$	1.50×10^{6}	4.92×10^{5}
^{76}Zn	5.6	3.43×10^{4} $^{\beta,\gamma}$	2.63×10^{6}	4.49×10^{5}
^{78}Zn	1.47	1.30×10^{4} $^{\beta}$	2.27×10^{6}	1.17×10^{6}
^{80}Zn	0.537	5.43×10^{3} $^{\gamma}$	8.93×10^{5}	2.50×10^{5}
^{81}Zn	0.29	5.50×10^{2} $^{\beta,\gamma}$	1.99×10^{5}	3.12×10^{5}
^{80}Ga	1.7	1.23×10^{2} $^{\gamma}$	7.21×10^{6}	4.11×10^{6}
^{81}Ga	1.22	1.52×10^{2} $^{\beta}$	6.55×10^{6}	5.91×10^{6}
^{120}In	47.3	1.54×10^{4} $^{\gamma}$	5.46×10^{7}	4.88×10^{6}
^{128}In	0.84	4.38×10^{3} $^{\gamma}$	4.49×10^{7}	8.95×10^{7}
^{129}In	0.61	1.09×10^{3} $^{\gamma}$	3.19×10^{7}	5.86×10^{7}
^{71}Cu	19.5	1.20×10^{3} $^{\beta}$	4.73×10^{5}	3.23×10^{5}
^{74}Cu	1.594	2.20×10^{2} $^{\beta}$	6.51×10^{5}	1.39×10^{5}
^{75}Cu	1.224	9.60×10^{1} $^{\beta}$	7.88×10^{5}	1.74×10^{5}
^{77}Cu	0.469	3.00×10^{1} $^{\beta}$	3.67×10^{5}	5.29×10^{4}

Table 8.1: Experimental yields and calculated in-target production rates. The experimental values are assessed by either beta (β) or gamma (γ) detection in the ISOLDE tape station or by using the ISOLTRAP MR-ToF (I).

The pulsed nature of the CERN-PSB proton beam allows for time-dependant isotope release measurements. This release curve is commonly approximated by the four parameter, triple exponential delay function

$$p(t) = \frac{1}{N}\Big(1 - e^{-\lambda_r t}\Big)\Big(\alpha e^{-\lambda_f t} + (1-\alpha)e^{-\lambda_s t}\Big), \tag{8.1}$$

where

- $p(t)$ is the delay function describing the probability that a radioactive isotope that was produced in the target at $t = 0$ will be released at time t;
- λ_r, λ_f and λ_s are the exponential rise, fast fall and slow fall time constants and t_r, t_f and t_s are the rise, fast fall and slow fall times, with: $\lambda_x = \frac{\ln 2}{t_x}$;
- α is a weighing factor between the slow and fast components;
- the factor $\frac{1}{N}$ normalises $p(t)$ to unity for $t \to \infty$.

The release efficiency ϵ_{rel} of a specific element as a function of its decay constant ($\lambda_i = \frac{\ln 2}{T_{1/2}}$) can be calculated by folding the delay function with the nuclear decay function [204]:

$$\epsilon_{rel}(\lambda_i) = \int_{t=0}^{\infty} p(t) e^{-\lambda_i t} dt \tag{8.2}$$

For isotopes with sufficiently long half-lives, $p(t)$ can be directly derived by fitting the experimental release curve. In cases where λ_i is much smaller than the time constant of the release process (λ_s) there is a large error associated to the release parameters and, thus, the decay function needs to be considered in the fitting procedure. Computing the integration in Eq. (8.1) yields to the expression

$$\epsilon_{rel}(\lambda_i) = \frac{1}{N}\left(\frac{\alpha}{\lambda_f + \lambda_i} + \frac{1-\alpha}{\lambda_s + \lambda_i} + \frac{\alpha}{\lambda_f + \lambda_r + \lambda_i} + \frac{\alpha - 1}{\lambda_s + \lambda_r + \lambda_i}\right). \tag{8.3}$$

As mentioned in previous chapters, the simulation results refer to in-target production rates, while the experimental data are obtained after the nuclei diffuse from the target and effuse to the ion source, are ionised, mass-separated and transported to the detection system, each of these processes having an associated efficiency. To be compared with the experimental yield, the in-target production has to be multiplied by the efficiencies of each process:

$$Y_{\text{exp}} = Y_{\text{in-target}} \cdot \epsilon_{\text{release}} \cdot \epsilon_{\text{ionisation}} \cdot \epsilon_{\text{transport}} \cdot \epsilon_{\text{detection}} \tag{8.4}$$

$$= Y_{\text{in-target}} \cdot \epsilon_{\text{release}} \cdot \epsilon_0, \tag{8.5}$$

where ϵ_0 includes all contributing losses from the production of the isotope until its detection, excluding the half-life dependant release efficiency which can be approximated experimentally

using Eq. (8.3). The efficiency ϵ_0 is kept as a free parameter, to match the experimental release parameters to the simulated data by minimising the sum of the squared relative differences on a logarithmic scale.

8.2.2.1 Production of Zn and Rb Isotopes

Figs. 8.9 and 8.10 show the experimental RIB intensities and in-target yields calculated with FLUKA and ABRABLA+TALYS, for Zn and Rb isotopes, respectively. The experimental results for the standard converter configuration of ISOLDE, taken from [188], are also shown for comparison. There seems to be a similar trend between the values obtained with FLUKA and the

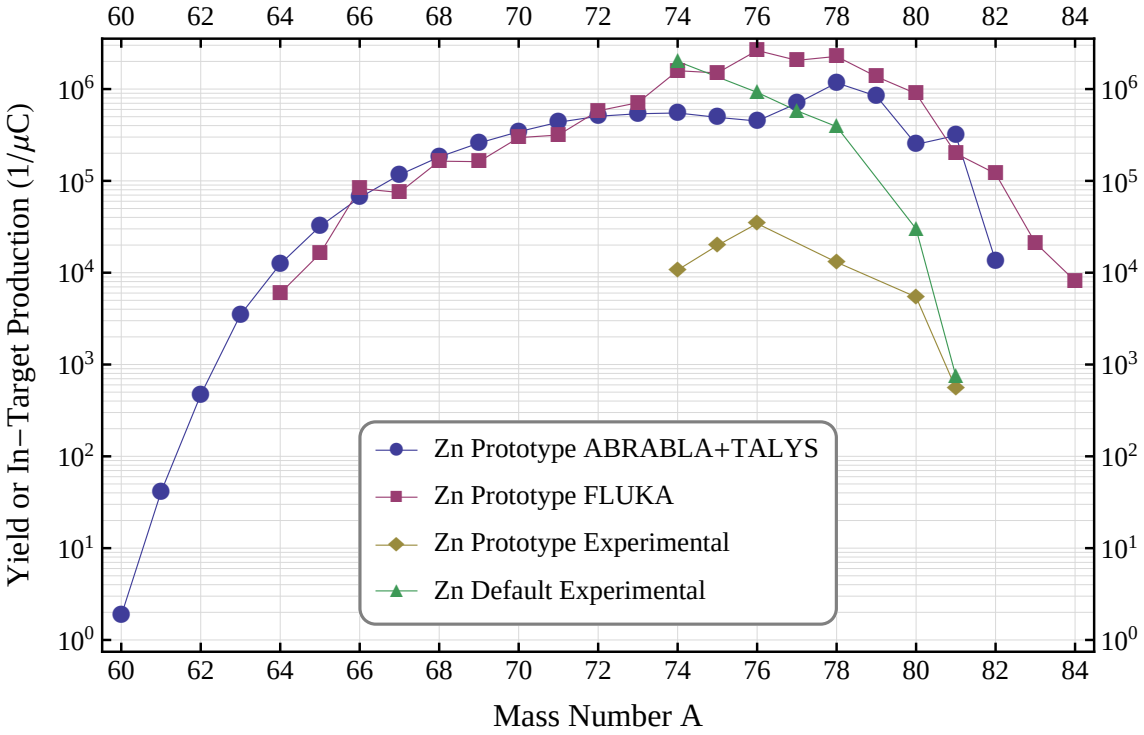

Figure 8.9: Experimental RIB intensities and simulated in-target production for Zn isotopes.

experimental data. The data obtained with ABRABLA+TALYS exhibit a small kink in the mass range A=73-78 for Zn and A=85-95 for Rb, which is not seen in the experimental data nor in the simulation results obtained with FLUKA. As for the experimental results, the yields of neutron-deficient isotopes of Rb (A=80-82) is indeed greatly decreased, while the yields of neutron isotopes of Zn are much less affected (for A=81, the yield is almost the same as in the standard ISOLDE converter configuration). The yield of ^{80}Rb in the prototype configuration is 90 ions/μC, as opposed to 1×10^5 ions/μC in the standard configuration, showing a suppression of the order of 10^3 ions/μC. The production of ^{80}Zn is decreased from 3×10^4 ions/μC to 5.43×10^3 ions/μC. This means that the ratio ^{80}Zn/^{80}Rb is improved by a factor of ~ 200, while ABRABLA+TALYS

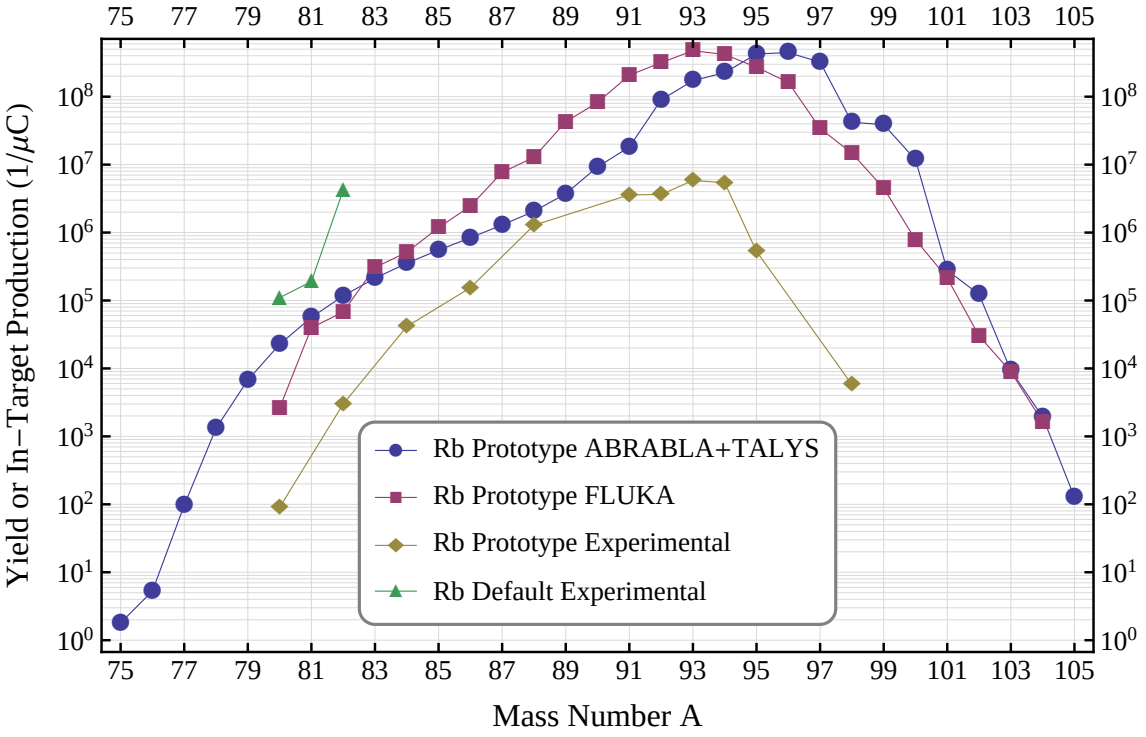

Figure 8.10: Experimental RIB intensities and simulated in-target production for Rb isotopes.

predicted an improvement by a factor of $\sim$ 22 and FLUKA predicted and improvement by a factor of $\sim$ 44; the improvement in the ratio exceeds the predictions by approximately one order of magnitude. The main reason could be production cross sections of the neutron-deficient isotopes of Rb, which may be lower than predicted by FLUKA or ABRABLA+TALYS, since these isotopes are suppressed to an extent not predicted by the simulations.

The calculated release efficiencies for Zn and Rb isotopes are shown in Figs. 8.11 and 8.12, respectively. The points illustrate the ratios between the experimental RIB intensities and the in-target yields predicted by the simulations. The lines represent the release function, which was found by fitting the experimental distribution of the isotope release (Equation (8.3)) to the calculated values by introducing an overall efficiency $\epsilon = \epsilon_{release} \cdot \epsilon_0$, evaluating the losses during ionisation and the half-life dependant losses of the release process. As mentioned before, the efficiency ϵ_0 was kept as a free parameter, to match the experimental release parameters to the simulated data. Since the experimental release curves were assessed for time constants shorter than 10 s, the fitting curve is not presented for longer half-lives.

It is clear that for most isotopes the yields obtained with FLUKA are closer to the experimental values than the yields obtained with ABRABLA+TALYS, both for Zn and Rb isotopes. The larger deviations of the ABRABLA+TALYS results seem to be consistent with the kink observed in the in-target production yields, which is not seen in the experimental values.

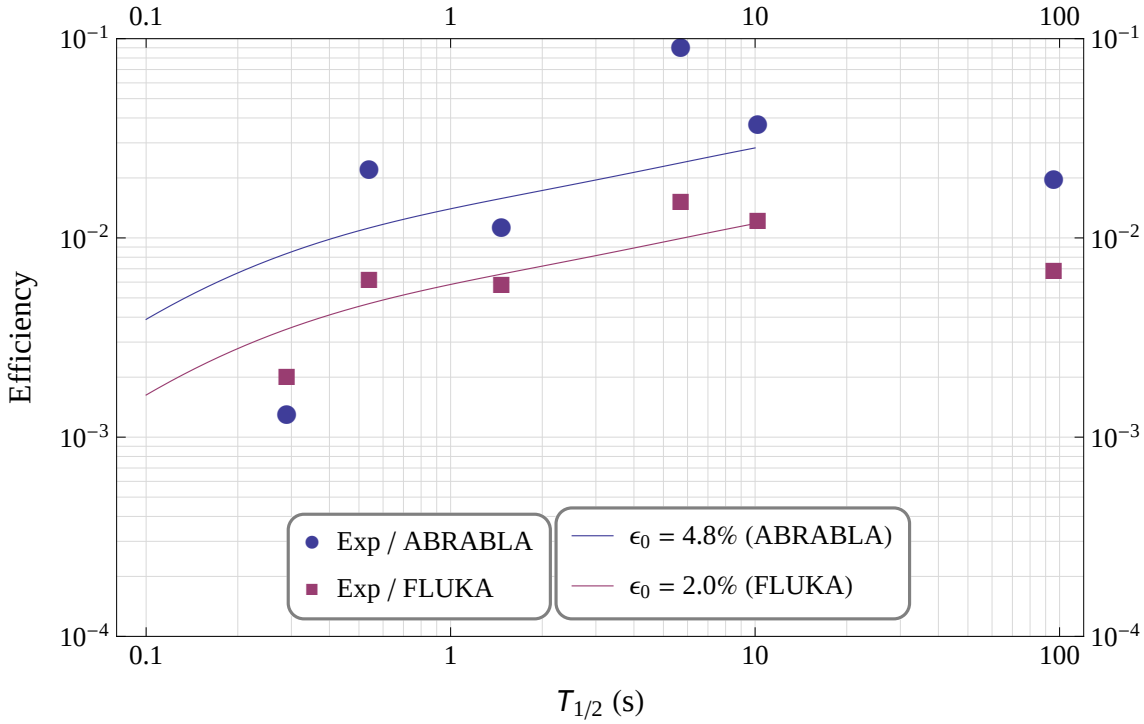

Figure 8.11: Efficiency curves as a function of the isotope half-lives, for Zn isotopes. The experimental release parameters used in the approximation are: $\alpha = 0.968$, $\lambda_f = 3.07$ s^{-1}, $\lambda_s = 0.0507$ s^{-1} and $\lambda_r = 27.7$ s^{-1}.

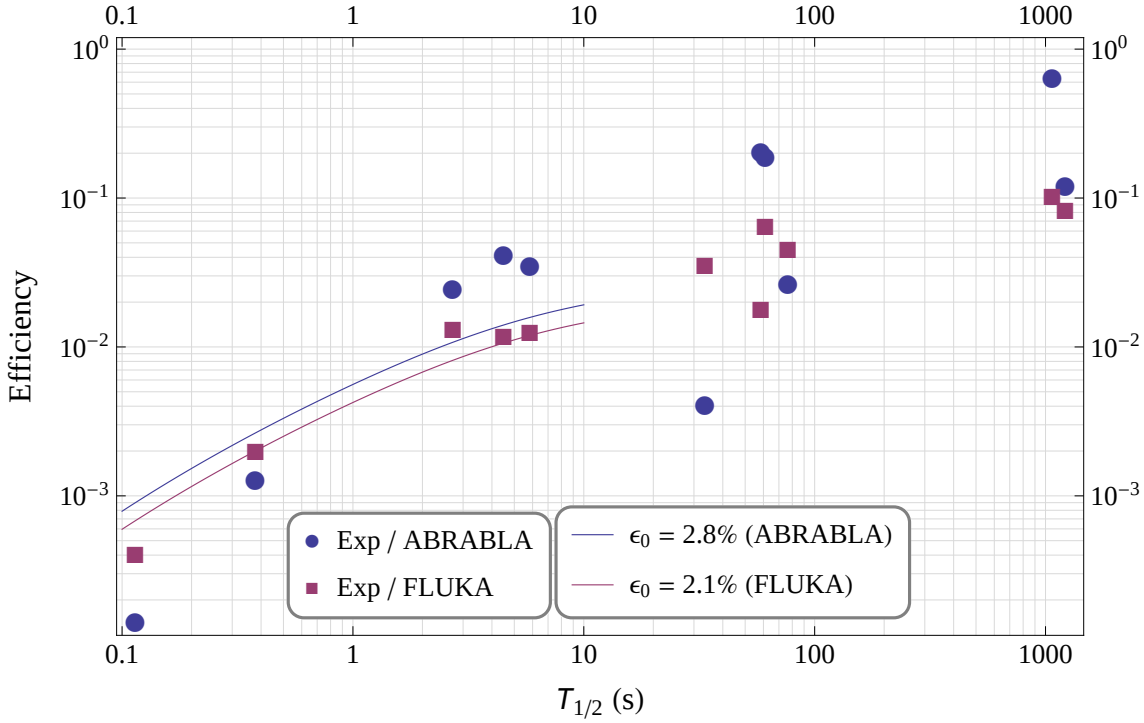

Figure 8.12: Efficiency curves as a function of the isotope half-lives, for Rb isotopes. The experimental release parameters used in the approximation are: $\alpha = 0.471$, $\lambda_f = 1.82$ s^{-1}, $\lambda_s = 0.140$ s^{-1} and $\lambda_r = 57.8$ s^{-1}.

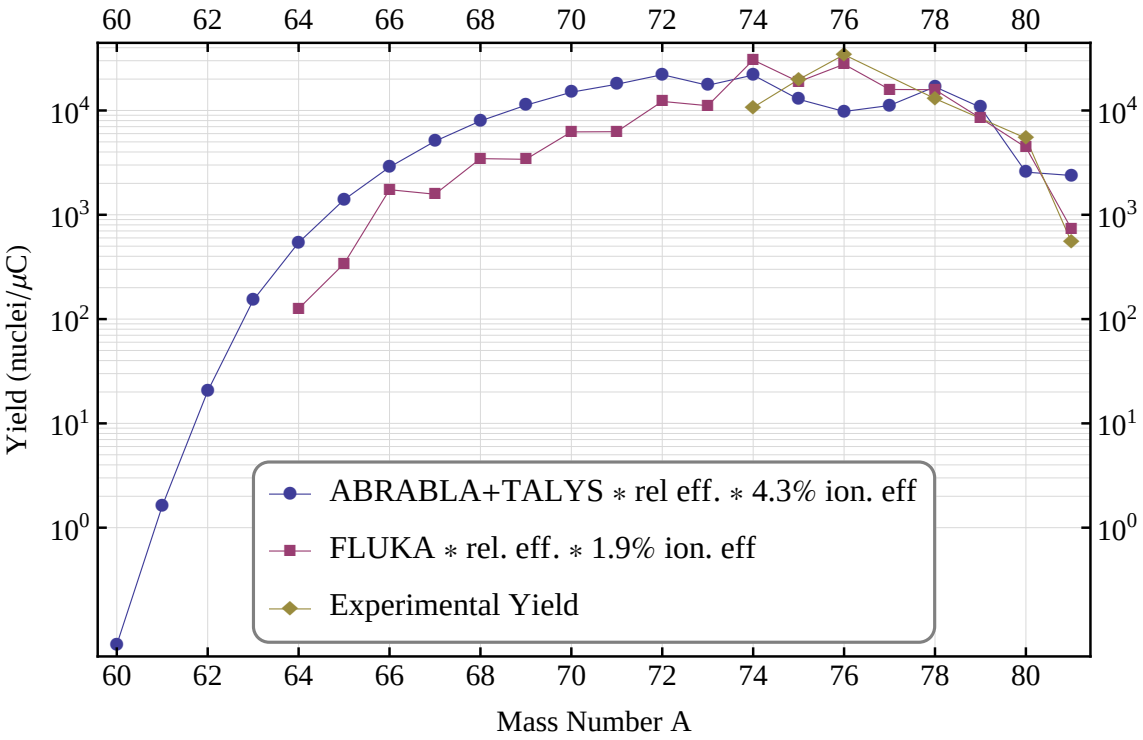

Figure 8.13: Experimental RIB intensities and simulated in-target production multiplied by the estimated release and ionisation efficiencies, for Zn isotopes.

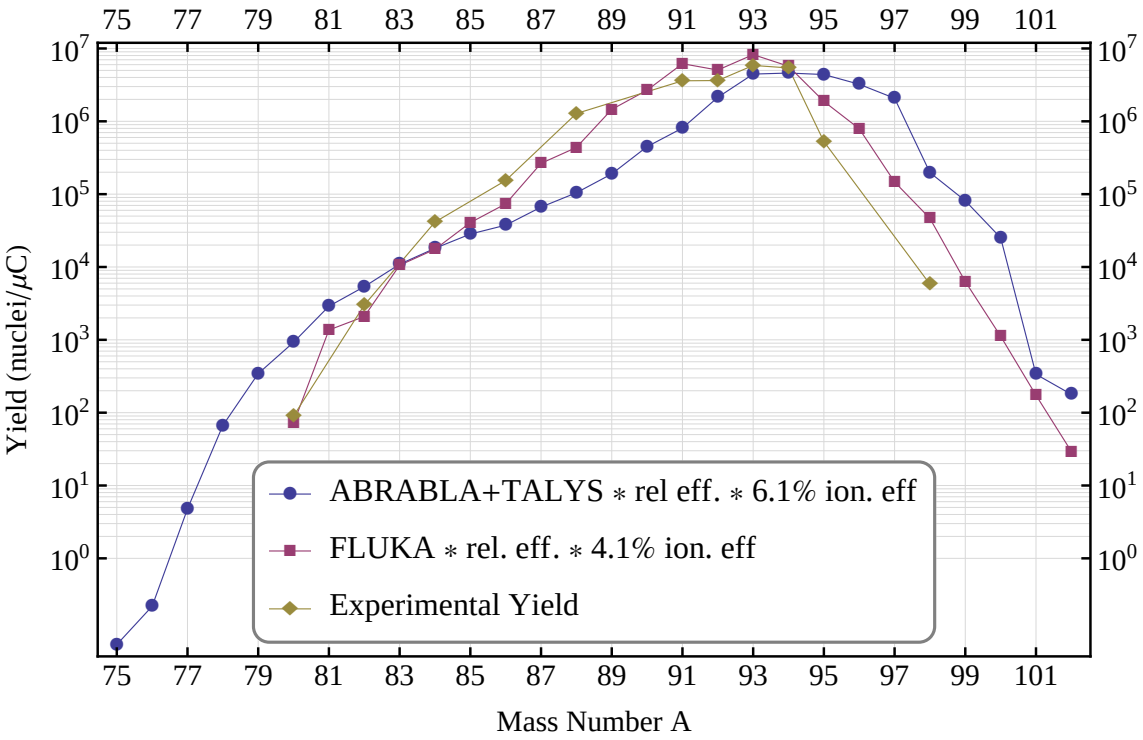

Figure 8.14: Experimental RIB intensities and simulated in-target production multiplied by the estimated release and ionisation efficiencies, for Rb isotopes.

Figs. 8.13 and 8.14 present comparisons between the simulated in-target yields multiplied by the calculated efficiencies and the experimental RIB intensities, for Zn and Rb isotopes. These direct comparisons are helpful to confirm that FLUKA is indeed closer to the experimental results than ABRABLA+TALYS. At this stage, it is important to notice that this fact contrasts with the benchmarks presented in Chapter 7. A possible reason is that the preference for ABRABLA+TALYS cross sections in the first benchmark was based on the results of the direct configuration. In the converter configuration, FLUKA was achieving a better agreement with the experimental results for mass numbers 77 and 78 (Zn isotopes), while ABRABLA+TALYS were closer for mass numbers 74 and 80. What seems to be happening is that FLUKA is giving better results for fission induced by neutrons and protons at lower energies (prototype configuration), while ABRABLA+TALYS make better predictions at higher energies (direct configuration of the standard ISOLDE target system). In the standard converter configuration, the "intermediate case", the choice between the two sets of cross sections is not clear.

8.2.2.2 Production of Cu, In, Ga and Cs Isotopes

Besides Zn and Rb isotopes, measurements of the intensities of Cu, In, Ga and Cs isotopes were also done during the experimental tests of the prototype target system. The results, also presented in Table 8.1 (except for Cs), are shown in Fig. 8.15, along with the simulation predictions. When compared to the predicted yields of Zn and Rb, the simulation results show similar trends in the in-target yields predicted by FLUKA and ABRABLA+TALYS, the latter exhibiting the already-mentioned kink in the intermediate masses. But the experimental RIB intensities are much lower than expected for Cu, In and Ga isotopes. For Cu isotopes, this is explained by the diffusion properties of this element, which is not easily released from the target. Since the target is thicker than the standard ISOLDE targets and its temperature, due to thermo-mechanical concerns, was kept at relatively low values ($\leq 1800°C$), the fraction of Cu nuclei released from the target is much lower than usual. For In and Ga isotopes, the low ionisation efficiencies of these elements and the low temperature of the ioniser tube (kept below $2000°C$) are the most probable causes for the low intensities.

For Cs isotopes, the problem does not seem to be related to the release or ionisation efficiencies. Most intensities were measured with a Faraday Cup, and the possibility of contamination by isobars from other elements (mainly Ba isotopes) was not contemplated during the experiment. Therefore, the yields of Cs isotopes are probably overestimated, at least for mass numbers between 131 and 142. When this was found, it was not possible to repeat the measurements, since, after three days of operation, the measurements started to show abnormal results. In the first place, it was found that the converter had presumably fallen from the copper holder. Odd results were also found after shooting directly in the UC_x target, possibly due to a defective electrical contact between the target and the transfer line. Further investigations will have to be

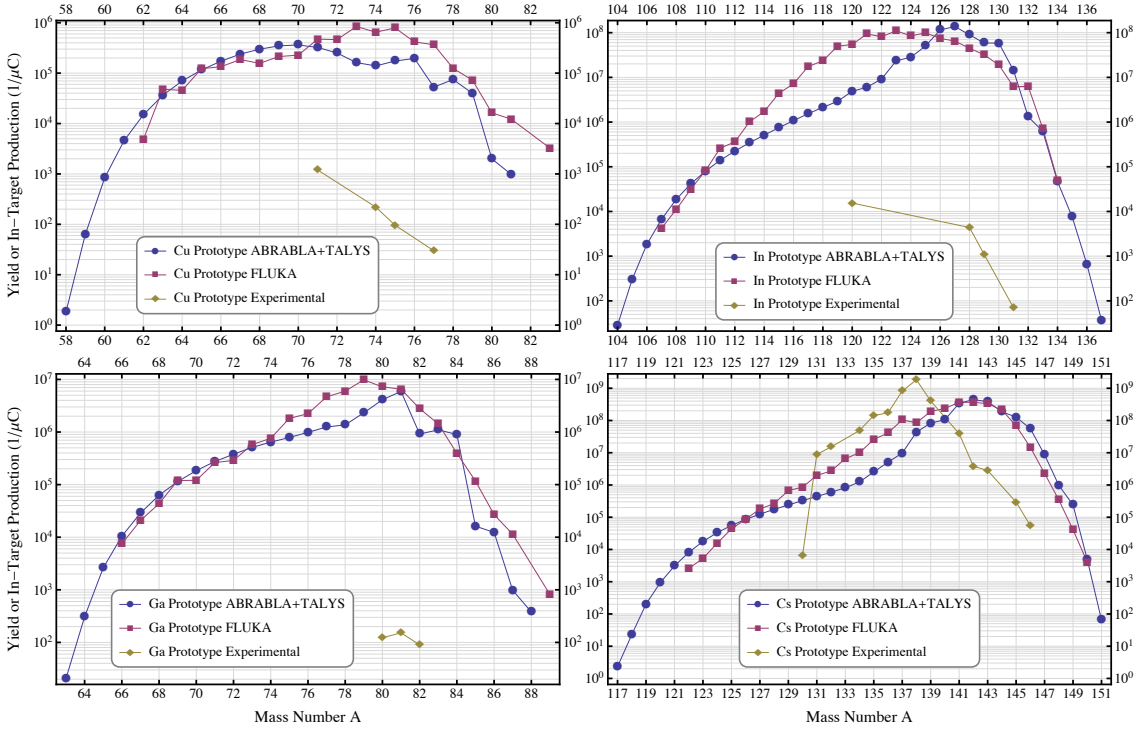

Figure 8.15: Experimental RIB intensities and simulated in-target production for Cu, In, Ga and Cs isotopes.

undertaken in the coming years to determine what happened to the target system.

8.3 Conclusions

In this chapter, a prototype target unit for the ISOLDE target station was presented, together with the experimental results from the assessment of the production of radioactive isotopes. The objective of the prototype unit was to validate experimentally the principles discussed in the optimisation studies presented in Chapter 7. This validation was successfully done at ISOLDE with a 1.4 GeV proton beam impinging on the newly-designed converter. A suppression of the order of 10^3 in the contaminant ^{80}Rb was observed, while the production of ^{80}Zn decreased by less than an order of magnitude. Overall, the ratio ^{80}Zn/^{80}Rb was increased by a factor of 200, 5-10 times more than predicted by the simulations. When compared to the measurements, the cross sections from FLUKA made better predictions than the TALYS+ABRABLA cross sections.

The experimental validation of the optimisation studies of Chapter 7 is the major achievement of this work. It shows not only the importance that Monte Carlo simulations can have in R&D studies for target development but also the role that existing ISOL facilities play in the development of innovative target systems for intermediate- and next-generation high-power facilities, like HIE-ISOLDE and EURISOL. The next step in the quest for purer beams of neutron-rich isotopes

around the doubly magic nuclei ^{78}Ni and ^{132}Sn should be the construction of the more-complex alternative target system proposed in Chapter 7, which will allow to increase the production of neutron-rich isotopes while decreasing the undesired contamination by neutron-deficient isobars.

Chapter 9

Dosimetry and Activation Studies

This chapter deals with radiological protection aspects of two of the previously studied target systems: the standard ISOLDE configuration and the prototype configuration, introduced in the previous chapter. In the first place, the dose rates during operation for the two target systems are presented and compared. The specific activities and dose rates in the targets region are then discussed, for several cooling periods after the stoppage of the beam.

9.1 Objectives and Methods

The main objective of this study is to compare the performance of the standard and prototype configurations from a radiological protection point of view. In order to achieve that, a mix of the methods discussed in chapters 5, 7 and 8 was employed: FLUKA was used to perform the neutronics calculations for the operation and cooling periods, similarly to what was done in Chapter 5 for the EURISOL multi-MW target station, but using the target systems and beam parameters presented in chapters 7 and 8.

The first step consisted in the comparison between the dose rates during operation in the two configurations, either shooting directly on the target or shooting on the converter. A 1.4 GeV proton beam was used in all calculations, with a radial Gaussian distribution with $\sigma = 3.5$ mm. The characteristics of the target materials in the standard and prototype target configurations can be found in Chapters 7 and 8, respectively. In addition to the comparison of the performances of the two configurations, it was also an objective of this study to compare the production of residual nuclei (and resulting residual dose rates) in the standard ISOLDE configuration when shooting on the target or on the converter, to compare the production of radioactive waste in the two modes of operation.

For the activation calculations, an irradiation profile of 10 days of continuous operation with

3×10^{13} protons/s was assumed. Although 10 days is a reasonable estimate of the lifetime of a target system, the irradiation profile is very conservative, since typically the proton beam has up to 3×10^{13} protons per pulse with 1.2 seconds between pulses. Furthermore, there are periods of operation with much longer time intervals between pulses, and periods of no operation. An overestimation of the residual activities and doses after shutdown can therefore be anticipated, but even in that case the comparisons between configurations remain valid. After the stoppage of the proton beam, 10 cooling periods were used in the calculations: 0 days (right after the beam is shut-off), 1 day, 10 days, 1 month, 2 months, 3 months, 6 months, 1 year, 5 years and 10 years. Besides dose rates and activities in the target materials, lists of the nuclides produced in the targets which contribute to the residual dose rates were also compiled – the results are summarised in tables listing the nuclides which contribute the most to the residual doses.

9.2 Results and Discussion

9.2.1 Dose Rates During Operation

The ambient dose equivalent rates during operation are presented in Fig. 9.1, for the standard (top) and prototype (bottom) configurations and shooting on target (right) and on converter (left). These calculations were performed with FLUKA using fluence-to-dose conversion factors from [71], and the presented values represent average doses for a thickness of 2.2 cm in the z direction. When shooting directly on target, the dose rates are very similar in magnitude; radially, they are higher in the centre of the target and gradually lower at larger radii, following the radial shape of the proton beam. This is easily seen in the prototype configuration, which has a larger radius than the standard configuration, and therefore a less homogeneous distribution of the dose rates in the radial direction. The opposite happens in the longitudinal direction, where the attenuation effects can be seen in the standard configuration but not in the prototype configuration, due to the difference in the target lengths. The dose rates have peak values of the order of 5-7$\times 10^7$ Sv/h in both configurations.

When shooting on the converter, more power is deposited in the prototype configuration, due to the increased radius of its converter; the dose rates surpass 10^8 Sv/h in the impact point of the proton beam. Overall, it is seen that the dose rate during operation is higher when shooting on the converter than when shooting on the target. The increased power deposition in the prototype converter (addressed in the previous chapter) does not have a major influence on the dose rate outside the targets region.

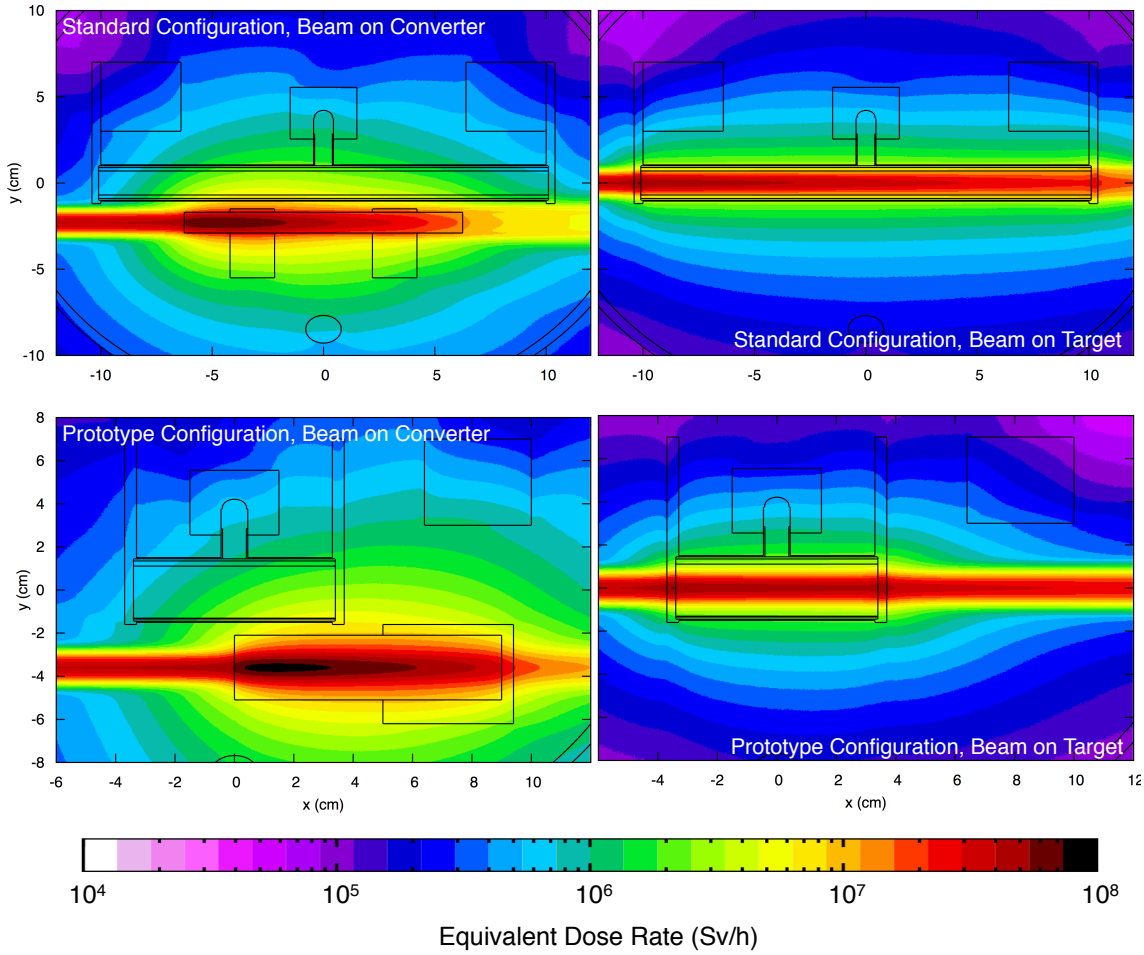

Figure 9.1: Ambient dose equivalent rate (Sv/h) during operation, calculated with FLUKA, in the standard (top) and prototype (bottom) configurations, shooting on target (right) and on converter (left). Average values for a 2.2 cm thickness in the z direction.

9.2.2 Activation Studies

9.2.2.1 Residual Dose Rates

The ambient dose equivalent rates (Sv/h) in the targets region after the stoppage of the beam are shown in Figs. 9.2 (shooting on target) and 9.3 (shooting on converter), for four cooling periods: 1 day, 1 month, 1 year and 10 years. The standard and prototype configurations are presented side-by-side, to allow an easy comparison between the two target systems. When compared to the dose rates during operation presented in Fig. 9.1, the dose rates drop by approximately four orders of magnitude after the stoppage of the beam, approximately the same drop in magnitude as seen in the activations studies for the EURISOL multi-MW target station, presented in Chapter 5.

When shooting on the converter, (Fig. 9.2), the magnitude and the evolution of the residual

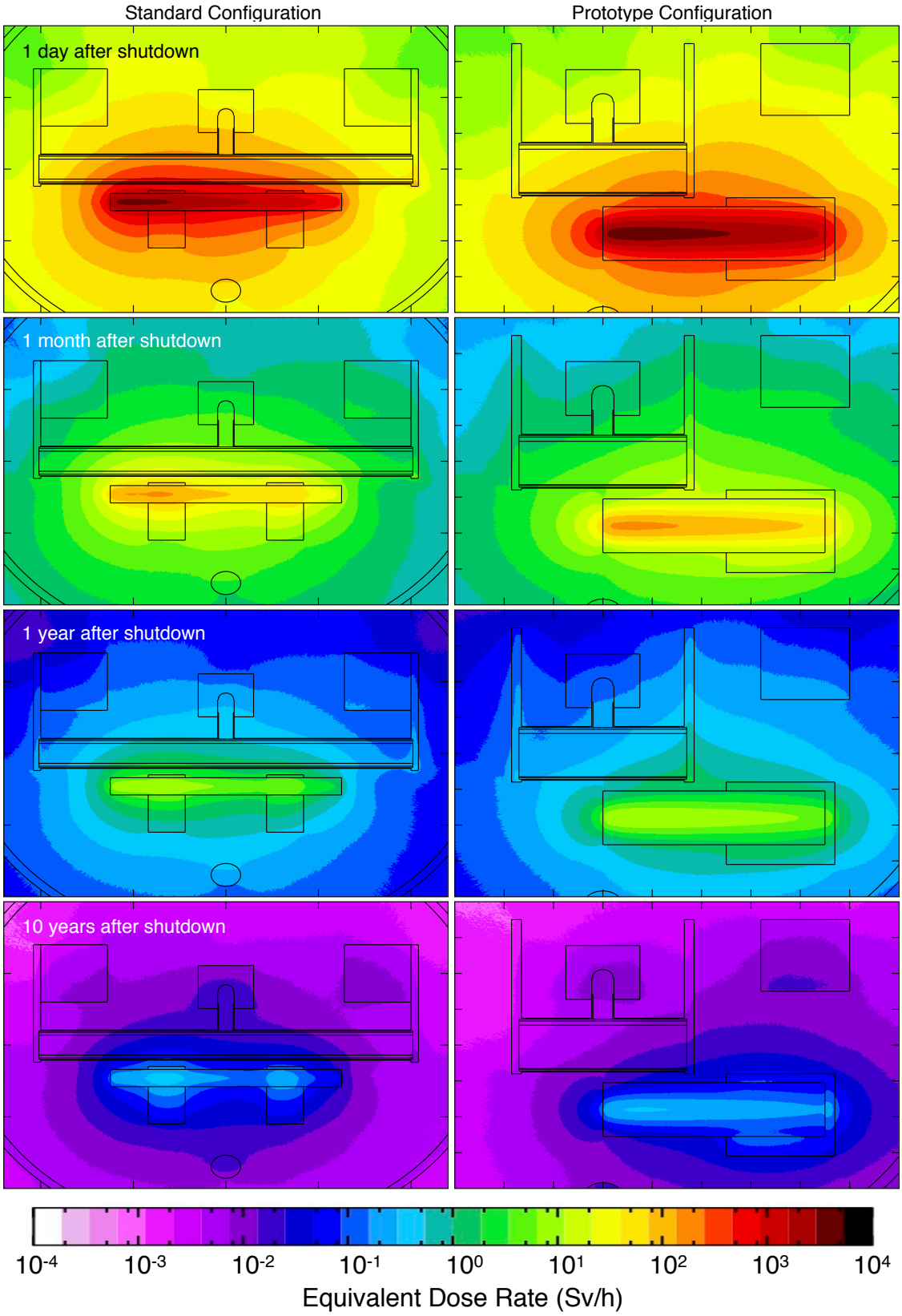

Figure 9.2: (Shooting on converter) Ambient dose equivalent rate (Sv/h) time evolution, calculated with FLUKA, in the standard (left) and prototype (right) configurations, for cooling periods of 1 day, 1 month, 1 year and 10 years. Average values for a 2.2 cm thickness in the z direction.

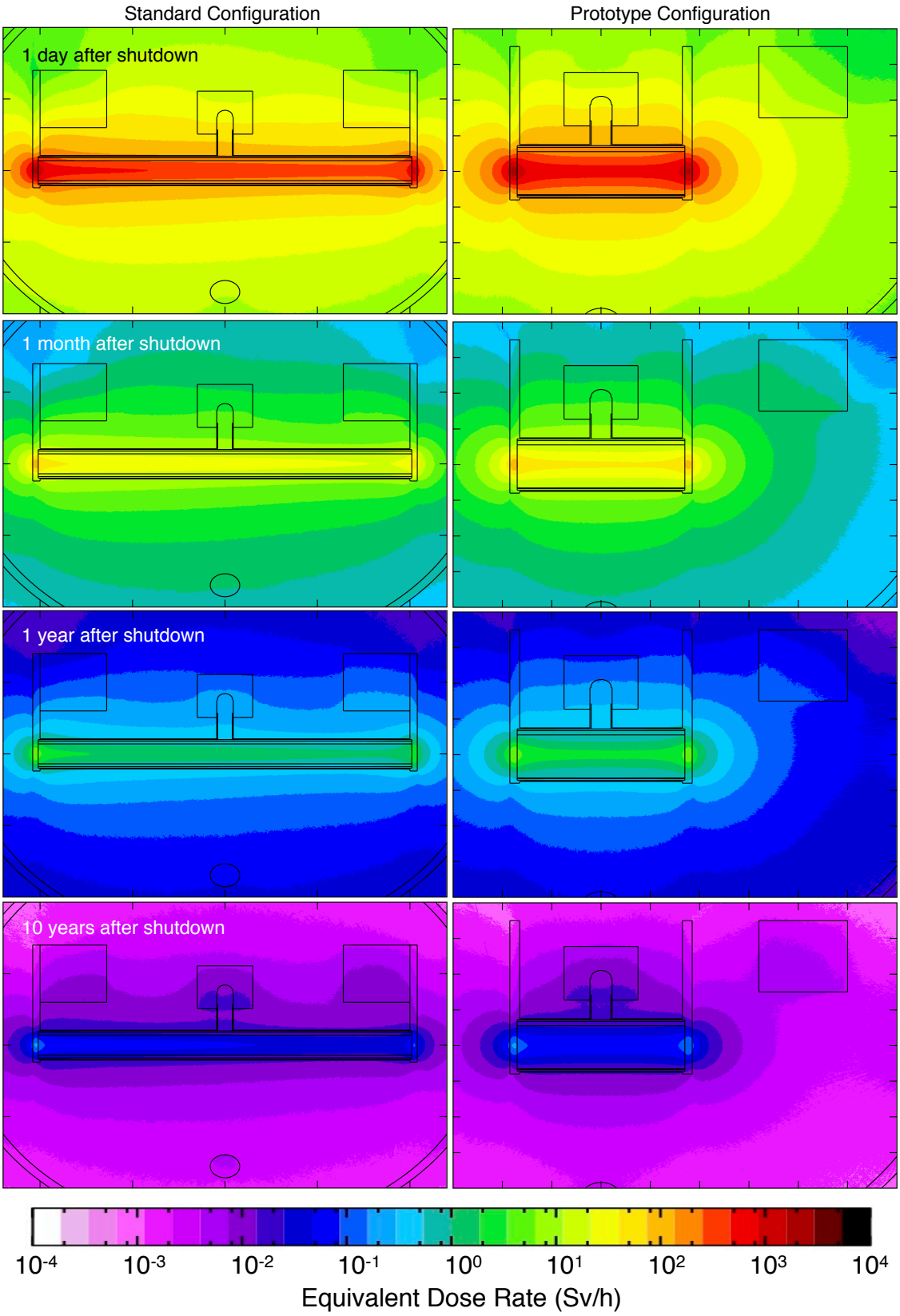

Figure 9.3: (Shooting on target) Ambient dose equivalent rate (Sv/h) time evolution, calculated with FLUKA, in the standard (left) and prototype (right) configurations, for cooling periods of 1 day, 1 month, 1 year and 10 years. Average values for a 2.2 cm thickness in the z direction.

dose rates are similar in the two target systems, dropping from a peak value of approximately $5 - 8 \times 10^3$ Sv/h (in the converter region) 1 day after shutdown to a value in the range $0.5 - 0.8$ Sv/h after 10 years. It is interesting to notice that in the EURISOL multi-MW target station the residual dose after 10 years was 100 Sv/h, between two and three orders of magnitude higher than at ISOLDE. Also important is to underline that these results, as well as the results for EURISOL, can vary to a great extent, depending on the assumed irradiation profile. The major source of radiation after shutdown is the tungsten converter, and in this sense it is important to state that the quantity of activated tungsten will be greater in the prototype configuration, since it has 4.5 times more mass than the standard converter.

When the proton beam hits the UC_x target directly (Fig. 9.3), the evolution of the residual dose rates is again very similar in both configurations, dropping from a peak value of approximately 1×10^3 Sv/h after the stoppage of the beam to approximately 0.1 Sv/h after 10 years, almost an order of magnitude lower than when shooting on the converter. From the radiological protection point of view, the activation of the tungsten converter is the most important problem to deal with in the first 10 years of cooling.

9.2.2.2 Specific Activities in the Targets

The residual dose rates presented in the previous section are due to the activation of the target materials, and thus it is also important to assess the evolution of the activities in those materials. In the first place, these calculations were done for the standard and prototype configurations when shooting on the converter. The evolution of the specific activities (Bq/g) in the target and converter are shown in Fig. 9.4, for cooling periods ranging from the moment when the beam is shut-off to 10 years after shutdown. Once again, it is seen that the converter is more activated than the UC_x target. Furthermore, the specific activity is higher in the standard configuration than in the prototype configuration, due to the fact that the specific activities are averaged over the target volume. A specific activity of 1.6×10^{11} Bq/g in the converter of the standard configuration (0 days after shutdown) means a total activity of 4.3×10^{13} Bq, while the corresponding 5.7×10^{10} Bq/g in the prototype configuration gives a total activity of 7.0×10^{13} Bq. While the specific activities averaged over the converter volume are higher in the standard configuration, the total activities are almost two times higher in the prototype configuration. In the case of the UC_x target, the mass of the prototype is lower than the mass of the standard target. Therefore, the total activities are also larger in the standard configuration than in the prototype configuration, with larger relative deviations between the two when compared to the specific activities.

The evolution of the specific activities in the converters is similar in the two configurations, but in the UC_x targets there are distinct trends. The specific activities in the standard configuration are followed closely by the evolution of the specific activities in the prototype configuration

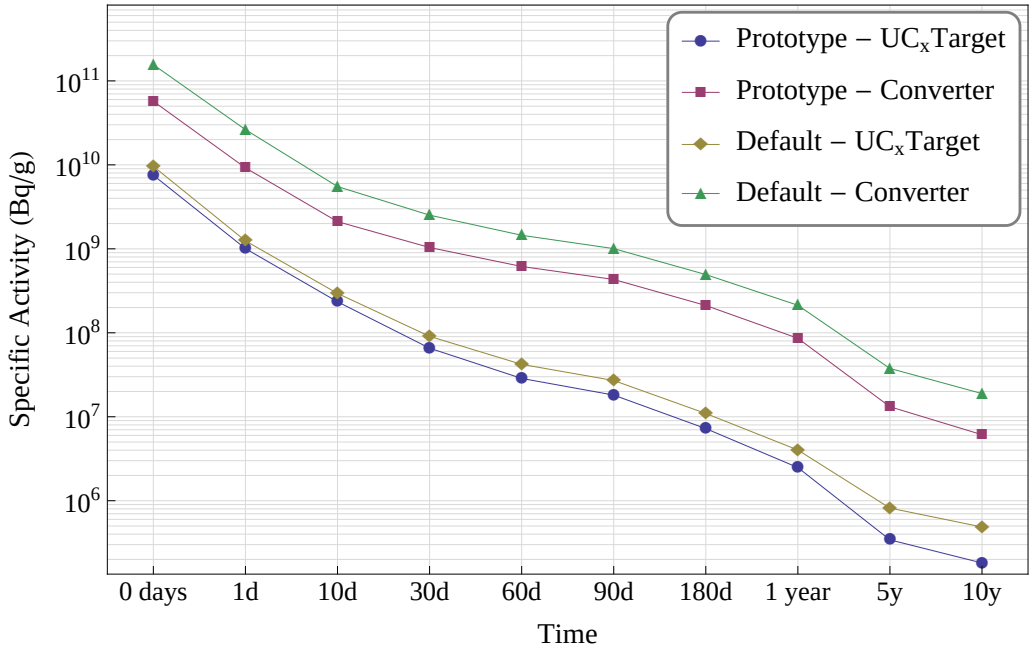

Figure 9.4: Specific activity (Bq/g) evolution in the converter and UC_x target, for both configurations (shooting on converter) and several cooling periods up to 10 years.

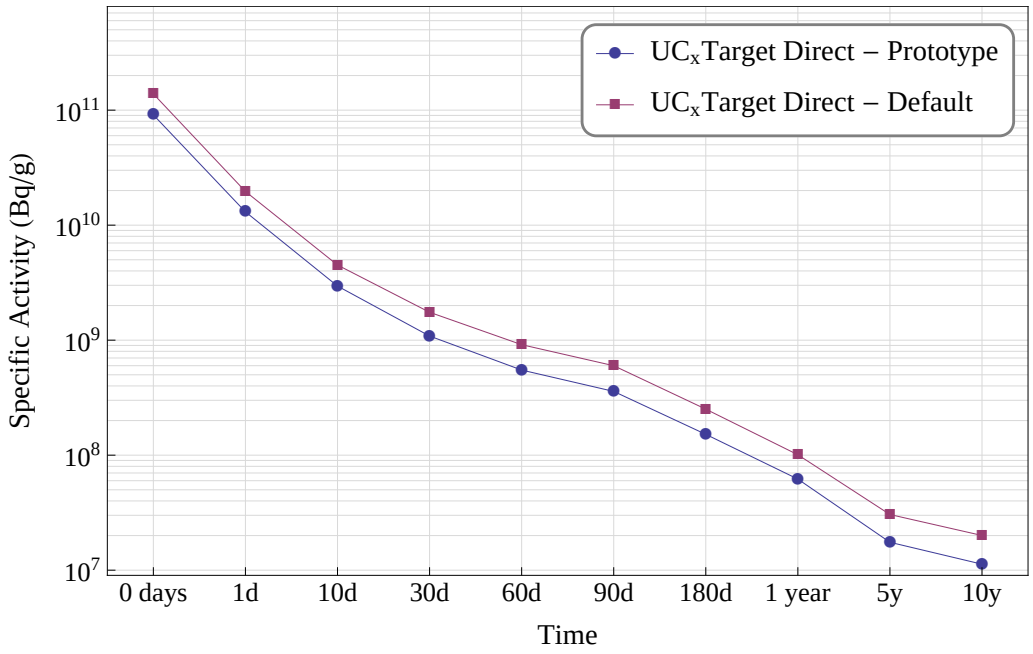

Figure 9.5: Specific activity (Bq/g) evolution in the converter and UC_x target, for both configurations (shooting on target) and several cooling periods up to 10 years.

during the first 10 days, but after that the two curves separate gradually from each other, with the activities in the prototype configuration falling faster than the ones of the standard configuration. This happens due to the very different neutron and proton fluence spectra reaching the

targets, the main objective behind the construction of the prototype, which changes the distribution of nuclides produced in the targets (see Fig. 8.8) and hence the specific activities of their activated materials. This does not happen in the converters, since they are basically subjected to the same radiation field (incoming proton beam).

The same comparison is made in Fig. 9.5 for the case when the proton beam is directed to the target. In this case, the specific activities in the standard and prototype configurations when the beam stops are 1.4×10^{11} and 9.1×10^{10} Bq/g, respectively, while the corresponding total activities are 1.4×10^{13} and 7.7×10^{12} Bq/g, lower than the corresponding total activities in the converters when the beam is directed to the converter. This is still true ten years after shutdown, if we compare the total activities instead of the specific activities.

9.2.2.3 Residual Nuclei in the Targets

The final step in this analysis was the assessment of the radionuclide inventory formed in the targets through activation. The methodology was similar to the one presented in Chapter 5, which involved, for each of the ten cooling periods mentioned in the previous sections, the extraction of the specific activity of each nuclide formed in the target from the FLUKA output files, the extraction of the exemption limits (according to the Swiss legislation) from a database and the calculation, for each nuclide, of the number of times that limit is exceeded (MEL - Multiple of the Exemption Limit). After that, the nuclides were ordered by their MEL values, the MEL values were summed and the contribution of each nuclide to the total MEL value was determined.

Table 9.1 shows the results of this analysis for the standard configuration, shooting on converter. Since the nuclide tables are too extent to be presented here, a selection of the two nuclides with the largest contributions to MEL is presented instead, along with the value of MEL. These data are presented in Table 9.1 for the UC_x target and for the converter. Once again, the total MEL number is two to three orders of magnitude lower than in the EURISOL case.

During the first 30 days after shutdown, ^{131}I, with 8 days of half-life, is the main contributor the total MEL value (it is a fission product of high radiotoxicity). After ^{131}I decays, ^{210}Po and ^{208}Po, spallation products of ^{238}U with half-lives of 138 days and 2.9 years, become the main contributors. These are α-emitters which can be sources of health hazard if ingested or inhaled, especially ^{210}Po, which has a shorter half-life. Furthermore, polonium melts at low temperature and can be volatile, increasing the risk of inhalation.

The values of MEL are higher in the converter, as expected, due to the accumulation of spallation products of tungsten. Isotopes of Lu and Yb have the largest contributions in the first days, and ^{148}Gd, an α-emitter with a long half-life of 74.6 years, is the main contributor 5 and 10 years after shutdown. Tritium, a low-energy β-emitter with a half-life 12.3 years which can be a source of

health hazard if ingested, inhaled or absorbed through the skin, is responsible for 5% of the total MEL value 10 years after shutdown.

Table 9.1: Nuclides formed through activation in the standard configuration, shooting on the converter.

Standard Configuration						
	UC_x Target			W Converter		
Time	Multiple of EL	Main contributors to MEL		Multiple of EL	Main contributors to MEL	
0d	7.71E+8	^{131}I (7.15%)	^{133}I (4.48%)	2.53E+9	^{170}Lu (6.77%)	^{166}Yb (5.56%)
1d	3.08E+8	^{131}I (16.8%)	^{237}U (6.50%)	1.37E+9	^{170}Lu (10.9%)	^{166}Yb (7.69%)
10d	7.95E+7	^{131}I (30.8%)	^{237}U (9.99%)	3.47E+8	^{171}Lu (14.3%)	^{169}Yb (7.92%)
30d	2.52E+7	^{131}I (17.3%)	^{223}Ra (11.9%)	1.39E+8	^{169}Yb (12.9%)	^{125}I (11.7%)
60d	1.18E+7	^{210}Po (12.0%)	^{223}Ra (11.6%)	7.97E+7	^{125}I (14.4%)	^{169}Yb (11.7%)
90d	8.38E+6	^{210}Po (14.6%)	^{106}Rh (10.3%)	5.47E+7	^{125}I (14.7%)	^{185}W (12.3%)
180d	5.30E+6	^{208}Po (15.3%)	^{210}Po (15.1%)	2.38E+7	^{185}W (12.2%)	^{125}I (11.8%)
1y	3.50E+6	^{208}Po (20.5%)	^{106}Rh (14.8%)	9.18E+6	^{172}Lu (19.2%)	^{172}Hf (15.2%)
5y	1.10E+6	^{208}Po (25.1%)	^{210}Pb (16.5%)	2.35E+6	^{148}Gd (56.5%)	^{172}Lu (17.0%)
10y	6.76E+5	^{210}Pb (22.9%)	^{232}U (19.2%)	1.52E+6	^{148}Gd (83.0%)	^{3}H (5.00%)

Table 9.2: Nuclides formed through activation in the prototype configuration, shooting on the converter.

Prototype Configuration						
	UC_x Target			W Converter		
Time	Multiple of EL	Main contributors to MEL		Multiple of EL	Main contributors to MEL	
0d	5.22E+8	^{131}I (8.66%)	^{133}I (6.08%)	9.13E+8	^{170}Lu (6.32%)	^{166}Yb (4.78%)
1d	2.01E+8	^{131}I (21.1%)	^{237}U (9.03%)	4.65E+8	^{170}Lu (10.8%)	^{171}Lu (7.70%)
10d	5.26E+7	^{131}I (38.0%)	^{237}U (13.7%)	1.20E+8	^{171}Lu (14.4%)	^{185}W (7.62%)
30d	1.45E+7	^{131}I (24.6%)	^{140}Ba (7.57%)	5.07E+7	^{185}W (15.0%)	^{169}Yb (11.6%)
60d	5.82E+6	^{91}Y (10.3%)	^{106}Rh (9.52%)	2.98E+7	^{185}W (19.3%)	^{125}I (11.0%)
90d	3.90E+6	^{106}Rh (13.5%)	^{106}Ru (13.5%)	2.07E+7	^{185}W (21.0%)	^{125}I (11.1%)
180d	2.26E+6	^{106}Rh (19.6%)	^{106}Ru (19.6%)	9.19E+6	^{185}W (20.6%)	^{182}Ta (9.55%)
1y	1.39E+6	^{106}Rh (22.7%)	^{106}Ru (22.7%)	3.38E+6	^{172}Lu (18.8%)	^{172}Hf (14.9%)
5y	3.70E+5	^{232}U (16.1%)	^{90}Sr (14.3%)	7.38E+5	^{148}Gd (51.3%)	^{172}Lu (19.5%)
10y	2.58E+5	^{232}U (22.1%)	^{90}Sr (18.2%)	4.47E+5	^{148}Gd (80.8%)	^{3}H (5.38%)

The same analysis is presented in Table 9.2 for the prototype configuration. The total MEL values are lower than in the standard configuration, an expected result since the MEL values are calculated using the specific activity, and the argument presented with the calculations of the

previous section remains valid. In the converter, the nuclides responsible for the activities are basically the same as in the standard configuration, since the converters are subjected to similar radiation fields. In the UC_x target this is also true for the first days after the stoppage of the beam, but different isotopes appear afterwards, as expected, since the concentrations of nuclides in the prototype configuration are very different from the ones of the standard configuration. The most important fact is the suppression of polonium isotopes, which could be anticipated by looking at Fig. 8.8 ($Z = 84$). The specific activity of ^{210}Po 60 days after shutdown is 8.5 times higher in the standard configuration than in the prototype configuration.

To finalise the analysis of the nuclides produced in the targets, Table 9.3 shows the total MEL values and the isotopes with the greatest contributions when shooting directly on the UC_x target, for both configurations. Polonium isotopes are produced in large quantities, namely ^{206}Po (half-

Table 9.3: Nuclides formed through activation, shooting directly on the UC_x target.

UC_x Target – Direct Beam						
	Prototype Configuration			**Standard Configuration**		
Time	**Multiple of EL**	**Main contributors to MEL**		**Multiple of EL**	**Main contributors to MEL**	
0d	9.05E+9	^{206}Po (10.5%)	^{131}I (3.54%)	1.39E+10	^{206}Po (11.5%)	^{131}I (3.08%)
1d	4.26E+9	^{206}Po (21.0%)	^{131}I (7.06%)	6.63E+9	^{206}Po (22.6%)	^{131}I (6.07%)
10d	1.37E+9	^{206}Po (32.0%)	^{131}I (10.4%)	2.16E+9	^{206}Po (34.0%)	^{131}I (8.82%)
30d	5.38E+8	^{210}Po (17.1%)	^{206}Po (16.9%)	8.62E+8	^{210}Po (17.8%)	^{206}Po (17.7%)
60d	3.01E+8	^{210}Po (26.3%)	^{208}Po (24.2%)	4.88E+8	^{210}Po (27.2%)	^{208}Po (25.0%)
90d	2.34E+8	^{208}Po (30.6%)	^{210}Po (29.2%)	3.81E+8	^{208}Po (31.4%)	^{210}Po (30.1%)
180d	1.64E+8	^{208}Po (41.0%)	^{210}Po (26.7%)	2.69E+8	^{208}Po (41.9%)	^{210}Po (27.3%)
1y	1.13E+8	^{208}Po (52.8%)	^{210}Po (16.0%)	1.85E+8	^{208}Po (53.9%)	^{210}Po (16.4%)
5y	3.75E+7	^{208}Po (60.9%)	^{210}Pb (10.4%)	6.17E+7	^{208}Po (62.0%)	^{210}Pb (10.3%)
10y	1.79E+7	^{208}Po (38.8%)	^{210}Pb (18.7%)	2.92E+7	^{208}Po (39.9%)	^{210}Pb (18.6%)

life of 8.8 days), ^{208}Po and ^{210}Po, the main nuclides responsible for the total MEL values for all cooling periods. The management of this radioactive waste has to be carefully planned, due to the radiotoxicity of these isotopes, most importantly ^{210}Po. It is also important to take notice of the high MEL values in the standard configuration when shooting directly on the target.

9.3 Conclusions

This chapter presented a Radiological Protection study comparing the performance of the standard ISOLDE target system with the prototype configuration presented in the previous chapter. The assessment of the ambient dose equivalent rates in the two configurations during operation,

either shooting on target or on converter, did not show substantial differences between the two target systems. It was also seen in both cases that the dose rate outside the targets region is higher when shooting on the converter than when shooting directly in the UC_x target. In the impact point of the proton beam, it reaches 10^8 Sv/h.

The calculations of the residual dose rates after the stoppage of the proton beam revealed that the dose rates drop by approximately four orders of magnitude when the beam stops. Once again, the magnitude and the evolution of the calculated residual dose rates were similar in the two target systems. The major source of radiation in the first 10 years after shutdown, when shooting on the converter, is the activated tungsten; the quantity of activated material will therefore be higher in the prototype configuration than in the standard configuration. When shooting directly on the target, the residual dose rates are almost one order of magnitude lower than when shooting on the converter.

The specific activities when shooting on the converter are higher in the converter than in the UC_x target, for all cooling periods (from shutdown time to ten years after shutdown). The total activities are almost two times higher in the prototype converter, since it has 4.5 times more tungsten than the converter of the standard configuration. The activities in the UC_x targets have different trends in the two configurations, due to the fact that the prototype configuration suppresses more neutron-deficient than neutron-rich isotopes. The activation is lower when shooting directly on the targets.

To complement the calculations of the specific activities in the targets, extensive lists with all the nuclides responsible for those activities were also produced, and a summary of these was presented. The production of polonium isotopes, and most importantly of ^{210}Po, is one of the major causes of concern, especially when shooting directly on the target. The activation calculations and the lists of residual nuclei which resulted from this study will be important in the future, when the analysis of irradiated targets gets underway, in the new ISOLDE hot-cell planned for 2014 [205].

Part IV

Conclusions

Chapter 10

Final Discussion and Conclusions

This work was mainly focused on two projects:

- ISOLDE, one of the most important facilities worldwide for the production of RIBs using the ISOL method, and
- EURISOL, the next-generation European ISOL facility.

ISOLDE has played, and will continue to do so, an important role in the research and development of the technologies that will be needed in order to build and operate the EURISOL facility. HIE-ISOLDE, an upgrade in energy and intensity of the ISOLDE facility which was also studied in this work, is currently under construction at CERN, and will be one of the intermediate-generation facilities operating in the transition period between the existing ISOL facilities and the construction of EURISOL.

To produce the RIBs, a very energetic proton beam is directed to a target, producing radioactive nuclei through fission, spallation and fragmentation reactions. The radionuclides are then extracted from the target, ionised, mass-separated and post-accelerated to different energies, depending on the applications. Alternatively, the proton beam can be directed to a converter, producing intense neutron fluences, which in turn induce fission in a fission target. Although the beam power varies greatly between the three (2 kW for ISOLDE, 6-10 kW for HIE-ISOLDE and 4 MW for EURISOL), these projects have many aspects in common related to Radiological Protection and Nuclear Engineering. The main goal of this work consisted on the study of key aspects related with target development and Radiological Protection in the production of RIBs using the ISOL method.

Computational studies were undertaken using Monte Carlo simulations in order to perform the neutronics, dose-rate and activation assessment of the two aforementioned facilities, to identify eventual "show stoppers" from the Radiological Protection and Safety point of view and to

optimise the target configurations to improve the perfomance of the systems.

10.1 EURISOL - Radiation Protection, Dosimetry and Activation Studies

The multi-MW target station of the EURISOL facility was the starting point for the studies presented in this thesis. A comprehensive Radiological Protection and Safety study of the target station was undertaken, assuming two alternative configurations with different materials. FLUKA was used to compute the very intense neutron fluences (with peak values of the order of 10^{15} neutrons/cm^2/s) in the targets region and the fission rates in the targets. In one of the configurations, a total fission rate of 6.4×10^{15} fissions/s in the six targets was predicted, using ^{235}U as fissile material, a result which surpasses the aimed fission rate of 10^{15} fissions/s foreseen for the EURISOL target station. From the neutronics point of view, this result shows that the design of the target system is well optimised for fission in ^{235}U. Furthermore, the flexible design of the fission targets allows the use of different combinations of moderators and target materials, an important feature in a facility which aims at increasing not only the intensity but also the variety of the produced beams.

The unprecedentedly high neutron and proton fluences in the targets area of the multi-MW target station of the EURISOL facility will raise several problems related to Radiological Protection. In the first place, adequate shielding is required to contain the extremely high radiation levels inside the facility; for this reason, the spallation and fission targets will be shielded from the control rooms by several meters of concrete. But as important as an adequate shielding is the assessment of the material activation in the targets and surrounding materials. In this study, the activation of the extraction tubes containing the fission targets was studied in detail. The extraction tubes are particularly important in this case since they have to be exchanged periodically (typically every three months), and the residual activities of their components must be known as accurately as possible to determine the conditions in which the extraction tubes will be handled and stored.

Different materials were tested in the fission target container and structural materials. In the container, tantalum was tested in the first place and molybdenum as an alternative. The simulations showed that the activation of tantalum was huge when compared to molybdenum, with even higher activities than the fissile material itself. In the structural materials, L316 stainless steel was the first candidate material, with aluminium as an option. In this case, aluminium was much less activated than stainless steel. From the Radiological Protection and Safety point of view, it is clear that molybdenum should be preferred to tantalum for the fission target container and aluminium preferred to stainless steel for the structural materials, as long as it meets the necessary structural requirements.

Besides the fission target container and the structural materials, the specific activities for several cooling periods were estimated in the fission target, cooling water, connectors and cables, moderators, reflectors and cryogenic panels. Along with the activities, the lists of the nuclides with the greatest contributions to the activities were also presented, containing important information about the long-lived isotopes which accumulate in the materials. The evolution of the ambient dose equivalent rates in the most important regions of the extraction tubes was also included, showing that the most activated regions could have doses of the order of 100 Sv/h ten years after the stoppage of the proton beam. The high residual doses resulting from the activated components will be a major issue to solve in the coming years, in order to prove the scientific, technological and engineering feasibility of the EURISOL concept before the construction of EURISOL gets underway. The manipulation of the targets and extraction tubes during the maintenance periods will have to be totally executed by advanced remote control systems.

10.2 ISOLDE - Target Optimisation and Radiological Protection Studies

10.2.1 Optimization Studies

The second part of this work consisted in the detailed study of the performance of the UC_x target system of the ISOLDE facility. The model of the target system was implemented in FLUKA, with and without converter, and simulations of neutron and proton fluences in the targets were carried out to evaluate the spectra of particles reaching the UC_x target. After that, additional simulations were performed to calculate the residual nuclei produced in the target. The main objective was to propose an optimisation for the target system that would enhance the production of neutron-rich isotopes while reducing the contamination by neutron-deficient isobars.

To benchmark the simulations, two sets of cross-sections were used:

- FLUKA cross sections, and
- ABRABLA+TALYS cross sections (TALYS from 0 to 200 MeV and ABRABLA from 200 MeV to 2 GeV).

In this first benchmark, which was conducted for the direct beam configuration (without converter), the yields calculated with ABRABLA+TALYS cross sections were closer to the experimental yields from the ISOLDE database than the ones calculated using FLUKA cross sections.

To produce beams of neutron-rich isotopes with low backgrounds of neutron-deficient isobars, a tungsten converter has been used at ISOLDE for the past ten years to produce neutron fluences

with the primary proton beam. When fission is induced by these neutrons, which, unlike the primary beam, have energies mainly in the MeV region, the production of neutron-deficient contaminants is reduced. The first simulations of the converter configuration showed clearly that, even when shooting on the converter, there was still a significant amount of energetic protons reaching the UC_x target. The first step after the benchmark was, therefore, to propose new designs of the converter-target system that minimised the fluences of energetic protons in the UC_x target, while keeping or even increasing the fluences of low-energy neutrons. Different radii and lengths were tested for the target and converter, and the effects of several combinations in the fluences of protons and neutrons reaching the target were evaluated. Two alternative target configurations were proposed based on these studies: a simpler version with thicker and shorter targets (Fig. 7.16) and a more complex version with a UC_x target with the shape of a cylindrical shell, concentric with the converter and surrounding it completely (Fig. 7.22).

Focus was given to the production of ^{80}Zn and ^{130}Cd, with the objective of suppressing the production of the corresponding isobars, ^{80}Rb and ^{130}Cs. Simulations of in-target yields with the proposed configurations predicted improvements in the purity of these neutron-rich isotopes by a factor of 10-50, depending on the tested configurations. Simulations with proton beam energies of 2 GeV were also run, and the results indicate that after ISOLDE is upgraded to HIE-ISOLDE the improvements with the new configurations may be further enhanced.

To test the improvements predicted by the simulations, a prototype target system was built at ISOLDE and tested during the week of October 22-26, 2012. The prototype version was based on the simplest of the two proposed configurations, but several compromises had to be taken to make it easier to build, in order to test it before the end of 2012. After the final design of the prototype was accomplished, simulations with the new configuration predicted improvements in the purity of the beams by factors in the interval 20-50. Although with reduced intensities, it was shown that the prototype system was well suited to test the validity of the proposed optimisations.

The experimental tests confirmed the expectations, showing an improvement in the ratio ^{80}Zn/^{80}Rb by a factor of 200, exceeding the predictions from the simulations by a factor of 5-10. This was the result of a suppression of the order of 10^3 in the production of the contaminant ^{80}Rb, while the production of ^{80}Zn was decreased by less than an order of magnitude. In this second benchmark, FLUKA was able to make better predictions of the distributions of nuclides produced in the target than ABRABLA+TALYS.

10.2.2 Radiological Protection Studies

Finally, a Radiological Protection study comparing the performance of the standard ISOLDE target system with the prototype configuration was presented, assessing the ambient dose equiv-

alent rates during operation and after shutdown, for several cooling periods. The specific activities due to the activation of the target materials were also assessed, and lists of the nuclides contributing to those activities were compiled. Furthermore, the performance of both target systems when shooting on the target or on the converter were also compared.

It was seen that the magnitude and the evolution of the residual dose rates were similar in the two target systems, shooting on target or on converter. When shooting on converter, tungsten is the major contributor to the ambient dose equivalent rate in the first 10 years after irradiation; since the prototype target system has more tungsten than the standard system, the amount of radioactive waste will be greater in the prototype configuration. The production of polonium isotopes, and most importantly of ^{210}Po, is one of the major causes of concern, especially when shooting directly on the target.

Overall, the results reported in this study show that it is possible, with simple changes in the layouts of the target systems, to increase the production of beams of neutron-rich isotopes while reducing the contaminations by neutron-deficient isobars, which are difficult to suppress through chemical selection. Since the absolute figure of merit for any radioactive ion beam facility comes from both its delivered beam intensities and their purities, this work provides a good example of how future increases of the primary beam intensities and energies at HIE-ISOLDE and EURISOL can be best exploited to deliver higher rates of purer beams around the doubly-magic nuclei ^{78}Ni and ^{132}Sn.

10.3 General Conclusions

Projects like ESS, MYRRHA and EURISOL are at the forefront of the ongoing pursuit for increasingly bright neutron sources; the construction of their proposed facilities involves complex Nuclear Technology and Radiological Protection design studies executed by multidisciplinary teams of scientists and engineers from different branches of Science and Engineering. Given the results presented in this work, it is not an overstatement to say that Monte Carlo simulation programs are nowadays an indispensable tool in the R&D studies associated with the design and operation of such facilities. For this reason, and in spite of the increasing availability of computer power and sophisticated codes, further improvements in the simulation tools are needed in order to improve the accuracy and reliability of the results. Accurate nuclear data sets covering wider energy ranges and more particles and reactions is one of the top requirements to improve the reliability of Monte Carlo simulations.

The studies presented in this thesis provide an overview of how those R&D studies are carried out. The neutronics and Radiological Protection studies for the multi-MW target station of the EURISOL facility are an example of how simulation tools can be used to identity and help to address the technological challenges posed by such innovative nuclear technology systems.

Alternative materials and designs can be proposed based on the simulations, to increase the neutronics performance of the systems or to reduce the residual dose rates after irradiation, arising from the activation of the targets and surrounding materials.

The second part of this work, on the other hand, illustrates the role that existing facilities play in the development of technologies to be used in future facilities. The optimisation studies of the ISOLDE target system resulted in the design of two alternative configurations; one of them, with some modifications, was built as a prototype to test the premises on which the optimisation studies were founded. The successful experimental tests with the prototype configuration show not only that it is possible to produce purer beams of neutron-rich isotopes using existing technology, but also how the increased beam energies and intensities that will become available in the future can be applied to produce even purer beams with increased intensities. With the knowledge acquired in these studies, it is easy to imagine new ways of exploring the flexible design of the EURISOL fission target systems to produce purer beams of neutron-rich isotopes.

10.4 Future Work

As mentioned in Chapter 8, the major achievement of this work was the successful experimental tests of the prototype configuration, which showed that the optimisations studies presented in Chapter 7 are valid and can be used to implement innovative designs in new target systems. The first obvious step after this work will be the construction of a target system similar to the more complex alternative proposed in Chapter 7, which should be able to produce beams of neutron-rich isotopes not only with enhanced purities but also with increased intensities, unlike the prototype configuration. The construction of such a target system was not possible in the limited amount of time before the Long Shutdown at CERN, which started in December of 2012, but will certainly happen in the near future. Furthermore, the lessons learned from this work will open the door to further developments of alternative target systems, and the construction of HIE-ISOLDE will present new opportunities to test the proposed optimisations with increased proton beam energies and intensities.

References

[1] IAEA. Development opportunities for small and medium scale accelerator driven neutron sources. Report of a technical meeting held in Vienna, International Atomic Energy Agency, Physics section, 2005.

[2] J. Carpenter. Neutron sources for materials research. In *Tenth National School on Neutron and X-ray Scattering*, September 2008.

[3] J. Cornell. The EURISOL report; a feasibility study for a European Isotope-Separation-On-Line Radioactive Ion Beam facility. Technical report, GANIL, France, 2003.

[4] Y. Blumenfeld et al. Facilities and methods for radioactive ion beam production. *Phys. Scr.*, T152, 2013.

[5] Y. Blumenfeld. Radioactive ion beam facilities in Europe. *Nucl. Instr. and Meth. B*, 266: 4074–4079, 2008.

[6] F. Chautard and G. Sénécal. Operation status of high intensity ion beams at GANIL. In *11th International Conference on Heavy Ion Accelerator Technology (HIAT09)*, 2009.

[7] F. Marti et al. Commissioning of the coupled cyclotron system at NSCL. *AIP Conf. Proc.*, 600(64), 2001.

[8] A. Adonin and R. Hollinger. Development of high current Bi and Au beams for the synchrotron operation at the GSI accelerator facility. *Rev. Sci. Instrum*, 83(02A505), 2012.

[9] H. Sakurai. Spectroscopy on neutron-rich nuclei at RIKEN. *Eur. Phys. J. A*, 25(s01):403–408, 2005.

[10] A. Herlert. The ISOLDE Facility. *Nucl. Phys. News*, 20(4), 2010.

[11] A. Villari et al. RNB production at SPIRAL/GANIL. *AIP Conf. Proc.*, 576(254), 2001.

[12] G. C. Ball et al. Physics with reaccelerated radioactive beams at TRIUMF-ISAC. *J. Phys. G: Nucl. Part. Phys*, 38(024003), 2011.

[13] NuPECC. Perspectives of Nuclear Physics in Europe – NuPECC Long Range Plan 2010. Technical report, Strasbourg: European Science Foundation, 2010.

[14] Y. Blumenfeld et al. EURISOL Design Study: toward the ultimate ISOL facility for Europe. *Nucl. Phys. News*, 19(1):22–27, 2009.

[15] Y. Blumenfeld. Developments at ISOL facilities: from ISOLDE towards EURISOL. *AIP Conf. Proc.*, 1024:467–474, 2010.

[16] Guenther Rosner. Future Facility: FAIR at GSI. *Nucl. Phys. B*, 167:77–81, 2007.

[17] G Münzenberg and H Geissel. NUSTAR - presence and prospects of nuclear structure research at GSI and FAIR. *J Phys. Conf. Ser.*, 413(012006), 2013.

[18] Marek Lewitowicz. Status of the SPIRAL2 Project. *Acta Phys. Pol. A*, 42, 2011.

[19] Marek Lewitowicz. The SPIRAL2 Project and experiments with high-intensity rare isotope beams. *J. Phys. Conf. Ser.*, 312, 2011.

[20] A. Andrighetto et al. Production of high-intensity RIB at SPES. *Nucl. Phys. A*, 834:754c–757c, 2010.

[21] G. Bollen. FRIB - Facility for Rare Isotope Beams. *AIP Conf. Proc.*, 1224(432), 2010.

[22] L. Merminga et al. ARIEL: TRIUMF's Advanced Rare Isotope Laboratory. In *Proceedings of IPAC2011, San Sebastian, Spain*, 2011.

[23] Jung Keun Ahn. Overview of the KoRIA Facility for Rare Isotope Beams. *Few-Body Syst*, 54:197–204, 2013.

[24] L. WeiPing. BRIF and CARIF progress. *Sci. China Phys. Mech. Astron.*, 54:s14–s17, 2011.

[25] Weiren Chou. Spallation Neutron Source and Other High Intensity Proton Sources. In *Accelerator Physics, Technology and Applications. Selected Lectures of the OCPA International Accelerator School 2002*, pages 231–255. World Scientific Publishing Co. Pte. Ltd., 2004.

[26] Jie Wei et al. China Spallation Neutron Source: Design, R&D, and outlook. *Nucl. Instr. and Meth. A*, 600(1):10–13, 2009.

[27] G. S. Bauer. Overview on spallation target design concepts and related materials issues. *J. Nucl. Mater.*, 398:19–27, 2010.

[28] T. Obara et al. Fundamental study of polonium contamination by neutron irradiated lead–bismuth eutectic. *J. Nucl. Mater.*, 343:297–301, 2005.

[29] Marisa Medarde et al. Lead–gold eutectic: An alternative liquid target material candidate for high power spallation neutron sources. *J. Nucl. Mater.*, 411:72–82, 2011.

[30] G.A. Bartholomew. The aecl-study for an intense neutron generator. Report aecl-2600, Chalk River Laboratory of Atomic Energy, 1966.

[31] J. Carpenter. History of spallation neutron sources. Australian Nuclear Science and Technology Organisation, Lucas Heights, 15 November 2012.

[32] Masayoshi Kawai et al. Fabrication of a tantalum-clad tungsten target for {KENS}. *Journal of Nuclear Materials*, 296(1–3):312–320, 2001.

[33] K.C Littrell et al. Present status and perspectives on neutron scattering instrumentation development at {IPNS}. *Physica B*, 311(1–2):112 – 116, 2002.

[34] Paul W. Lisowski and Kurt F. Schoenberg. The los alamos neutron science center. *Nucl. Instr. and Meth. A*, 562(2):910 – 914, 2006.

[35] Andrew Taylor. PROGRESS at the ISIS Facility. *Physica B*, 385-386:728–731, 2006.

[36] W.E. Fischer. {SINQ} — the spallation neutron source, a new research facility at {PSI}. *Physica B: Condensed Matter*, 234–236:1202–1208, 1997.

[37] D. Reggiani et al. Simulation of a Beam Rotation System for the SINQ Spallation Source at PSI. In *Proceedings of IPAC2013*, Shanghai, China, 2013.

[38] A.Yu. Konobeyev et al. Analysis of nuclide production in the {MEGAPIE} target. *Nucl. Instr. and Meth. A*, 605(3):224–232, 2009.

[39] M. Wohlmuther and W. Wagner. PIE preparation of the MEGAPIE target. *J. Nucl. Mater.*, 431(1–3):10–15, 2012.

[40] 24.05.2013 - MEGAPIE samples delivered to partners for post irradiation investigation. Retrieved on June 3, 2013. URL `http://www.psi.ch/gfa/large-research-facilities-gfa`.

[41] Fujio Maekawa et al. First neutron production utilizing J-PARC pulsed spallation neutron source JSNS and neutronic performance demonstrated. *Nucl. Instr. and Meth. A*, 620:159–165, 2010.

[42] Shoji Nagamiya. J-PARC project and its science. *Prog. Part. Nucl. Phys.*, 67(2):580–593, 2012.

[43] Takashi Naoe. Damage inspection of the first mercury target vessel of JSNS. *J. Nucl. Mater.*, http://dx.doi.org/10.1016/j.jnucmat.2013.04.049, 2013.

[44] K. Yamamoto. J-parc recovery status. In *52nd ICFA Advanced Beam Dynamics Workshop on High-Intensity and High-Brightness Hadron Beams*, 2012.

[45] How SNS Works. Retrieved on September 26, 2013. URL `http://neutrons.ornl.gov/facilities/SNS/works.shtml`.

[46] T.E. Mason et al. The spallation neutron source in oak ridge: A powerful tool for materials research. *Physica B: Condensed Matter*, 385–386, Part 2:955 – 960, 2006.

[47] T. Hardek. Status of the Oak Ridge Spallation Neutron Source (SNS) RF Systems. In *Proceedings of 2011 Particle Accelerator Conference, New York, NY, USA*, 2011.

[48] M. Lindroos et al. The european spallation source. *Nucl. Instr. and Meth. B*, 269(24):3258–3260, 2011.

[49] M. Magán. Neutron performance analysis for ESS target proposal. *Nucl. Instr. and Meth. A*, 680:61–68, 2012.

[50] Colin Carlile. The current status of the ESS project. NUPECC, NBI, Copenhagen, 15th June, 2012.

[51] G. S. Bauer. Concept of a Fault Tolerant Linear Accelerator as Proposed in the SNQ Project. In *Utilisation and Reliability of High Power Proton Accelerators*, pages 211–226. Nuclear Energy Agency, 1998.

[52] H. Abderrahim et al. ADS White Paper. Accelerator and Target Technology for Accelerator Driven Transmutation and Energy Production. Retrieved on June 4, 2013, from http://science.energy.gov/~/media/hep/pdf/files/pdfs/ADS_White_Paper_final.pdf, 2010.

[53] IAEA Power Reactor Information System. The Database on Nuclear Power Reactors. Retrieved on June 4, 2013. URL `http://www.iaea.org/pris/`.

[54] A. Stanculescu. Accelerator Driven Systems (ADSs) for nuclear transmutation. *Ann. Nucl. Energy*, http://dx.doi.org/ 10.1016/j.anucene.2013.02.006, 2013.

[55] Guojun Hu. Investigation of target in C-ADS and IAEA ADS benchmark. *arXiv:1211.0093 [nucl-th]*, 2012.

[56] H. Geng et al. The MEBT design for the china accelerator driven system. In *Proceedings of IPAC2011, San Sebastian, Spain*, 2011.

[57] H. Abderrahim. MYRRHA – A multi-purpose fast spectrum research reactor. *Energ. Convers. Manage.*, 2012.

[58] H. Abderrahim. MYRRHA, a Multipurpose hYbrid Research Reactor for High-end Applications. *Nucl. Phys. News*, 20(1):24–28, 2010.

[59] MYRRHA: Multi-purpose hybrid research reactor for high-tech applications. Retrieved on June 4, 2013, from http://myrrha.sckcen.be, 2013.

[60] MYRRHA Figures. Retrieved on September 30, 2013. URL `http://myrrha.sckcen.be/en/Media_gallery/`.

[61] W. Maschek others. Safety and design concepts of the 400 MW_{th}-class EFIT accelerator driven transmuter and considerations for further developments. *Energ. Convers. Manage.*, 51(9):1764–1773, 2010.

[62] G. Lawrence et al. ATW accelerator technology in US roadmap. *Prog. Nucl. Energ.*, 38 (1–2):25–64, 2001.

[63] ICRP. The 2007 Recommendations of the International Commission on Radiological Protection. ICRP Publication 103. *Ann. ICRP*, 3(2-4), 2007.

[64] ICRP. 1990 Recommendations of the International Commission on Radiological Protection. ICRP Publication 60. *Ann. ICRP*, 21(1-3), 1991.

[65] ICRP. Recommendations of the ICRP. ICRP Publication 26. *Ann. ICRP*, 1(3), 1977.

[66] ICRP. Relative Biological Effectiveness, Radiation Weighting and Quality Factor. ICRP Publication 92. *Ann. ICRP*, 33(4), 2003.

[67] ICRU. ICRU Report 33 - Radiation Quantities and Units, 1980.

[68] C. Wernli. External Dosimetry: Operational Quantities and their Measurements. In *11th International Conference of the International Radiation Protection Association (IRPA), Madrid*, 2004.

[69] ICRU. ICRU Report 85 - Fundamental Quantities and Units for Ionizing Radiation (Revised). *Journal of the ICRU*, 11(1), 2011.

[70] L. Papiez and J. Battista. Radiance and particle fluence. *Phys. Med. Biol.*, 39:1053–1062, 1994.

[71] ICRP. Conversion Coefficients for use in Radiological Protection against External Radiation. ICRP Publication 74. *Ann. ICRP*, 26(3–4), 1996.

[72] ICRP. Conversion Coefficients for Radiological Protection Quantities for External Radiation Exposures, ICRP Publication 116. *Ann. ICRP*, 40(2–5), 2010.

[73] I. Kawrakow et al. The EGSnrc Code System: Monte Carlo Simulation of Electron and Photon Transport. PIRS Report 701. Technical report, National Research Council of Canada, Ottawa, 2009.

[74] G. Battistoni et al. The FLUKA code: Description and benchmarking. *AIP Conf. Proc.*, 896: 31–49, 2007.

[75] A. Ferrari et al. *FLUKA: a Multiparticle Transport Code.* CERN, 2005-10, INFN/TC-05/11, SLAC-R-773, 2011.

[76] H. Iwase et al. Development of a general-purpose particle and heavy ion transport Monte Carlo code. *J. Nucl. Sci. Technol.*, 39:1142–1151, 2002.

[77] D. B. Pelowitz. *MCNPX user's manual version 2.5.0.* Los Alamos National Laboratory (LANL), LA-CP-05-0369, 2005.

[78] S. Agostinelli et al. GEANT4 – a simulation toolkit. *Nucl. Instr. and Meth. A*, 506:250–303, 2003.

[79] ICRP. Adult Reference Computational Phantoms. ICRP Publication 110. *Ann. ICRP*, 39(2), 2009.

[80] Y. Romanets. *Nuclear Technology, Dosimetry and Radiological Protection Aspects of Accelerator Driven Systems (ADS) and Radioactive Ion Beam (RIB) facilities.* PhD thesis, Instituto Superior Técnico, Universidade Técnica de Lisboa, 2012.

[81] A. Gerasimov et al. Accumulation of Activation Products in Pb-Bi, Tantalum and Tungsten Targets of ADS. In *Actinide and Fission Product Partitioning and Transmutation.* Nuclear Energy Agency - Organisation for Economic Co-operation and Development, 2000.

[82] ICRP. Compendium of Dose Coefficients based on ICRP Publication 60. ICRP Publication 119. *Ann. ICRP*, 41(Suppl.), 2012.

[83] I. Slessarev. Long term radiotoxicity. In *Lectures given at the Workshop on Nuclear Data and Nuclear Reactors: Physics, Design and Safety*, Trieste, 2000.

[84] R. Moormann et al. Safety aspects of high power targets for European spallation sources. In *International Conference on the Physics of Reactors "Nuclear Power: A Sustainable Resource"*. Casino-Kursaal Conference Center, Interlaken, Switzerland, September 14-19, 2008.

[85] Firooz Khosraviyani and James McCarry. The buffon needle problem extended. *Texas College Mathematics Journal*, 2005.

[86] Roger Eckhardt. Stan Ulam, John Von Neumann, and the Monte Carlo Method. *Los Alamos Science*, 1987.

[87] N. Metropolis. The beginning of the Monte Carlo Method. *Los Alamos Science*, 1987.

[88] F James. Monte carlo theory and practice. *Reports on Progress in Physics*, 43(9):1145–1189, 1980.

[89] I. Sobol. *A Primer for the Monte Carlo Method.* CRC Press, 1994.

[90] A. Bielajew. *Fundamentals of the Monte Carlo Method.* The University of Michigan, 2001.

[91] Malvin H. Kalos and Paula A. Whitlock. *Monte Carlo Methods: Basics.* John Wiley and Sons, 1986.

[92] K. S. Krane. *Introductory Nuclear Physics.* John Wiley and Sons, 1988.

[93] S. Glasstone and A. Sesonske. *Nuclear Reactor Engineering.* D. Van Nostrand Company, 1963.

[94] OECD/NEA Data Bank. The JEFF-3.1.1 Nuclear Data Library. JEFF Report 22, 2009.

[95] James J. Duderstadt and Louis J. Hamilton. *Nuclear Reactor Analysis.* John Wiley and Sons, 1976.

[96] OECD/NEA Data Bank. The JEFF-3.1 Nuclear Data Library. JEFF Report 21, 2006.

[97] L. Marques. Determinação da secção eficaz de captura neutrónica do ^{94}Zr utilizando o espectrómetro TOF no CERN. Master's thesis, Universidade de Lisboa, 2004.

[98] C. Pardo. *New radiative neutron capture measurement of ^{207}Pb and ^{209}Bi.* PhD thesis, Universidad de Valencia, 2004.

[99] Ronald Allen Knief. *Nuclear Energy Technology - Theory and Practice of Commercial Nuclear Power.* McGraw-Hill, 1981.

[100] A. D. Galanin. *Thermal Reactor Theory.* Pergamon Press, 1960.

[101] John R. Lamarsh. *Introduction to Nuclear Reactor Theory.* Addison-Wesley, 1966.

[102] A. X. da Silva and V. R. Crispim. Moderator-collimator-shielding design for neutron radiography systems using ^{252}Cf. *Applied Radiation and Isotopes*, 54(2):217–225, 2001.

[103] M. M. El-Wakil. *Nuclear Heat Transport.* American Nuclear Society, 1981.

[104] Herbert S. Isbin. *Introductory Nuclear Reactor Theory.* Reinhold Publishing Corporation, 1963.

[105] Raymond L. Murray. *Introduction to Nuclear Engineering.* Prentice-Hall, 1961.

[106] D. Filges and F. Goldenbaum. *Handbook of Spallation Research.* WILEY-VCH Verlag GmbH & Co. KGaA, Weinheim, 2009.

[107] L. deBroglie. Recherches sur la théorie des quanta. *Ann. Phys-Paris*, 10(III), 1925.

[108] T. Enqvist et al. Isotopic yields and kinetic energies of primary residues in 1 A GeV ^{208}Pb+p reactions. *Nucl. Phys. A*, 686(1–4):481–524, 2001.

[109] G. Russell. Spallation physics – an overview. In *Proceedings of ICANS XI, October 22 – 26, 1990, Tsukuba, Japan, KEK Report 90-25*, pages 291–299, 1991.

[110] H. Bertini. Intranuclear-cascade calculation of the secondary nucleon spectra from nucleon – nucleus interactions in the energy range 340 to 2900 mev and comparisons with experiment. *Phys. Rev.*, 8(4):1711–1730, 1969.

[111] R. Hofstadter. Electron scattering and nuclear structure. *Rev. Mod. Phys.*, 28(3):214–254, 1956.

[112] D. Griffiths. *Introduction to Elementary Particles.* WILEY-VCH Verlag GmbH & Co. KGaA, Weinheim, 2004.

[113] E. Segre. *Nuclei and Particles: An Introduction to Nuclear and Subnuclear Physics.* W. A. Benjamin, Inc, 1965.

[114] W. M. Yao et al. Review of Particle Physics. *J. Phys. G: Nucl. Part. Phys.*, 33(1), 2006.

[115] J. Cugnon et al. The INCL model for spallation reactions below 10 GeV. *Adv. Space Res.*, 40(9):1332–1338, 2007.

[116] A. Boudard et al. Intranuclear cascade model for a comprehensive description of spallation reaction data. *Phys. Rev. C*, 66(4):2002, 2002.

[117] Y. Yariv and Z. Frankel. Intranclear cascade calculation of high-energy heavy-ion interactions. *Phys. Rev. C*, 20(6):2227–2243, 1979.

[118] S. Mashnik and A. Sierk. Recent developments of the cascade-exciton model of nuclear reactions. *J. Nucl. Sci. Tech.*, S2(arXiv:nucl-th/0208074):720–725, 2002.

[119] V. Weisskopf. Statistics and nuclear reactions. *Phys. Rev.*, 52:295–303, 1937.

[120] I. Dostrovsky et al. Monte carlo calculations of nuclear evaporation processes. V. emission of particles heavier than ^{4}He. *Phys. Rev.*, 118(3):791–793, 1960.

[121] S. Furihata and T. Nakamura. Calculation of nuclide production from proton induced reactions on heavy targets with INC/GEM. *J. Nucl. Sci. Technol.*, Suppl.(2):758–761, 2002.

[122] J. J. Gaimard et al. A reexamination of the Abrasion-Ablation model for the description of the nuclear fragmention reaction. *Nucl. Phys. A*, 531:709–745, 1991.

[123] A.R. Junghans. Projectile-fragment yields as a probe for the collective enhancement in the nuclear level density. *Nucl. Phys. A*, 629:635–655, 1998.

[124] R. Charity et al. Systematics of complex fragment emission in niobium-induced reactions. *Nucl. Phys. A*, 483:371–405, 1988.

[125] G. Battistoni and P. Sala. The treatment of nuclear effects for neutrino interactions in the FLUKA code. *Acta Phys. Pol. B*, 37(8):2361–2369, 2006.

[126] V. Vlachoudis. FLAIR: A Powerful But User Friendly Graphical Interface For FLUKA. In *Proc. Int. Conf. on Mathematics, Computational Methods & Reactor Physics (M&C 2009), Saratoga Springs, New York*, 2009.

[127] S. Simakov. Nuclear Data Activities at the IAEA Nuclear Data Section. In *20th International Conference "Nuclear Energy for New Europe", Bovec, Slovenia, September 12-15*, 2011.

[128] M.B. Chadwick et al. ENDF/B-VII.1 Nuclear Data for Science and Technology: Cross Sections, Covariances, Fission Product Yields and Decay Data. *Nucl. Data Sheets*, 112(12): 2887–2996, 2011.

[129] A. Koning et al. Validation of the JEFF-3.1 Nuclear Data Library. JEFF Report 23, OECD-NEA, 2013.

[130] K. Shibata et al. JENDL-4.0: A New Library for Nuclear Science and Engineering. *J. Nucl. Sci. Technol.*, 48(1):1–30, 2011.

[131] Chen Guo-Chang et al. Neutron nuclear data evaluation of actinide nuclei for CENDL-3.1. *Chin. Phys. C*, 36(9):823, 2012.

[132] ROSFOND-2010 Library, Retrieved on June 13, 2013. URL `http://www.ippe.ru/podr/abbn/english/libr/rosfond.php`.

[133] L. Aldama and A. Trkov. FENDL-2.1 – Update of an evaluated nuclear data library for fusion applications. Technical report, IAEA, 2004.

[134] A. Koning and D. Rochman. Modern Nuclear Data Evaluation With The TALYS Code System. *Nucl. Data Sheets*, 113:2841, 2012.

[135] R. Forest. Nuclear science and data needs for advanced nuclear systems. *Energ. Procedia*, 7:540–552, 2011.

[136] R. Capote et al. International Reactor Dosimetry and Fusion File . *Journ. ASTM Intern.*, 9 (4), 2012.

[137] The Nuclear Energy Agency. Retrieved on June 13, 2013. URL `http://www.oecd-nea.org/nea/`.

[138] N. Otuka et al. The Role of the Nuclear Reaction Data Centres in Experimental Nuclear Data Knowledge Sharing. In *Proceedings of the International Conference on Nuclear Data for Science and Technology (ND2010), Jeju, Korea, 26-30, April*, 2010.

[139] H. Henriksson. *CINDA Compilers Manual.* OECD/NEA Data Bank for the NRDC, May 2008.

[140] N. Soppera et al. Recent Upgrades to the Nuclear Data Tool JANIS. *J. Korean Phys. Soc.*, 59(2):1329–1332, 2011.

[141] A.J. Koning et al. *TALYS-1.4 – A nuclear reaction program*, 2011.

[142] R. Michel et al. Cross sections for the production of residual nuclides by low- and medium-energy protons from the target elements C, N, 0, Mg, Al, Si, Ca, Ti, V, Mn, Fe, Co, Ni, Cu, Sr, Y, Zr, Nb, Ba and Au. *Nucl. Instr. and Meth. B*, 129:153–193, 1997.

[143] F. Vivès et al. Investigation of the fission fragment properties of the reaction ^{238}U(n,f) at incident neutron energies up to 5.8 MeV. *Nucl. Phys. A*, 662:63–92, 2000.

[144] M. Ricciardi et al. Light nuclides produced in the proton-induced spallation of ^{238}U at 1 GeV. *Phys. Rev. C*, 73(014607):1–25, 2006.

[145] J. Taïeb et al. Evaporation residues produced in the spallation reaction ^{238}U + p at 1 A GeV. *Nucl. Phys. A*, 724(3-4):413–430, 2003.

[146] M. Bernas et al. Fission-residues produced in the spallation reaction ^{238}U + p at 1 A GeV. *Nucl. Phys. A*, 725:213–253, 2003.

[147] NuPECC. NuPECC Roadmap - Nuclear Physics in Europe: Highlights and Opportunities, Retrieved on June 4, 1997. URL `http://www.nupecc.org/report97/report97_pre/report97_pre.html`.

[148] J. Cornell. EURISOL-DS final report. Technical report, GANIL, France, 2009.

[149] A. Herrera-Martínez and Y. Kadi. Preliminary Study of the Liquid Metal Proton-to-Neutron Converter. Technical Report CERN-AB-06-013 ATB, European Organization for Nuclear Research (CERN), www.eurisol.org, 2006.

[150] A. Herrera-Martínez and Y. Kadi. EURISOL-DS multi-MW target: neutronic calculations for the baseline configuration of the multi-MW target. Technical Report CERN-AB-Note-2006-035-ATB, European Organization for Nuclear Research (CERN), www.eurisol.org, 2006.

[151] PIAFE, Collaboration. Radioactive beam production using a uranium fission source placed in the ILL high flux reactor. Technical report, Laboratoire de Physique Subatomique et de Cosmologie (LPSC), 1997.

[152] H. J. Maier et al. Target conception for the munich fission fragment accelerator. *Nucl. Instr. and Meth. A*, 438(1):185–189, 1999.

[153] O. Alyakrinskiy et al. EURISOL fission target design adapting MAFF concept. Technical report, Laboratori Nazionali di Legnaro (INFN-LNL) and Hulubei National Institute of Physics and Nuclear Engineering (IFIN-HH), http://www.eurisol.org, 2007.

[154] C. Kharoua and Y. Kadi. EURISOL-DS multi-MW target: preliminary study of the thermal behavior of the fission target inspired by the MAFF project. Technical Report CERN-AB-Note-2008-060 ATB, European Organization for Nuclear Research (CERN), http://www.eurisol.org, 2008.

[155] Y. Romanets and R. Luís. EURISOL multi-MW target MAFF configuration. radiological protection, radiation safety and shielding aspects. Technical report, CERN, http://cds.cern.ch/record/1356495/files/document.pdf, 2009.

[156] Swiss Legislation > SR 814.501 Radiological Protection Ordinance, Annex 3, Data for Operational Radiation Protection. Retrieved on October 5th, 2013. URL `http://www.admin.ch/ch/e/rs/814_501/app3.html#ahref0`.

[157] E. Lebbos et al. CERN n-TOF facility: waste calculations and dose rate simulations of the n-TOF spallation target. Technical report, CERN, 2007.

[158] L.P. Ekström and R.B. Firestone. WWW Table of Radioactive Isotopes, database version 2/28/99. From URL http://ie.lbl.gov/toi/index.htm, Retrieved on October 5th, 2013.

[159] A. Peurrung. Predicting ^{232}U content in uranium. Technical report, Pacific Northwest National Laboratory, 1998.

[160] A. V. Zvonarev et al. ^{60}Co production in BN-350 reactors. *Atom. Energy*, 77(6), 1994.

[161] IAEA. Manual for reactor produced radioisotopes. Technical report, IAEA, 2003.

[162] K. Langen et al. Production of 22na and other radionuclides by neutrons in al, sio2, si, ti, fe and ni targets: Implications for cosmic ray studies. In *32nd Annual Lunar and Planetary Science Conference, March 12-16, 2001, Houston, Texas, abstract no.1302*, 2001.

[163] K. Kim et al. Excitation Functions for the 27Al(p,x)22,24Na Nuclear Reactions up to 40 MeV. *J. Korean Phys. Soc.*, 59(2):1821–1824, 2011.

[164] Yu. E. Titarenko et al. Cross sections for monitor reactions 27Al((p, x)24Na, 27Al(p, x)22Na, and 27Al(p, x)7Be at proton energies in the range 0.04–2.6 GeV. *Phys. Atom. Nucl.*, 74(4):507–522, 2011.

[165] S. Rokni et al. Radiation studies for the environmental protection at the beam delivery system of the next linear collider. SLAC-PUB-8488, June 2000.

[166] ICRP. Conversion coefficients for use in radiological protection. *Ann. ICRP*, 26(3-4), 1996.

[167] K. Riisager. The HIE-ISOLDE project. *AIP Conf. Proc.*, 1012:106–110, 2008.

[168] S. Galés. Towards the next generation of radioactive ion beam facilities. *Nucl. Phys. A*, 722:148c–156c, 2003.

[169] ISOLDE-CERN. The ISOLDE Facility. Retrieved on March 6, 2013, from http://isolde.web.cern.ch/isolde/, 2013.

[170] J. Aysto. CERN's longest serving experimental facility. *Physics Reports*, 403-404:459–469, 2004.

[171] CERN. The accelerator complex. Retrieved on March 6th, 2013. URL `http://public.web.cern.ch/public/en/research/AccelComplex-en.html`.

[172] M. A. Fraser. *Beam Dynamics Studies of the ISOLDE Post-accelerator for the High Intensity and Energy Upgrade.* PhD thesis, University of Manchester, 2011.

[173] O. Kester et al. Accelerated radioactive beams from REX-ISOLDE. *Nucl. Instr. and Meth. B*, 204:20–30, 2003.

[174] J. Cederkall et al. REX-ISOLDE - experiences from the first year of operation. *Nucl. Phys. A*, 746:17c–21c, 2004.

[175] D. Voulot et al. Radioactive beams at REX-ISOLDE: present status and latest developments. *Nucl. Instr. and Meth. B*, 266:4103–4107, 2008.

[176] P.A. Butler et al. Through the looking glass: probing the nucleus using accelerated radioactive beams. *Nucl. Phys. A*, 751:485c–493c, 2005.

[177] M. Turríon et al. Management of ISOLDE yields. *Nucl. Instr. and Meth. B*, 266:4674–4677, 2008.

[178] V.N. Fedosseev et al. ISOLDE RILIS: New beams, new facilities. *Nucl. Instr. and Meth. B*, 266:4378–4382, 2008.

[179] M. Lindroos et al. HIE-ISOLDE. *Nucl. Instr. and Meth. B*, 266:4687–4691, 2008.

[180] P. Van Duppen and K. Riisager. Physics with REX-ISOLDE: from experiment to facility. *J. Phys. G: Nucl. Part. Phys.*, 38, 2011.

[181] P. Van Duppen. Isotope separation on line and post acceleration. *Lect. Notes Phys.*, 700: 37–77, 2006.

[182] E. Kugler. The ISOLDE facility. *Hyperfine Interact.*, 129:23–42, 2000.

[183] J. Ramos. Effect of calcium oxide microstructure on the diffusion of isotopes. Master's thesis, Universidade de Aveiro, 2012.

[184] F. Ames et al. Cooling of radioactive ions with the Penning trap REXTRAP. *Nucl. Instr. and Meth. A*, 538:17–32, 2005.

[185] I. Podadera. Preparation of cooled and bunched ion beams at ISOLDE-CERN. *Eur. Phys. J. A*, 25:743—744, 2005.

[186] B. H. Wolf et al. Commissioning results from the REXEBIS charge breeder. *Rev. Sci. Instrum.*, 2002.

[187] R. Catherall. The radioactive laboratory upgrade at ISOLDE, CERN. *Nucl. Phys. A*, 746: 379c–383c, 2004.

[188] U. Koster et al. ISOLDE beams of neutron-rich zinc isotopes : yields, release, decay spectroscopy. *AIP Conf. Proc.*, 798:315–326, 2005.

[189] R. Catherall et al. Radioactive ion beams produced by neutron-induced fission at ISOLDE. *Nucl. Instr. and Meth. B*, 204(235–239), 2003.

[190] T. Nilsson and M. Lindroos. HIE-ISOLDE: the technical options. Technical Report CERN-2006-013, European Organization for Nuclear Research (CERN), 2006.

[191] A. Herlert and Y. Kadi. The HIE-ISOLDE project. *J. Phys. Conf. Ser.*, 312(5):052010, 2011.

[192] Y. Kadi et al. Status and future perspectives of the HIE-ISOLDE project at CERN. In *Proceedings of IPAC2012, New Orleans, Louisiana, USA*, 2012.

[193] M. Borge et al. Motivations to receive a 2 GeV proton beam at ISOLDE / HIE-ISOLDE: Impact on radioisotope beam availability and physics program. Technical report, CERN, http://cds.cern.ch/record/1482729/files/INTC-O-016.pdf, 2012.

[194] R. Luís et al. Optimization studies of the CERN-ISOLDE neutron converter and fission target system. *Eur. Phys. J. A*, 48(90), 2012.

[195] U. Koster. Intense radioactive-ion beams produced with the ISOL method. *Eur. Phys. J. A*, 15:255–263, 2002.

[196] M. Dombsky and P. Bricault. High intensity targets for ISOL, historical and practical perspectives. *Nucl. Instr. and Meth. B*, 266:4240—4246, 2008.

[197] Y. Zhang and G.D. Alton. Design of high-power ISOL targets for radioactive ion beam generation. *Nucl. Instr. and Meth. A*, 521:72–107, 2004.

[198] C. Baktash et al. Scientific opportunities with an advanced isol facility. Technical report, Columbus White Paper, 1997.

[199] Hendrik Schatz. Rare isotopes in the cosmos. *Phys. Today*, 61:40–45, 2008.

[200] J. Lettry et al. Pulse shape of the ISOLDE radioactive ion beams. *Nucl. Instr. and Meth. B*, 126:130–134, 1997.

[201] T. E. Cocolios. Resonant laser ionization of polonium at RILIS-ISOLDE for the study of ground- and isomer-state properties. *Nucl. Instr. and Meth. B*, 266:4403–4406, 2008.

[202] ANSYS® Academic Research, Release 14.0, Help System, Coupled Field Analysis Guide, ANSYS, Inc.

[203] W. Wolf et al. On-line separation of short-lived nuclei by a multi-reflection time-of-flight device. *Nucl. Instr. and Meth. B*, 686:82–90, 2012.

[204] R. Kirchner. On the release and ionization efficiency of catcher-ion-source systems in isotope separation on-line. *Nucl. Instr. and Meth. B*, 70(1–4):186–199, 1992.

[205] R. Catherall. Future Developments at ISOLDE. ISOLDE Workshop and Users Meeting, CERN, 2012.